Proceedings of

ISUD 11

The 11th International Symposium on Ultrasonic Doppler Methods for Fluid Mechanics and Fluid Engineering

September 5-7, 2018
Berlin, Germany

Edited by:
Markus Juling
Noriyuki Furuichi

Proceedings of the 11th International Symposium on Ultrasonic Doppler Methods for Fluid Mechanics and Fluid Engineering

5-7 September 2018, Berlin, Germany

Editors:

- M. Juling *Physikalisch-Technische Bundesanstalt (PTB), Germany*
- N. Furuichi *National Institute of Advanced Industrial Science and Technology (AIST), National Metrology Institute of Japan (NMIJ), Japan*

Organizing Committee:

- Chair: M. Juling *Physikalisch-Technische Bundesanstalt (PTB), Germany*
- N. Furuichi *National Institute of Advanced Industrial Science and Technology (AIST), National Metrology Institute of Japan (NMIJ), Japan*
- S. Eckert *Helmholtz-Zentrum Dresden-Rossendorf (HZDR), MHD Department, Dresden, Germany*
- F. Heitmann *Physikalisch-Technische Bundesanstalt (PTB), Germany*
- J. Steinbock *Physikalisch-Technische Bundesanstalt (PTB), Germany*
- I. Huck *Physikalisch-Technische Bundesanstalt (PTB), Germany*
- R. Peper *Physikalisch-Technische Bundesanstalt (PTB), Germany*

Scientific Committee:

- Chair: J. Windhab *Food Process Engineering, Swiss Federal Institute of Technology Zurich (ETH), Switzerland*
- G. De Cesare *Laboratory of Hydraulic Constructions (LCH), Ecole Polytechnique Fédérale de Lausanne (EPFL), Switzerland*
- M. Mori *Division of Energy & Environmental Systems, School of Engineering, Hokkaido University, Sapporo, Japan*
- H. Kikura *Research Laboratory for Nuclear Reactors, Tokyo Institute of Technology, Ohokayama, Japan*
- Y. Tasaka *Division of Energy & Environmental Systems, School of Engineering, Hokkaido University, Sapporo, Japan*
- V. Bareš *Department of Hydraulics and Hydrology, Faculty of Civil Engineering, Czech Technical University (CTU) Prague, Czech Republic*
- J. Wiklund *INCIPIENTUS Ultrasound Flow Technologies AB, Sweden*
- B. Birkhofer *Swiss Re, Switzerland*
- C. Rennie *Department of Civil Engineering, University of Ottawa, Canada*
- S. Fischer *Ubertone, France*
- S. Eckert *Helmholtz-Zentrum Dresden-Rossendorf (HZDR), MHD Department, Dresden, Germany*
- R. Kotzé *INCIPIENTUS Ultrasound Flow Technologies AB, Sweden*
- D. Hurther *Université Grenoble Alpes, Laboratoire des Ecoulements Géophysiques et Industriels*
- H. Murakawa *Department of Mechanical Engineering, Kobe University, Kobe, Japan*

Quotation:

Juling, Markus and Furuichi, Noriyuki. Proceedings of the 11th International Symposium on
Ultrasonic Doppler Methods for Fluid Mechanics and Fluid Engineering, ISUD 11:
5 - 7 September 2018, Berlin, Germany. 2018. Physikalisch-Technische Bundesanstalt (PTB).

DOI: https://doi.org/10.7795/810.20190809

Table of Contents

Applied Flow I

Flow Metering and Mapping I

Signal Processing and Methodology I

* not included due to copyright restrictions

Fundamental and Enviromental Flow I

Signal Processing and Methodology II

Applied Flow II

* not included due to copyright restrictions

Flow Metering and Mapping II

Fundamental and Enviromental Flow II

* not included due to copyright restrictions

Author Index

Experimental Investigations of the Influence of Different Bottom Shapes on the Temperature and Velocity Fields in a Fermentation Tank with a Biological Multiphase Flow

Daniel Klembt[1], Heiko Meironke[1]

[1]University of Applied Science Stralsund, Department of Fluid Mechanics and Apparatus Engineering,
Zur Schwedenschanze 15, 18435 Stralsund, Germany

In this investigation, the influence between different bottom shapes of fermentation tanks and the different resulting velocity and temperature fields at the beer production are investigated. The difficulties of an investigation with a biological fermentation fluid (wort) are the many complex interactions between the different three phases (yeast, carbon dioxide bubbles, wort). Furthermore, natural convection processes are superimposed by rising gas bubbles and the high turbidity of the fluid only allows acoustic or magnetic resonance tomography velocity measurements. This leads to high requirements for the measurement technology and the following evaluation. In this study, latest measurements with two coupled UDV-Systems for a high-resolution velocity field combined with a data acquisition unit for the temperature field in the fermentation tank with two bottom shapes (conical, hemispherical) are presented. The new experimental setup consists of a velocity field of 16 x 2 MHz and 19 x 4 MHz transducers, 56 temperature sensors and enables an improved resolution compared to the previous measurements. For a precise evaluation, the filtering of interferences is carried out by an additional, self-written program. Finally, the experimental analysis of the flow and temperature measurements and the transport mechanism (momentum and heat) with a real fermentation fluid, in different bottom shapes, are presented.

Keywords: Ultrasonic Doppler Velocimetry, flow field measurements, biological fluid, multiphase flow

1. Introduction

In the context of investigations of multiphase flows, the beer production is currently being investigated, especially fermentation, maturation and storage in cooperation with the local brewery. Beer may not be as old as man himself. But beer-like, fermented beverages have always been an important part of human civilization. The ancient Babylonians, for example, knew 20 different varieties. These include black beer, red beer, sweet beer, sour beer. Before them, the Sumerians were regarded as the high culture of brewing beer. The oldest proof of beer in Germany dates to around 800 BC. Many cultures regarded beer not only as a staple food, but also as a currency. In ancient Egypt, for example, slaves were paid exclusively in beer. Brewing beer is a craft that requires meticulous planning. [1]

The university has its own 350 litre fermentation tank with comprehensive acoustic flow and temperature measurement technology for the systematical investigation of the influence of the fermentation activity, distribution of yeast and occurring convection phenomena.

The description of the thermo-fluid dynamic processes and the economic benefit of this knowledge have despite increasing scientific and technological progress in this field still innovative potential especially in the structural design of the fermenter and in the effective control of the cooling zones.

In this study, the structural design will be analyzed against the background of the influence of different bottom shapes on the temperature and velocity fields in a fermentation tank with a biological multiphase flow.

There are two different configurations of the fermentation tank for the investigation. The first configuration is the conical and the second configuration is the hemispherical bottom. Nowadays the conical bottom shape is preferred in a modern European brewery and has a 60° to 70° cone angle.

2. Experimental Setup

2.1 Experimental Arrangement

For the experimental investigation of the flow and temperature fields, an existing experimental setup with a 350 litre fermentation tank with different bottom shapes will be used (see at figure 1). In this study, the tank is equipped with two different bottom shapes, a conical and a hemispherical bottom (375 litre). Several openings in the fermentation tank allows the integration of temperature sensors for the temperature field measurement and transducer for the flow field measurement.

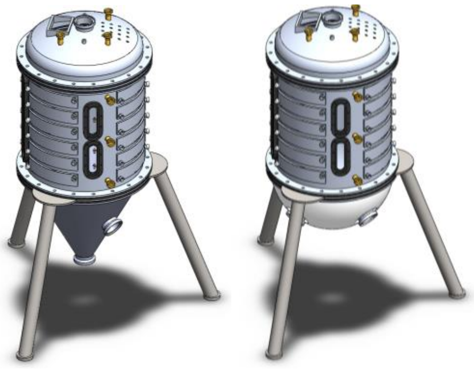

Figure 1: Fermentation tank with conical bottom shape (left) and hemispherical bottom shape (right)

https://doi.org/10.7795/810.20190809

For a defined managed fermentation process the tank is equipped with six separately controlled cooling or heating zones and one additional zone in each bottom (in figure 2 and figure 3 the cooling zones are additionally shown). To control the cooling zones during the fermentation and maturation process, a new completely re-engineered program was created on the software tool “LabView” for the triggering of control valves. This program is not only used for the control of the cooling zones but also allows the automated continuous data acquisition of the temperature and flow rates of the cooling liquid flow in the cooling zones. In this study, the program is used to hold defined temperatures at the selected process of the beer production.

2.2 Implementation of the temperature measurement

The temperature detection inside the tank, in contrast to earlier investigations, is now adjusted for the flow measurement system to enable a simultaneous measurement process. The temperature measurement arrangement for this study is carried out by a conventional measuring method in a grid array of 56 resistance temperature detectors (RTD). The installed temperature sensors in the grid of the fermentation tank are shown in figure 2. For a high accuracy, all detectors are calibrated with five cycles of a thermometer with the accuracy class A and the grid will be adjusted for each bottom shape.

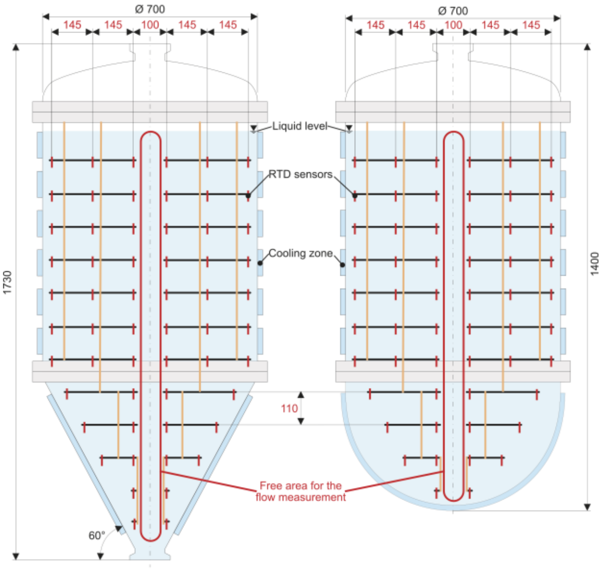

Figure 2: Temperature implementation and measuring fields in the cylindrical part and the conical (left) and hemispherical (right) bottom shape

2.3 Implementation of the flow measurement

The difficulties of a flow investigation with a biological fermentation fluid (wort) are the many complex interactions between the different three phases (yeast as solid, carbon dioxide bubbles as gas, wort as fluid). Furthermore, natural convection processes are superimposed by rising gas bubbles and the high turbidity of the fluid only allows acoustic or magnetic resonance tomography velocity measurements. This leads to high requirements for the measurement technology and the following evaluation. In case of that, the Ultrasonic Doppler Velocimetry are used. The measurement of the flow field is carried out by means of the Ultrasonic Velocity Profile Monitor System UVP-DUO from Met-Flow S.A. In this study, two coupled UDV-Systems for a high-resolution velocity field are combined with two different frequencies (2 MHz, 4 MHz). To reduce interference and for a higher accuracy, the transducers are now implemented with small sleeves, in the bottom shapes. The transducers are furthermore protected in front of the matching layer against destruction (acid and base cleaning, disinfection, fermentation residues) by a 0.5 mm plastic plate. The new implementation allows a cartesian grid not only in the cylindrical part but also in the bottom shapes.

The experimental setup consists of a velocity field of 19 x 4 MHz, 16 x 2 MHz transducers and enables an improved resolution compared to the previous measurements with model liquids. The velocity measuring arrays are shown in figure 3.

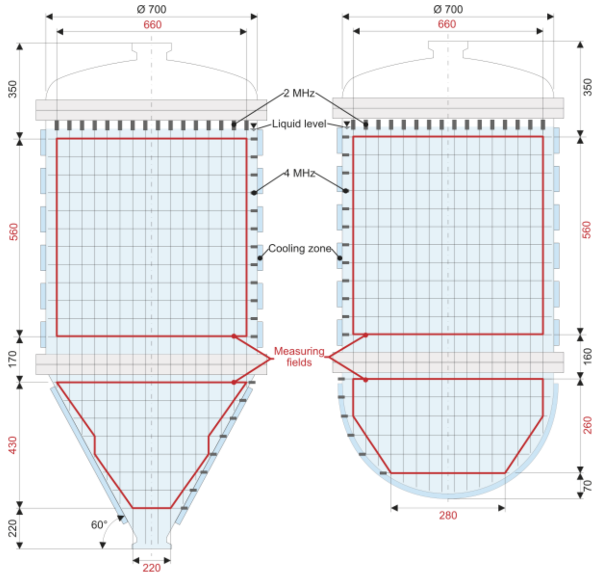

Figure 3: Measuring arrays for the velocity measurement in the cylindrical with conical (left) and hemispherical (right) bottom shape

The properties of the measuring field are shown in table 1. In the new arrangement, are 192 intersection points in the cylindrical part and additional 80 intersection points in the conical bottom and 84 intersection points in the hemispherical bottom.

Table 1: Properties of the measuring fields

measuring fields	cylindrical part	conical bottom	hemispherical bottom
Transducer (2 MHz)	16 (for the cylindrical part and the bottom shapes)		
Transducer (4 MHz)	12	8	6
intersection points	192	80	84

Each intersection point represented in table 1 consists of three-dimensional measuring volumes in the form of two combined truncated cones or in simplified form of two disks. In each disk, all Doppler shifted frequencies are calculated, averaged and checked for possible errors with a self-written program in order to reduce or remove the influence of bubbles, echoes and interferences. Finally, only one resulting vector is calculated for each intersection point. For a better understanding of the intersection points, the two special intersection points of the 2 MHz and 4 MHz transducer are shown in figure 4 and figure 5.

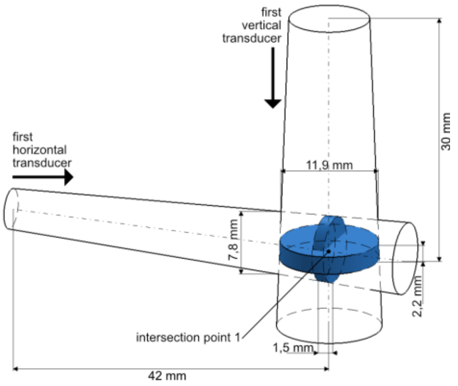

Figure 4: Smallest intersection point for both bottom shapes

Figure 4 shows the smallest intersection point in the investigation with a volume of 0.31 cm³, over which the average is calculated. Figure 5 shows the largest intersection point in the conical bottom shape with a volume of 14.33 cm³.

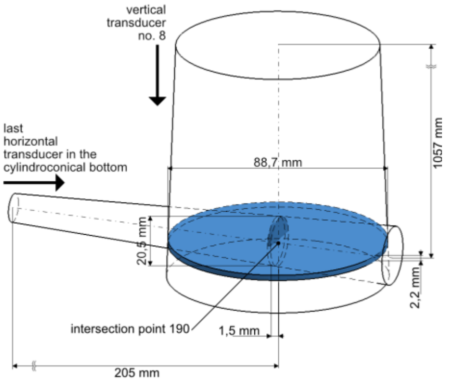

Figure 5: Largest intersection point in the conical bottom shape (lower middle)

2.4 Physical properties of the investigated fluid (fermenting wort)

In cooperation with the local brewery, two comparable beer wort`s with an original wort content of 12 %, two similar bottom-fermented yeasts and identically processes were used to compare the complex processes during real fermentation in the two bottoms.

Table 2 shows the experimental results for the physical properties of the fermenting wort. These properties change with the fermentation process and are therefore specified as a range.

Table 2: Physical properties of the fluid and gas

measuring fields	physical properties	
	fluid	gas
Density [kg/m³]	1051 - 1105	1.913
dynamic viscosity [kg/(m·s)]	2258E-6 - 2624E-6	14.151E-6
sound velocity[m/s]	1482 - 1492	261.958
specific heat capacity [J/(kg·K)]	4065	8354
thermal conductivity [W/(m·K)]	0.555	0.015
thermal diffusivity [m²/s]	1.325E-7	97.145E-7

3. Results and Discussion

3.1 Measurement of temperature fields

The temperature field was measured continuously every five minutes. The thermal boundary conditions of the investigation were adapted to the real brewing process. Only the two upper cooling zones (flow temperature approx. 4.5 °C) are cooled and the heat is generated by the yeast (in this study 3.5 litre). Figure 6 shows the temperature field of the fermentation tank with both bottom shapes on the eighth day of fermentation. The temperature field inside the first configuration (hemispherical bottom shape - on the left) is 0.4 K on average cooler than the second configuration (conical bottom shape - on the right). The reason for this can be a better natural convection flow. Furthermore, figure 6 shows the cooling of the upper two cooling zones and the heat influence of the yeast in the entire tank.

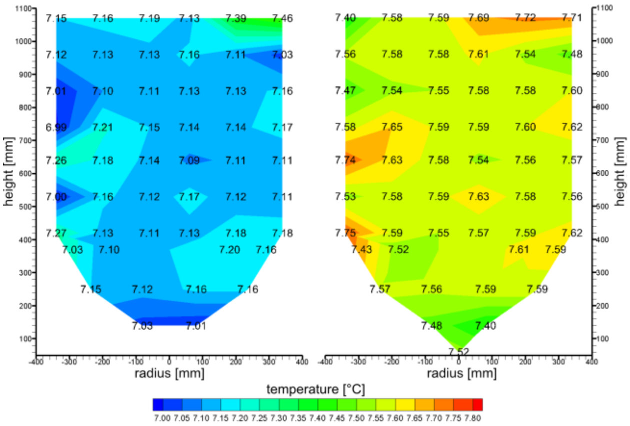

Figure 6: Temperature fields inside the cylindrical tank with hemispherical bottom (left) and conical bottom (right) on the 8th day of fermentation

3.2 Measurement of flow fields

The temperature field was measured continuously every 30 minutes. The sound velocity required for the UDV measurement system was also determined periodically by using a transit time method in the fermentation tank and averaged approx. 1485 m/s. The following two figures show the results of the velocity field measurement and the final calculation of the self-written program [3].

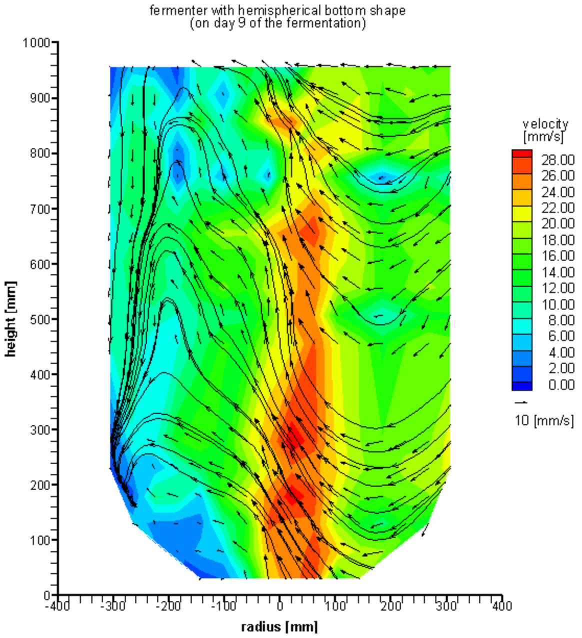

Figure 7: Velocity field and streamlines in the cylindrical tank with hemispherical bottom on the 9th day of fermentation

Figures 7 and figure 8 show the velocity fields of the fermentation tank during the ninth day of fermentation with the different bottom shapes. In figure 7, the velocity at the middle and the ground of the bottom shape is higher than in figure 8. This phenomenon is due to the hemispherical bottom shape and would allow a better, more controlled influence on natural convection.

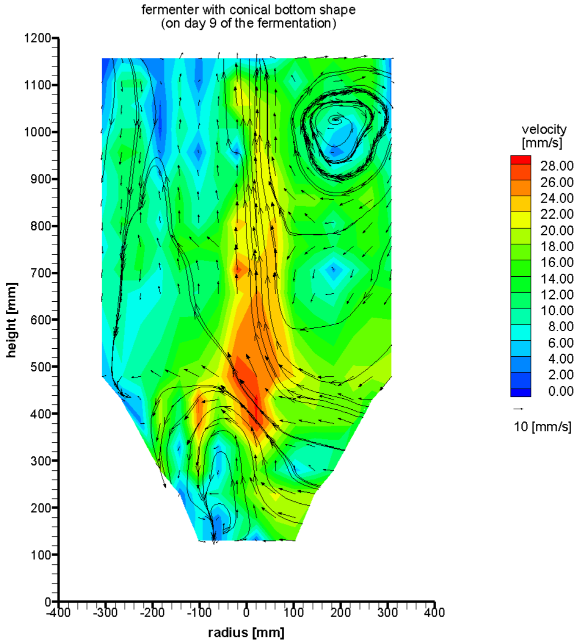

Figure 8: Velocity field and streamlines in the cylindrical tank with conical bottom on the 9th day of fermentation

3.3 Dimensionless numbers of the flow

To compare similar flow processes, dimensionless numbers are quite useful. The most important dimensionless numbers for current biological multiphase flow are listed below in table 3.

Table 3: Dimensionless numbers during fermentation

	relevant parameters	value
Prandtl		7.62
Grashof	vertical temperature difference: 9 K characteristic length: 1.150 m	4.66E10
Rayleigh		2.08E11
Nußelt	heat transfer coefficient: 1200 W/(m^{2}K)	346
Reynolds	bubble diameter: 2.5E-3 m	221.08
Morton	surface tension: 7.28E-2 N/m	1.09E-9
Eötvös		0.93
Weber	relative lift velocity: 0.210 m/s	1.67
Froude		1.34

4. Conclusion

In this investigation, the temperature and velocity fields in a fermenter with two different bottom shapes in a real fermentation process were measured and described. In summary, the investigation has shown that the connection and evaluation of two coupled ultrasound Doppler measuring devices can be very complicated and self-written program algorithms are absolutely necessary. Furthermore, the measurement volumes of the vertical 2 MHz transducers in the area of the bottom shapes are extraordinarily large due to the divergence and average over a wide range. Basically, the flow field is driven in the tank by the natural convection phenomena and is thus subject to very high fluctuation movements at very low speeds and is additionally superimposed by rising gas bubbles. Another result of the investigation is the distribution of the bottom-fermented yeast, because in contrast to the cylindroconical tank, the yeast is evenly distributed over the entire area in the hemispherical bottom. The next step will be the complete automation of data acquisition and above all processing and output. In addition, investigations will be carried out to reduce the influence of bubble columns on UDV measurement technology and a device for avoiding gas bubbles on the transducers.

Acknowledgements

The authors gratefully acknowledge by the “European Regional Development Fund” (ERDF) for the financial support of the fermentation tank (FHHST23, GHS-150050) and for the measurement technique "Ultrasound Velocimetry System" (GHS-170021).

References

[1] Heyse K. U.: Handbuch der Brauerei-Praxis, Getränke-Fachverlag (1994), ISBN 3-418-00736-8

[2] Delgado A., Hartmann C., Baars A., Meironke H., Szymczyk J. A., Bewegung im Gärtank: Messtechnische Diagnose und Simulation, Tagungsband Brautechnologisches Seminar, Freising (2004)

[3] Meironke H., Klembt D., Panten T.: Untersuchungen zum Einfluss von Gasblasen auf die Ultraschall Doppler Messtechnik mittels optischer und numerischer Methoden, GALA e.V. Karlsruhe (2017), ISBN 978-3-9816764-3-3

[4] Takeda Y.: Ultrasonic Doppler Velocity Profiler for Fluid Flow, Springer, (2012), ISBN 978-4-431-54025-0

11th International Symposium on Ultrasonic Doppler Methods for Fluid Mechanics and Fluid Engineering
Berlin, Germany (5.-7. September 2018)

Optical versus Acoustic Turbidity in Heavy Loaded Flows

P. Schmitt[1], A. Pallarès[1], M. Burckbuchler[2] and S. Fischer[2]

[1] Laboratoire ICube – UMR 7357, Université de Strasbourg / CNRS, 2, rue Boussingault, 67000 Strasbourg, France.
[2] UBERTONE, 14, rue du Brochet, 67300 Schiltigheim, France.

Knowledge on Suspended Sediment Concentration (SSC) leads to a better understanding of sediment transport dynamics, which is of main interest to understand river geomorphology or handle the wastewater regulation and treatment. For this purpose, optical and acoustic turbidity are both used to monitor continuously the suspended solids content in water. Optical turbidity is the mainly used method, and brings benefit in comparison to classical sampling. However, recent studies showed optical measurements inconsistency.

A long term acoustic and optical monitoring campaign in a wastewater network reveals noticeable differences between the two techniques, especially during storm weather recordings.
In regard to the latest studies, in exceptional situations such as rainy periods in wastewater or floods in rivers, the optical turbidity data are false and may lead to a huge underestimation of the SSC. This misinterpretation can have heavy consequences on water treatment and management. Our laboratory work will compare the acoustic and optical behaviour for suspension of fine material (mineral and organic) at huge concentrations, e.g. 50 g/l, as expected during floods or rain events.

Keywords: Optical turbidity, Acoustic, Backscattering, Attenuation, Suspended Sediment, Monitoring, Wastewater.

1. Introduction

Optical and acoustic turbidity are both used to monitor continuously the suspended solids content in water. As optical turbidity is well established as a valued suspended solids concentration (SSC) measurement in wastewaters [1], work on acoustics is still in progress [2]. Indeed, the use of inexpensive optical turbidimeters installed at spill points in wastewater networks makes it possible to meet the regulatory requirements for the estimation of the pollutant loads in transfer and discharge in terms of SSC. By using rigorous calibration protocols for monitoring and correlation of optical turbidity, estimation of SSC load at the event and annual scales is known with a much better precision level than what can be achieved by classical sampling. However recent studies [3, 4] showed optical measurements inconsistency.

In addition, during a long term acoustic and optical monitoring campaign in a wastewater network, major differences between the two techniques have been observed [5]. The two techniques behave differently during dry weather or storm weather recordings. During dry weather conditions, all techniques reflect the daily cycle of human activity. During a storm event, the daily cycle of human activity can still be guessed on the optical turbidity. However it has an unexplained lower average value. The daily cycle becomes invisible on the acoustic turbidities which increase by a factor 100 during the rainfall. This increase of the acoustic turbidity values could be explained by an increase in SSC and/or a modification of the particle composition [6].

In this paper, we try to confirm, through laboratory measurements, our hypothesis explaining these observations: for optical turbidity, a huge increase in SSC can lead first to a signal saturation, followed by erroneous measurements.

2. Methods and means

2.1 Methodology

In this study we used wheat starch, which is a good surrogate of organic wastewater mixture and river mud. Particles have an ovoid shape with a diameter around 18µm. Concentration of wheat starch varies from 0.05 g/l up to 60.5 g/l. The goal is to check the linearity of the acoustic response and to observe saturation and following decrease of the optical turbidity.

2.2 Material

In order to evaluate both acoustic and optical characteristics of the particles, all measurements were performed at room temperature in a 50 L water tank (figure 1).

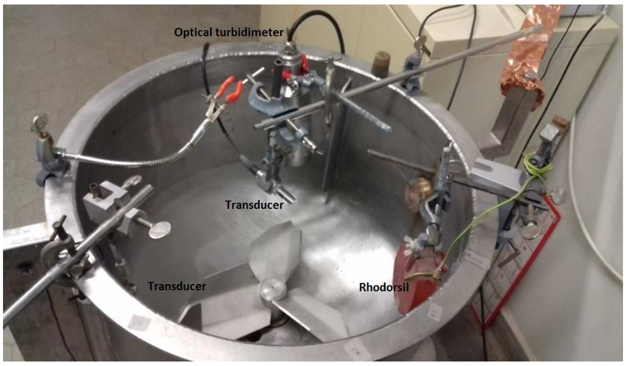

Figure 1: Experimental set-up.

The tank is filled with tap water, no dispersal is used. Homogeneous suspensions of particles are obtained by continuous stirring with a propeller at the bottom of the tank, with an adjustable frequency depending on the particles nature. The optical turbidimeter and the transducers are attached to the tank wall. An attenuator is placed on the beam near the tank wall in order to avoid multiple scattering. Optical and acoustic (at two frequencies) measurements were performed simultaneously.

2.3 Acoustic measurements

The measurements were performed with an UB-Lab system (Ubertone, France) and several stand-alone transducers allowing measurements at different frequencies going from 2.2 MHz up to 10 MHz. This instrument is the laboratory replica of the one used for the field measurements, the UB-Flow.

The measurement method is based on the incoherent backscattering along a beam from an emitted pulse on particles in the medium. The principle is well describe in [7], and gives a linear relation between the backscattered signal V_{rms} and the range r:

$$\ln(rV_{rms}) = \eta - \kappa r \qquad (1)$$

Applying this method, an information concerning backscattering (intercept η) and the attenuation (slope κ) is obtained for a given configuration of particle type, frequency and concentration.

In a second step, another linear regression is done on η and κ versus the particle concentration, for a given frequency.

For the η fit, $\eta = a_i.\ln C + b_i$, a slope of $a_i = ½$ is expected as seen in [7]. The value of η is directly related to the backscattering properties of the particles. If the instrumentation constant k_t, the near field function and the particle size and density are known, it gives access to the backscattering form function of the particle. As our aim isn't the exact determination of the particles acoustic characteristics but their comparison to the optical ones, in our measurements, k_t is and will remain unknown. Also, rather to use some empirical formula to correct our data, we choose to remove the near field thus introducing no bias to the raw data.

For κ, the fit of $\kappa = a_s.C + b_s$, allows a determination of the normalized total scattering cross section of the particle if density and particle radius are known [7].

For each measurement, the water temperature was recorded for accurate calculation of the speed of sound. The acoustic measurement cell dimensions were identical at all frequencies. The pulse repetition frequency and the presence of a Rhodorsil absorbent allow each pulse emission to dissipate before the next. Each measurement was repeated and showed excellent reproducibility. For each acoustic data acquisition, two frequencies were screened. One acquisition cycle takes about 20 minutes.

2.4 Optical measurements

The optical turbidity was continuously recorded by a turbidimeter (Solitax sc, Hach Lange). The measuring principle is based on a combined infrared absorption scattered light technique. Using this method, the light scattered sideways by the turbidity particles is measured over an angle of 90 degree. It was calibrated with a Formazin Standard, giving values in Nephelometric Turbidity Units (NTU). The used optical turbidity value is the measured value averaged over an acoustic cycle.

In order to define the theoretical relationship between turbidity and concentration, we used a simple linear regression on the experimental data:

$$T = aM + b \qquad (2)$$

where T is the optical turbidity, M the particle concentration, and *a* and *b* constants obtained by least squares method.

3. Results and discussion

3.1 Acoustic measurements

The analyses were done at two frequencies, 2.88 MHz and 7.5 MHz. Figure 2 shows the attenuation of the particles at 2.88 MHz.

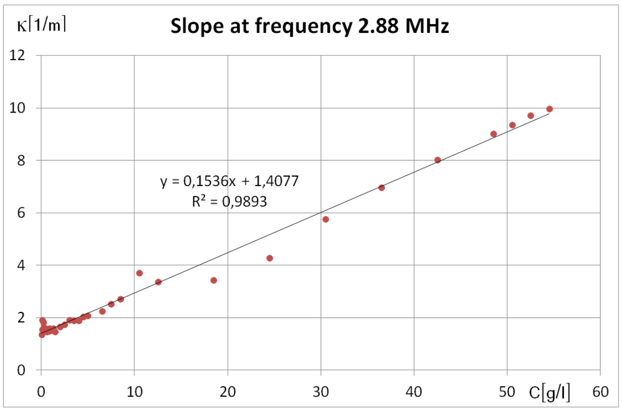

Figure 2: attenuation as a function of concentration at 2.88 MHz.

One can see that linearity is present between the attenuation κ and the particle concentration. Nevertheless, the standard deviation around the fit is relatively large, especially at low concentration values (under 1.6 g/l). This is easily explained by the ultrasonic wavelength which is largely higher than the particle circumference.

A zoom to the band [0; 1.6 g/l] is given in Figure 3.

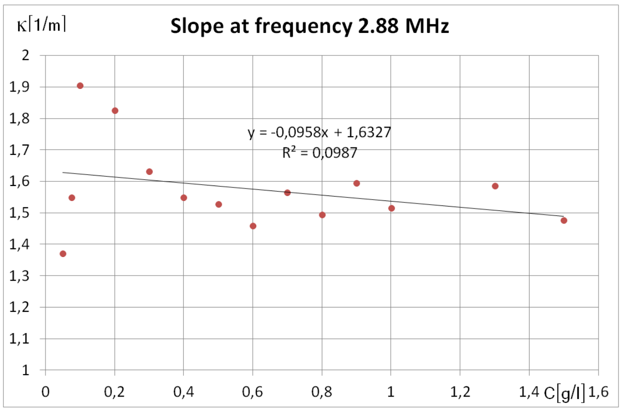

Figure 3: attenuation as a function of concentration between 0 and 1.6 g/l at 2.88 MHz.

In this concentration range, the low concentrations combined with inappropriate wavelength lead to unexploitable records, because of the poorness of the signal present in the records.

Figure 4 shows the backscattering of the particles at 2.88 MHz. As theoretically expected, a slope value near 0.5 is observed. Also, the value of b_i is nearly invariant. This shows that ultrasound backscattering at this frequency can be a good tracker of particle concentration in the range [1.6; 55 g/l].

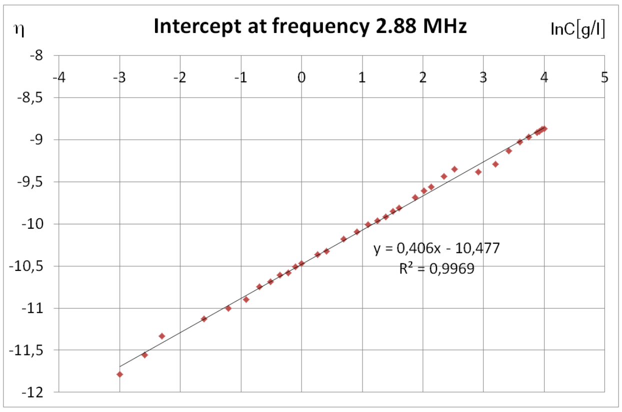

Figure 4: backscattering versus concentration at 2.88 MHz.

Figure 5 shows the attenuation and figure 6 the backscattering for the 7.5 MHz frequency.

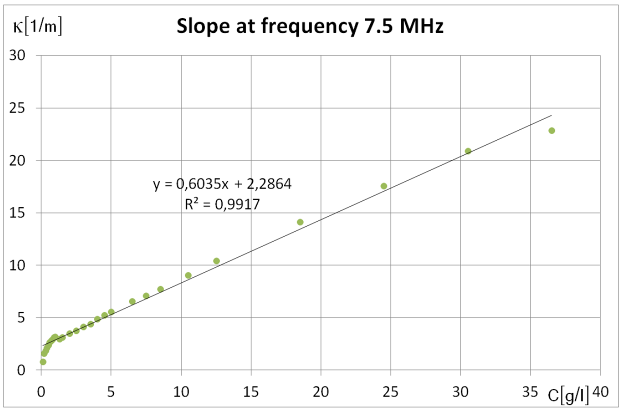

Figure 5: attenuation as a function of concentration at 7.5 MHz.

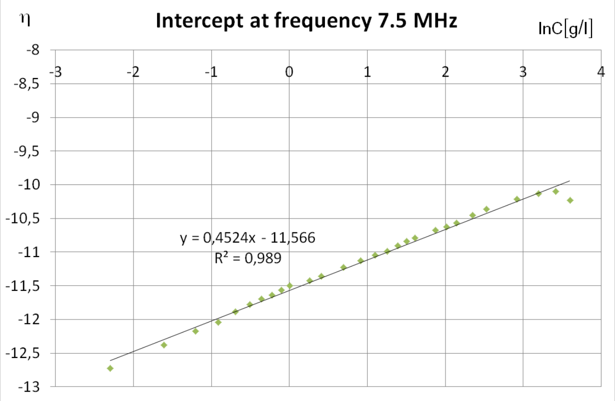

Figure 6: backscattering as a function of concentration at 7.5 MHz.

At 7.5 MHz, the main problem is the acoustic beam attenuation by the medium. This can be observed on both curves, and shows that the operating range extends only up to 36.5 g/l. Concerning backscattering, the regularity of the curve, with here also a slope near 0.5, reveals that it can be a good concentration indicator already at 0.05g/l.

3.2 Optical measurements

Figure 7 shows the response of the optical turbidimeter (Solitax sc, Hach Lange) over the whole range of wheat starch concentration (0.05g/l up to 60.5g/l).

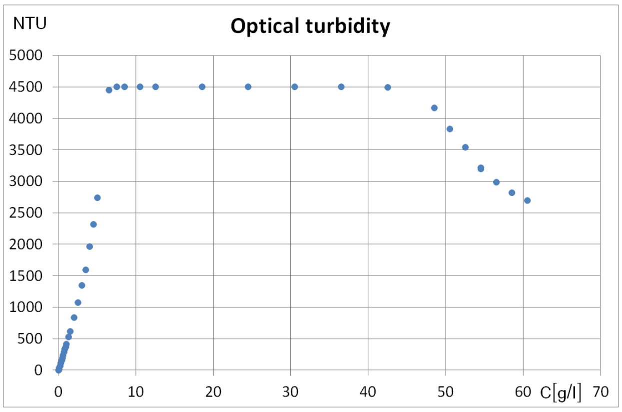

Figure 7: optical turbidity as a function of the concentration.

There is a very good linearity for the optical measurement in the range [0; 2 g/l] (figure 8), and the response is globally linear up to 5 g/l.

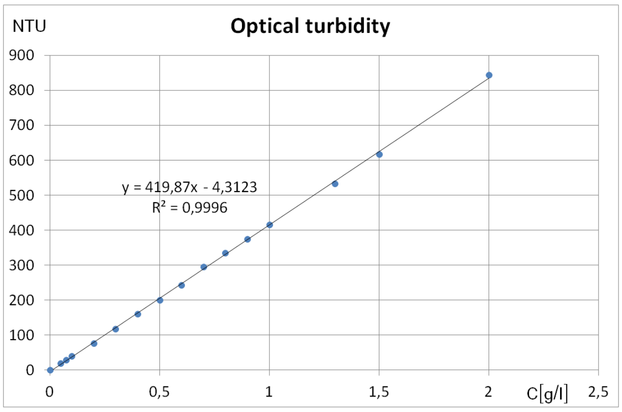

Figure 8: optical turbidity in the range [0; 2g/l].

After 6.5g/l the turbidimeter leaves its operating span and goes into saturation. Another phenomenon is observed when the wheat starch concentration exceeds 42.5 g/l. For these high values, the optical turbidity decreases with the increase in particle concentration. This behaviour is strongly problematic, because it leads to possible erroneous evaluations of SSC.

3.3 Discussion

The knowledge of sediment transport characteristics is an important issue in terms of sewer and surface water management. Indeed, the suspended solids transported by the water are a vector of pollution and they may also be physically damaging. A noticeable part of the sediment transport is performed during exceptional events such as storm periods in wastewater or floods in rivers. During these events, the SSC can grow strongly, largely over the typical dry weather value which is around 0.5 to 1g/l.

For acoustic measurements, the used frequency efficiency is directly correlated to the mean particle diameter. Low frequencies are not adapted to fine particles. This explains the poor response at 2.88 MHz for low wheat starch concentrations. By increasing concentration, the attenuation of the medium increases also, especially for higher frequencies. This stops the operating range at 36.5g/l for the 7.5 MHz frequency. Nevertheless, a combination of acoustic frequencies gives the possibility to cover a wide range of particle concentrations, including exceptional events.

For optical measurements, a very good linearity in the range [0; 2g/l] allows the monitoring of the SSC in dry weather conditions. But the saturation effect appearing at concentrations of several g/l prevents its use during storm weather conditions. Furthermore, in the case of high concentration, the fact that the optical turbidity decreases by increase of concentration can lead to huge underestimation of SSC by the water resource decision-makers and practitioners.

An example of field measurements that illustrates this behaviour is given on figures 9 and 10. The measurements were done in the entry chamber of the wastewater treatment plant of Greater Nancy (250 000 p.e.). Its reference flow is 120 000 m^3/day. 65% of the water comes from a combined sewer system.

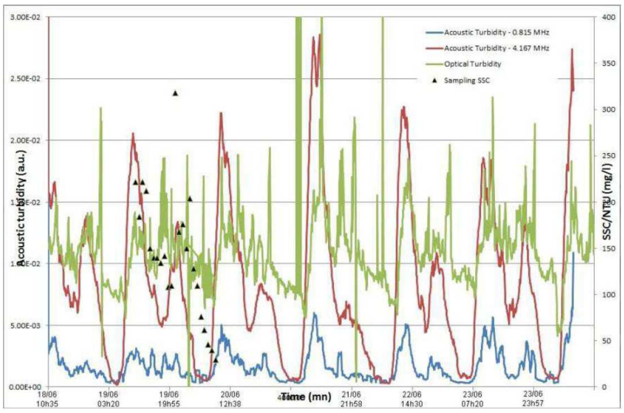

Figure 9: Six days recording in dry weather conditions

Both figures show two online acoustic measurements (at 0.815 MHz and 4.167 MHz), one online optical turbidity measurement, and several samplings. Figure 9 reflects the daily cycle of human activity during dry weather. Optical turbidity has an average value of 150 NTU, and acoustic measurements have values around 10^{-2} arbitrary unit (a.u.). Figure 10 shows a storm event. The daily cycle of human activity can still be seen on the optical turbidity which has a slighter lower average value than during dry weather (70 NTU). In contrast to optical turbidity, both acoustic measurements considerably increased, by a factor 100 compared to dry weather. In this situation, the acoustic measure at 0.815 MHz is dominant suggesting the presence of bigger particles, around 600 µm diameter.

The increase of acoustic turbidities linked to a fall of optical turbidity value in a situation with strong presence of suspended solids is a situation which can be explained by the dysfunction of optical turbidimeter as described previously.

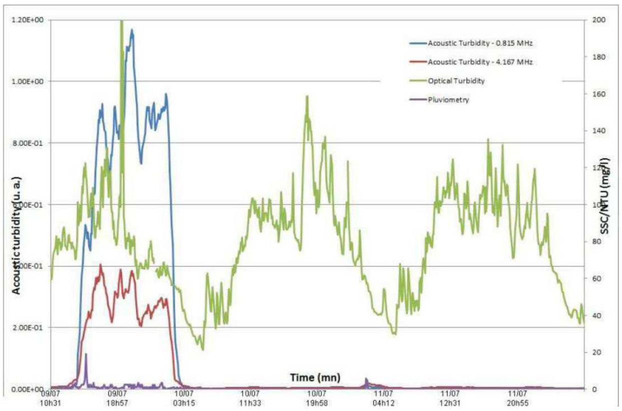

Figure 10: Three days recording with rainfall event on the first day.

4. Summary

In this paper, we compared optical and acoustic turbidity in heavy loaded flows. The goal was to verify optical measurements inconsistency when the concentration grows strongly. Results show that, in conditions which can occur during rainy periods in wastewater or floods in rivers, optical turbidity can not only saturate, but also give erroneous results with behaviour opposite to the specifications: turbidity decreases when SSC increases. This phenomenon is a physical behaviour of optical turbidimeters, most probably linked to light attenuation. The acoustic measurements show their usefulness as a robust qualitative description of SSC in a medium. By using adequate frequencies, the acoustic information is consistent during dry weather as well as during storm weather conditions.

References

[1] Métadier M & Bertrand-Krajewski J L: The use of long-term on-line turbidity measurements for the calculation of urban stormwater pollutant concentrations, loads, pollutographs and intra-event fluxes, Water Research 46, 6836–6856 (2012).

[2] Guerrero M & Di Federico V: Suspended sediment assessment by combining sound attenuation and backscatter measurements – analytical method and experimental validation, Advances in Water Resources, 113, 167-179 (2018).

[3] Rymszewicz A, *et al.*: Measurement differences between turbidity instruments, and their implications for suspended sediment concentration and load calculations: A sensor inter-comparison study, Journal of Environmental Management, 199, 99 (2017).

[4] Voichick N, *et al.*: Technical Note: False low turbidity readings during high suspended sediment concentrations, Hydrol. Earth Syst. Sci. Discuss. https://doi.org/10.5194/hess-2017-528 (2017).

[5] Pallarès A, *et al.*: Long-term acoustic and optical turbidity monitoring in a sewer, IWA World Water Congress & Exhibition 2016, Brisbane, Australia (2016).

[6] Pallarès A, *et al.*: Suspended Sediment Monitoring: Comparison between Optical and Acoustic Turbidity, Proceedings of the 14th International Conference on Urban Drainage, Prague (2017).

[7] Schmitt P, *et al.*: Suspended Sediment characterization by Multifrequency Acoustics, ISUD10, Tokyo (2016).

11th International Symposium on Ultrasonic Doppler Methods for Fluid Mechanics and Fluid Engineering
Berlin, Germany (5.-7. September 2018)

Comparison of Flow Measurements in a Cold Liquid Metal Model for Continuous Casting of Steel Carried Out by an Arrangement of Individual US Transducers and a Linear US Array

Dennis Schurmann[1], Sven Franke[1], Bernd Willers[1], Sven Eckert[1]

[1] Helmholtz-Zentrum Dresden-Rossendorf e.V. (HZDR), Bautzner Landstraße 400, 01328 Dresden

Flow measurements by means of the Ultrasound Doppler Velocimetry (UDV) have been carried out in a cold liquid metal mockup experiment to model the continuous casting process of steel. The setup was realized in the mini-LIMMCAST facility and represents a 1:3 scale model of a typical industrial bloom caster. An arrangement of ten individual ultrasonic sensors attached to a commercial system and an academic UDV system with linear ultrasound array was mounted along the mold to capture the velocity distribution near the meniscus and the submerged entry nozzle (SEN). The results obtained by the two measurement systems are compared and show the superiority of the academic system due to its higher spatial resolution.

Keywords: Model Experiments in Liquid Metal, Continuous Casting, UDV

1. Introduction

1.1 Continuous casting and the need for model experiments

The Continuous Casting process is currently responsible for 96% of the steel production in the world and the annual amount of steel produced doubled in the last 20 years [1]. Due to its high energy and resource consumption and the customers increased demand for high quality steel products it is a process that needs to be investigated and optimized.

In the continuous casting process liquid steel is located inside the tundish and flows, driven by gravity, through the submerged entry nozzle (SEN) into a water-cooled mold, which has the shape of the desired end product, e.g. a slab, bloom or billet. The steel solidifies at the walls of the mold but the core stays liquid until after several meters of length, the whole cross-section has solidified completely. The cast product is continuously pulled through the mold, so that it’s length is much greater than the cross-section.

Flow control by means of electromagnetic fields is widely employed in industry to improve the casting process. In bloom and billet casting electromagnetic stirring (EMS) is applied. EMS uses alternating magnetic fields to induce a rotational motion near the solidification zone to improve the grain structure of the cast product.

Unfortunately, the real casting process is not accessible to complex flow measurement techniques due to the harsh conditions and high temperatures (around 1500 °C). Only few limited measurements are available, mainly approximations of the free surface velocity obtained by so called “nail-board tests”. The main experimental data that can be obtained from the real process is related to the properties of the final cast product, like grain structure, number of casting failures, inclusions and so on. To obtain a deeper understanding of the dominating flow phenomena in continuous casting and to provide data to validate numerical simulation codes, it is therefore necessary to perform model experiments.

The LIMMCAST experimental facilities at HZDR are used to model the continuous casting process in low temperature liquid metal experiments [2], [3]. The facilities allow investigations of several aspects of the continuous casting process and focus mainly on the determination of the flow structures that develop in the continuous casting mold. The high versatility of the facilities allow measurements in different casting geometries, also under the influence of magnetic fields.

2. Experimental Setup

2.1 Mechanical Setup

The study presented in this work is performed at the mini-LIMMCAST facility, which is composed of a liquid metal loop, operated at room temperature with GaInSn. Some physical properties of the model fluid are compared to those of liquid steel and water in Table 1. From the low electrical conductivity of water compared to that of steel it can be concluded that the use of a liquid metal as a model fluid is compulsory when the influence of magnetic fields has to be investigated.

The PMMA model of a round mold and strand for continuous casting of round blooms (see Figure 1) represents an industrial configuration in a scale of 1:3. It is located in the mini-LIMMCAST, has an inner diameter of 80 mm and a length of 800 mm. The submerged entry

https://doi.org/10.7795/810.20190809

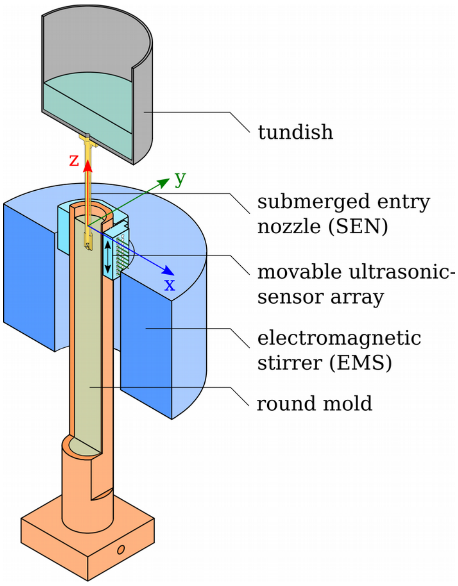

Figure 1: Schematic representation of the continuous casting model. The positioning of individual ultrasonic sensors is shown.

nozzle is of a swirl-type and induces a rotational flow inside the mold by four jets exiting the four twisted ports of the nozzle. Optionally the mould electromagnetic stirrer can be used to apply a rotating magnetic field to the set up. The coordinate system for the measurements is located in the center of the cylindrical model with the z-axis pointing to the top and z = 0 located on the free surface in the model mold.

Table 1: Physical properties of liquid steel at 1500 °C and GaInSn and water at 20 °C. The values for liquid steel are exemplary values from [4], [5], GaInSn values are from measurements [6] and water from [7].

		Liquid Steel	GaInSn	Water
density	kg / m³	~ 7 000	6 353	988
speed of sound	m / s		2 740	1 500
dyn. viscosity	mPa s	~ 2 ... 18	2.1	1
el. conductivity	1 / Ω m	~ 0.833 × 10^6	3.29 × 10^6	<50

2.2 Measurement Setup

For the application of Ultrasound Doppler Velocimetry (UDV) the walls of the model are milled even to enable measurements through the wall. The transducers measure the velocity component in x-direction (u) inside the model and are placed at several z-positions, at y = 15 mm. The diffraction of the ultrasonic beam due to the curvature of the inside wall of the round model mold can be neglected since the ultrasound velocity of PMMA (2700 ... 2800 m/s, according to [8]) is similar to that of GaInSn (c.f. Table 1). Sequential polling of neighboring transducers returns a two dimensional representation of the velocity component u in the xz-plane.

2.3 Description of the UDV devices

Ultrasound Doppler Velocimetry (UDV) is employed by a commercial system, the DOP 3010 by Signal Processing (Savigny, Switzerland) [9] and an academic UDV system by Franke [10].

The commercial DOP 3010 system can be used to measure the velocity profiles of up to ten individual transducers sequentially and returns the processed velocity profiles. The individual transducers are connected to the device, which is connected to the measurement PC via a USB connection. To apply measurement settings and record data a proprietary software for Microsoft Windows is supplied by the manufacturer of the DOP.

The multiplexing of the sensors is conducted by mechanical relays, which limits the switching time from sensor to sensor. The device's intended operational mode is to evaluate several profiles at one sensor before the velocities at the next sensor are evaluated. This operational scheme results in a good temporal resolution for each sensor but limits its use when a velocity information in two dimensions is required since the velocities at the sensors are not measured at the same time.

The academic UDV system can be used to obtain velocities with up to two linear ultrasonic arrays (Figure 2, [11]). Each linear array consist of 25 rectangular transducers, with piezo dimensions of 5 x 2.5 mm^2, which can be polled in user defined patterns, allowing parallel measurements by multiple transducers at the same time and therefore an increased measurement frequency. Also in sequential operation the switching time between the transducers is shorter and therefore results in a higher measurement frequency compared to the commercial system. The system consists of an electronic measuring system that handles the multiplexing and delivers the raw time-dependent echo for each transducer. The data is recorded by a PC which is

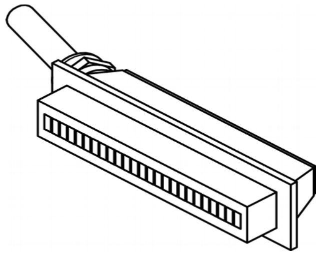

Figure 2: Representation of the linear ultrasound array.

https://doi.org/10.7795/810.20190809

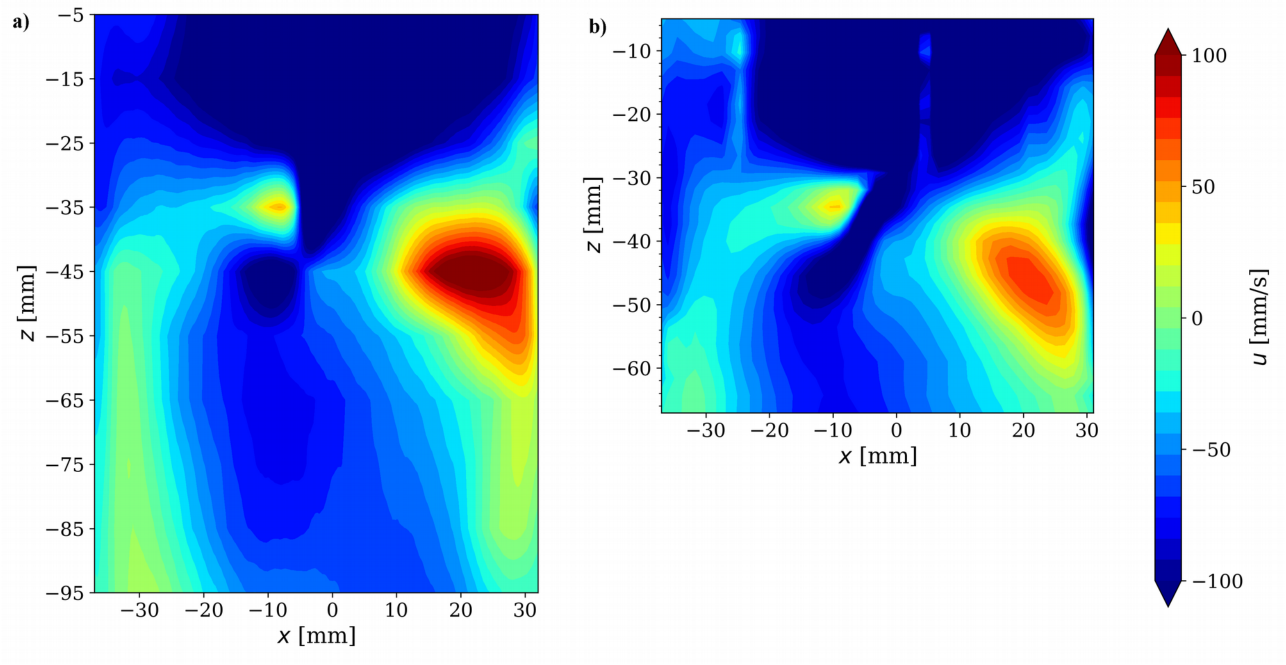

Figure 3: Time average contour plots of the measured horizontal velocity u at y = 15 mm. Measured with a) a DOP 3010 and ten individual transducers with a spacing of Δz = 10 mm, and b) the academic system and a linear ultrasound array of 24 measurement lines (Δz = 2.7 mm).

connected to the measurement system via a PCIexpress connection. Once the data is recorded the velocity estimation algorithm is applied to the raw data and returns the velocity data.

In this study both instrument are operated with a ultrasonic frequency of 4 MHz and achieve a frame rate of approx. 5 fps.

3. Results

Time average contour plots of the horizontal velocity u at y = 15 mm are shown in Figure 3 for the measurement with the commercial and academic system. In the DOP 3010 measurement (Figure 3a), the ten individual ultrasound transducers with a piezo diameter of 5 mm cover a vertical range of 90 mm with a spacing between the measurement lines of Δz = 10 mm. The main flow structures inside the mold can be identified by this measurement: The highest negative velocities appear under the free surface, while also at z = -35 mm and -45 mm two areas of high negative velocities can be seen. These two areas of negative velocities are caused by the twisted jet, that exists one port of the SEN. Positive velocities occur at z = -45 mm and correspond to a second jet, which exists the SEN from a second port perpendicular to the measurement plane. A high gradient of the velocity can be seen at z = -35 mm where positive and negative velocities occur in direct vicinity between x = -15 mm and x = 0.

Figure 3b) depicts the results obtained by the linear ultrasound array, which consists of 24 measurement lines with a spacing of Δz = 2.7 mm and covers a measurement range of 62 mm in z-direction. The higher z-resolution results in a much better representation of the flow structures inside the mold: The elliptic shape of the jet from the second port (at z = -45 mm, x = 20 mm) can be clearly identified. The lower maximum velocity compared to that in the DOP measurement might be caused by slightly different operating conditions since the two measurements were not conducted at the same time. Also the shape of the jet from the first port can be seen only in the array measurement. The interpolation in the contour plot together with the lower z-resolution of the measurement with individual transducers, is responsible for the misleading shape appearance. The contour plot of the array system shows two areas (x > -30 mm, y = 5 mm and y = 27 mm), where a standing echo caused by the SEN interferes and disturbs the velocity measurement. This could possibly be overcome by the application of a special filter to the recorded raw data in the velocity estimation algorithm.

Figure 4 shows velocity profiles over z at x = 15 mm, y = 15 mm for the commercial and academic system. The component u at this point was measured directly. Under the assumption of flow symmetry to the xz- and yz-plane, it is possible to introduce virtual measurements by rotating the measurement plane by 90° and therefore obtain the v-component of the velocity as $v_{x15,y15}$ =

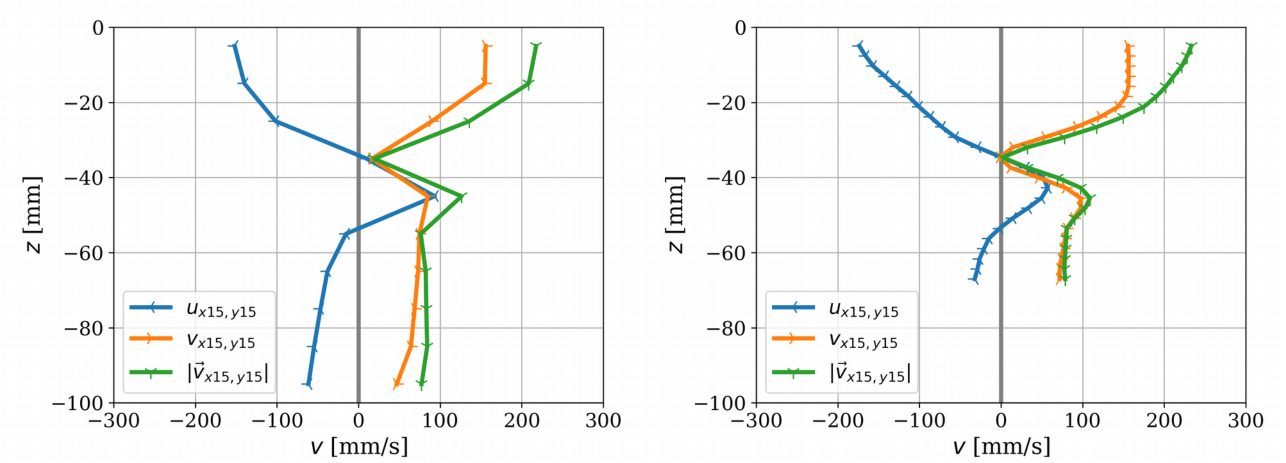

Figure 4: Time average velocity components and absolute velocity at x = 15 mm, y = 15 mm obtained from the measurements. $u_{x15,y15}$ measured directly, $v_{x15,y15}$ from symmetry assumption. Measured with a) a DOP 3010 and ten individual transducers, and b) the academic system and a linear ultrasound array.

$-u_{x-15,y15}$. The absolute velocity at x15, y15 is then calculated and shown in the figure.

The overall trend can be seen in both diagrams: The highest velocities occur under the free surface, above the nozzle ports, which are located between z = -35 mm and -25 mm. At the lower edge of the nozzle (z = -35 mm) the time average velocity is zero and rises again until z = -45 mm where a local maximum can be seen. At this depth the jet from the nozzle port crosses the measurement line. At depths below $z < -52$ mm the velocity stays quite constant until the end of the measurement area at z = -67 mm.

The higher resolution in z-direction by the academic linear array (Figure 4b) enables a better identification of the local velocity maxima around z = -45 mm. In contrast to the measurement with individual transducers it is possible to see that the maxima for u and v occur at a slightly different z-position.

4. Conclusions

Measurements with Ultrasound Doppler Velocimetry by a commercial system with individual transducers and an academic system with a linear transducer array in a liquid metal model for continuous casting of round blooms have been presented and compared. It was shown that the overall representation of the flow structures could be elaborated by both systems. While the commercial system is less complicated to use, the academic UDV system showed its superiority due to its higher number of channels, the much finer resolution of the linear array and the possibility to adjust all parameters and apply different data processing since the source code of the software is fully available.

References

[1] world steel association, ‘Steel Statistical Yearbook 2017’, Brussels.

[2] K. Timmel, S. Eckert, G. Gerbeth, F. Stefani, and T. Wondrak, ‘Experimental Modeling of the Continuous Casting Process of Steel Using Low Melting Point Metal Alloys - the LIMMCAST Program’, *ISIJ Int.*, vol. 50, no. 8, pp. 1134–1141, 2010.

[3] K. Timmel, C. Kratzsch, A. Asad, D. Schurmann, R. Schwarze, and S. Eckert, ‘Experimental and Numerical Modeling of Fluid Flow Processes in Continuous Casting: Results from the LIMMCAST-Project’, *IOP Conf. Ser. Mater. Sci. Eng.*, vol. 228, p. 012019, Jul. 2017.

[4] C. Y. Ho and T. K. Chu, ‘Electrical resistivity and thermal conductivity of nine selected AISI stainless steels’, DTIC Document, 1977.

[5] M. Korolczuk-Hejnak, P. Migas, and W. Ślęzak, ‘Determination of the liquid steel viscosity curves using a high temperature rheometer’, *J. Phys. Conf. Ser.*, vol. 602, p. 012037, Apr. 2015.

[6] Y. Plevachuk, V. Sklyarchuk, S. Eckert, G. Gerbeth, and R. Novakovic, ‘Thermophysical Properties of the Liquid Ga–In–Sn Eutectic Alloy’, *J. Chem. Eng. Data*, vol. 59, no. 3, pp. 757–763, Mar. 2014.

[7] VDI, Ed., *VDI-Wärmeatlas*, 11th ed. Berlin, Heidelberg: Springer, 2013.

[8] ‘Eigenschaften von PLEXIGLAS’. [Online]. Available: http://www.plexiglas.de/product/plexiglas/de/ueber/faq/Pages/eigenschaften.aspx. [Accessed: 01-Aug-2017].

[9] S. A. Signal Processing, ‘DOP3000 series User’s manual’.

[10] S. Franke, L. Büttner, J. Czarske, D. Räbiger, and S. Eckert, ‘Ultrasound Doppler system for two-dimensional flow mapping in liquid metals’, *Flow Meas. Instrum.*, vol. 21, no. 3, pp. 402–409, Sep. 2010.

[11] S. Franke *et al.*, ‘Two-dimensional ultrasound Doppler velocimeter for flow mapping of unsteady liquid metal flows’, *Ultrasonics*, vol. 53, no. 3, pp. 691–700, Mar. 2013.

11th International Symposium on Ultrasonic Doppler Methods for Fluid Mechanics and Fluid Engineering
Berlin, Germany (5.-7. September 2018)

Development of a Hybrid Ultrasonic Flow Meter With the Use of Pulsed Doppler and Time-of-Flight

Hideki Murakawa[1], Ei Muramatsu[1], Daijiro Akizuki[1], Hitoshi Asano[1]
Sanehiro Wada[2], and Noriyuki Furuichi[2]

[1] Graduate School of Engineering, Kobe University, 1-1 Rokkodai, Nada, Kobe 657-8501, Japan
[2] National Institute of Advanced Industrial Science and Technology, Tsukuba Central 3, 1-1-1 Umezono, Tsukuba 305-8563, Japan

The time-of-flight ultrasonic flow meter (TOF) derives flow rate from line-average velocity based on transit time of ultrasonic pulse on the ultrasonic path. Hence, accuracy of the TOF is strongly influenced by the velocity profile in a pipe. On the other hand, the ultrasonic pulsed Doppler method (UDM) enables to derive the flow rate from the velocity profile. Therefore, it does not require the profile factors (PFs). Hybrid ultrasonic flow meter between TOF and UDM is useful for on-site calibration for determining the profile factor. However, the UDM has relatively large uncertainty in comparison to TOF. Despiking method is useful to eliminate the uncertain data as a post-processing. In this study, a method to eliminate the uncertain velocity profiles was proposed. Line-average velocities were obtained using TOF and UDM simultaneously, and these were compared to eliminate the scattering data. As a result, it was shown that the hybrid ultrasonic flow meter made possible to determine the PF under asymmetrical flow condition. The PFs obtained for the symmetrical and asymmetrical flows were in good agreement with the calibration results of the reference flow meter. The error could be reduced to ±1% of the flow rate

Keywords: Hybrid ultrasonic flow meter, Time-of-flight, Profile factor, Despiking method

1. Introduction

Time-of-flight ultrasonic flow meter (TOF) has been widely applied in industrial field due to its advantages, such as small pressure loss, applicability to large diameter pipe. The TOF derives flow rate from the difference of the transit time of ultrasonic pulse which depends on the line-average velocity on ultrasonic path. Hence, the profile factors, PFs, to convert the transit time to the flow rate are required. The PFs are calibrated before shipment of the flow meter under the ideal flow conditions. However, there is a demand to calibrate the PFs at on-site because accuracy of the flow meter might change owing to the aging effect.

On the other hand, the ultrasonic pulsed Doppler method (UDM) enables to derive the flow rate from the velocity profile. Therefore, it does not require the PFs. Even if velocity profile in the pipe is distorted, flow rate can be obtained accurately using multiple measuring lines [1]. However, the UDM requires ultrasonic reflectors in the flow, and it is difficult to use the UDM usual. Hence, a hybrid ultrasonic flow meter which calibrates TOF by using UDM has been proposed [2]. Because maximum detectable velocity of the UDM was limited by the Nyquist sampling theorem, the hybrid ultrasonic flow meter could be applied only for low flow-rate conditions. Authors developed a dealiasing method, namely, the feedback method for measuring higher flow rate and six times higher flow rate could be measured [3,4].

The uncertainty of velocity measurement becomes worse with increasing the maximum measurable velocity using the feedback method. If the velocities are not accurately obtained, spike data appears in the velocity distributions. In order to eliminate the spike data, despiking methods have been developed [5].

In this study, in order to improve the average velocity profile for the UDM, despiking method was applied for the feedback method. Furthermore, a hybrid system with UDM and TOF was applied for eliminating the uncertain data for calculation of the average velocity profile.

2. Measurement uncertainty and despiking method

2.1 Spike velocity

Feedback method [3] is based on difference between the phase shifts between the echo signals. In the calculation, the higher signal-to-noise ratio is required for obtaining the velocity profile accurately in comparison to the conventional UDM, *i.e.* single pulse repetition frequency, PRF. Further, the measurement volume is important as well. If the measurement volume is not large enough to allow consideration of the moving distance of a reflector during the pulse emission period, the velocity cannot be correctly determined.

Figure 1 shows an example of reliable and noised instantaneous velocity profiles. Feedback method was applied for measuring higher velocity under distorted velocity condition. If reflectors are not enough or not appropriately distributed on the ultrasonic path during the measurement, it can be found that some velocities are not correctly obtained. These velocities are called as spike velocities.

https://doi.org/10.7795/810.20190809

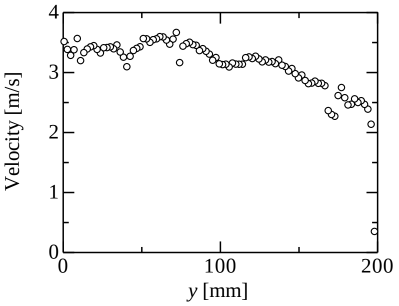

(a) Reliable velocity profile

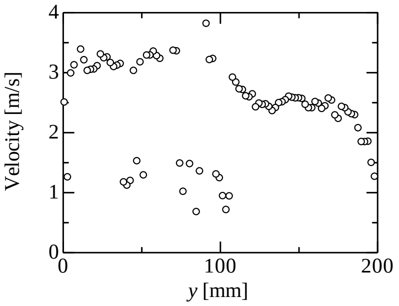

(b) Noised velocity profile

Figure 1: Instantaneous velocity profile measured using Feedback method under distorted flow condition.

2.2 Despiking method

Figure 2 shows an example of time-series of velocity data at a measurement position. It can be confirmed that it includes some spike data, *i.e.* error data. To detect the spike data, despiking methods have been developed. Here, we employ Goring and Nilora's method [5]. They proposed the phase-space thresholding method. It is based on the differentiation of the high frequency components of a signal in three-dimensional phase space.

Examples of the relation between the velocity data in phase space are shown in Figure 3. v is the velocity, Δv is the derivative of v and $\Delta^2 v$ is the second derivative of v. The solid line of ellipsoidal represents the threshold in each phase. Velocities outside the thresholding are considered as spike data. Some data appears at position where far from the center region. These data represent that the Nyquist holding number is wrongly evaluated. Thus, velocities discretely appears $v \pm n v_{\max}$, where n is the Nyquist holding number and $v_{\max}$ is the maximum measurable velocity.

Figure 2 also shows the spike data. For removing the spike data, uncertainty of the statistical error can be improved. The despiking method is useful for evaluating the flow properties. However, this method is post-processing and is difficult to evaluate at short times and on-time measurement.

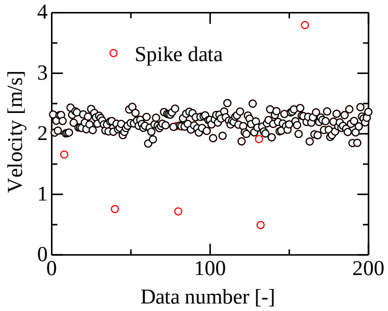

Figure 2: Time-series of velocity data.

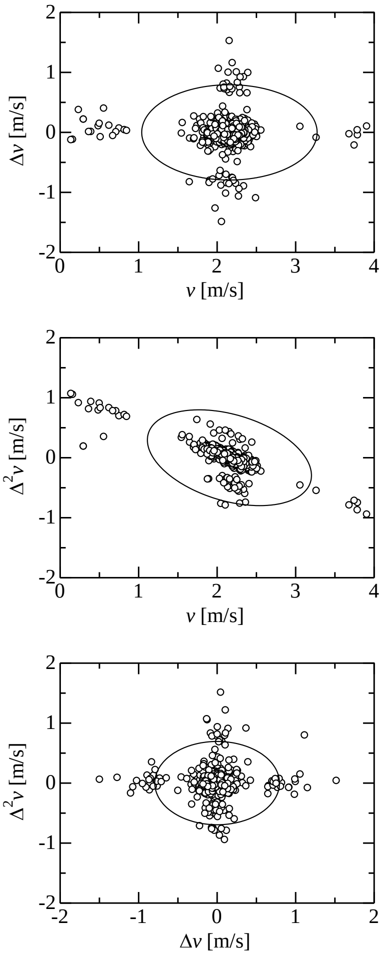

Figure 3: Phase-space thresholding method for evaluating the spiked velocities. Ellipsoidal represents the threshold, and velocities outside the thresholds are considered as spiked data.

3. Hybrid ultrasonic flow meter

3.1 Transit-time measurement

To evaluate uncertainty of velocity profile as well as the flow rate, hybrid ultrasonic measurements of time-of-flight (TOF) and UDM was developed.

Figure 4 shows the measurement principle of the TOF. A pair of ultrasonic transducers is installed with inclination angle, θ, on the pipe wall; t represents the transit time of an ultrasound signal between transducers in stagnant flow. If the ultrasonic pulse is emitted from the upstream transducer, the transit time is shortened to $t - \Delta t$ by the flow velocity, whereas the transit time from the downstream transducer is delayed to $t + \Delta t$. The Δt is related to the line-averaged velocity along the measuring line between the sensors, $V_{L,\mathrm{TOF}}$, and the relationship is expressed as

$$V_{L,\mathrm{TOF}} = \frac{c^2}{D \tan\theta} \Delta t \tag{1}$$

As shown in the above equation, the TOF can derive only the line-averaged velocity. In order to evaluate the flow rate, profile factor, *PF*, is used to convert V_L to flow rate:

$$Q_{\mathrm{TOF}} = PF \cdot \frac{\pi D^2}{4} \cdot V_{L,\mathrm{TOF}} \tag{2}$$

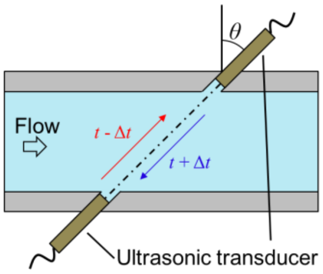

Figure 4: Schematic of time-of-flight measurement.

3.2 Measurement system

In the hybrid ultrasonic flow meter, UDM is used for measuring velocity profile. By integrating the obtained velocity profile over the cross-sectional area of a pipe, the flow rate, *Q*, can be calculated. Using *Q*, the *PF* can be determined as

$$PF = \frac{Q}{V_{L,\mathrm{UDM}} \cdot \pi D^2 / 4} \tag{3}$$

Thus, the *PF* can be obtained by using the UDM in conjunction with the feedback method. Further, V_L obtained from TOF and the UDM was compared to eliminate the uncertain data. It can be considered that the V_L calculated from the TOF is more accurate than that obtained from UDM. Thus, if V_L differs at more than ±5% between TOF and UDM, the velocity profiles were eliminated for the flow rate calculation.

The developed measurement system is schematically shown in Figure 5. The system consists of an ultrasonic pulser/receiver (JPR-2CH-KB, Japan Probe Co., Ltd.), a high-speed digitizer (PXI-5114, National Instruments Corp.). The two ultrasonic transducers are connected to the pulser/receiver. One transducer emits ultrasonic pulses and receives echo signals from the reflectors, and the other transducer receives the transmitted ultrasonic pulse. Signals recorded by the digitizer are transferred to the PC. Thus, both the echo and transmitted signals can be simultaneously recorded.

Experiments were conducted at a flow rate calibration facility of National Metrology Institute of Japan (NMIJ) of Advanced Industrial Science and Technology (AIST). Working fluid was water. Figure 6 shows schematic of the test section. Test section was horizontal pipe and its inner diameter, *D*, was 200 mm. A couple of transducers were set at $\theta = 45°$ and submerged into the water. f_0 of the transducers was 1 MHz and its effective diameter was 12 mm. Small air bubbles were injected into the flow as ultrasonic reflector, and a rectifier was installed at upstream of the test section. The distance from the rectifier and the test section was 55*D*. Installing the obstacle plate at 8*D* upstream from the test section, flow can become asymmetric. The obstacle plate has a semicircle-shaped aperture and its aperture ratio is 0.66.

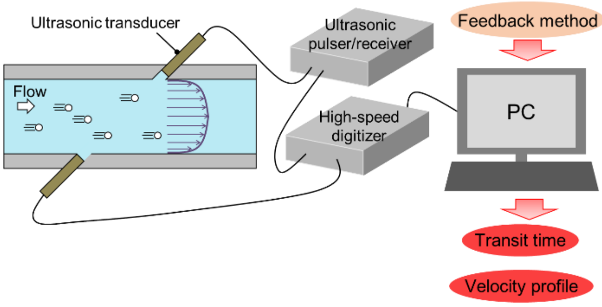

Figue 5: Schamatic of the hybrid ultrasonic flow meter.

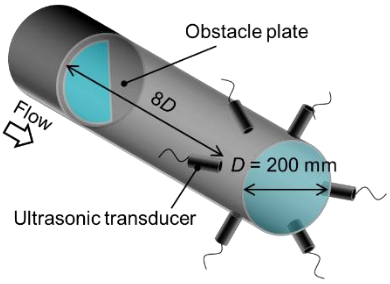

Figue 6: Schamatic of the test section. An obstacle plate was installed for measuring asymmetrical flow condition.

4. Results and discussion

4.1 Line-averaged velocity

The $V_{L,\mathrm{TOF}}$ and $V_{L,\mathrm{UDM}}$ were compared as shown in Figure 7 under symmetrical and asymmetrical flow conditions at flow rate of 320 m^3/h. Temporal resolutions of UDM and TOF was 69 ms and 0.54 ms, respectively. For direct comparisons, moving average was applied for $V_{L,\mathrm{TOF}}$. Tendencies of $V_{L,\mathrm{UDM}}$ were in good agreement with that of $V_{L,\mathrm{TOF}}$. The velocity fluctuation is more significant at asymmetrical flow than that at symmetrical flow, and the difference of V_L is large at asymmetrical condition. There were some velocities that the difference of V_L between TOF and UDM exceeds 5%. Thus, theses data were eliminated for calculating the averaged velocity profile.

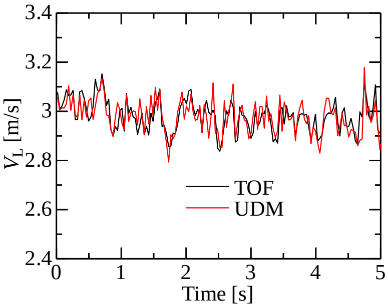

(a) Symmetrical flow

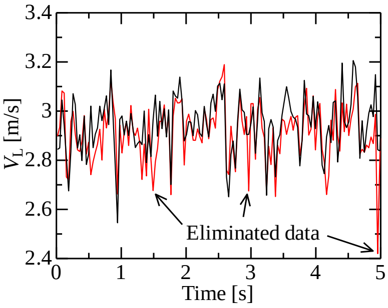

(b) Asymmetrical flow

Figure 7: Simultaneous measurement of V_L in TOF and UDM.

1,000 instantaneous velocity profiles were averaged. For the symmetrical flow, the flow rate was calculated from the velocity profile for one-half region of the pipe. For the asymmetrical flow, the flow rate cannot be derived from a single line measurement. Therefore, multiple velocity profiles were measured along the three measuring lines. Each transducer was used to obtain the velocity profile in one-half of the pipe, and using six transducers, the velocity profiles along the three measuring lines were obtained, as shown in Figure 8.

PFs were determined using Eq. (3) based on the flow rate calculated from the velocity profiles. For averaging the PFs in each flow condition, PFs were determined at 0.948 for symmetrical and at 0.966 for asymmetrical flow conditions as shown in Figure 9. In the asymmetrical flow, the PFs were calculated along each measuring line. The flow rates obtained using the UDM were substituted for Q, and the obtained $V_{L,\mathrm{TOF}}$ values were substituted for V_L in the equation. The PFs under the asymmetrical-flow conditions were higher than those under the symmetrical flow conditions, because V_L for the asymmetrical flow was lower than that for the symmetrical flow. In the asymmetrical flow, the PFs depend on the measuring lines because the velocity profile is different along different measuring lines. The average PFs were determined under the symmetrical and asymmetrical flow conditions for each measuring line by averaging the PFs of each flow rate. The PFs obtained for the symmetrical and asymmetrical flow were in good agreement with the calibration results of the reference flow meter. The error could be reduced to ±1% of the flow rate.

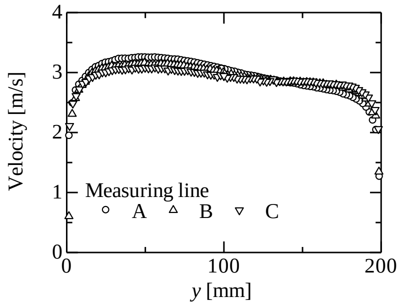

Figure 8: Average velocity profile at Q = 320 m^3/h for asymmetrical flow.

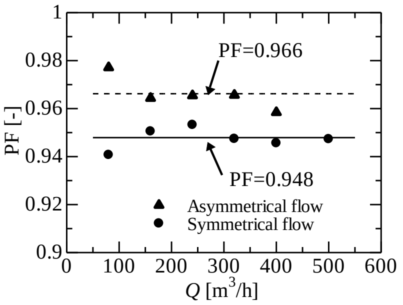

Figure 9: PF in each flow rate under symmetrical and asymmetrical flow conditions. The PFs were determined by the flow rate obtained by using UDM.

5. Conclusions

Hybrid ultrasonic flow meter between TOF and UDM is useful for on-site calibration for determining the profile factor. However, the UDM has relatively large uncertainty in comparison to the TOF. Despiking method was useful to eliminate the uncertain data as a post-processing for the UDM velocity distributions. In this study, a method to eliminate the uncertain velocity profiles was proposed. Line-average velocities were obtained using TOF and UDM simultaneously, and these were compared to eliminate the scattering data. As a result, it was shown that the hybrid ultrasonic flow meter made it possible to determine the PF under asymmetrical flow condition.

References

[1] Wada S *et al.*: Development of pulse ultrasonic Doppler method for flow rate measurement in power plant: multilines flow rate measurement on metal pipe, J. Nucl. Sci. Technol., 41 (2004), 339-346.

[2] Tezuka K *et al.*: Ultrasonic pulse-Doppler flow meter application for hydraulic power plants, Flow Meas. Inst., 19 (2008), 155-162.

[3] Murakawa H *et al.*: A dealiasing method for use with ultrasonic pulsed Doppler in measuring velocity profiles and flow rates in pipes, Meas. Sci. Tech., 26 (2015), 085301, 11pp.

[4] Muramatsu E *et al.*: Multi-wave ultrasonic Doppler method for measuring high flow-rates using staggered pulse intervals, Meas. Sci. Tech., 27 (2016), 025303, 11pp.

[5] Goring DG & Nikora V.I.: Despiking acoustic Doppler velocimeter data, J. Hydraulic Engineering 128 (2002), 117-126.

11th International Symposium on Ultrasonic Doppler Methods for Fluid Mechanics and Fluid Engineering
Berlin, Germany (5.-7. September 2018)

A New Industrial Hybrid Ultrasonic Flow Meter for Oil Drilling Applications

Reinhardt Kotzé[1], Johan Wiklund[1], and Morten Lien[2]

[1] Incipientus Ultrasound Flow technologies, RISE Research Institutes of Sweden, Division Bioscience and Materials, Frans Perssons Väg 6, 412 76, Göteborg, Sweden, Box 5401.
[2] Drilling and Well Technology, Statoil ASA, Research and Technology, Arkitekt Ebbels veg 10, 7053 Ranheim, Norway.

The measurement of the flow rate of drilling fluids is critically important for safe and effective drilling. Coriolis technology offers accuracy and reliability in measuring material flow and is often used in the oil and gas industry due to direct mass flow, fluid density, temperature, and precisely calculated volume flow rates. However, pressure loss could be a critical consideration in heavy oil applications, since frictional losses increase with increasing viscosity. There is therefore an incentive to minimize flow meter pressure drop and to reduce cost of installation and ownership. Ultrasonic flow meters are popular due to their clamp-on and non-invasive designs. They typically use the transit-time or continuous Doppler technique. However, both methods require a correction or profile factor (PF) to determine the correct flow rate. In an attempt to overcome the current limitations we combined the pulsed Doppler and transit-time techniques. The prototype hybrid flowmeter technology was installed and commissioned in a 2” stainless steel flow loop using water as commissioning fluid. It was then tested in a bentonite suspension (non-Newtonian) during laminar and turbulent flow and results were compared with a Coriolis mass flow meter as well as first principles (bucket and stop watch). Sensors were also deliberately misaligned to test the performance of the algorithms in low signal-to-noise environments. It was found that by including the complex flow profiles with the transit-time measurement the true flow rate could be determined with improved accuracy. Good agreement was found with the reference (BASW) flow rate across the entire range (0-300 l/min). New algorithms were developed to extract weak RF signals for accurate time-of-flight measurements. An important feature of the hybrid flow meter is that it can be used in open channel applications (free surface flows). The next step is to upscale the flow meter to 8” carbon steel pipe size and test in real drilling muds in partially filled pipes.

Keywords: Ultrasonic Doppler velocimetry, Transit-time ultrasonic flow meter, hybrid ultrasonic flow meter, in-line calibration

1. INTRODUCTION

The measurement of the flow rate of drilling fluids is critically important for safe and effective drilling. Accurately measuring the balance of the drilling fluids as a system (barrels-in versus barrels-out) provides important information to the driller and mud logger. It gives for example early warning kick detection and allows accurate monitoring of the mud transport velocity and lag times [1]. Drilling mud flow measurement can be a very challenging measurement for traditional flow meter technologies. Wide variations in the type of mud (water based, oil based, synthetic, emulsion), the solids content, the type of solids and other factors requires flow meters that can measure drilling fluids with wide ranges of fluid viscosity, density, conductivity and resistivity. Unfortunately, the performance of conventional flow meters when applied to complex viscous fluids remains relatively poorly known. Some technical challenges are immediately identifiable. These include the viscosity and non-Newtonian flow behavior of drilling fluids, varying velocity profiles due to changes in flow regime as well as secondary components in liquids such as settling solids or gas/air.

Different metering devices will be affected by these phenomena in different ways. Magnetic flowmeters are used to measure the flow of conductive liquids and slurries, including paper pulp slurries and black liquor. Their main limitation is that they cannot measure hydrocarbons very well, which are nonconductive. This makes them a bad fit for oil and gas drilling applications where drilling muds need to be monitored. Coriolis technology offers accuracy and reliability in measuring material flow and is often used in the oil and gas industry due to direct mass flow, fluid density, temperature, and precise calculated volume flow rates. However, pressure loss might be a critical consideration in heavy oil applications, since frictional losses increase with increasing viscosity. There is therefore an incentive to minimize flow meter pressure drop to avoid excess pumping power requirement and reduce cost of ownership. Coriolis flow meters are known to have a larger pressure drop than many other conventional flow meters due to the small diameter of the internal measurement tubes. Furthermore, due to the pipe diameter size the flow meter becomes excessively large and it becomes a challenge to install the flow meter and to calibrate due to installation issues. Ultrasonic flow meters have negligible pressure drop due to their non-invasive designs, have high turndown capability, and can handle a wide range of applications. Installation of ultrasonic meters is relatively straightforward, and maintenance requirements are low, which makes this an attractive solution for the oil and gas industry. They typically use the transit-time or continuous Doppler. However, both methods require a correction or profile factor (PF) to determine the correct flow rate. This factor strongly depends on the velocity profile in the pipe. Typically this value is determined by using theoretical

https://doi.org/10.7795/810.20190809

simulations or experimental tests at a calibration facility. However, this is not sufficient as the velocity profile also depends on the pipe roughness, complex fluid properties that change with pressure and temperature. Therefore, in-line calibration of the PF is required to maintain the accuracy of the flow meter and to reduce maintenance / calibration costs. The development of multipath transit time flowmeters, which use more than one ultrasonic signal or "path" in calculating flowrate, has led to greater accuracy and is even used for custody transfer applications. However, these provide limited information on the flow profile as normally 4-6 paths are used. These flow meters also cannot be used in partially filled pipes and open channel applications found in drilling mud transportation.

To solve the current limitations in accurate flow metering we combined the pulsed Doppler and transit-time techniques. One of the performance areas of the industrial flow meter is robustness in a reduced signal-to-noise environment ratio due to large ultrasound attenuation and electromagnetic noise. This is because drilling muds contain water droplets, gas/air, wide particle size distribution and cause wax layer build-up (fouling) inside the pipe. The hybrid flowmeter technology was commissioned in tap water and then evaluated in a bentonite suspension that is typically used in drilling muds. Tests were conducted during laminar and turbulent flow and results were compared with Coriolis flow meter as well as first principles (bucket and stop watch) that served as the reference value.

2. METHODS AND APPARATUS

2.1 Hybrid ultrasonic flow meter

The Incipientus^{TM} system is a commercial and fully integrated platform for high resolution Doppler measurements as well as in-line rheometry. It features 2 transmit/receive (TX/RX) channels that can work in stand-alone or pitch-catch configuration. The transmitters, based on an Arbitrary Waveform Generator (AWG), are capable of producing bursts, typically at up to 80 Vpp with a frequency ranging between 0.7–7 MHz. The inputs are amplified with Time Gain Control (TGC) units featuring a gain up to 55 dB, converted to digital at 16-bit 100 MS/s, and processed in an FPGA. The FPGA include coherent demodulators, filters and a FFT processor for spectral analysis [3-4]. Non-invasive sensors that can measure velocity profiles in highly attenuating suspensions through stainless steel formed part of the hybrid flow meter setup [5].

2.2 Experimental flow loop

The DN51 MM, 2" flow loop consists of a storage tank, a frequency-controlled positive displacement pump and a closed stainless steel piping circulation system including PT100 temperature sensors (Pentronic, Gunnebo, Sweden), a coriolis mass flow meter (Krohne Optimass 6400 S50, ATEX) and two non-invasive ultrasound sensor units (Incipientus AB, Gothenburg, Sweden) for Doppler and transit-time measurements. Two differential in-line pressure sensors (Incipientus AB) were installed adjacent to the ultrasound sensors with a distance 0.65 m apart for in-line rheology measuremens. The rheology was measured to determine non-Newtonian Reynolds numbers [6] during the experiments with bentonite suspensions. The bentonite suspension was characterized with a yield stress of 5.4 Pa and consistency index of 50 mPa.s. The reason for choosing bentonite was to test in non-Newtonian yield stress fluids (plug-flow). Real drilling fluids have viscosities more than ten times higher, but with similar yield stress. Figure 1 shows a photo of the experimental flow loop at the Incipientus AB laboratory in Gothenburg, Sweden.

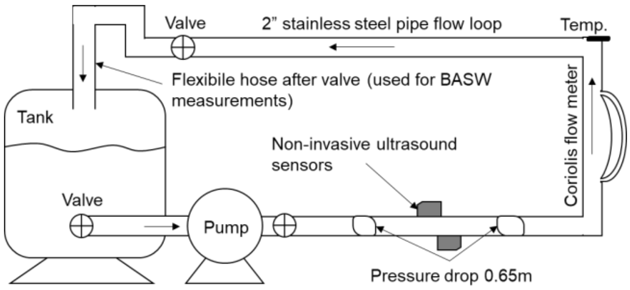

Figure 1: Schematic of experimental flow loop consisting of non-invasive ultrasound sensors (hybrid ultrasonic flow meter) and Coriolis mass flow meter.

2.3 Experimental procedures

Six flow rates (25, 50, 100, 150, 200, 250, 300 l/min) were tested. The flow rates were confirmed by using the gravitational "bucket and stop-watch" (BASW) method. These values were used as the reference and an error difference was calculated between the results obtained using the Coriolis and hybrid ultrasonic flow meter. For each flow rate an average of three BASW readings were used and any outliers were excluded from this (at high flow speeds up to five readings were done depending on outliers). Measurement time depended on the flow rate and ranged from 60 to 10 seconds. The density reading from the Coriolis mass flow meter was used to convert the BASW values to volume flow rate. An average of 64 Doppler profiles were taken in both directions of the pipe flow. For transit-time (flow metering) and speed of sound measurements 3000 pulses were used up- and downstream in total. The temperature during experiments varied between 19 and 21 ºC. The Coriolis flow meter output was logged using an DAQ (National Instruments) setup during the same time.

3. RESULTS AND DISCUSSION

3.1 Low SNR performance

Drilling fluids exhibit unique acoustic properties and one important parameter is the velocity of sound in the fluid medium. This parameter is also influence the accuracy of velocity profiles and transit-time measurements. Usable RF data and velocity of sound measurements can be used to determine density, homogeneity and to study aeration effects. Having access to this data in-line may provide the oil industry a powerful tool to investigate and monitor complex flow properties during processes/transportation.

One objective was therefore to simulate an environment with where SNR is low. This was done by misaligning the ultrasound sensors opposite to one another and therefore only measuring a weak or low amplitude signal in the presence of electromagnetic noise. Figure 2 shows a graph of fifty RF signals received up- and downstream in the presence of noise. The measurements were done in the bentonite suspension at 100 l/min.

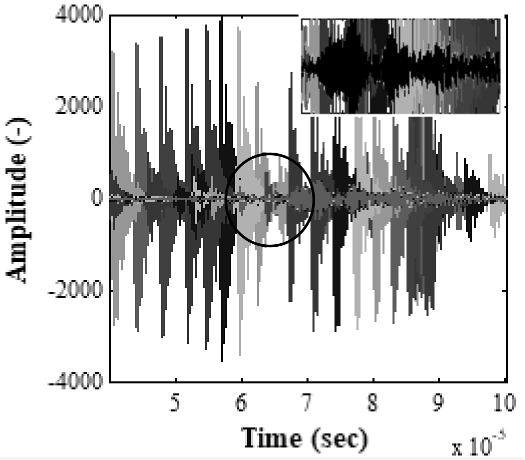

Figure 2: Fifty RF signals received (pitch-catch mode) in the presence of electromagnetic noise in bentonite. The waveform inside the circle (magnified) is extracted to for velocity of sound and transit-time measurements.

Note that in total 3000 pulses are sent in pitch-catch mode and thus with time the received waveform becomes completely embedded within noise. The noise amplitude level is more than 11 times higher than the signal amplitude level in this example. Figure 3 shows the up- and downstream time-of-flight values after signal processing. It can be observed that the upstream (Tup) time-of-flight (ToF) values fluctuate more than the downstream ToF values probably because the one sensor was not coupled correctly. Even so it was still possible to achieve accurate ToF measurements. Due to the flow velocity (volume flow rate 100 l/min) it can be clearly observed that there is a difference between the up- and downstream tof measurements. The average Tup = 71.335 us and Tdown = 71.3 us, which yields a time difference of 35 ns. Using cross-correlation the difference obtained was 27.4 ns. This means that the accuracy achieved is less than one sample (sampling time = 10 ns), bearing in mind that the sampling frequency of the electronics is 100 MHz. The fluctuations decrease with increasing flow rate as the time difference between up- and downstream increases (higher accuracy achieved). A new algorithm had to be developed that work together with the electronics digitizing output to extract the weak or attenuated RF signals. Based on the results it can be concluded that the hybrid flow meter can successfully extract the important data needed for speed of sound and transit-time calculations. The next step will be to evaluate the hybrid flow meter in real drilling fluids (oil- and water based) and on oil-drilling platforms.

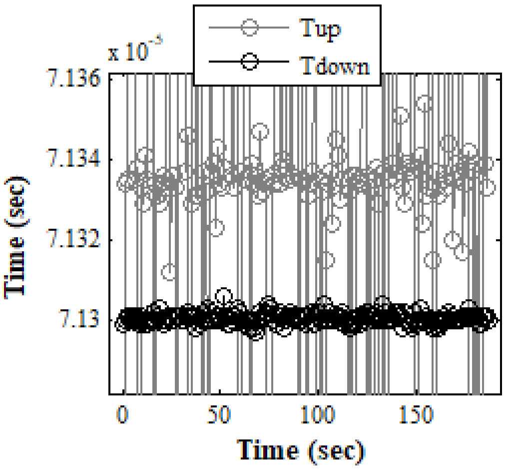

Figure 3: Time-of-flight measurements for up- and downstream measurements in bentonite suspension (flow rate 100 l/min).

3.2 Flow meter performance in water

Figure 4 shows the error percentage difference for both flow metering methods (compared to BASW reference). Note that the hybrid flow meter has a good agreement to the Coriolis flow meter over the entire range. At the lowest flow rate the hybrid flow meter retained its accuracy. The average percentage deviation for the hybrid flow meter was 2.4% over the entire flow rate range. The Coriolis average error was 4.3%.

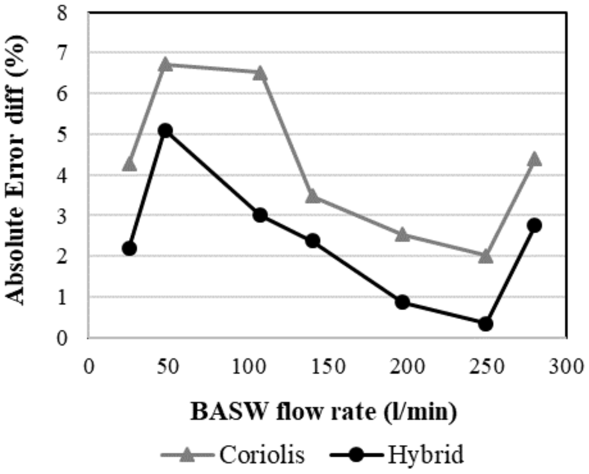

Figure 4: Comparison of Coriolis and hybrid ultrasonic flow metering methods with reference measurements (BASW) in water.

3.2 Flow meter performance in bentonite suspension

During the bentonite experiments the flow regime varied from laminar (25 – 150 l/min) to turbulent (200 – 300 l/min) flow. Figure 5 shows two Doppler profiles (spectra) measured in bentonite during laminar (25 l/min) and turbulent flow (300 l/min). Non-Newtonian Reynolds numbers varied from 322 to 6400. The hybrid flow meter adjusted the PF to compensate for the change in velocity profile. Good agreement to the Coriolis flow meter (and reference value) over the entire range was found, see

Figure 6. It is interesting that the error percentage deviation for the Coriolis flow meter decreased in the bentonite suspension, probably due to the increase in viscosity.

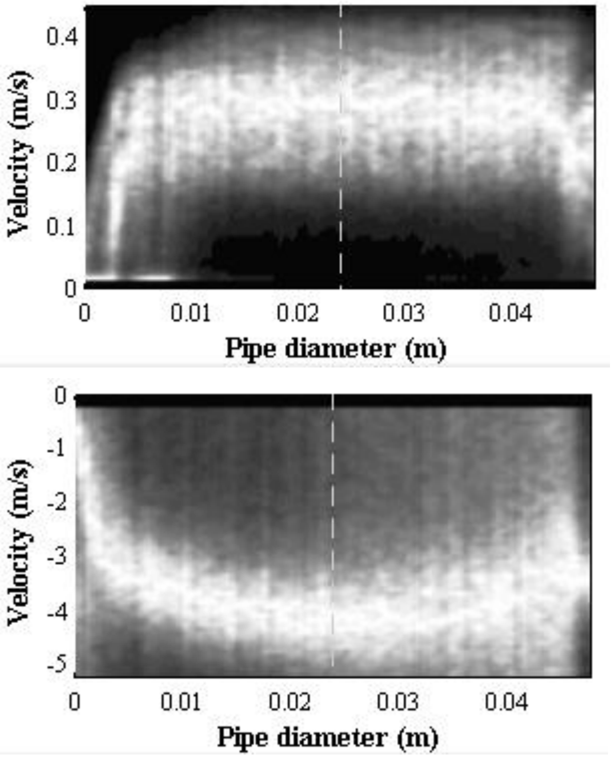

Figure 5: Laminar Doppler profile (top) and turbulent Doppler profile (bottom) measured in bentonite suspension.

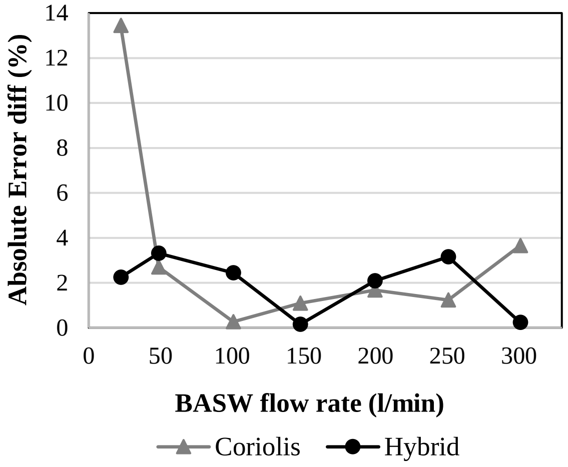

Figure 6: Comparison of Coriolis and hybrid ultrasonic flow metering methods with reference measurements (BASW) in bentonite suspension.

At the lowest flow rate (25 l/min) the hybrid flow meter retained its accuracy. The average percentage error for the hybrid flow meter was 1.9% over the entire flow rate range. The Coriolis flow meter had a higher total error difference of 3.4%, which was mainly due to the larger error at the lowest flow rate. When excluding that value the error difference reduced to 1.8%, similar to what was obtained with the hybrid ultrasonic flow meter.

4. SUMMARY AND CONCLUSION

The key benefits of ultrasonic technology, low pressure and low maintenance are highly attractive for the oil industry. Transit-flow meters are best operated at the higher flow ranges for optimum accuracy. However, with the combined Doppler technique accurate measurement at the lower flow ranges can also be achieved. No pressure loss results in reduced operating costs. No moving parts results in increased service life and may reduce the frequency of proving since usage wear is a key reason why meters must be recalibrated. One disadvantage is the need for upstream piping, however, less than 0.5% accuracy can be achieved by adding more sensors (up to three), even for asymmetrical flow [2].

There are still other challenges remaining before a commercial system for oil-drilling applications can be deployed. This mainly revolves around the automation of ultrasound parameter settings to maintain accuracy and robustness as critical measurement parameters are today still operator dependent. This includes automatic PRF control, de-aliasing profiles and automatic gain control. This is already under development [7-8]. One limitation that can be easily overcome is the electronics sampling rate. By increasing the sampling rate higher time resolution can be achieved as well as higher accuracy at lower flow rates. The next steps are to upscale to 8” carbon steel pipes and test real drilling fluids. An important feature of the hybrid flow meter is that it can be used in open channel applications (free surface flows). In the next phase flow rates will also be measured in partially filled pipes (8”) using real field oil-based drilling muds.

REFERENCES

[1] Tombs M *et al.*: High precision Coriolis mass flow measurement applied to small volume proving, Flow. Meas. Instrum, 17-6 (2006), 371-382.

[2] Muramatsu E *et al.*: Applicability of hybrid ultrasonic flow meter for wide-range flow-rate under distorted velocity profile conditions, Exp. Therm. Fluid. Sci, 94 (2018), 49-58.

[3] Ricci S *et al.*: Embedded Doppler system for industrial inline rheometry, IEEE Transactions on Ultrasonics, Ferroelectrics, and Frequency Control, 59 (2012) 1395-1401.

[4] Kotze R *et al.*: Application of ultrasound Doppler technique for in-line rheological characterization and flow visualization of concentrated suspensions, The Canadian journal of Chemical Engineering, 94-6 (2016) 1066-1075.

[5] Kotze R *et al.*: Performance tests of a new non-invasive sensor unit and ultrasound electronics, Flow. Meas. Instrum, 48 (2016) 104-111.

[6] Slatter PT, Lazarus JH: Critical flow in slurry pipelines. British Hydromechanics Research Group, 12th Int. Conf. Slurry Handling & Pipeline Transport, (1993) 639-654.

[7] Wiklund J *et al.*: Flow-Viz pulsed ultrasonic Doppler system with autotuning of analog- digital gain and threshold, Transactions ISUD10, Tokyo, Japan, 10 (2016) 29-33.

[8] Ricci S *et al.*: Real-time staggered PRF for in-line industrial fluids characterization. DOI: 10.1109/ULTSYM.2017.8091778. Ultrasonics Symposium (IUS), (2017) IEEE International.

11th International Symposium on Ultrasonic Doppler Methods for Fluid Mechanics and Fluid Engineering
Berlin, Germany (5.-7. September 2018)

Transient Flow Rate Measurement by Means of Ultrasonic Pulsed Doppler Method

Noriyuki Furuichi[1], Sanehiro Wada[1], and Yasushi Takeda[2]

[1] National Institute of Advanced Industrial Science and Technology, 1-1-1 Umezono, Tsukuba, 305-0861, Japan
[2] Laboratory for Food Research Engineering, Swiss Federal Institute of Technology Zurich, Zurich 8092, Switzerland

This paper reports the investigations of the transient flow rate of the several flow meters and the ultrasonic flowmeter based on the pulsed Doppler method. The reference flow rate is given by the gravimetric method which is newly established in NMIJ. The flow rates are investigated for pulsation flow with 0.5 Hz – 8 Hz frequency. The fluctuations of flow rate by ultrasonic pulsed Doppler method and Coriolis flowmeter are agreed well each other and with the reference flow rate. The influence of the fluctuation of flow rate is less than 2% for the pulsed Doppler method. The result gives new advantage, which is high response for transient flow, for the ultrasonic flowmeter based on the pulsed Doppler method.

Keywords: Flow rate, Transient flow, Weighing method, Flowmeter, Pipe flow

1. Introduction

Flow rate is one of the most important parameters in engineering fields, such as power generation, chemical, food and so on. Many types of flowmeter have been developed depends on the measurement target and are using in each flow field because there is no flowmeter which is applicable for any flow field. Every type of flow meter has both advantage and disadvantage. The advantage of an ultrasonic flowmeter, which is recently applied to many flow fields, is generally no pressure loss and maintenance free. The disadvantage of the ultrasonic flowmeter depends on the principle. A transit-time ultrasonic flowmeter, which is the most popular principle, is strongly influenced by the velocity profile in the pipe because the flow rate is calculated from a line averaged velocity between ultrasonic sensors. The disadvantage of the ultrasonic flowmeter based on pulsed Doppler method is a necessity of reflector. To obtain flowrate or velocity information, sufficient reflector is necessary in the target flow field. However, this flowmeter is not influenced by the velocity profile because the principle is based on the direct integration of it. The ultrasonic flowmeter based on the pulsed Doppler method was firstly proposed by Mori et al. [1], and has been applied several flow fields [2][3]. From the uncertainty analysis by author [4], the accuracy of this method has been established.

The principle of the pulsed Doppler method brings another advantage. That is high response for transient flow, which is very important for process control. High response of flowmeter installed in a process line achieves an optimal management and reducing the start-up procedure and so on. Mori et.al [1] reported that the flow rate fluctuation measured by the pulsed Doppler method agreed well with orifice flowmeter. Wiklund et al.[5] reported the dynamic response for several type of flowmeter. They reported that the response of the differential pressure type flow meter was the highest. However, both experiments investigated only a responsibility of each flowmeter and did not mention about the accuracy for the measurement of the transient flow rate, in other word, an instantaneous flow rate. To know the accuracy of the transient flow rate measurement, the comparison with reference flow rate is required. Unfortunately, there is no reference standard for the “dynamic” flow rate although there are many reference standards for “static” flow rate all over the world. However, one trial for the dynamic flow rate measurement by modifying the static gravimetric method, which is widely used as the reference standard of the flow rate measurement, has been done by Shinder et al [6]. They claimed that the standard uncertainty of the dynamic flow rate measurement using the weighing tank method is 0.015%. This result indicates that this method is possible to use as the reference standard of the transient flow rate.

In this paper, we establish the reference standard for the transient flow rate using weighing tank method and investigate the response of the pulsed Doppler method for a pulsation flow.

2. Experimental set up and method

2.1 Experimental apparatus

The flow sheet of this experiment is shown in Fig.1. In this experiment, the national standard of small water flow rate in Japan [7] was used with small modification. This national standard consists of the 10 kg weighing tank system with high accurate rotating diverter. The flow rate range is from 0.002 m^3/h to 1.2 m^3/h. The temperature of working fluid which is water is controlled by the temperature control unit and the stability is less than 0.1

https://doi.org/10.7795/810.20190809

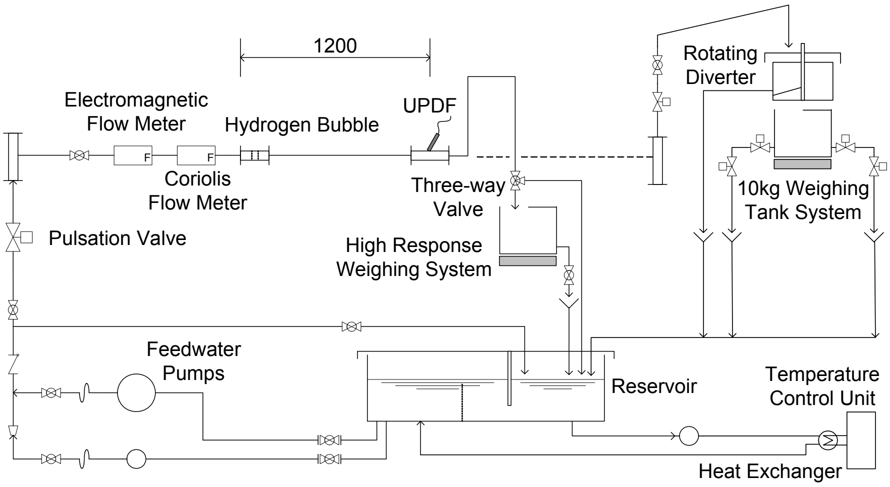

Figure 1: Flow sheet of experimental facility. The facility is managed as the national standard of flow rate in Japan.

°C. The flow rate is given by the static gravimetric method and the expanded uncertainty of the flow rate measurement is 0.04% with coverage factor of 2.

In this experiment, the pulsation valve and the high response weighing tank are added to the original facility. The pulsation valve is driven by air pressure and repeats the shut on-off operation. The frequency of the on-off operation can be controlled from 0.5 Hz to 10 Hz. Note that the pulsation flow cannot be observed at the test section from the velocity measurement when the frequency is over 8 Hz.

The high response weighing system is consists of the 8 kg tank which is set on the single load cell. The response time in the specification of the load cell is less than 2 msec. To avoid the influence by the direct shock of water, porous bodies with different mesh size are installed in the tank. The flow line is changed by the three-way valve installed downstream of the test line. The example of the time-dependent weight of the water in the tank is shown in Fig. 2. The pulsation frequency is 1 Hz. The instantaneous flow rate is given by the differential of the time-dependent weight. The results will be shown in Section 3.

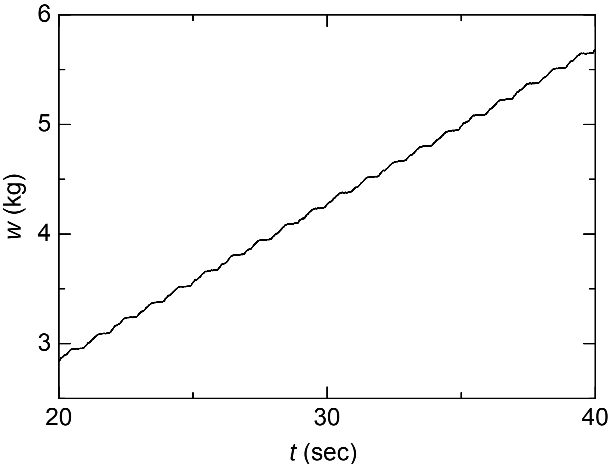

Figure 2: Dynamic weight with 1 Hz pulsation.

2.2 Examined flowmeters

The inner diameter of the pipe in the test section is 25 mm. The test meters were electromagnetic, Coriolis and ultrasonic pulsed Doppler flowmeter, which is called as UPDF hereafter. Electromagnetic and Coriolis flow meters are installed in series as shown in Fig.1. At downstream of the Coriolis flow meter, hydrogen micro bubble is generated. The distance between the bubble generation section and the measurement location by UPDF is 1200 mm. At the downstream of UPDF, two weighing tank systems are equipped, which can be selected depends on the experiment. The measurement for all flow meter was done synchronized with the weight measurement of the high response weighing system. The signal output frequency of electromagnetic and Coriolis flow meters is set to 1 kHz for 1.5 m^3/h. The frequency is linear with flow rate. Using the converter from the frequency to voltage, the flow rate is calculated. In this experiment, the frequency is less than 0.57 kHz.

For the UPDF, the ultrasonic transducer with 4 MHz was used. The ultrasonic transducer was set with 45° inclination angle against to the horizontal axis. The measurement section for the UPDF is covered by the water chamber to avoid the reflection noise of the ultrasonic. The measurement of the velocity field was performed using the UVP-Duo by Met-Flow. The time interval of the velocity profile was 16 msec. The measurement of the velocity was also synchronized with the other flow meter measurement.

2.3 Experimental condition

The flow rate without pulsation was set to 0.85 m^3/h in this experiment. The bulk velocity in the test section was app. 0.5 m/s. Temperature of water was 20 °C and was controlled ±0.2 °C using temperature control unit.

The pipe length from the electromagnetic flow meter to the high response weighing tank is 1800 mm. Assuming that the delay time of the velocity profile is equivalent with the propagation speed of the pressure wave, it between the electromagnetic flowmeter and the

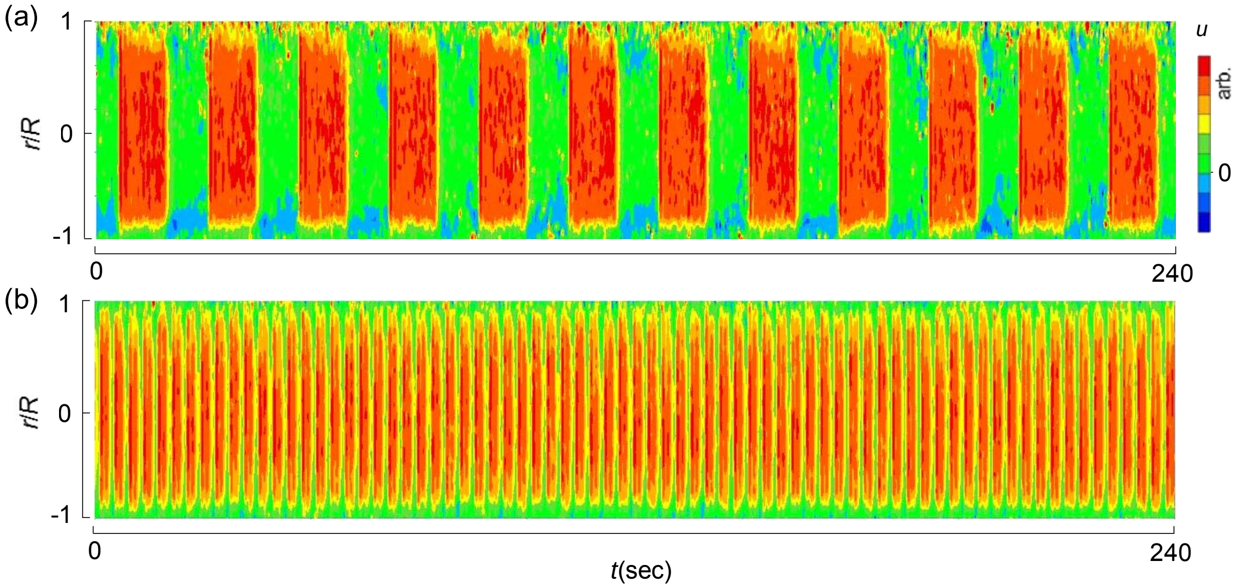

Figure 3: Flow field of $u(r,t)$ with (a) 0.5 Hz, (b) 3 Hz pulsation.

high response weighing system is estimated less than 2 msec at most. Therefore, the delay time is equivalent with the time resolution of the flow meters and smaller than UPDF.

3. Result and discussion

The velocity profiles $u(r,t)$ in the time-space domain, which are measured by UPDF, are shown in Fig.3. Here, r is the radial position and R is the radius of the pipe. The pulsation frequencies in these figures are 0.5 Hz and 3 Hz. The pulsation flow can be investigated clearly. The velocity in the whole pipe is fluctuated depends on the on-off of the pulsation valve. In the result for 0.5 Hz, negative flow, which is the secondary flow, is also investigated near the wall. This negative flow might influence to the flow rate measurement since it is obtained by the direct integration of the velocity profile.

Firstly, the influence of the pulsation flow for the average flow rate is investigated. The relation between the deviation from the non-pulsation flow and the on-off frequency of the pulsation valve is shown in Fig.4. This result is obtained by the 10 kg weighing tank system. The horizontal axis is the deviation from non-pulsation flow, which is given by the following.

$$E = \frac{k_\mathrm{p} - k_\mathrm{n}}{k_\mathrm{n}} \tag{1}$$

where, the subscripts p and n are for the pulsation flow and non-pulsation flow, respectively. k is the correction factor given by the following,

$$k = Q_\mathrm{f} / Q_\mathrm{r} \tag{2}$$

Q_f is the flow rate indicated by flow meters and Q_r is the flow rate given by the reference, here 10 kg weighing tank system.

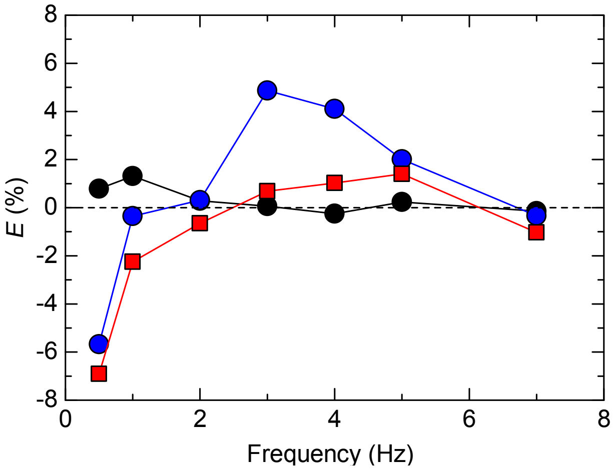

Figure 4: Influence of the pulsation for averaged flow rate. The blue points and line are the electromagnetic, the blacks are Coriolis flow meter and the reds are UPDF. E is the deviation from the non-pulsation flow.

The electromagnetic flowmeter and UPDF shows large deviation flow the lowest frequency. This might be caused by the reverse flow as shown in Fig.3 since these flowmeters are influenced by the velocity profile. On the other hand, since the Coriolis flow meter is not influenced by the velocity profile, the deviation is relatively smaller. With increase pulsation frequency, the deviation of UPDF decreases. Over than 2 MHz, the deviation is less than 2%. The electromagnetic flow meter is strongly influenced by the pulsation flow around 3 MHz, however it decreases with frequency. The deviation for all examined meters approaches to zero around 7 Hz. The amplitude of the pulsation flow decrease with the on-off frequency of the pulsation valve and it is almost zero around 8 Hz as mentioned.

The transient flow rate given by for each flow meter and the high response weighing system is shown in

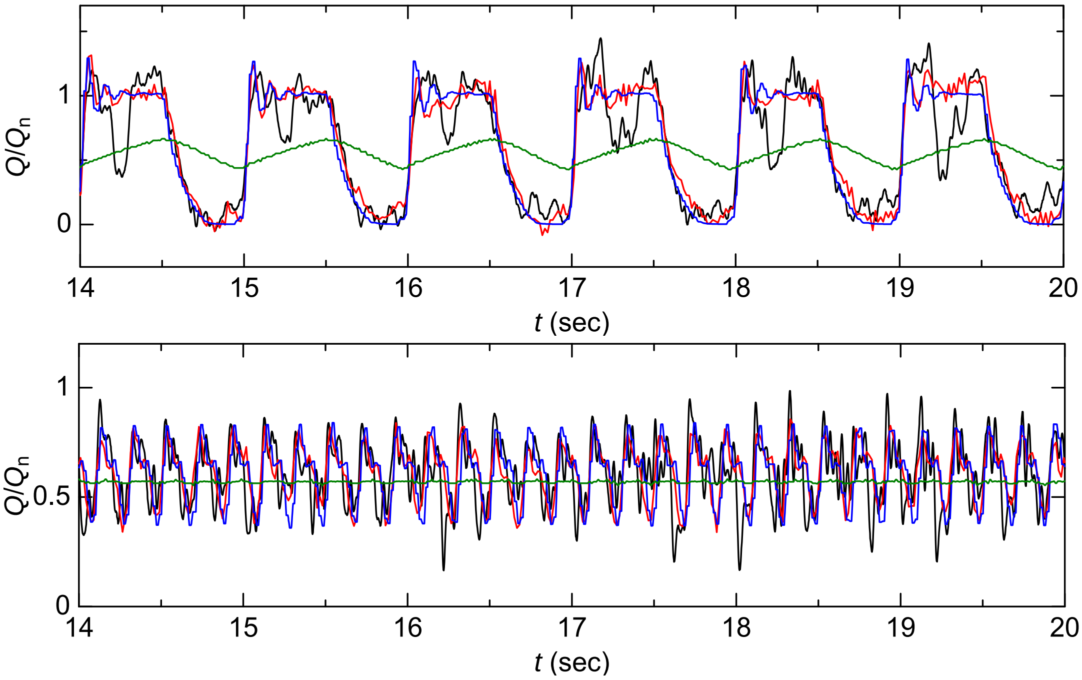

Figure 5: Transient flow rate with (a) 1 Hz, (b) 5 Hz pulsation. The black line is weighing tank, the red is ultrasonic pulsed Doppler method, the blue is Coriolis flow meter and the green is electromagnetic flow meter. Q_n is the nominal flow rate without pulsation.

Fig.5. Under 1 Hz pulsation, the transient flow rate given by the UPDF is very nice agreement with the Coriolis flowmeter for not only the rise-up and fall down but also small fluctuation of flow rate. The result UPDF also agree with the flow rate by high response weighing system for the raise-up and fall down flow rate behavior. However, the flow rate behavior at when the valve is open is largely deviated. This might be caused by the dead volume between the test section and weighing system. On the other hand, the flow rate given by the electromagnetic flow meter is largely different with the UPDM and high response weighing system. Obviously, the time response of the electromagnetic flow meter is very low although the averaged flow rate does not deviate from them as shown in Fig.4.

For higher frequency pulsation flow, the transient flow rate given by UPDF, Coriolis and the high response weighing system agree well. This result guarantees the reliability of measurement results for the transient flow rate each other. In contrast, the electromagnetic flowmeter indicates almost stable flow rate.

As showing in the previous, UPDF and the Coriolis flowmeter has high response for flow rate measurement. The rise-up time of flow rate in Fig.5(a) is app. 40 msec. From this result, the response time of both flow meters are better than 40 msec. The advantage of UPDF is the applicability for wide range size of the pipe, no pressure loss and no entrance length. From the result of this paper, new advantage which is high response for transient flow is established.

4.Summary

This paper reports the investigations of the transient flow rate of the several flow meters and the ultrasonic flowmeter based on the pulsed Doppler method (UPDF). The reference flow rate is given by the gravimetric method which is newly established in NMIJ. The fluctuations of flow rate by UPDF and Coriolis flowmeter are agreed well each other and with the reference flow rate. The influence of the fluctuation of flow rate is less than 2% for UPDF.

References

[1] Mori, M., Takeda, Y., Furuichi, N., et al, Development of a novel flow metering system using ultrasonic velocity profile measurement, Experiments in Fluid, 32 (2002), pp.153-160

[2] Tezuka, K., Mori, M., Suzuki, T., Takeda, Y., Calibration tests of pulse-Doppler flow meter at national standards loops, Flow Measurement and Instrumentation, 19 (2008), pp.181-187

[3] Wada, S., Kikura, H., Aritomi, M., Mori, M., Takeda, Y., Development of pulse ultrasonic Doppler method for flow rate measurement in power plant, Journal of Nuclear Science and Technology, 41 (2004), pp.339-346

[4] Furuichi, N., Fundamental Uncertainty Analysis of Flowrate Measurement using the Ultrasonic Doppler Velocity Profile Method, Flow Measurement and Instrumentation, 30 (2013), pp.202-211

[5] Wiklund, D., Peluso, M., Quantifying and specifying the dynamic response of flowmeters, ISA2002, Technical Conference (2002)

[6] Shinder, I. I., Moldover, M.R., Feasibility of an accurate dynamic standard for water flow, Flow Measurement and Instrumentation, 21 (2010), pp.128-133

[7] Furuichi. N., Terao, Y., Ogawa, S., Cordova, L., Shimada, T., Inter-laboratory comparison of small water flow calibration facilities with extremely low uncertainty, Measurement, 91 (2016), pp.548-556

Estimation of 2D Velocity Vector Fields by Ultrasonic Doppler Velocimetry and Echography

Koki SAWADA, Megumi AKASHI, Hyun Jin PARK, Yuji TASAKA, and Yuichi MURAI
Graduate School of Engineering, Hokkaido University, N13W8, Sapporo 060-8628, Japan

This study aims to establish novel methodology to estimate 2D velocity vector fields with limited number of measurement lines of UVP. To obtain velocity components perpendicular to the measurement line, particles with two-different-diameters are used; the velocity components are measured by particle-tracking-type velocimetry with echo intensity on the larger particles (sufficiently larger than the wavelength of ultrasound), while velocity components in the measurement line direction are obtained by Doppler velocimetry with the smaller particles. As results of the extended measurement above, velocity vector fields with dense one-directional velocity information along the measurement line and coarse information of the component perpendicular to the line are obtained. The coarse information on the present measurement results is supplemented using interpolation method to estimate 2D velocity vector fields from knowledge of particle tracking velocimetry (PTV). Interpolated velocity vector fields take further correction obeying equation of continuity for 2D incompressible flows. Benchmark tests on simple quasi-2D circulating flow in a thin square container indicated that the present methodology works well to estimate, at least, steady, quasi-2D flow fields.

Keywords: echo intensity, multi-directional velocity components, flow field measurement

1. Introduction

Ultrasonic velocity profiler (UVP) [1] has been used for velocity field measurements on opaque liquids such as liquid metal [2-3] and food [4] because of its relatively high temporal and spatial resolution. UVP provides however only one-directional velocity components parallel to the measurement line, and they would be insufficient to discuss characteristics of the field in comparison with multi-directional velocity components obtained by Particle Imaging Velocimetry (PIV) used for measurements of transparent fluids. Using multiple ultrasonic transducers (TDXs) or an array of TDXs can provide multi-directional velocity components at intersections of the measurement lines [5]. The number of velocity vectors is therefore determined by the number of TDXs, and velocity information with the fine spatial resolutions by original UVP measurements has not been used efficiently. Recent applications of medical ultrasonic echography have made possible to achieve PIV on echographic images of tracer particles dispersed into test fluids, termed ultrasonic imaging velocimetry (UIV) [6]. While UIV provides velocity vector filed with a high spatial resolution, it has a low the temporal resolution. It is because UIP requires to transmit an ultrasonic pulse with time lags between the TDXs to do not occur interferences between ultrasonic waves emitted from different TDXs.

Our research group has been trying to extend a dimension of velocity components obtained from UVP by applying information of the echo intensity provided from UVP. This method uses two types of particles with different diameters. In this paper, smaller particle means particle in the range of diameter from a quarter to a half of the wavelength of ultrasonic wave, while larger particle means particle with the diameter comparable to the wavelength. With the smaller particles, the velocity component parallel to the measurement line is obtained with fine spatial resolution comparable to the wavelength by Doppler velocimetry as well as conventional UVP. The larger particles provide relatively stronger reflection echo intensity in comparison with the smaller particle during passage through a measurement line. In the proposed methodology, additional velocity component is given by tracking the particles using echo intensity information like particle tracking velocimetry (PTV). The velocity information to be provided includes the velocity component perpendicular to the measurement line (Fig. 1(a)). The number of larger particles is limited with relatively small to distinguish the echo intensity from individual larger particles, and thus the velocity information provided by the

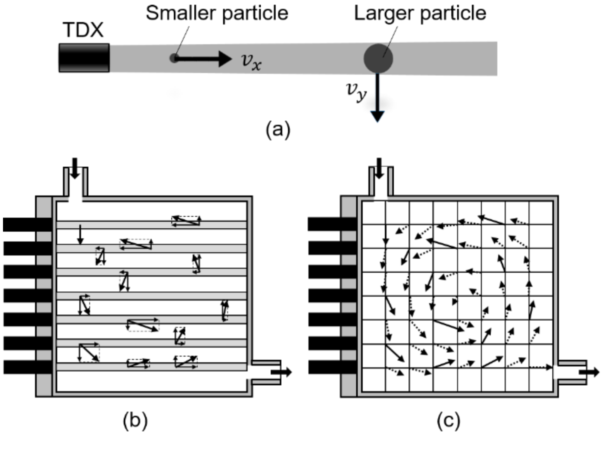

Figure 1: (a) each velocity component obtained from particles with two-difference-diameter; (b) formation derivation of the velocity vectors from Doppler velocimetry and echo intensity method, and (c) processing of interpolation

https://doi.org/10.7795/810.20190809

larger particles is sparse in comparison with the velocity component provided by normal UVP. As a result, dense velocity components parallel to the measurement line and course perpendicular velocity components are obtained on the measurement line (Fig. 1(b)). The information is still insufficient on the combination of them to describe the velocity field. Spatial interpolation on the velocity vector field, which is used for velocity field obtained by PTV, is thus adopted (Fig. 1(c)).

In this paper, as a preliminary step, a relatively simple method to obtain a velocity from time in which the larger particle crosses through an ultrasonic beam is adopted. At first, algorithm to realize the measurement method is established and its applicability is evaluated. Then, a circulating flow in a thin container, which has been often used as benchmark tests for PIV, is measured using the present methodology to evaluate, especially, how the interpolation works to represent velocity fields.

2. Experimental setup

Fig. 2 shows dimensions of the test container, 120 mm × 120 mm × 15 mm, and arrangement of the TDXs for the circulating flows. The container is made of acrylic resin and has an inlet and an outlet; these are connected to a pump for circulation of tap water as the test fluid. By adjusting flow rate from the pump, steady, quasi-two-dimensional circulating flow, which is suitable for evaluation of the present methodology, is formed. For comparison of the measured velocity field, PIV is also adopted; a high-speed video camera was set above the container, and the flow field was illuminated by a green laser sheet at the half height of the container.

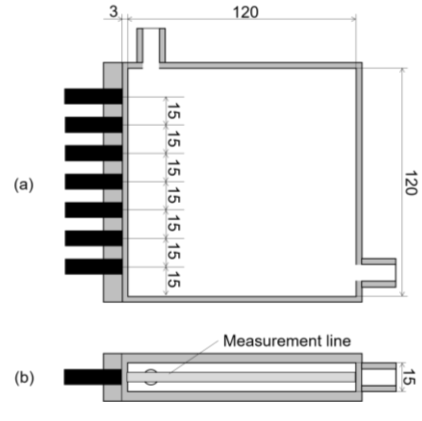

Figure 2: Illustration of experimental container; (a) top view of the vessel and locations of transducers, and (b) side view and UVP measurement line.

Seven TDXs are embedded in the left side wall of the container with equally spacing, 15 mm, and central position of TDX at the end of array places 15 mm from the side wall (Fig. 2). The basic frequency and effective diameter of the TDX are 4 MHz and 5 mm, respectively. The measurement line passes through the half height of the container. Porous resin particles, HP20SS and HP20 (Mitsubishi chemical Co.), were used as "smaller" and "larger" ultrasonic reflection particles. HP20SS has 63-153 µm in diameter and 1.01 in specific gravity. HP20 has 300-700 µm in diameter and 1.01 in specific gravity. For generating ultrasonic waves and signal processing for UVP, UVP monitor model Duo (Met-Flow S.A.) was adopted. Table1 specifies main parameters of present UVP measurement. Because of steadiness of the test flow field, Measurement by each TDX was performed sequentially.

Table 1: Setting parameters of UVP

Base frequency	4.0	MHz
Temporal resolution	4.0	ms
Spatial resolution	0.74	mm
Velocity resolution	3.551	mm/s
Number of cycles	4	-
Number of repetitions	8	-

3. Data processing

3.1 Measurement using echo intensity

In this section, method to measure the velocity component perpendicular to the measurement line using echo intensity information from individual larger particles is explained. As shown in Fig. 1, UVP can measure the velocity component parallel to the measurement line along the line with certain spatial resolution, 0.74 mm in the present setting. Thus, a single TDX obtain two-different velocity components to form 2D velocity vectors.

Because two-different-diameters particles are suspended in the same flow field, it is necessary to distinguish echo information from individual larger particles using magnitude of echo intensity. Both particles used here provide Mie scattering against incident ultrasonic waves and echo intensity from the particle depends on its size. Fig. 3 shows echo intensity with time elapse in the same setting parameter of UVP. The horizontal axis is the time and vertical axis is echo intensity. Fig. 3(a) is echo intensity from HP20SS (smaller particle), while Fig. 3(b) is for that from mixture of HP20SS and HP20 (larger particle) with small amount. There are two different levels of echo intensities that should be provided by the smaller and larger particles in Fig. 3(b). This large variation on the time trace is caused by passage of the larger particles. In this study, perpendicular velocity component is obtained from time in which a larger particle passes through a

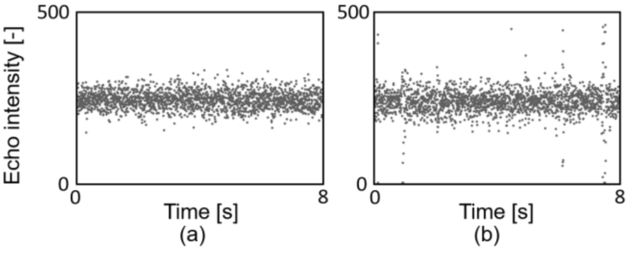

Figure 3: Time traces of echo intensity for (a) only smaller particles, and (b) smaller and larger particles

measurement line, and thus it is necessary to detect only echo variations caused by passage of the larger particles on noisy echo distributions with smaller and larger particles. To extract the echo information from only the larger particles, filter processing is performed. Laplacian filter is used to emphasize echo variations corresponding to passages of the larger particles. Fig. 4(a) shows original data, while Fig. 4(b) shows data with processing Laplacian filtering. After the filtering, echo variations corresponding to motions of smaller particles are removed by giving a threshold value determined by standard deviation (Fig. 4(c)). On the echo distribution after the filtering processes, a traveling time of a larger particle passing through the measurement line, Δt, is determined by counting a part of remaining echo intensity (Fig. 4(d)). The velocity component perpendicular to the measurement line, v_y, is thus calculated as

$$v_y = \frac{D_\mathrm{u} + D_\mathrm{p}}{\Delta t},$$

where D_u and D_p are diameters of ultrasonic beam and the larger particle, respectively.

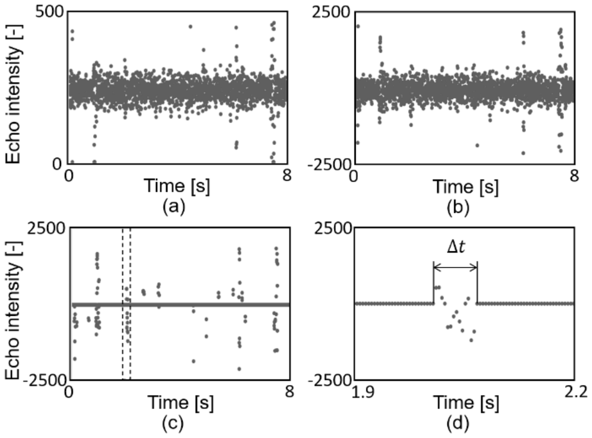

Figure 4: Time traces of echo intensity; (a) raw data, (b) processing Laplacian filter, (c) elimination of small intensities by thresholding, and (d) enlarged view at a part of strong echo intensity scattered by a larger particle

3.2 Validation

A preliminary experiment for validation of the present methodology was conducted by evaluating velocity obtained from echo intensity method. Larger particles were settled in an acrylic pipe filled with water. Porous resin particles, PK216 (Mitsubishi chemical Co.), were used as ultrasonic reflection particles. The particle has 400 μm in median diameter and 1.29 in specific gravity. The acrylic pipe with 1000 mm long and 52 mm inner diameter was used as the test pipe. The expected Reynolds number is around 12 and the flow is not in Stokes regime. For obtaining echo intensity distributions, an ultrasonic transducer with 4 MHz basic frequency was mounted perpendicular to the pipe wall, and the measurement line was set at the center line of pipe. The particles were settled in test pipe under hydrostatic pressure. The sedimentation velocity of particle was measured by the present method mentioned in the last section and compared to the result of PTV, which performed simultaneously. Fig. 5 shows probability density distribution of velocity measured by the present method and PTV. Based on both measurement range, the sampling number of both is different. Averaged velocity from echo intensity method is 33.3 mm/s (Fig. 5(a)), while that from PTV is 31.8 mm/s (Fig. 5(b)). With considering that the velocity measured by PTV contains that from particles passing out of the measurement line of ultrasonic echo intensity, this difference on the probability density function is in quite reasonable range. We therefore conclude that the present velocimetry using echo intensity method works well.

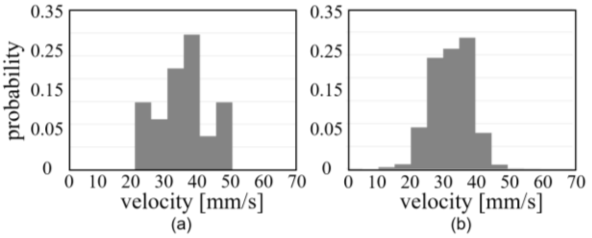

Figure 5: Probability density distribution of the sedimentation velocity from (a) echo intensity method, and (b) PTV

3.3 Interpolation

The dense velocity components parallel to the measurement line by Doppler velocimetry, and the course perpendicular velocity components by echo intensity method are obtained on the measurement lines. At some points on the measurement lines, a velocity vector is formed from these two velocity components (see Fig. 6(a) as an example). At the other points, however, there are only the parallel velocity components. We can imagine flow filed in the container using only few velocity vectors shown in Fig. 6(a) because this experimental set-up is very simple system, but they will be insufficient for more complex system to be understood. That is a similar situation for measurements by PTV; velocity vectors are given at some dispersed points on flow fields. Our research group has often used 2D linear interpolation on dispersed velocity vectors to form regularly arranged velocity vector fields, termed Laplace equation rearrangement (LER) [7]. The Laplace equation in a 2D coordinate system is given as

$$\frac{\partial^2 v_x}{\partial x^2} + \frac{\partial^2 v_y}{\partial y^2} = 0.$$

Lacking velocity vectors (also components) are interpolated to satisfy the equation and boundary conditions by iteration calculations. Lattice point of the flow field to demonstrate LER is set with spatial resolution of UVP data, 0.74 mm as the lattice distance. The iteration calculation was performed with boundary conditions, constant inflow and outflow with averaged flow velocity at the inlet and outlet, slip boundary conditions for other parts, until a convergence condition was satisfied. In the calculation, the original velocity components obtained by

Doppler velocimetry and echo intensity method are not modified.

Interpolations by LER do not guarantee that estimated velocity vector fields satisfy equation of continuity. As an additional process, in cases that quasi-2D velocity fields can be assumed, postprocessing based on data compensation to satisfy equation of continuity, termed velocity correction potential (VCP) [7], has been performed. VCP corrects estimated velocity field by LER. Equation of continuity for 2D incompressible flows is given as

$$\frac{\partial v_x}{\partial x} + \frac{\partial v_y}{\partial y} = 0.$$

VCP is also performed by iteration calculations for satisfying the equation above with a convergence condition; here the original velocity data are not conserved unlike LER.

Fig. 6(b) shows a velocity distribution after those processing. LER and VCP are independently processed. VCP also works to correct erroneous velocity vectors originally measured. In the present case, Doppler velocimetry provides higher accuracy than the echo intensity method, and later information may be mainly modified.

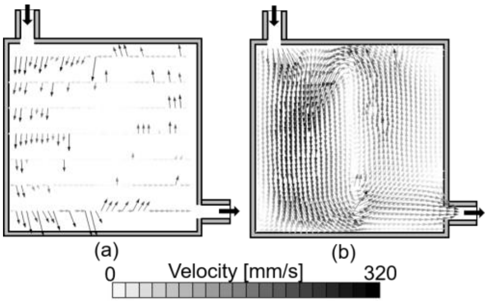

Figure 6: Velocity vectors distribution obtained from (a) Doppler velocimetry and echo intensity method, and (b) after processing LER and VCP

4. Evaluation of estimated velocity field

The velocity vector fields estimated from the present method with LER and VCP, and importance to provide the velocity component perpendicular to the measurement line on the estimation are evaluated. Fig. 7(a) shows a velocity vector field reconstructed by LER and VCP on velocity data with only the component parallel to the measurement line given by Doppler velocimetry, while Fig. 7(b) includes velocity data captured by the echo intensity method. Also, Fig. 7(c) shows a velocity vector field measured by PIV with standard cross-correlation algorithm. Fig. 7(a) does not show the circulating flow exactly. Fig. 7(b) represent faster velocity vectors around the inlet as Fig. 7(c), the PIV result, indicate it, but Fig. 7(a) does not it. Fig. 7(c) shows strong, wider flow along the inlet flow. Fig. 7(b) represents it. Additional information obtained by echo intensity method makes estimations of flow structure more detailed.

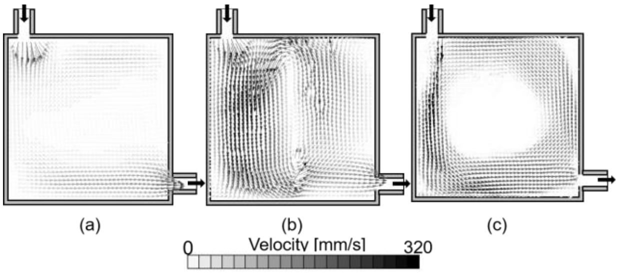

Figure 7: Comparison of velocity vector distributions estimated from (a) velocity data measured by Doppler velocimetry, (b) velocity data measured by Doppler velocimetry and echo intensity method, and (c) corresponding velocity field measured by PIV

5. Sumarry

This study aims to extend a dimension of UVP's measurable velocity components by applying information of the echo intensity with conventional UVP, that provides single velocity component parallel to the measurement line, to capture 2D flow fields. As the initial stage of the development, the velocity component perpendicular to the measurement line is obtained from echo intensity method, where the velocity component is estimated from time of larger particles passing through the measurement line detected by the echo intensity. Velocity vectors, with two components in parallel and perpendicular directions of the measurement line, are thus given at some points on the line. Velocity fields are estimated from dispersed velocity vectors and dense information of the parallel velocity components along the measurement line with interpolation method (LER) and correction method (VCP).A performance test of the present methodology on quasi-2D circulating flow and PIV measurement for comparison indicated that taking additional velocity component perpendicular to the measurement line provides better estimation of the flow field even though the number of data of the velocity component is small.

References

[1] Takeda Y: Ultrasonic Doppler velocity profiler for fluid flow, Springer, (2012).

[2] Tasaka Y, *et al.*: Regular flow reversals in Rayleigh-Bénard convection in a horizontal magnetic field. Phys. Rev. E. 93, (2016), 043109

[3] Yanagisawa T, *et al.*: Convection patterns in a liquid metal under an imposed horizontal magnetic field, Phys. Rev. E. 88, (2013), 063020.

[4] Johan Wiklund, *et al.*: Methodology for in-line rheology by ultrasound Doppler velocity profiling and pressure difference techniques, Chem. Eng. Sci. 62, (2007), 4277-4293.

[5] Takeda Y, *et al.*: Flow mapping of the mercury flow, Exp. Fluids. 32, (2002), 161-169

[6] Poelma C: Ultrasound Imaging Velocimetry: a review, Exp. Fluids. (2017), 58

[7] Ido T, *et al.*: Postprocessing algorithm for particle-tracking velocimetry based on ellipsoidal equations, Exp. Fluids. 32, (2002), 326-336

11th International Symposium on Ultrasonic Doppler Methods for Fluid Mechanics and Fluid Engineering
Berlin, Germany (5.-7. September 2018)

OpenUVP in Comparison with Commercially Available Devices

Yasushi Takeda[1], Tomonori Ihara[2], Tatsuya Kawaguchi[3], and Hiroshige Kikura[3]

[1] Swiss Federal Institute of Technology Zurich, Schmelzbergstrasse 7, 8092 Zürich, Switzerland
[2] Tokyo University of Marine Science and Techonology, 2-1-6 Etchujima, Koto, Tokyo 135-8533, Japan
[3] Tokyo Institute of Technology, 2-12-1 Ookayama, Meguro, Tokyo 152-8550, Japan

The OpenUVP system was proposed in the ISUD9 and started to prepare a standard configuration of the system, which could be a model for the general users. The simplest hardware configuration is composed of pulsar/receiver and fast ADC unit plus PC. Software was developed on LabVIEW platform. The system was designed as a general measurement instrumentation rather than machines targeting any specific application field such as pipe flow or field flow. It was aimed to maintain the highest flexibility in measurement range as well as velocity range. The software is open for each researcher to modify for implementing or incorporating his own idea of signal processing or on-line data analysis algorithm. Specifications of the developed system are compared with commercially available four machines; UVP Duo of Met-Flow, UB-lab and Peacock UVP of UBERTONE and a unit of Incipientus, assuming for the system to be a standard machine, so as to find the most adequate fields for those instruments to be used.

Keywords: Minimum hardware components, Flexible signal processing methods, Comparison with commercial machines

1. Introduction

UVP has been established and accepted and now used widely worldwide after its first appearance in 1980s [1]. At present, many commercial UVP machines areavailable on the market. As the user community expands along with ISUD conference [2], many advanced users crave highly flexible UVP machines since commercial devices are often designed under restrictions from certain limited application targets. We have proposed the OpenUVP system in ISUD9 as such an option. The OpenUVP is intended to be simple and flexible in its philosophy to expand the applicability of UVP as well as modifiability of the system. This paper explains the standard configuration and software of the OpenUVP system and discusses its feature in comparison with commercially available devices.

2. OpenUVP

2.1 Standard configuration

A standard configuration of the OpenUVP system is illustrated in Fig. 1. The hardware is composed of (1) a pulser/receiver (P/R), (2) a fast ADC (Analog to Digital Converter) unit, (3) a PC and (4) a transducer. The system is intended to be as simple as possible to pursue the highest flexibility, which will be the ideal machine for a general measurement instrumentation. This high flexibility is achieved by open-source OpenUVP software running on the PC which absorbs different hardware configuration and performs Doppler signal processing from echo sequence. In addition, the PC controls both the P/R and the ADC. Those general-purpose components can be selected from the market with few points to be considered.

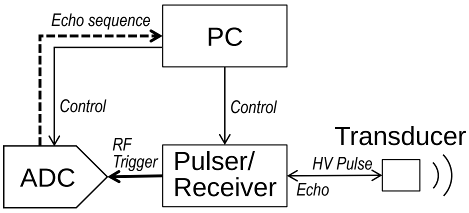

Figure 1: Configuration of the OpenUVP system.

(1) P/R is readily available on NDE (Non-Destructive Evaluation) market. Many devices, however, cannot transmit ultrasound pulse at a certain pulse repetition frequency (PRF). A device as such is able to transmit pulses at the rate of 100 to 10,000 Hz since UVP detects Doppler shift frequency among pulse repetitions. Ideal pulse shape is ideally tone burst to achieve higher quality measurement while it is reported that spike pulse can be utilized with some optimization [3]. Amplifier gain of the receiver circuitry is at least 0 to 40 dB in order to observe echoes from small tracer particles. Many P/Rs have integrated ADCs. Nevertheless, those ADC cannot be used for UVP measurement since they are not designed to capture echo RF signals as pulse to pulse sequence. Therefore, external RF out is required for the P/R.

RF signal is sampled with (2) ADC. Sampling speed shall be decided considering the Nyquist criteria, but usually it should be faster than 5 times of the basic frequency of ultrasound. (Namely, 20 MS/s for 4 MHz) Ideally, pulse to pulse sequence is sampled upon trigger signal. Even though such a sampling mode is not available, many ADCs have longer sample memory length. Then, pulse repetition sequence can be recorded as one long continuous waveform and latter divided into the sequence. This post-triggering technique enables for user to select a cheap oscilloscope as an ADC. Note that that post-triggering cause jittering noise due to different clock domain between the P/R and the ADC.

(3) PC can be any device even a microcomputer as long as it can handle relatively broadband ultrasound RF signal. In our experience, a standard PC (<1,000 USD) can well handle UVP signal processing in real-time. Many commercial UVP devices have a certain overhead time gap between profiles due to signal processing, data transfer, etc. This time gap was troublesome when it comes to the data synchronization with other measurements. On the other hand, zero-gap can be realized if an ADC is installed in a PC through a broadband data bus. Since the entire pulse-echo sequence is stored, UVP output from the sequence can be stored without any time gap between profiles as well.

(4) transducer selection requires a certain consideration. NDE transducers can be utilized in general. However, narrow band transducer designed for UVP gives higher quality measurement.

Considering above mentioned criteria, one of the standard configurations are as follows: (1) Pulser/receiver: JPR-10CN, Japan Probe Co, Ltd. (2) ADC: APX-5040, Aval Data Corp. (3) Standard PC with PCI Express bus

2.2 Software

The UVP software is written on LabVIEW platform in order to achieve higher flexibility. Fig. 2 shows the snapshot of the main screen. The software has sub-routines: ADC control, signal processing core, post-processing and display control. The key of the OpenUVP software is the signal processing core. Current version integrates several signal processing methods such as autocorrelation [4], FFT [5, 6], phase difference [7], UTDC[8]. The basic signal processing method is autocorrelation technique.

Autocorrelation technique is also termed as pulse-pair technique. Digital echo sequence acquired with the hardware is Doppler frequency modulated echo signal. Thus, demodulation is required to obtain in-phase and quadrature phase as complex sequence $z(t)$.

$$z(t) = \mathrm{LPF}\left[E(t)\{\cos(2\pi f_0 t) + j\sin(2\pi f_0 t)\}\right] = \frac{A}{2}e^{j2\pi f_D t} \qquad (1)$$

As Doppler frequency f_D is sampled at the pulse repetition frequency f_{PRF}., cut-off frequency will be $f_{\mathrm{PRF}}/2$. Due to a static wall echo, amplifier distortion, ADC bias, etc., DC component is often observed. UVP usually applies high gain setup and saturation of an amplifier causes strong DC component noise. These noises can be minimized by subtracting average amplitude from the sequence. These procedures are illustrated in Fig. 3 (a). Parallel signal processing is performed to increase the performance in the implementation. After the demodulation, Doppler shift frequency is estimated.

$$f_D = \frac{f_{PRF}}{2\pi}\arg\sum z^*(t)\cdot z(t + 1/f_{PRF}) \qquad (2)$$

Some measurement configuration has slowly moving wall. HPF or BEF can be useful in such case.

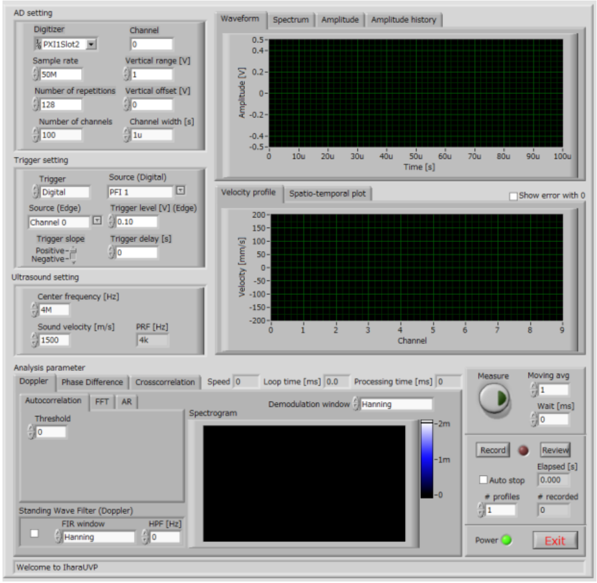
AD setting
Digitizer PXI1Slot2
Channel 0
Sample rate 50M
Vertical range [V] 1
Number of repetitions 128
Vertical offset [V] 0
Number of channels 100
Channel width [s] 1u
Trigger setting
Trigger Digital
Source (Digital) PFI 1
Source (Edge) Channel 0
Trigger level [V] (Edge) 0.10
Trigger slope Positive Negative
Trigger delay [s] 0
Ultrasound setting
Center frequency [Hz] 4M
Sound velocity [m/s] 1500
PRF [Hz] 4k
Analysis parameter
Speed 0
Loop time [ms] 0.0
Processing time [ms] 0
Threshold 0
Demodulation window Hanning
Standing Wave Filter (Doppler)
☐ FIR window Hanning
HPF [Hz] 0
Moving avg 1
Wait [ms] 0
☐ Auto stop
Elapsed [s] 0.000
profiles 1
recorded 0
Welcome to IharaUVP

Figure 2: Main screen of the OpenUVP software.

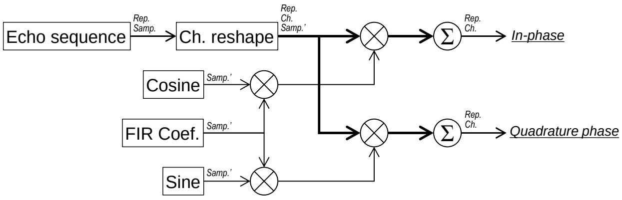

(a) Quadrature demodulation.

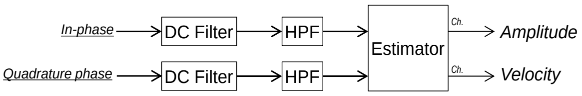

(b) Doppler signal processing.

Figure 3: Implementation of the autocorrelation technique.

3. Comparison with other devices

3.1 List

Table 1 shows comparison with commercially available devices. Four devices are listed from the market: UVP Duo of Met-Flow (Switzerland), UB-lab and Peacock UVP of Ubertone (France) and ILV In-Line Flow Visuzlizer of Incipientus (Sweden). Note that Peacock UVP is a multi-purpose module, and not a device for velocity profile measurement by itself. Important parameters are tabulated. Listed values and parameter ranges are typical obtained from their open data, and do not show their maximum capability.

Table 1: Comparison with commercially available devices

Model	UVP Duo (Met-Flow)	UB-lab (Ubertone)	Peacock UVP (Ubertone)	IFV Incipientus Flow Visualizer (Incipientus)	Open UVP (tentative)
Number of transducers	1 (5/20 MUX available)	2 (TRX) 2 (RX)	2 (TRX)	2 (TRX), 2 (RX) (Independent Tx/Rx stages)	1
Frequency range	0.5, 1, 2, 4, 8 MHz	0.5–7.5 MHz	0.4–3.6 MHz	0.2–3 MHz, 1–7 MHz, 5–7 MHz (module depends)	0.03–10 MHz
Ultrasound pulse	Tone burst	Tone burst, Coded	Tone burst, Coded	Arbitral wave, DDS (14 bit / 4096 word)	Tone burst, Coded (3 level)
Voltage ($V_{\text{p-p}}$)	30, 60, 90, 150	30, 60	-	1–80 by step of 1	10–300 by step of 10
Wave cycle	2–32 by step of 1	2–128	2–128	1–40 (DDS/AWG) Pulse windowing available	0.5–32 by step of 0.5
PRF (f_{PRF})	244 to 443,114 Hz	9 to 10,000 Hz	-	Any value practical, Staggered/Dual PRF	100, 500, 1k, 2k, 4k, 8k or Ext. Trig.
Repetitions per profile (N_{rep})	8 to 2048 by step of 1	2–128	2–128	2–16384 by step of 1	min. 2 by step of 1
Amplifier gain	6–54 dB (TGC available)	20–68 dB (TGC, AGC available)	13.7–61.7 dB (TGC, AGC available)	7–55 dB (TGC, AGC available)	0–80 dB (Flat gain)
Sampling range (water)	min. 0.37 mm	5–4,000 mm	0.5–10,000 mm	min. 15 μm	min. 0.37 mm
Number of cells	2–2,048	2–200	1–200	min. 1	min. 1
Cell distance	min. 0.19 mm	3.5–100 mm (0.3 mm optional)	0.2–30 mm	min. 0.21 mm	min. 0.19 μm
Profiles per display update	1 (Moving average available)	>1	>1	>1 (Moving average available)	1 (Moving average available)
Update rate	up to 1 kHz	up to 1 Hz (100 Hz optional)	up to 5 Hz	up to 5 Hz (via ethernet) up to 25 Hz (FPGA onboard)	up to 5 kHz ($f_{\text{PRF}}/N_{\text{rep}}$)
Velocity resolution	256	0.25 ppm (4,000,000)	65,536	65,536 (16 bit ADC)	-
Analog output	RF, TRIG Out, SYNC In	n.a.	n.a.	RF, TRIG Out, SYNC In	RF, TRIG Out, SYNC In
Digital output	Velocity, Amplitude, IQ	Velocity, Amplitude, IQ, Turbidity, Mean RF, Quality	Velocity, Amplitude, Quality	Velocity, Amplitude, RF, IQ, FFT	Velocity, Amplitude, RF, etc.
Communication	Ethernet	Ethernet	Modbus, USB	Ethernet	USB, PCI-Exp.
Power	-	<12 W	0.5–1 W	<7.5 W	-
Size Weight	340×130×400 mm 9.3 kg	55×113×385 mm 1.45 kg	21×85 mm 14 g	90×295×285 mm 3.82 kg	-
Other features	ActiveX API available	Sensor: Temperature Internal data logger eq.	Sensors: Temperature, Rotation angles (pitch, roll)	Decimation 4–128 (RF), Aluminum box with superior EMC characteristics	Zero-gap measurement

3.2 Features

Each device has its own history for development and marketing, and therefore machines are specialized for their marketing fields and areas. UVP-Duo (Met-Flow S.A.) has a long history of development as a starter and its specification has been prepared for an engineering lab use. They have rich experience and expertise in applications of UVP for fluid mechanical and engineering problems. UB-Lab (Ubertone.) is a model converted from their original machine for their civil engineering applications (UB flow), and it has wider flexibility for parameter setting than original machine. It is ideal to be worked in good net-work situation for remote application and data processing. Peacock UVP module of Ubertone is an excellent extension of their device for integrating this unit in sensor system for flow monitoring. From its physical size and low power consumption, it is easy to install this unit in harsh environment such as deep sea or far offshore. It is expected to be a module for engineering and industrial sensory system. ILV of Incipientus has been prepared for rheological application and specialized for civil engineering or construction engineering. They have experience in field installations and for solid-liquid two phase flow.

All those devices are prepared for practical application of UVP, so-called ready-to-go unit. OpenUVP was intended to develop for those researching the UVP method itself. University researchers wish to try their own idea of signal processing, flow analysis from the measured profiles, and extension of UVP application itself. Therefore it is OPEN and free to test their own ideas.

4. Summary

A development of OpenUVP has reached to its first stage for general audience to participate. System construction has been finalized and the first machine is available to be used. A comparison with commercial machine indicates that the OpenUVP might be a basic tool for further improvement and/or new application of the UVP method. Information regarding this unit and others would be accumulated in its own website as http://openuvp.org/.

References

[1] Takeda Y: Ultrasonic Doppler velocity profiler for fluid flow, Springer (2012).
[2] http://www.isud-conference.org/
[3] Nguyen TT, *et al.*: Ultrasonic Doppler velocity profile measurement of single- and two-phase flows using spike excitation, Exp. Tech., 40 (2016), 1235-1248.
[4] Kasai C, *et al.*: Real-time two dimensional blood flow imaging using an autocorrelation technique, IEEE Trans. Son. Ultrason., 32 (1985), 458-464.
[5] Aydin N, *et al.*: Implementation of directional doppler techniques using a digital signal processor, Med. Biol. Eng. Comput, 32 (1994), S157-S164.
[6] Fischer S, *et al.*: A new velocity estimation method using spectral identification of noise, Flow Meas. Inst., 19 (2008), 197-203.
[7] Ihara T, *et al.*: Application of ultrasonic Doppler velocimetry to molten glass by using broadband phase difference method, Flow. Meas. Inst., 48 (2016), 90-96.
[8] Hein, I.A, *et al.*: A real-time ultrasound time-domain correlation blood flowmeter: part I–Theory and design, IEEE Trans. Ultrason. Ferro. Freq. Cntl., 40 (1993), 768-775.

https://doi.org/10.7795/810.20190809

11th International Symposium on Ultrasonic Doppler Methods for Fluid Mechanics and Fluid Engineering
Berlin, Germany (5.-7. September 2018)

Development of New Ultrasonic Transducer for Multi-Dimensional Velocity Profile Measurement Using Ultrasonic Doppler Method

Jevin Tanius Owen[1], Naruki Shoji[1], Ari Hamdani[2], Tomonori Ihara[3], Hideharu Takahashi[2], and Hiroshige Kikura[2]

[1] Department of Mechanical Engineering, Tokyo Institute of Technology, 2-12-1, Ookayama, Meguro-ku, Tokyo, Japan
[2] Laboratory for Advanced Nuclear Energy, Tokyo Institute of Technology, 2-12-1, Ookayama, Meguro-ku, Tokyo, Japan
[3] Tokyo University of Marine Science and Technology, 2-1-6 Etchujima, Koto-ku, Tokyo, Japan

A new ultrasonic array transducer with a special configuration of five elements, using 5 elements as a transmitter and 4 elements as a receiver had been designed. With this configuration, there are four Doppler frequencies that can be obtained, hence the three-dimensional velocity information along the measurement line can be reconstructed. We evaluated the transducer ultrasound characteristic and performance by sound pressure measurement and fully developed laminar pipe flow. From sound pressure measurement, the 5 elements generate one main lobe (one measurement volume), hence all the Doppler frequencies have the same information (in position and time). Therefore, the three-dimensional measurement is possible. From the flow measurement, the result has a good agreement with theory. Finally, we applied the transducer to a different flow condition, *i.e.* turbulent and swirling flow for a vector measurement.

Keywords: ultrasonic transducer, five-elements array, three-dimensional velocity profile, Doppler, vector

1. Introduction

Ultrasonic Doppler measurement technique was first used in a medical application, proposed by Satomura [1]. Baker [2] performed a one-dimensional blood flow measurement, assuming the blood flow parallel to the vessel axis (unidimensional). However, many areas of clinical interest cannot employ this assumption due to the occurrence of complex flow (multi-dimensional). Peronneau *et al.* [3] proposed a single element cross beam system using two transducers as a transceiver (transmitter/receiver) to measure two-dimensional at the cross point. Further development of a similar measurement system for measuring three-dimensional by using three transducers was shown in the work of Fox [4]. However, this system is time-consuming since the transducers have to be operated separately to avoid the interference of the sound beam. Later, Dunmire *et al.* [5] developed a three-dimensional measurement system using 5 transducers (1 transmitter, 4 receivers). With only 1 transmitter, the measurement occurs at the same time and same measurement volume. In fluid engineering, ultrasonic Doppler measurement was proposed by Takeda [6]. The area of investigation is wider, therefore depth varying (profile) measurement is necessary. Similar to Dunmire *et al.* measurement system, Hurther and Lemmin [7] developed three-dimensional with varying depth measurement system in open-channel flow. Based on this idea, Obayashi *et al.* [8] investigate this system accuracy in rotating cylinder flow. They found that the velocity in receiver line has a relatively high error with the reason of low signal to noise ratio.

These studies are very important to be continuously improved since the flow in fluid engineering often exists with multi-dimensional velocity. For example, in the case of the flow inside the reactor of Pressurized Water Reactor (PWR), specifically in the between of reactor core, the flow is three-dimensional swirling flow promoted by the grid spacer. This flow information is very important because it affects the reactor power and cooling. Through a previous study case, this present study proposed a new measurement system using an array transducer with a special configuration of five elements. It consists of one big element at the center as a transmitter and four small elements at the side with a small gap as transmitter/receiver. By using all elements as a transmitter and with the small gap, the received echo is expected to have a good signal to noise ratio, while the challenge is the sound beam interference will occur with the undesired side lobe. With the small gap between transmitter and receiver, one main lobe can be generated and the small receiver could minimize the uncertainty of echo angle from measurement volume to the receiver. Finally, with this configuration, we aim to measure the three-dimensional velocity profile with the same timing of four echo acquisition in one measurement volume with good accuracy.

2. Five elements transducer design and measurement principle

The transducer with five elements is designed and manufactured (see Figure 1) with the specification in Table 1. Using this configuration, the transducer can obtain four Doppler frequencies (f_D) (see Figure 2) from the echo of the measurement volume to each element with a certain echo angle (θ). The echo angle depends on channel distance and receiver position. For the receiver position, we assumed the echo will reach to the middle of the receiver element with the minimized uncertainty since the element size (b) is specifically designed to be very

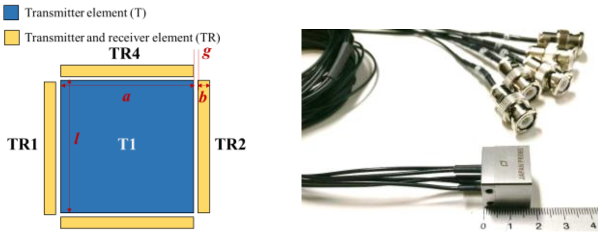

(a) Element configuration.

(b) Manufactured transducer.

Figure 1: Five elements transducer design.

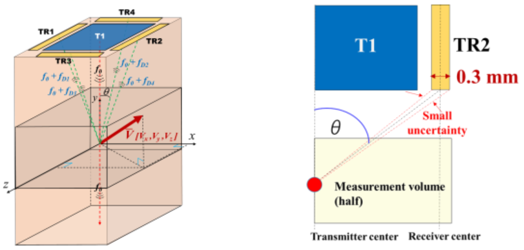

(a) Four Doppler frequencies

(b) Echo angle (θ)

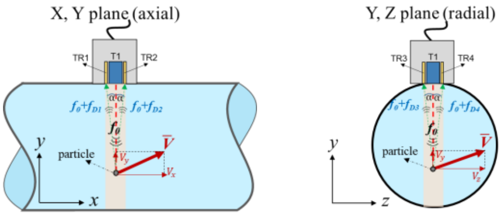

(c) Axial plane view.

(d) Tangential plane view.

Figure 2: Five elements transducer measurement principle.

small (approximate the wavelength). Finally, using the four Doppler frequencies from one measurement volume, the three-dimensional velocity, *i.e.* axial velocity (V_x), radial velocity (V_y) with the information of f_{D1} and f_{D2}, tangential velocity (V_z) with the information of f_{D3} and f_{D4} and vector in axial plane view (V_x-V_y) and tangential plane view (V_z-V_y) can be reconstructed with the equations below.

$$V_x = \frac{c}{2f_o}\frac{f_{D1}-f_{D2}}{\sin\theta} \tag{1}$$

$$V_y = \frac{c}{2f_o}\frac{f_{D1}+f_{D2}}{1+\cos\theta} \tag{2}$$

$$V_z = \frac{c}{2f_o}\frac{f_{D3}-f_{D4}}{\sin\theta} \tag{3}$$

$$\overline{V}_{axial} = \sqrt{V_x^{\,2}+V_y^{\,2}} \tag{4}$$

$$\overline{V}_{\tan gential} = \sqrt{V_z^{\,2}+V_y^{\,2}} \tag{5}$$

Table 1: Design of new transducer for 3D velocity measurement

Specification	Detail
Basic Frequency (f_o)	4 MHz
Wavelength in water, 20 °C (λ)	0.37 mm
Transmitter element width (a)	5 mm
Receiver element width (b)	0.3 mm
Transmitter- receiver gap (g)	0.1 mm
Element length (l)	5 mm

3. Experimental apparatus

The developed transducer was evaluated experimentally for the ultrasonic propagation characteristic, flow measurement evaluation in the reference flow, and applicability to measure three-dimensional swirling flow. The experiment consists of sound pressure measurement, fully developed laminar, turbulent and swirling flow measurement. Each experiment was conducted with same measurement system (Figure 3) which are five elements transducer (manufactured by Japan probe), 8 channel pulser receiver (Japan probe JPR-10C-8CH3R), and 8 channel A/D converter (National Instrument PXI-1033). The measurement system used LabVIEW software to process the echo signal (Doppler signal) into the velocity profile with autocorrelation technique [9].

3.1 Sound pressure measurement

The ultrasound propagation characteristic was investigated by sound pressure measurement. The transducer transmits with all elements simultaneously in water (20°C) and the needle hydrophone (diameter 0.5 mm) collects the pressure data in several positions with the spatial resolution of 1 mm, controlled by XYZ stage (see Figure 4).

3.2 Fully developed laminar flow measurement

To check the measurement performance, the measurement was being conducted in fully developed laminar flow on a vertical pipe apparatus (Figure 5) which has a good theoretical reference. The pipe inner diameter (D) is 50 mm with the water as the working fluid, Reynolds number (*Re*) 420 and the tracer particle, Nylon with a diameter of 80µm is dispersed. To ensure the flow is fully developed laminar flow, the measurement is conducted in the position of 30D from the inlet where the theoretical of the fully developed laminar flow pipe length is 21D (0.05*ReD*). The experiment conditions and measurement parameters are given in Table 2.

Table 2: Fully developed laminar flow experiment condition and measurement parameters

Condition and parameter	Detail
Reynolds number (*Re*)	420
Pulse repetition frequency	100 Hz
Number of repetitions	128
Number of profiles	2,000
Number of cycles	4
Channel distance	0.74 mm

3.3 Turbulent and swirling flow measurement

After applying in the reference flow (laminar flow), the transducer was applied in different flow conditions which are turbulent and swirling flow in horizontal pipe apparatus (Figure 6) to check further the measurement system capability. Swirling flow can be generated if the swirl generator (rotating pipe) is activated. The experiment conditions and measurement parameters are given in Table 3

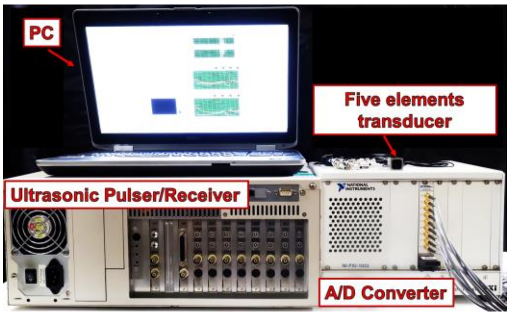

Figure 3: Measurement system.

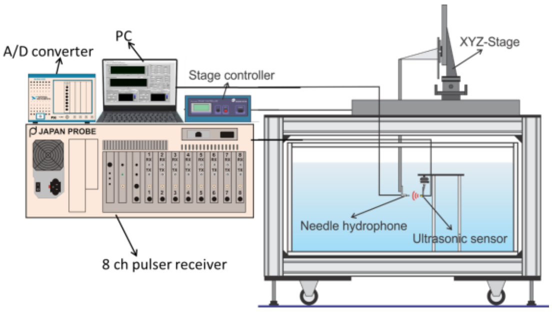

Figure 4: Sound pressure measurement in water.

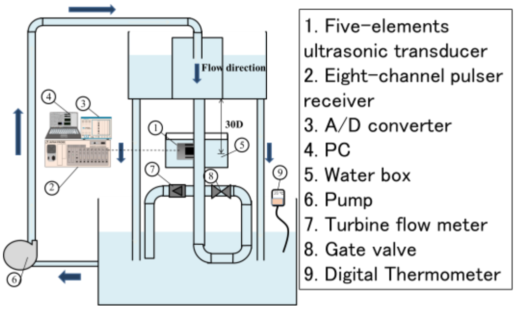

Figure 5: Vertical pipe apparatus.

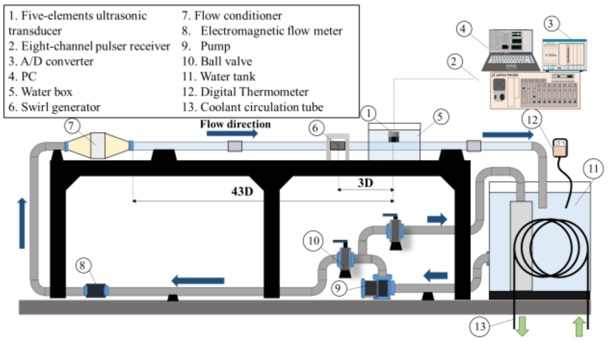

Figure 6: Horizontal pipe apparatus.

Table 3: Turbulent and swirling flow experiment condition and measurement parameters

Condition and parameter	Detail
Reynolds number	13,000
Pipe inner diameter (*D*)	50 mm
Motor frequency (in swirling case)	600 rpm
Pulse repetition frequency	2,000 Hz
Number of repetition	128
Number of profile	5,000
Number of cycles	4
Channel distance	0.74 mm

4. Results and Discussion

4.1 Sound pressure measurement

The transducer sound pressure characteristic recorded by the hydrophone is plotted in the color graph in dB scale (Figure 7). From the result, we confirmed that there is one main lobe of the transmission wave of all elements, hence one measurement volume for all transmitter/receiver and no side lobe found. Therefore, the measurement principle defined in section 2 can be applied and three-dimensional velocity measurement can be possibly done.

4.2 Fully developed laminar flow measurement

The measurement result (Figure 8) is the average of 2000 instantaneous three-dimensional velocity profile. The result of the axial velocity is compared to the theory (laminar parabolic curve). The comparison is in a good agreement except in the region of near field (0-8 mm) and far field (40-50 mm). The result is acceptable, considering in the near field, the sound intensity is oscillating and in the far field, the sound intensity is weaker. The radial and tangential velocity are found to approach zero value with a small standard deviation which is as expected in the fully developed laminar flow. With this array elements configuration, there will be a elements cross-talk, mainly between the center transmitter and side receiver, however, since the gap is very small, the cross-talk will only effect the initial measurement region, which overlaps with the near-field region. Finally, we can confirm the capability of the measurement system in the three-dimensional flow measurement.

4.3 Turbulent and swirling flow measurement

The measurement result of turbulent and swirling flow is an average of 5000 instantaneous three-dimensional velocity profile, plotted into vector profile in axial and tangential plane view. The result of turbulent and swirling flow can be seen in Figure 9 and 10 respectively. From the result of turbulent flow, the comparison with single element transducer is in a good agreement. In the swirling flow result, we can find higher standard deviation (compare to laminar flow), higher radial and tangential velocity which is the behaviour expected in swirling flow. Finally, we confirm that the measurement system can be applied to measure the three-dimensional velocity profile in different flow condition.

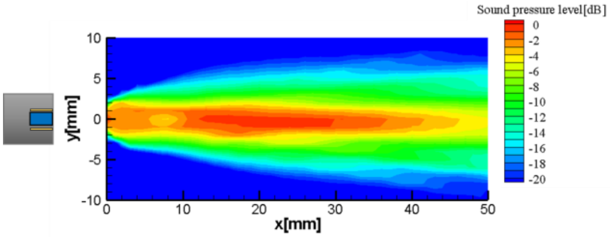

Figure 7: Sound pressure measurement result.

https://doi.org/10.7795/810.20190809

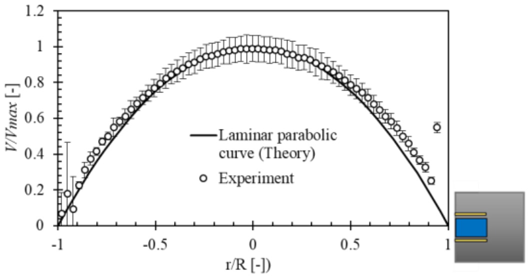

(a) Axial velocity (V_x).

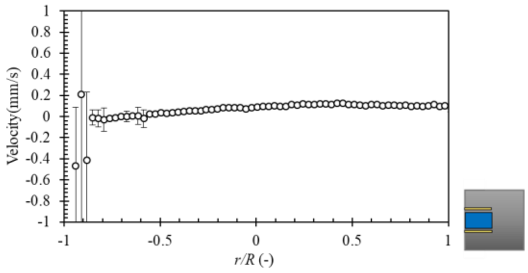

(b) Radial velocity (V_y).

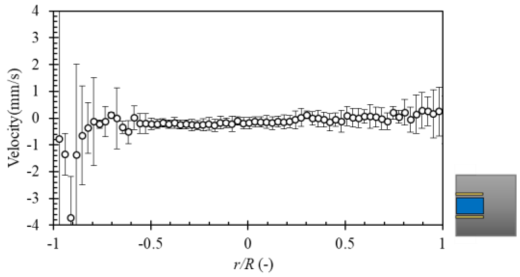

(c) Tangential velocity (V_z).

Figure 8: Three-dimensional velocity profile of fully developed laminar flow

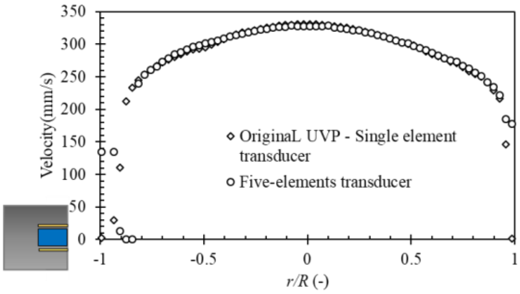

(a) Axial velocity (V_x).

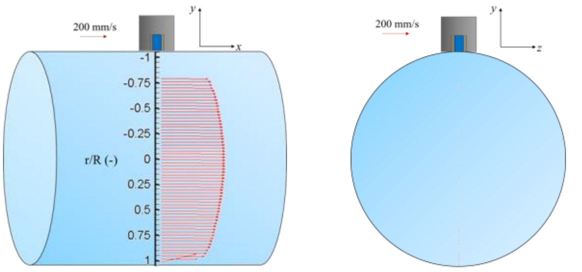

(b) Axial plane view.

(c) Tangential plane view.

Figure 9: Three-dimensional velocity measurement of turbulent flow

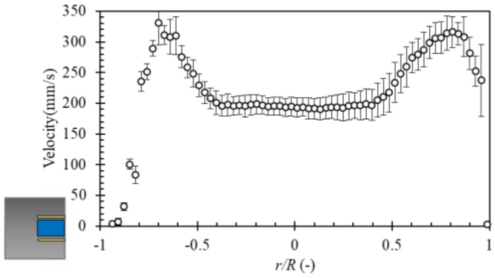

(a) Axial velocity (Vx).

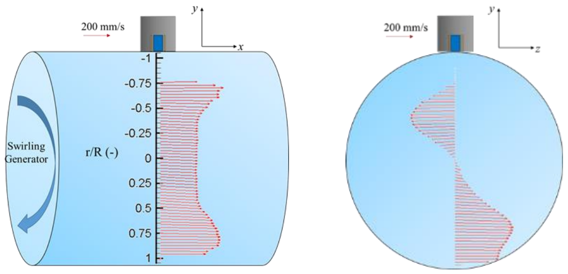

(b) Axial plane view.

(c) Tangential plane view.

Figure 10: Three-dimensional velocity measurement of swirling flow

5. Summary

The new configuration of five elements transducer has been designed and the three-dimensional velocity profile measurement system has been developed. From the sound pressure measurement, we confirmed that three-dimensional measurement is possible since one main lobe is generated (one measurement volume) with no side lobe. From the flow measurement, we confirm the performance by fully developed laminar flow measurement and the capability to measure flow in different conditions.

References

[1] Satomura S: Ultrasonic Doppler method for the inspection of cardiac functions, The Journal of the Acoustical Society of America 29 (1957), 1181-1185.

[2] Baker D.W: Pulsed ultrasonic Doppler blood-flow sensing, IEEE Transactions on Sonic and Ultrasonic 17 (1970), 170-185.

[3] Peronneau P, *et al.*: Blood flow patterns in large arteries, Ultrasound in Medicine (1977), 1193-1208.

[4] Fox MD & Gardiner MW: Three-dimensional Doppler velocimetry of flow jets, IEEE transactions on biomedical engineering 35(1988),834-841.

[5] Dunmire BL, *et al.*: A vector Doppler ultrasound instrument, In Ultrasonics Symposium, Proceedings (1995), 1477-1480.

[6] Takeda Y: Development of an ultrasound velocity profile monitor, Nuclear Engineering and Design 126(1991), 277-284.

[7] Huther D & Lemmin U: A constant-beam-width transducer for 3D acoustic Doppler profile measurements in open-channel flows, Measurement Science and Technology (1998).

[8] Obayashi H, *et al*: Velocity vector profile measurement using multiple ultrasonic transducers, Flow Measurement and Instrumentation 19 (2008),189-195.

[9] Kasai, C., *et al*: Real-time two-dimensional blood flow imaging using an autocorrelation technique. IEEE Transactions on sonics and ultrasonics, *32*(1985), 458-464.

https://doi.org/10.7795/810.20190809

11th International Symposium on Ultrasonic Doppler Methods for Fluid Mechanics and Fluid Engineering
Berlin, Germany (5.-7. September 2018)

Flow Measurement for the Design Optimization of Fish Pass Entries in a Run of River Hydropower Plant

Pierre Bourqui[1], Cédric Bron[1], and Giovanni De Cesare[1]

[1] Laboratory of hydraulic constructions (LCH), Swiss Federal Institute of Technology Lausanne, Lausanne 1015, Switzerland

The International Commission for the Protection of the Rhine (ICPR) has set the objective of guarantying the upstream migration of the salmons up to Basel, Switzerland, at horizon 2020. One of the last dams to be equipped is the one of Rhinau, in France. The large turbined discharges and the specificities of the hydroelectric facility require a detailed study of the flow in the tailrace channel to guaranty a proper visibility of the fishway entries for the fish. The study is not intended to the design of the fish pass itself, but to assure that fish can find its entries located in the tailrace channel within a highly fluctuation and structured flow field. Therefore, a physical model has been built at LCH-EPFL, on which the flow in the tailrace is assessed under different turbining configurations with the help of UVP transducers. Two transducers are used to create 2D representations of the measured flow field. The transducers are mounted on a robot capable of moving in all X, Y and Z directions within an area of 2x2 meters and able to manage the triggering of the UVP at each new robot location. Three types of datasets are recorded with this system: surface flow (longitudinal and lateral velocities), sections across each fishway entry (longitudinal and vertical velocities) and temporal variations of the longitudinal jet velocities. A last numerical step filters and interpolates the raw data to render clearly interpretable plots.

Keywords: Flow field monitoring, physical modeling, fishway optimization, run of river hydropower plant

1. Introduction

The design of fishway entries has traditionally been done through the use of physical models. This is due to the complexity of the interaction between the flow in the tailrace and the flow coming from the fishway entry. This work aims at modeling the flow in the tailrace and afterbay of the Rhinau powerplant (France) in order to optimize the design of the fishway entries. A physical model and a 3D numerical model were built and are complementary for the design. Here we focus only on the physical model, and in particular on the flow measurement facility using UVP transducers.

2. Description of the physical model

2.1 Overview

The physical model has been built in accordance with the original civil drawings and actual latest laser measurements. The chosen geometric scale is 1/35, large enough to create the flow turbulence in the afterbay and in the tailrace while respecting the space restriction in the laboratory. The model's dimensions are approximatively 5x10 m^2 and its main components are (Figure 1):

1. Water supply from the pumping system of the lab, with the monitoring of the total discharge.
2. Two reservoirs for the distribution of the total discharge toward the four groups, with individual discharge control through electro-magnetic flowmeters.
3. Four turbine units, preceded by deflectors to give the flow the rotational speed observed at the turbine's outlet.
4. Fishway entries located on top of the afterbays' outlets. The discharge through those entries is controlled individually with rotameters.
5. Downstream connecting walls, at the end of which the bank fishway entries will be placed.
6. Tailrace channel
7. Restitution basin with a weir that controls the water level in the tailrace channel

2.2 Conception

The model has been first designed and assembled using CAD. Two materials have been used for the construction of the different parts. The afterbays, the body of the powerplant, the connecting walls and the fishways are made with PVC. The topography of the afterbay and the tailrace has been fixed with a 50mm thick concrete layer. The level of precision for each component of the model depends on the material it is made of: ± 1mm for the PVC parts and ± 5mm for the concrete parts.

2.3 Scale effect

The model is scaled in respect to the Froude similarity, meaning that the ratio between the inertial and gravity forces is preserved. This admits a same Froude number for both the prototype and the model. The Reynolds number has been found larger than 3.5×10^4 for all discharges, with the consequence that the turbulence level is high enough to limit scale effects in the model [1].

2.4 Measuring devices and accuracy

To evaluate the flow in the model, velocities are measured in 3 directions with Ultrasound Velocity Profiler (UVP, Met-Flow SA). The UVP represents both a method and a device for measuring an instantaneous velocity profile in liquid flow by detecting the Doppler shift frequency of echoed ultrasound as a function of time and space [2]. The accuracy of the velocity measurements with the UVP reaches ±1mm/s, corresponding to a potential error of less

https://doi.org/10.7795/810.20190809

than 1% of the mean velocity in the tailrace channel.

The UVP transducers are placed on a robotic traversing system (pointed by the red arrow on Figure 1, right) that allows to program automatic measurement sequences on a 2x2m^2 square. The robot itself can be moved on a frame that spans the model and that can be moved up and downstream on lateral rails. Thanks to this infrastructure, the measurement procedure is flexible and replicable.

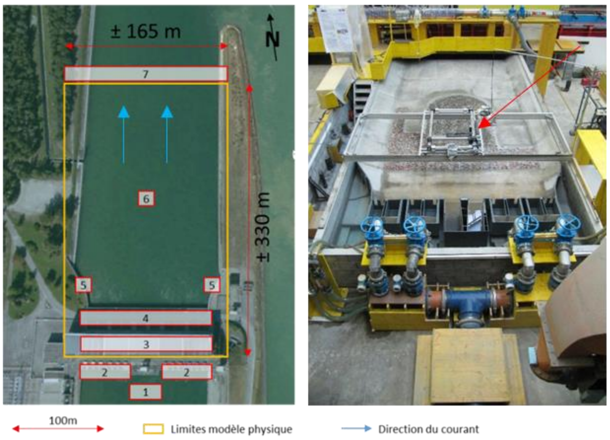

Figure 1: Left and middle – main components and dimensions of the physical model. Right – physical model in the laboratory. (Satellite background image: Google Earth)

2.5 Measurement procedure

Two transducer axes are used to create 2D representations of the measured flows. The robot on which they are mounted on moves automatically to cover the surface to be measured and also manages the triggering of the measurements at each new location. Three types of datasets are recorded with this system: surface flow (longitudinal and lateral velocities), sections across each fishway entry (longitudinal and vertical velocities) and temporal variations of the longitudinal jet velocities.

The UVP transducers measure at each location a velocity profile along the beam axis, with a resolution of 5.2mm (18cm in prototype). Each profile used for the results is an average of several profiles, the number being chosen by the user. For the surface and the cross-section flows, the number of profiles taken at each location was set to 512. For the analysis of the temporal variations of the jet X-velocities, this number was increased to 1024. In order to avoid the effect of the transducer on the local velocities, the measurement starts 10cm away from the transducer for the surface flow and 1cm for the subsurface flow.

The global resolution of the measurements depends on the largest distance between two robot locations. The precision was set in accordance to the project phases need. Therefore, two types of grids have been built: one for the validation of the model, with a mesh size of 100mm (Figure 2) and one for the analysis of the fishway entries, with a mesh size between 25 to 50mm (Figure 4). In total, 83’440 points were recorded for the surface flow validation of one single turbining configuration. It covers the whole width of the tailrace and the first 160m downstream of the powerplant. The 10 X-Z planes (Figure 3) represent 68’568 measured points, covering the whole depth and the first 160m downstream of the powerplant. Those numbers were increased to 122’000 (surface flow) and 38’000 (cross-sections) during the analysis of the fishway entries.

Each point is characterized by its spatial coordinates X, Y, Z and its associated velocity. At the end, the interpolation over the whole domain of the data of each transducer creates the velocity field.

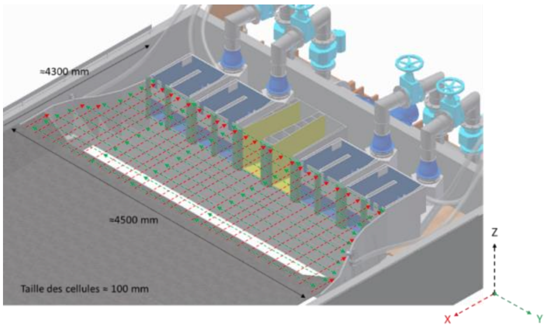

Figure 2: Schematic representation of the surface flow (X-Y plane) measurement procedure for the model validation.

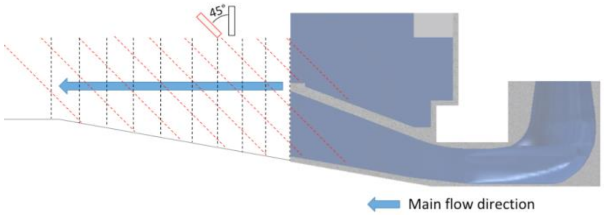

Figure 3: Schematic representation of the subsurface flow measurement procedure (X-Z planes). Cross-section through a fishway entry placed over the turbine draft tube.

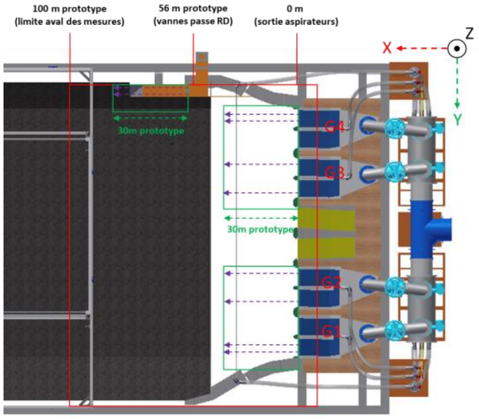

Figure 4: Schematic representation of the flow measurement procedure for the fishway entries analysis. In the red square: surface flow (X-Y plane) with a mesh size of 1.75m (prototype scale). In the green square: surface flow with a mesh size of 0.875m. Along the violet arrows: subsurface flow (X-Z planes) with a mesh size of 0.875m.

3. Validation of the model

Two types of information have been recorded on site: observations of the surface flow and ADCP (Acoustic Doppler Velocity Profiler) measurements of the subsurface. The same data were collected on the physical model according to the measurement procedure described before.

Four turbining configurations have been chosen to compare the results of the physical model with the on-site measurements. Figure 5 and Figure 6 presents the results for one of those four exploitation cases. The discharges turbined by group 1 to 4 are : 0, 0, 300 and 300m^3/s.

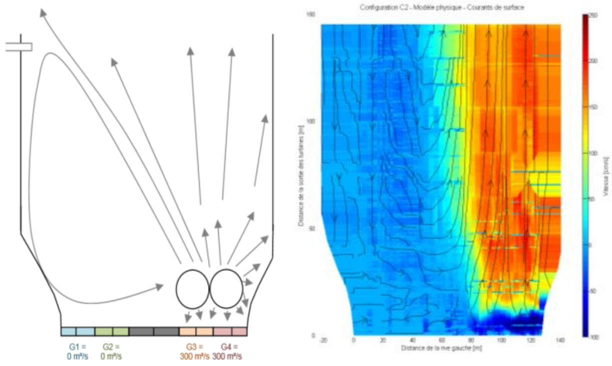

Figure 5: Exploitation case 2 – qualitative comparison of the observed surface flow patterns (left) and the one measured on the physical model (right). The colours correspond to the value of the X-velocity, from -100 (blue) to 200 cm/s (red).

Figure 5 (left) shows a large recirculation, well reproduced by the physical model, where the velocities range between -50 and 0cm/s. This recirculation seems to be larger on the physical model than in reality; the recirculation has been observed approximatively on the first 150m after the turbine outlets while on the physical model, it reaches the downstream end, corresponding to a distance of 280m. The positions of the resurgences are well represented by the model. However, one can observe a slight deviation of the turbulences toward the right bank on the physical model.

This deviation is also visible in the comparison of the subsurface flow at 50m from the exit of the afterbays (Figure 6). However, the physical model shows good velocity magnitude in front of groups 3 and 4 and along the right bank. On the other side of the model, the recirculation shows velocities closer to zero than in reality.

The validation of the physical model with all 4 exploitation cases has shown that the model is able to represent appropriately the flow field occurring on site, both for surface and cross-profile flows. The turbulences and resurgences observed on site can also be observed on the model with precise longitudinal positions. In contrast, the lateral positions of the jets and main resurgences is systematically deviated 5 to 10 meters toward the right bank, independently of the group used. Also, the lateral spreading of the jets is higher than in reality. As all groups have been built after the same construction drawings, this deviation is likely to be a consequence of the design, creating a preferential path in the right afterbay. Globally, the physical model creates trustfully the flow in the afterbays and in the tailrace channel.

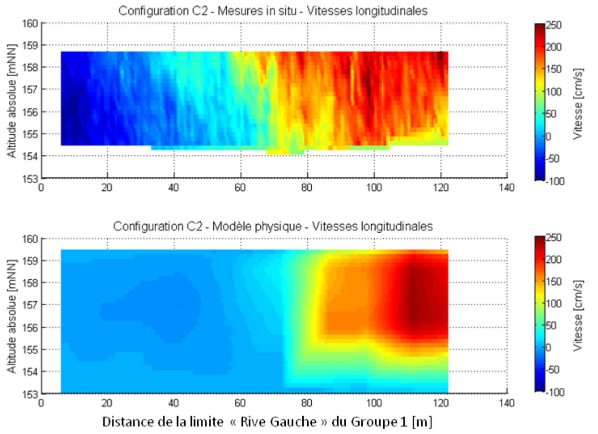

Figure 6: Exploitation case 2 – mean velocity field at 50m from the exit of the afterbays. On-site measurements are on top, and the physical model situation at the bottom. The colors represent the magnitude of the longitudinal velocity from -100 to 250 cm/s.

4. Analysis of the fishway entries

After the validation phase, the fishway entries have been installed on the model. 8 entries are located at the top of the afterbays outlet and 4 are placed 30 to 55m downstream in the left and right banks. The objective of the lateral entries is to guaranty the visibility of the fishway entrance even for high turbined discharges. A design optimization was needed to assure their hydraulic efficiency.

4.1 Test exploitation cases and inlet conditions

The functionality of the fishway has to be guaranty up to discharges of 1'400m^3/s (installed capacity). Nine exploitation cases have been chosen to test the behavior of the fishway entries, covering a range of turbined discharges between 600 and 1'400m^3/s. For the purpose of this article, one exploitation case, a medium total discharge unequally divided between the groups has been selected. The exact distribution is presented in Table 1. The discharge injected through the fishway entries is constant and equal to 5m^3/s. 1 entry is composed of two slice gates, so 2.5m^3/s per gate. The elevation of the gate was adapted to the downstream water level (which depends on the turbined discharge) to keep a constant drop of 30cm. This drop creates a jet with velocities around 2m/s.

Table 1: Exploitation case Q900 to test the behavior of the fishway entries

Case	Q_{total} [m^3/s]	G1 [m^3/s]	G2 [m^3/s]	G3 [m^3/s]	G4 [m^3/s]
Q900	900	350	350	0	200

4.2 Temporal analysis of one entry

The first observations of the fishway entries behavior rapidly show that the visibility of an entry jet depends mostly of the discharge turbined by the group where the entry is located on. Therefore, a systematic temporal jet analysis has been conducted on the right-bank entry of group 4 (see Figure 4), while changing the turbined discharge from 200 to 350m^3/s with steps of 50m^3/s. Figure 7 shows the longitudinal velocities of the jet 0.5m below the water surface for a zero discharge of group 4 and 350m^3/s (maximal discharge). The velocity at each point along the beam axis has been measured 1024 times, representing measurement duration of 5’30’’ at prototype scale.

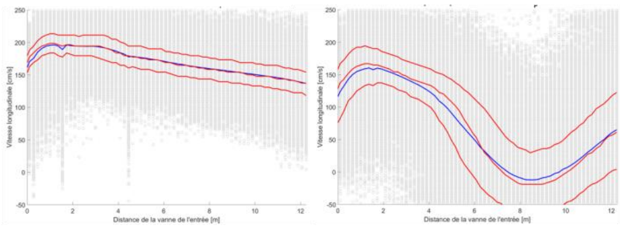

Figure 7: Temporal analysis of the jet longitudinal velocities (cm/s) in function of the distance to the fishway entry gate. Left: the group under the entry is stopped. Right: the group turbines the maximal discharge (350m^3/s).

If group 4 is stopped, the jet of the fishway entry is clearly visible, with average velocities above 150cm/s up to 12m downstream of the entry gate. In addition, the difference between the quartiles 25% and 75% is almost constant, around 35cm/s. With a turbined discharge of 350m^3/s, the behavior of the jet is completely different. The turbulences created by the turbined water confine the evolution of the jet in the tailrace channel and increase the velocity variations. Already 8m after the gate, the mean jet velocity is close to 0cm/s and the difference between the quartiles 25 and 75% at the same distance is above 100cm/s. This clearly shows that the fishway entry is no longer visible for the fish.

4.3 Flow analysis

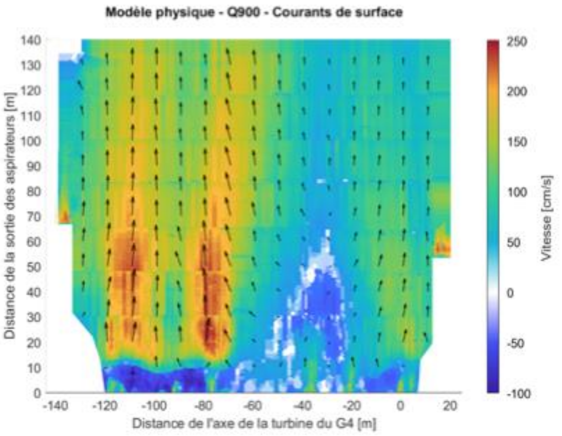

Figure 8: Surface average flow (X-Y plane) for the exploitation case Q900 (see Table 1).

The analysis of the surface flow of the exploitation case Q900 (see Table 1) shows that in front of group 1 and 2, turbining the maximal discharge, the highest velocities are between 200 and 250cm/s, while the minimal velocities approach -50cm/s in the 10 first meters after the turbines outlets. Those negative velocities are related to the high turbulences created by the turbined flow. As a consequence, the development of the jet coming from the fishway entries of those two groups is rapidly blocked. This observation corresponds to the results of the systematic analysis of the jet velocities presented in the preceding chapter. In front of group 3 (stopped), the longitudinal velocities in the tailrace channel are small, allowing the expansion of the jets up to 30m. In front of group 4, turbining 200m^3/s, this expansion reaches 10m, before the jets vanish in the global flow. The same conclusions can be drawn by observing the cross-sections across a fishway entry of group 1 and an entry of group 4.

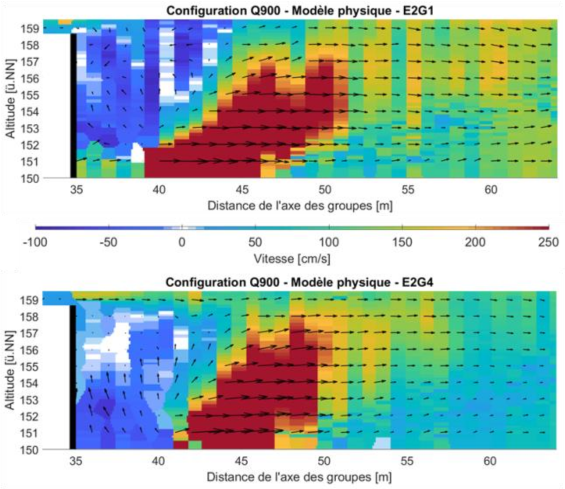

Figure 9: Subsurface average flows (X-Z planes) across one fishway entry of group 1 (turbined discharge 350m^3/s) and one of group 4 (turbined discharge 200m^3/s).

5. Conclusion

With the help of the UVP technology, it was possible to evaluate and optimize the fishway entries on the physical model of the Rhinau Hydropower plant. Installed on a robot, the measuring system allowed a flexible and replicable procedure, as it was required to compare the 2D flow fields for different exploitation cases. The validation of the model with measurements taken on site has confirmed the agreement of the physical model with the prototype and the accuracy of the measurements with the UVP. Even if small echoes issues have been observed in the measured data, in particular near the model borders, leading to a local loss of information, the global and interpolated results showed truthfully the flow field in the afterbays and in the tailrace channel.

References

We acknowledge EDF France as the hydropower plant owner and operator for having mandated this study to the LCH. The collaboration was with UP EST (Unité de Production), CIH (Centre d’Ingénierie Hydraulique) and LNHE (Laboratoire National d’Hydraulique et Environnement).

References

[1] Pfister M. and Chanson H. (2012). Scale Effects in Physical Hydraulic Engineering Models. Discussion, Journal of Hydraulic Research, vol. 50, pp. 244-246

[2] Met-Flow (2014). UVP-Duo Monitor User's Guide

11th International Symposium on Ultrasonic Doppler Methods for Fluid Mechanics and Fluid Engineering
Berlin, Germany (5.-7. September 2018)

Effect of Spilling from Adjacent Orifices on the Velocity Field and Pressures in Front of Needle Stop-Logs

Ivan Stojnić[1], Cédric Bron[1], Azin Amini[1] and Giovanni De Cesare[1]

[1] Laboratoire de Constructions Hydrauliques (LCH), Ecole Polytechnique Fédérale de Lausanne (EPFL), CH 1015 Lausanne, Switzerland

In this study, the effect of spilling from neighboring sluice gates on stop-logs was experimentally investigated on a 1:65 physical scale model comprised of a double arch dam, a reservoir area, six spillway orifices and two stop-logs. Two types of measurement were performed: 2D velocity field in approach flow zone at the central horizontal plane of the orifices using two 0.5 MHz long range UVP transducers and dynamic pressures acting on the needle stop-logs at nine relevant positions using piezo-resistive pressure transmitter. The results showed that the pressure acting on the needle stop-logs followed hydrostatic distribution and velocity magnitudes in the zone of the needle stop-log are low and mostly unaffected by the spilling of the neighboring sluice gates.

Keywords: Stop-logs, pressure, velocity field

1. Introduction

Stop-logs are temporary hydraulic structures placed to close openings in order to perform maintenance work. In case of multiple spillway openings, maintenance work is usually performed sequentially in order to ensure passage of flood events. In this study, the effect of spilling from neighboring sluice gates is studied experimentally on the 1:65 physical scale model of Kariba Dam [1-3]. The Kariba Dam, commissioned in 1959, is located on the Zambezi River between Zambia and Zimbabwe, Africa. It is a double curvature arc dam, 128 m high, 617 m long. The dam spillway consists of six submerged sluice gates 8.8 m high and 9.5 m wide with a total spilling capacity of 9'000 m^3/s. Due to the decades of exploitation, the spillway orifices and gates were damaged. In order to repair damaged spillway orifices, needle stop-log are planned for blocking the spillways temporarily during the repair works. The temporary stop-logs are held in place by hydrostatic forces acting upon them and are sealed using a membrane on its upstream face. Therefore, it is necessary to ensure that the needle stop-log surface is not exposed to negative pressure since it could lead to its dislodgment. In order to assess the effect of spilling on stop-logs, two type of measurements were carried out, namely pressure measurements on the stop-logs and velocity field in the approach zone of the gates.

2. Experimental facility and instrumentation

All experiments were carried out at the Laboratory of Hydraulic Constructions (LCH) of EPFL, Switzerland. The physical model (Figure 1) consists of a reservoir area of 190 m by 220 m horizontally and of 100 m vertically, the Kariba dam with its crest and complete set of spillway sluices (six), the free falling jets, the complete plunge pool and the tailwater zone with two power house outlets. The physical model is constructed with geometrical scale factor of 1:65 and the model is operated following Froude similitude and therefore the maximum discharge for the entire spillway of 9'000 m^3/s in prototype corresponds to 264 l/s in the model. Needle stop-logs were manufactured using 10 mm thick PVC plates with variable dimensions corresponding to the appropriate sluice and the stop-logs were placed and sealed to gates (Figure 1).

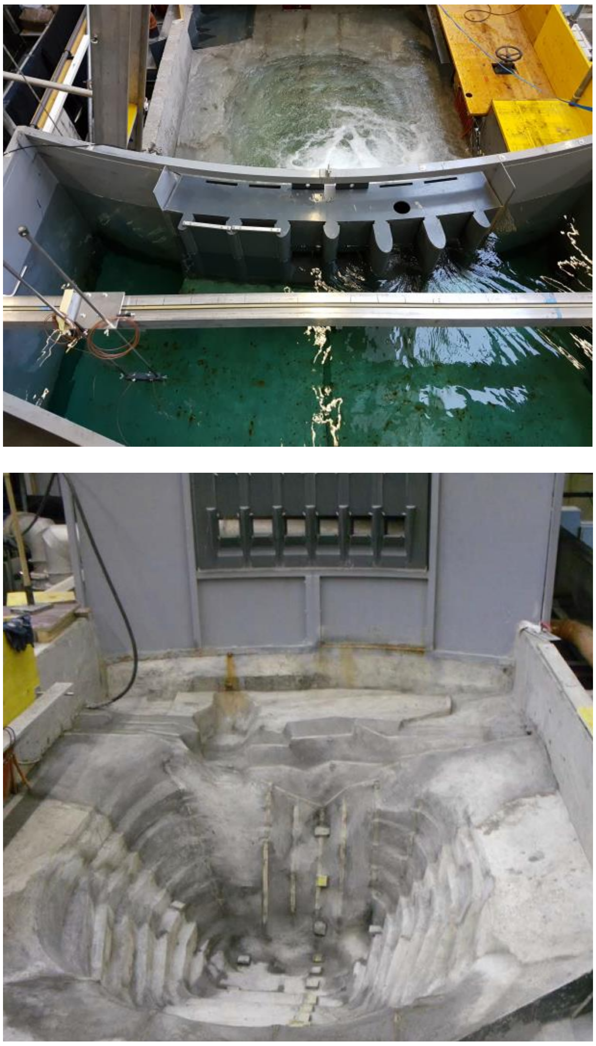

Figure 1. Physical model at LCH, view from upstream of Kariba dam orifice spillways with two stop-logs (top), view from downstream of the plunge pool towards the dam (bottom).

Each of the stop-log is equipped with 9 pressure taps (Figure 2), 15 mm long with 8 mm diameter which are pierced with a 2 mm micro tube. On each pressure tap, tubes with inner diameter of 8 mm were placed and connected to a multiplexer. The outlet tube of a multiplexer was connected to a piezo-resistive pressure transmitter for dynamic pressure measurement. The piezo-resistive pressure transmitter is of flush diaphragm type (Baumer, Switzerland) with an acquisition range between +/- 0.1 bar with an accuracy of +/- 0.001 bar. Pressures were collected at a sampling rate of 1 kHz for 66 s. The transmitter was calibrated before pressure measurements and the tubes were purged before each measurement.

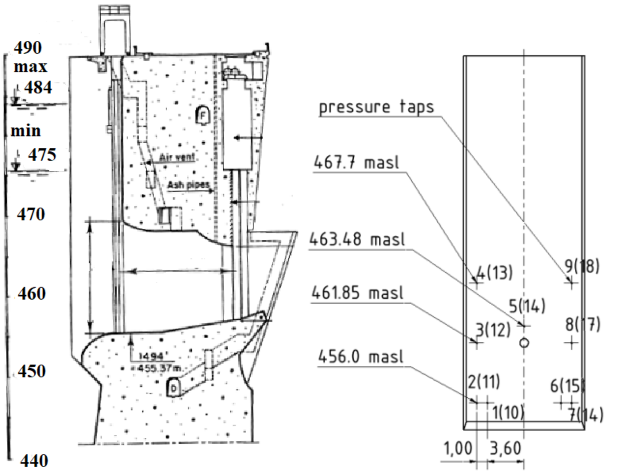

Figure 2. Sluice gate cross-section (left) and pressure taps position and designation-values in brackets correspond to second stop-log plate (right).

Velocity measurements were performed using a non-intrusive Ultrasound Doppler Velocity Profiler (Metflow, Switzerland). 2D velocities were recorded in the approach zone of the dam covering an area of 33.8 m by 156.0 m using two 0.5 MHz long range transducers with active diameter of 40 mm.(Figure 3). The transducers were placed horizontally in a frame (Figure 3) so that the beam axis formed a mutual angle of 60°.

Figure 3 UVP sensors, frame and carriage

The vertical position of the transducers axis was kept constant at the centre axis of the sluice opening corresponding to 462.3 meters above sea level (masl). The frame, which was attached to a carriage (Figure 3), was moved in 49 positions transversally across the width of the reservoir (with a step of 3.25 m) in which velocity profiles were recorded. The position of the carriage was measured with Leica D150 laser distometer with an accuracy of +/-1 mm. In such a way, a diamond shaped grid presented in Figure 4 is formed. In each intersection recorded velocity components were extracted from the corresponding velocity profiles giving 2D velocity components.

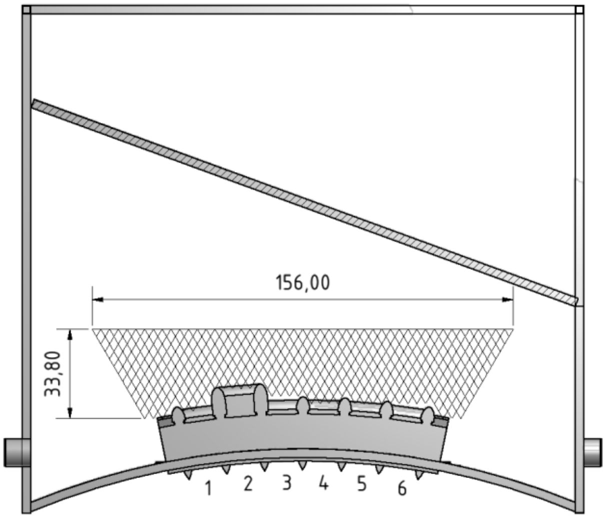

Figure 4 Velocity measurement grid and sluice gate designation

No particular seeding was used during velocity measurements since acoustic scattering was satisfactory. Water used in the model was a part of a large recirculating system of the laboratory and it contained impurities which enhanced acoustic scattering.

Each velocity profile was sampled 512 times with 64 repetitions that corresponds to a sampling frequency of around 15 Hz. The maximum depth was set to 750 mm and velocity bandwidth was therefore ±730 mm/s (± 5.89 m/s in prototype). In some cases, in particular in the zone of the open gates, velocity exceeded the maximum velocity bandwidth and aliasing effect was observed. In such cases, tailor-made Matlab® code was used to post process velocity profiles. All results are presented up-scaled with a scale of 1:8.06 for velocities and 1:65 for pressures in meters water column (m WC) following Froude similitude.

3. Test program

The physical model tests were conducted with two gates closed using stop-logs. In total three configurations were investigated: 1) Sluice no. 5 and 6 closed with stop-logs; 2) Sluices no. 3 and 4 closed with stop-logs; 3) Sluices no. 1 and 2 closed with stop-logs (see Figure 4). Herein only the second configuration will be presented since other configurations yield similar results. For each configuration, four different scenarios were tested, in

https://doi.org/10.7795/810.20190809

which four other gates (that are not closed using stop-logs) were either completely open or closed (Table 1). Each scenario was then tested for three water levels namely 475.5, 482.0 and 488.5 masl.

Table 1: Definition of test scenarios where C is closed, O is open and S.L. is stop-log.

	Gate No					
Scenario	1	2	3	4	5	6
I	C	C	S.L.	S.L.	C	O
II	O	C	S.L.	S.L.	C	O
III	O	C	S.L.	S.L.	O	O
IV	O	O	S.L.	S.L.	O	O

4. Results

Up-scaled mean pressures P_{mean}, standard deviation σ and corresponding hydrostatic pressures P_{HS} for scenario IV at water level 488.5 masl for 18 pressure points (pressure taps 1-9 correspond to stop log at gate No. 3 and 10-18 at No. 4) are given in Table 2. Since results for other configurations and scenarios yield similar results and due to space limitation they are not presented herein. For all tested scenarios and water levels time averaged pressures on stop logs follow hydrostatic pressure distribution (Table 2). Standard deviations of pressure readings for all tested scenarios and water levels are below 0.15 m WC and are less than 1% of water depth. These results were supported with visual observation made during the tests. In the zone of the stop-logs, water surface is smooth, horizontal and undisturbed by the spilling of adjacent sluices (Figure 5 and 6). No negative pressure has been observed in the physical model.

Figure 5. Model in operation for scenario IV at 488.5 masl, view of the approaching zone from the right side.

Time averaged velocity vector plot superimposed on velocity contour line plot of time averaged velocity field in the approaching zone of the dam for scenarios I-IV at 475.5 masl and for scenario IV at 482.0 and 488.5 masl are given in Figures 7-12.

Table 2. Up-scaled time averaged pressure, standard deviation and corresponding hydrostatic pressures for scenario IV at 488.5 masl

Pressure tap	1	2	3	4	5	6
P_{mean} [m WC]	32.5	32.6	26.5	20.7	24.9	32.4
P_{HS} [m WC]	32.5	32.5	26.7	20.8	25.0	32.5
σ [m WC]	0.12	0.12	0.10	0.14	0.10	0.10
Pressure tap	7	8	9	10	11	12
P_{mean} [m WC]	32.6	26.6	20.8	32.5	32.5	26.6
P_{HS} [m WC]	32.5	26.7	20.8	32.5	32.5	26.7
σ [m WC]	0.09	0.11	0.14	0.10	0.09	0.09
Pressure tap	13	14	15	16	17	18
P_{mean} [m WC]	20.9	24.9	32.4	32.5	26.7	20.8
P_{HS} [m WC]	20.8	25.0	32.5	32.5	26.7	20.9
σ [m WC]	0.13	0.10	0.10	0.11	0.09	0.09

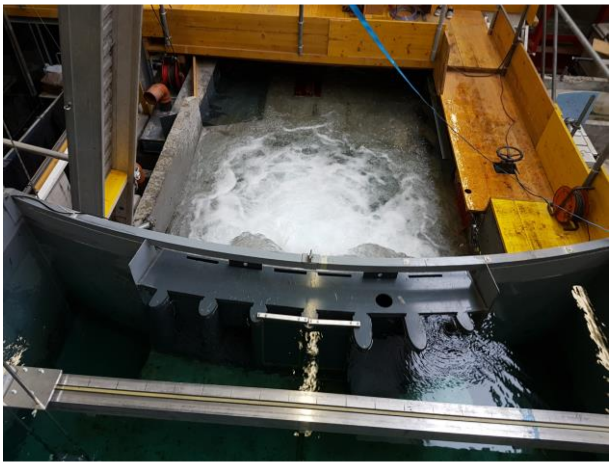

Figure 6 Model in operation for scenario IV at 488.5 masl, top view of the approaching zone.

Time averaged velocity magnitudes increase with the increase of water level as well as with the increase of the number of opened sluices. Velocity magnitudes in the zone of the opened sluices can reach up to 10 m/s. In the zone of the stop-logs time averaged velocity magnitude for scenarios No. I and II are below 2 m/s whereas for scenario III and IV they may reach up to 4.5 m/s (in the close proximity of the neighboring sluice no 5).

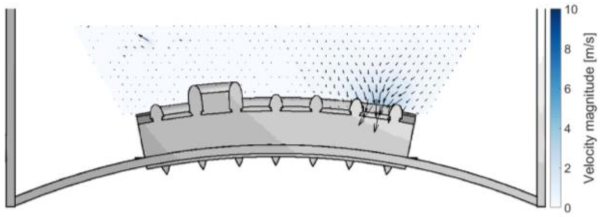

Figure 7 Time averaged velocity field in approaching zone of the dam for scenario I at 475.5 masl

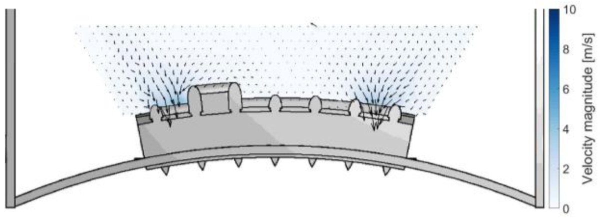

Figure 8 Time averaged velocity field in approaching zone of the dam for scenario II at 475.5 masl

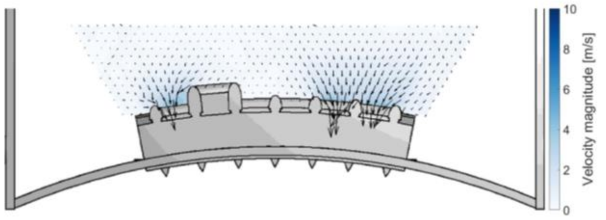

Figure 9 Time averaged velocity field in approaching zone of the dam for scenario III at 475.5 masl

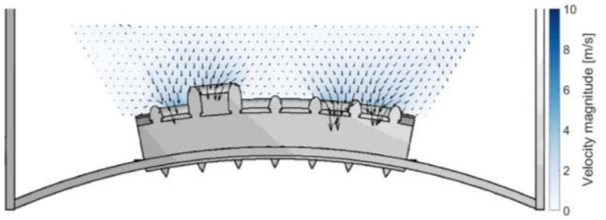

Figure 10 Time averaged velocity field in approaching zone of the dam for scenario IV at 475.5 masl

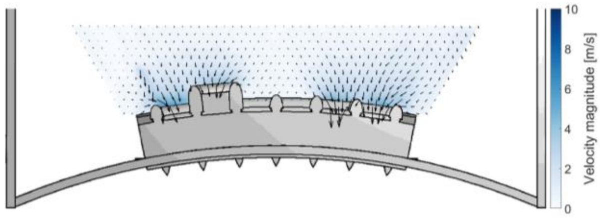

Figure 11 Time averaged velocity field in approaching zone of the dam for scenario IV at 482.0 masl (Table 1.).

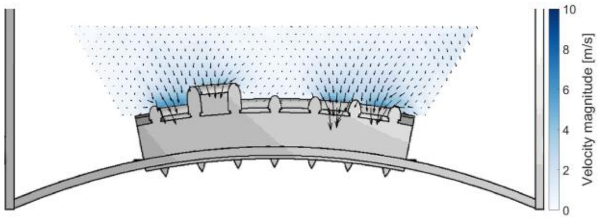

Figure 12 Time averaged velocity field in approaching zone of the dam for scenario IV at 488.5 masl

It can be noticed that mean velocity magnitude are low and mostly unaffected by the spilling of adjacent sluices. This observation is in agreement with visual observations and pressures measurements on the stop-log. Based on the above presented measurements it can be concluded that, for the tested conditions, stop-logs are very limited affected by the spilling effects of neighboring sluices.

5. Summary

Stop logs are temporary hydraulic structures frequently used to block the flow through a spillway or canal during routine maintenance. Needle stop-logs are held in place by hydrostatic forces acting upon them and therefore it is necessary to ensure that the stop-logs are not exposed to negative pressure. This study is based on an experimental approach using a 1:65 physical scale model of Kariba dam to investigate the effect of spilling from adjacent sluice gates on the velocity field and pressure in front of needle stop-logs. Two types of measurements were performed, namely dynamic pressure measurements on the stop-logs and velocity field in approaching zone of the dam. Two long range UVP transducers with an emitting frequency of 0.5 MHz were used to record 2D velocity field in the approaching zone of the dam. UVP sensors were place horizontally in a frame so that the sensors axis formed a mutual angle of 60°. The frame, which was attached to a carriage, was moved in 49 positions transversally across the width of the reservoir and by extracting the velocities components 2D velocity field was generated. No seeding was using during the velocity measurements since acoustic scattering was satisfactory. The physical model tests were conducted for three different configurations in which two gates were closed using needle stop-logs while remaining ones were either fully closed or fully open. Pressure measurements have shown that for all configurations time averaged pressure readings followed hydrostatic pressure distribution. Standard deviations of pressure reading were less than 1% of the available water depth and therefore it can be concluded that the needle stop-logs were not exposed to negative pressure for the tested conditions. Velocity measurements in the approaching zone of the dam have shown that velocity magnitudes in the zone of the needle stop-logs are low and mostly unaffected by the spilling of the neighboring sluice gates.

6. References

[1] Pfister M., *et al.* : Cavitation risk estimation at orifice spillway based on UVP and dynamic pressure measurements, Proceedings of ISUD8, ISUD J.,(2012), 137-140.

[2] Noret C., *et al.*: Kariba dam on Zambezi river: stabilizing the natural plunge pool, La Houille Blanche (1) 34-41 (2013).

[3] LCH-EPFL: Hydraulic modeling of Kariba dam spillway, Kariba dam rehabilitation Phase I: Needle Stop-logs, Rapport LCH no 03/17 (2017).

Flow Limitation and Riverbank Protection Design Using Asymmetrical Flow Mapping on a Physical Hydraulic Model

Vecsernyes Zsolt[1], Andreini Nicolas[1]

[1] Laboratory for Applied Hydraulics, University of Applied Sciences Western Switzerland, HES-SO, HEPIA Geneva 1202, Switzerland

The experimental monitoring of an asymmetrical flow pattern, realised on a physical model at the Laboratory for Applied Hydraulics of HEPIA, yielded accurate dimensioning of a flow limitation device and appropriate riverbank protection design. The studied structures were then implemented on the Aire River in Geneva. The main goals of the Aire River revitalization program in Geneva are: hazard and risk mitigation. Inundation risk is mitigated for the Q300y=120 m³/s design discharge by an orifice-weir structure yielding a 400’000 m³ flood retention. A free transit flow is achieved for all hydrological conditions by an innovative two-stage driftwood retention device [1] preserving the orifice of driftwood clogging. Since upstream from the orifice flow conditions are strongly asymmetrical, velocity field needed to be monitored on a physical hydraulic model [2]. Velocity measurement was carried out by means of Met-Flow UVP probes and the shear stress calculated. The experimental analysis results yielded an appropriate orifice geometry and riverbank protection design.

Keywords: Asymmetrical flow, Velocity field mapping, Orifice geometry design, Rive bank protection

1. Introduction

In the frame of the third stage of the Aire River revitalisation project, inundation risk of Geneva is mitigated by an orifice-weir structure yielding flood retention (Figure 1). Upstream from this discharge limitation structure the revitalised reach of the Aire River is implemented over its former right bank and connected to the orifice through a gravel pit. The flood retention field extends over the gravel pit and the revitalised river reach. The former rectilinear river reach axially connected to the orifice is only supplied by drainage. A convergent flow is therefore encountered at the orifice.

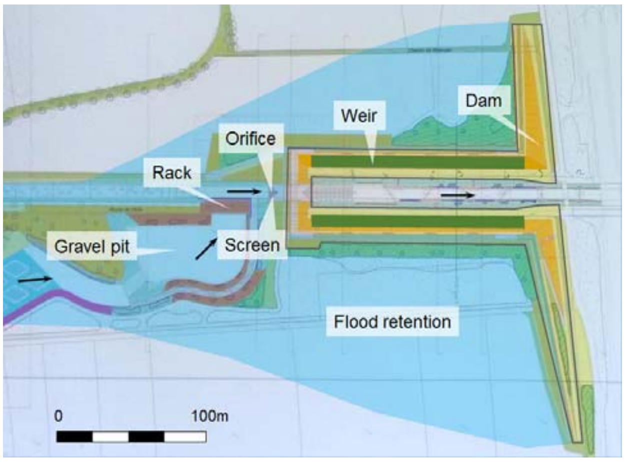

Figure 1: Synoptic view of the Aire River inundation risk mitigation structures. The orifice implemented in the dam yields discharge limitation by flood retention.

Due to the predominant contribution of the revitalised stream, the flow takes an S shape in the vicinity of the discharge limitation device in order to pass the bottom opening of the dam. The resulting asymmetrical flow expands into abutment of the left river bank and induces uncommon axial forces and shear stress on the latter which must be fought in order to avoid bank erosion. The asymmetrical flow pattern may also alter the hydraulic comportment of the orifice responsible of the discharge limitation. For these raisons flow pattern needed to be monitored on a physical hydraulic model.

2. Experimental set-up

The experimental investigations were conducted at the Laboratory for Applied Hydraulics (LHA) of HEPIA Geneva, CH. The physical model of the Aire River was constructed with a 1:40 (model : prototype) length scale (Figure 2). Flow analyses obeyed Froude similarity. Velocity scale in these conditions became 1:6.325.

The velocity field monitoring required permanent flow conditions achieved by means of the closed circuit facilities of the laboratory. Hence a constant hydraulic head corresponding to 100 m³/s (prototype) was guaranteed upstream from de orifice opening with a free supercritical downstream outflow.

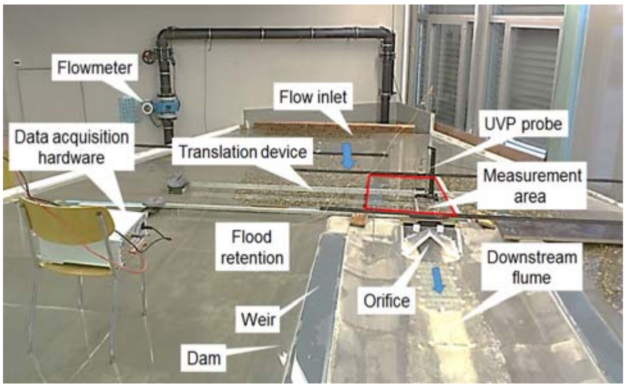

Figure 2: Partial view of the Aire River physical model at the LHA of HEPIA, with the flow monitoring facilities installed upstream from the discharge limiting orifice.

A single Met-Flow, 1 MHz, UVP ultrasound probe was implemented upstream from the orifice (Figure 3). The

https://doi.org/10.7795/810.20190809

flow mapping was obtained by moving the probe step-by-step over the measurement area, in 16 points and 3 rows. Rows were positioned at respectively y = 15 m; y = 30 m; y = 45 m; upstream from the orifice.

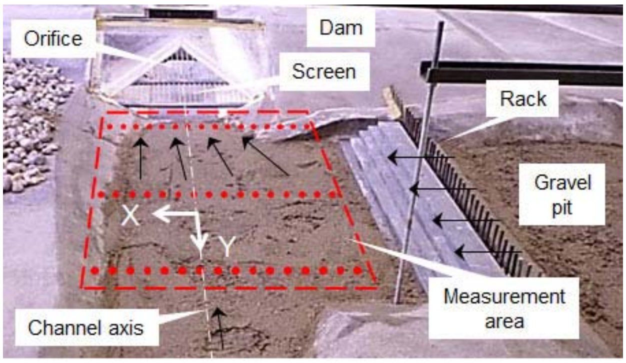

Figure 3: Upstream view of the dam showing the UVP measurement scheme composed of 16 points set in 3 rows.

The probe was installed with an angle of 30° from the vertical (Figure 4). Two measurement series were carried out: **a.** the horizontal projection of the ultrasonic beam pointed upstream and parallel to the channel axis, and then **b.** towards the gravel pit and perpendicular to the channel axis. A complete velocity mapping could be achieved upstream from the orifice, in two perpendicular orientations.

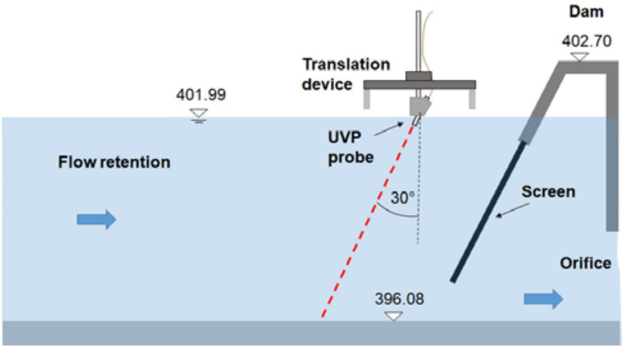

Figure 4: UVP probe implemented upstream from the discharge limiting orifice of the dam.

3. Results

3.1 Flow velocity mapping

The recorded velocity data was post processed with the help of a MATLAB subroutine yielding the graphical representations of the flow field. All values are hence considered as according to prototype.

Under permanent flow conditions (Q100y = 100 m^3/s, prototype), the flow patterns were analysed in 13 different levels above the channel bed, between 396.00 AMSL and 302.00 AMSL. Thus, the velocity vectors were plotted in horizontal plans, every 0.50 meter.

Over the channel bed (Figure 5) flow is inhibited by the encountered boundary effect yielding a weak velocity field. In the vicinity of the bottom opening flow is strong due to continuity reaching 1.2 m/s. Flow pattern is clearly directed in the axis of the orifice.

In the upstream part of the analysed channel velocity increases with measurement level. This transition can be followed over Figures 5-6-7.

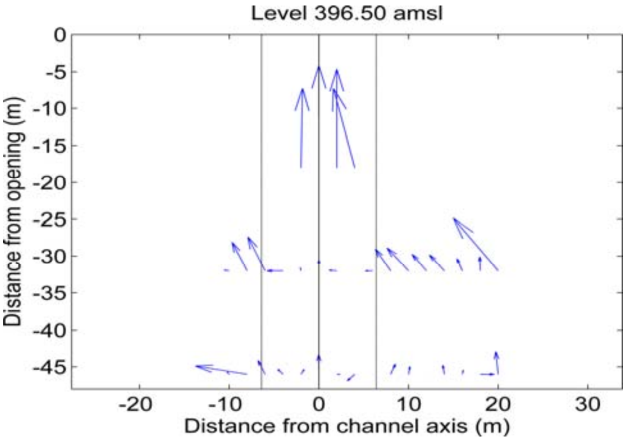

Figure 5: Flow velocity pattern shown near the channel bed, at level 396.50 AMSL. Bed boundary effect reduces the velocity in the upstream analysed channel portion. Near the opening flow takes an axial path towards the orifice.

In Figure 6, the velocity field at level 397.50 AMSL is shown. The asymmetrical flow pattern takes progressively place with the rise of measurement level. Flow pattern at the orifice is mainly axial, yet with a growing lateral component due to flow arriving from the gravel pit.

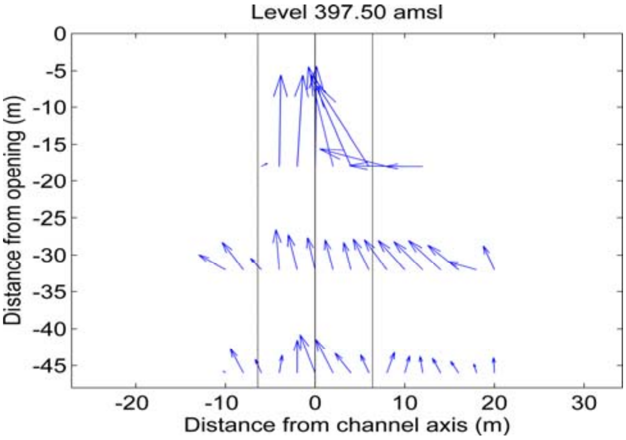

Figure 6: Flow velocities shown at level 397.50 AMSL, revealing the increase flow in the upstream part of the examined channel. Close to the opening flow takes a lateral component.

In Figure 7, the velocity field at level 399.50 AMSL is shown. The expected asymmetrical flow pattern is clearly developed and thus pointed out. Flow remains relatively strong close to the orifice, with a main axial component.

https://doi.org/10.7795/810.20190809

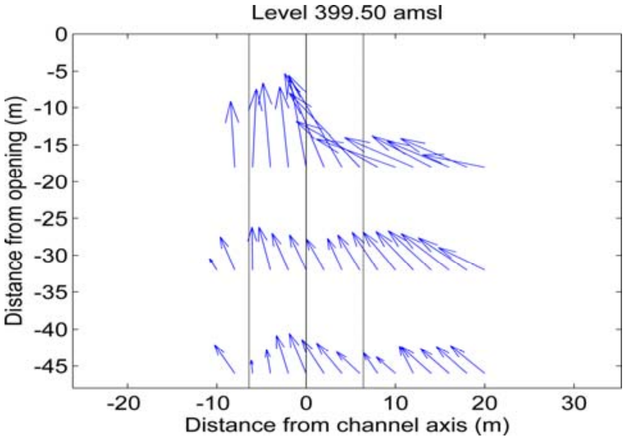

Figure 7: Flow velocities shown at level 395.50 AMSL, revealing the expected asymmetrical pattern.

The velocity field integrated over the whole water column is plotted as two orthogonal 2D flow intensity maps in Figure 8 and Figure 9. These presented results were obtained for the probe positioned at y = 15 m upstream from the orifice, and respectively for Y and X axes (c.f. Figure 3).

Since the discharge limitation device is built as a bottom opening of the dam, the main flow takes a tube shape close to the orifice as shown in Figure 8. This vein characterised by values larger than 1.0 m/s sinks from the gravel pit (Figure 9) and bends right towards the orifice.

Flow velocity reduction observed in Figure 8 (at 398.60 ASML; on channel axis) is induced by the horizontal bar of the drift wood protection screen.

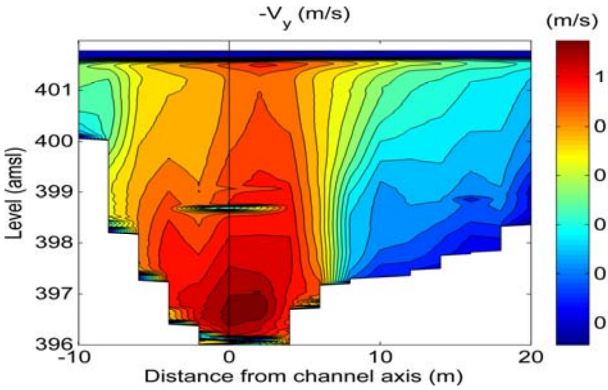

Figure 8: Flow map achieved on the physical model (c.f. Figure 3). Velocity vector field, -Vy, parallel to the channel axis. Core velocity takes place near the channel axis.

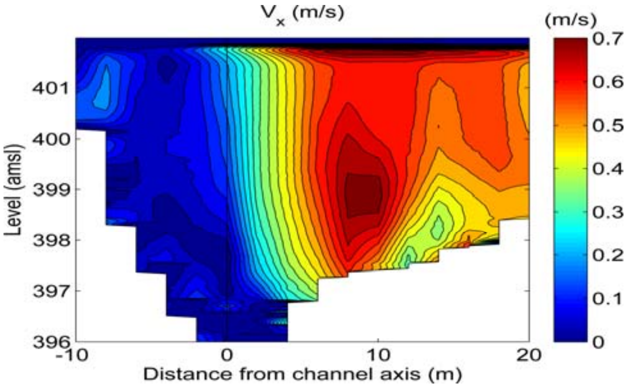

Figure 9: Flow map achieved on the physical model. Velocity vector field, Vx, perpendicular to the channel axis. Core velocity found close to rack of the gravel pit.

3.2 Impact on the orifice's rating curve

In order to respect the inundation risk mitigation goals of the Aire River project, the hydraulic comportment of the orifice needed to be analysed on the physical model. As shown in Figure 10, a hexagonal geometry was proposed respecting architectural aspects.

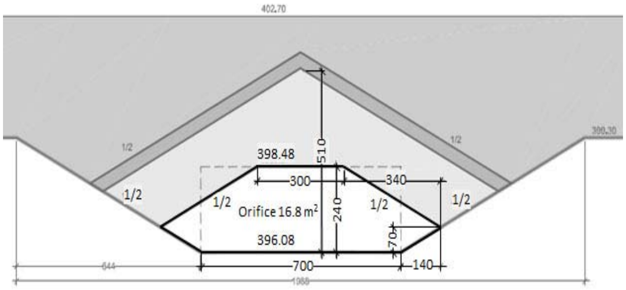

Figure 10: Discharge limiting orifice, with a 9.8 m large, 2.4 m high hexagonal bottom opening of the dam.

Even though the asymmetrical upstream flow pattern may impact the rating curve of the bottom opening, the analyses could yield an appropriate orifice geometry. The rating curves shown in Figure 11 point out that a hexagonal geometry could be correctly fitted to the defined hydraulic constraints. Therefore a 9.8 m large and 2.4 m high bottom opening could be adopted for construction on the Aire River.

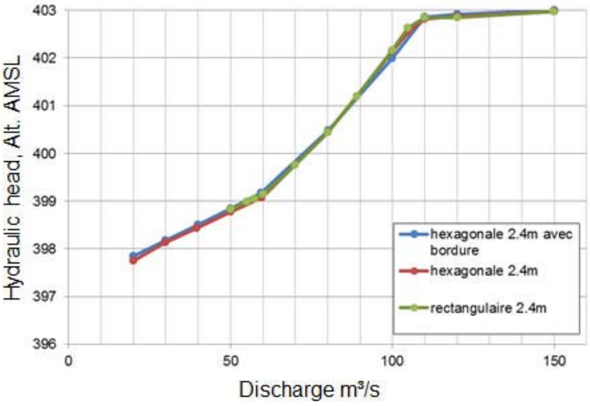

Figure 11: Rating curves for three different orifice geometries, proving the appropriate choice of the hexagonal one.

3.3 Shear stress applied on the left channel bank

As demonstrated above (Figure 5 to Figure 9), flow expands into abutment of the left river bank over the whole water column, inducing shear stress. It is therefore appropriate to determine shear stress as a function of velocity, as followed

$$\tau = \rho\left(\frac{U \cdot \kappa}{ln\left(\frac{l_m}{l_0}\right)}\right)^2 \tag{1}$$

According to [3], in Eq. 1, ρ is the specific mass of water, U is the velocity near the wall, κ is the von Karman's constant which equals 0.408, l_m is a distance measured as 8% of the total curvilinear ray from river bank taken into account for shear stress (Figure 12), and l_0 is the roughness height.

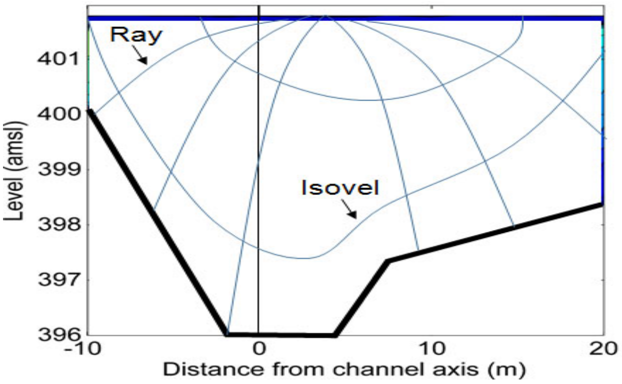

Figure 12: Orthogonal Ray-Isovel network taken into account for shear stress analysis in the upstream vicinity of the orifice.

Typical shear stress values reach τ ≤ 200 N/m² near the left channel bank upstream from the orifice. This value has to be scaled up by a 1.35 multiplication factor due to the velocity component normal to the left river bank, yielding values larger τ ≥ 270 N/m². These constraint require a rip-rap bank protection [4].

3.4 Constructed structures on the Aire River

As demonstrated on Figure 13, the analyses carried out at the Laboratory for Applied Hydraulics of HEPIA yielded the construction of a hexagonal discharge limiting orifice on the Aire River as defined on the physical hydraulic model. Upstream from the orifice a rip-rap channel bank lining was adopted.

Figure 13: Structures constructed on the Aire River as defined on the physical hydraulic model. A hexagonal orifice and a rip-rap channel bank lining were adopted upstream from the latter.

6. Summary

The achievements of the present study underline that the appropriate choice of structural measures in river restoration may be assisted by physical model tests in particular when uncommon flow pattern conditions are encountered.

In the Aire River revitalisation programme in Geneva the velocity field mapping of an asymmetrical flow pattern revealed pertinent on physical hydraulic model.

The experimental study carried out by means of a Met-Flow UVP probe at the Laboratory for Applied Hydraulics of HEPIA – Geneva, pointed out that despite the encountered asymmetrical flow pattern the hydraulic low of the orifice opening is weakly affected. Yet, in order to respect the inundation risk mitigation goals of the Aire River revitalisation project the dimensions of the proposed hexadecimal opening had to be tested on physical model and adjusted.

The study results also pointed out that in the upstream vicinity of the discharge limiting orifice, notable shear stress is applied on the left rived bank due the encountered asymmetrical transverse flow. These results yielded the re-evaluation of the bank protection technique initially planned by plant engineering. Therefore, a rip-rap structure was erected over the entire height of the left bank as channel lining.

References

[1] Vecsernyés Z. *et al.*: Innovative driftwood retention device on the Aire River in Geneva, Interpraevent Congress, Luzern, Switzerland (2016)

[2] Vecsernyés Z. *et al.*: Physical modelling of the third stage of Aire River revitalisation project. Swiss Competences in River Engineering and Restoration, Symposium CIPC KOHS, Switzerland (2014)

[3] Kean J.W. *et al.*: Test of a Method to Calculate Near-Bank Velocity and Boundary Shear Stress, Journal of Hydraulic Engineering, ASCE, pp. 588-601 (2009)

[4] Chen Y.H. and Cotton G.K.: Design of Roadside Channels with Flexible Linings, Hydraulic Engineering Circular No. 15 Report No. FHWA-IP-86-5. Washington, D.C., Federal Highway Administration, USA (1986)

11th International Symposium on Ultrasonic Doppler Methods for Fluid Mechanics and Fluid Engineering
Berlin, Germany (5.-7. September 2018)

Accuracy and Robustness Evaluations on Algorithms of Ultrasonic Spinning Rheometry

Taiki Yoshida, Yuji Tasaka, Hyun Jin Park, and Yuichi Murai

Laboratory for Flow Control, Faculty of Engineering, Hokkaido University, Japan

We present a novel methodology using ultrasonic velocity profiling (UVP) to overcome some fatal problems in conventional torque rheometry, such as shear banding, wall-slip, viscoelastic instabilities, and so on. Termed ultrasonic spinning rheometry, the methodology can evaluate rheological properties from unsteady simple shear flows in a rotational cylindrical vessel. Different algorithms have applied to various kinds of fluids to evaluate the properties, there is, however, no trials on accuracy and robustness evaluations for the algorithms yet. We investigated apparent noise characteristics of velocity distributions in our measurement system and examined statistical calculations of effective viscosity profiles analyzing velocity profiles simulated by a numerical solution with artificial random noise.

Keywords: Rheometry, Newtonian viscosity, Accuracy evaluation, Error analysis, Shear flow

1. Introduction

In the present industry, it is of great importance not only to comprehend fluid-product properties but also to deal with the fluid material in the producing systems. The complete comprehension of rheology has great significance to enhance and keep the products quality. Rheometry which quantitatively evaluates shear-rate dependent properties has been studied and developed to deal with complex fluids, such as dense suspensions, bubbly liquids, etc. Conventional rheometry using torque measurements are widely used in the industry and can evaluate the properties of test materials when deformations of the materials accord with the theory. There are many complications due to non-Newtonian characteristics, although most industrialized fluid products are included in the non-Newtonian fluids. The complications occur measurement limitations in the application to complex fluids. The most dominant factor is called the “Couette inverse problem” [1], which is caused by ambiguities of knowledge in “local” deformations of non-Newtonian fluids. To overcome the problems, a rheometry coupled with velocimetry are desired as a novel approach, hence UVP [2] has great advantages of wide applicability due to high spatiotemporal resolution.

We proposed a rheometry using UVP for complex fluids in rotating cylindrical systems without requiring an inner cylinder to measure the axial torque, termed ultrasonic spinning rheometry (USR). This rheometry performs rheological evaluations, such as effective viscosity, shear modulus, linear viscoelasticity, yield stress, etc. Analytical procedures of USR (Fig. 1) have been developed in our previous works [3−9]. Yoshida *et al.* [7] reported an algorithm to measure effective viscosity using the phase-lag analysis, and Yoshida *et al.* [9] revealed macro-rheological properties of clay dispersions using the phase-lag analysis. Since there are still no detailed evaluations of the accuracy of the method, in this report, accuracy on viscosity measurement of USR is evaluated by velocity profiles of the analytical solution with artificial random noises. To investigate the accuracy by calculating statistically, $O\ (10^3 - 10^4)$ trials are performed by iterative calculations.

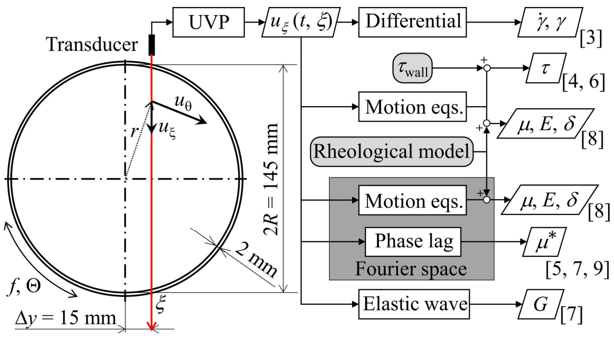

Figure 1: Schematic of the experimental setup in the arrangement of the ultrasonic transducer to a cylindrical container, and flow diagram of details of analytical procedures

2. Ultrasonic spinning rheometry (USR)

2.1 Experimental setup and overview of USR

Experimental setup consisted of an open vertical rotating cylinder made of acrylic resin with 145 mm inner diameter ($2R$) and 65 mm high, 2 mm thick lateral wall (Fig. 1). Cylinder oscillations were controlled at setting oscillation amplitude, $\Theta = \pi/2$ rad, and frequency, $f = 1$ Hz. Instantaneous velocity fluctuations exerted by regular oscillations are measured using UVP, where UVP-model Duo (Met-Flow S.A., Switzerland) was adopted as a velocity measurement system. When velocity vectors in radial direction are negligible compared to the azimuthal component, the azimuthal velocity, u_θ, at a radial position, r, is given as

$$u_\theta = \frac{u_\xi r}{\Delta y}. \qquad (1)$$

Installation of the transducer position, Δy, requires careful handling due to: (1) A much smaller Δy creates significant error and enhances measurement errors. (2) Larger Δy induces an inflection at the cylinder wall due to the large curvature. Since obtained velocity component, u_ξ, contains unavoidable noises due to errors in UVP, it affects the analysis using rheological model, shown in Fig. 1, due to differential amplification of the noises. To overcome the influence, frequency-domain analyses were proposed so

https://doi.org/10.7795/810.20190809

that the obtained data are evaluated without noise influences due to spectral decomposition [5, 7−9].

Yoshida *et al.* [7] developed a method adopting the phase-lag analysis. This method compares the phase lag between the analytical solution and experimental results, so it is possible to quantitatively evaluate the effective Newtonian viscosity. To represent momentum propagations as phase-lag profiles in unsteady shear flows, Tasaka *et al.* [5] derived an analytical solution for spatiotemporal velocity fluctuations of Newtonian fluids. When a unidirectional flow in azimuthal direction is assumed, the Navier-Stokes equation for incompressible fluids is reduced into

$$\frac{\partial u_\theta}{\partial t} = \nu \left(\frac{\partial^2 u_\theta}{\partial r^2} + \frac{1}{r}\frac{\partial u_\theta}{\partial r} - \frac{u_\theta}{r^2} \right), \tag{2}$$

where ν indicates kinematic viscosity of the test fluids. Given appropriate conditions as initial and boundary definitions, an analytical solution is determined. It is derived as $u_\theta = U_{\mathrm{wall}} A(r) \sin[\omega t + \phi(r)]$, where $\omega = 2\pi f$ and $U_{\mathrm{wall}} = 2\pi^2 f R \Theta / 180$. The term of $\phi(r)$ is given as

$$\phi(r) = \tan^{-1} \frac{\Phi_R \Psi(r) - \Phi(r) \Psi_R}{\Phi(r)\Phi_R + \Psi(r)\Psi_R}, \tag{3}$$

where the Φ_R, $\Phi(r)$, Ψ_R, and $\Psi(r)$ define terms of infinite series. Further details of the derivation of Eq. (3) are given in [5]. The analytical solution may be adequate in describing unsteady flows in the present system. It has been reported that the phase-lag profile, $\phi(r)$, is in good agreement with experiments using UVP [7].

2.2 Effective Newtonian viscosity measurement

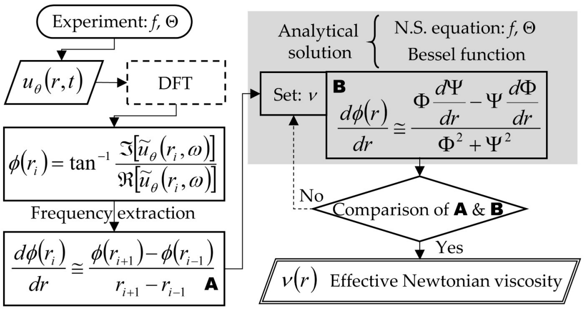

Figure 2: Schematic outline of the analytical process of USR to evaluate "local" effective Newtonian viscosity [7]

Flow diagram of procedure to evaluate rheological property is summarized in Fig. 2. The phase-lag of the velocity fluctuation at a radial point from the cylinder wall was calculated using the discrete Fourier transform (DFT) on the velocity fluctuations. It relates to momentum propagation of the fluid flow depending on its local rheological behavior. Hence, spike-like noises, which is typical of UVP measurements, can almost be removed with the DFT. It was applied to results with an oscillation period, $\Delta t \geq 1$ s, thus this method can track drastic changes in instantaneous viscosity, such as shear thinning, Bingham, and thixotropic fluids. Averaged by N-times measurements in every oscillating cycle periods, the phase-lag profiles are expected to reduce the noises caused by relative errors from UVP. Since there are no results of accuracy in viscosity measurement, accuracy evaluations of the effective Newtonian viscosity measurement are examined by applying numerical solution with artificial random noises to the viscosity measurement explained in §4. A method to generate the random noises assuming the measurement noises is proposed in §3.

3. Noise evaluation in measured velocity

3.1 Statistical calculation for obtained velocity

To obtain velocity fluctuations of unsteady shear flows in silicon oil ($\nu = 1000$ mm^2/s), an ultrasonic transducer of resonance frequency 4 MHz and 5 mm effective element diameter was selected. Important parameters of UVP are temporal resolution $\Delta\tau = 50$ ms, spatial resolution $\Delta\xi = 0.74$ mm, and speed of sound $c = 980$ m/s.

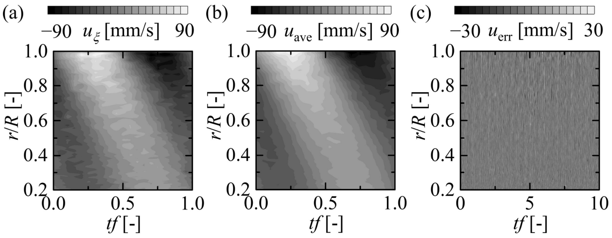

Figure 3: (a) Instantaneous velocity distribution, u_ξ, in experiment, (b) averaged velocity distribution, u_{ave}, with $N = 100$, (c) relative error velocity subtracted u_{ave} from u_ξ

Instantaneous spatiotemporal velocity u_ξ, cycle-averaged velocity u_{ave}, and residual velocity u_{err} are shown in Fig. 3a-c, where the horizontal and vertical axes indicate cycle-period, tf, and radial position normalized by the cylinder radius, r/R. The gray scale indicates velocity amplitude. u_{ave} and u_{err} were calculated by cycle average of u_ξ for $N = 100$ ($\Delta t = 1$ s) and $u_\xi - u_{\mathrm{ave}}$. The velocity fluctuations propagate according with phase-lag from the cylindrical wall, $r/R = 1.0$ (Fig. 3a and b), where the result of Fig. 3a has more noisy profiles than that of Fig. 3b. From u_{err} distribution (Fig. 3c), these noises increase with getting closer to the wall, because quality of velocity obtained by UVP may change depending on velocity magnitude.

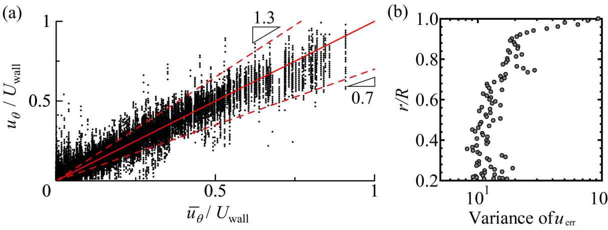

Figure 4: (a) Comparison of instantaneous and averaged velocity, where a total number of plotted data is 2000 × 96, (b) variance profile of u_{err} calculated from Fig. 3c

To confirm factors in the generation of u_{err}, instantaneous velocity was compared to the averaged velocity (Fig. 4a), where differences between u_ξ and u_{ave} were compared in all data of r/R and tf. Two significant findings were observed: (1) Deviations in the measured velocity increase as measurement target velocity increases. (2) Measured velocity profiles have the lowest noise level observed from low velocity in Fig. 4a. Moreover, the variance profile of

https://doi.org/10.7795/810.20190809

u_{err} also indicates the deviation tendency of obtained instantaneous velocity (Fig. 4b), where the horizontal and vertical axes show variance and normalized radial position in the cylindrical container. The variance profiles converged to almost 10 mm^2/s^2 when r/R get closer to the cylinder center. The reason for the significant increase in the variance near the wall is co-reflection of the ultrasound at the interface between acrylic resin the fluid media.

3.2 Production of artificial random noises with normal distribution

Considering the tendency of noises estimated from u_ξ (see Fig. 4), artificial random noises assuming experimental conditions are created by a noise-model function using Box-Muller method [10] to create uniform random values with (0, 1], which are generated by Mersenne Twister [11]. The noises are defined as n (μ, σ^2) with Gaussian distribution, where μ and σ indicate average and standard deviation. The noise-model considered from the experimental result is given as

$$u_{err} = n_1\left(0, \alpha\left|u_\xi\right|\right) + n_2\left(0, \sigma_{min}^2\right), \tag{4}$$

where α and $\sigma_{min}{}^2$ indicate a noise amplitude coefficient and the lowest noise level. n_1 and n_2 are a Gaussian random function with normal distribution and are independent of each other. The noise amplitudes were determined by α, included in a function, n_1. On the other hand, the standard deviation of n_2 was determined from the lowest noise level of the experimental result as shown in Fig. 4b. Produced noise at $\alpha = 0.5$ and velocity distribution with noises to the analytical solution are shown in Fig. 5a and b. The produced noises of Fig. 5b are qualitatively agree with that of Fig. 3a. Variance profiles at the case of $\alpha = 0.5$ have good agreement with experimental result (Fig. 5c), so these parameters were determined in §4 to evaluate the accuracy of the viscosity measurement algorithms.

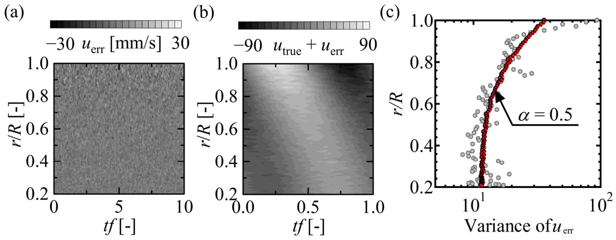

Figure 5: (a) Produced artificial random noises at $\alpha = 0.5$, (b) velocity distribution with noise (a) to velocity calculated form numerical solution, (c) u_{err} variance in noise amplitude $\alpha = 0.5$

4. Accuracy evaluations and improvement

4.1 Phase lag averaging with short time DFT

By utilizing the method to produce velocity distributions by numerical solution with artificial random noises as mentioned above, it is possible to evaluate the accuracy as a probability density distribution P_{vis} (= M_{count}/M) by repetitive computing. M_{count} and M indicate the count number of how many values fall into each bin and number of trials. P_{vis} is calculated by numerical computation with $M = 2000$. Histograms of simulated results were calculated by counting M_{count} at every step of ν in 20 mm^2/s from 0 mm^2/s to 2000 mm^2/s. Probability density distribution of viscosity profiles was evaluated from simulated velocity distribution at cases of averaging cycle times, N = 1, 80, 320 (Fig. 6). The horizontal and vertical axes indicate kinematic viscosity and normalized radial position, where the true value of kinematic viscosity to solve the analytical solution is emphasized by the dashed line. The gray scale shows the probability of viscosity measurement using the phase-lag analysis. To evaluate the viscosity profiles, phase lag obtained from the velocity distribution is needed to calculate the differential. Noises in the phase lag influences viscosity measurements due to noise amplification of differential in phase-lag profiles. So, before the calculations are processed, noise reductions of phase-lag profiles are required to reduce viscosity scattering. When the phase-lag profiles are $N = 1$, the evaluated viscosity profiles are scattered with large difference from the true value (Fig. 6a). Since the noises in phase-lag profiles decreases by calculating arithmetic mean profiles in $N > 1$, histograms of the viscosity show higher accuracy and precision than that of $N = 1$ (Fig. 6b and c).

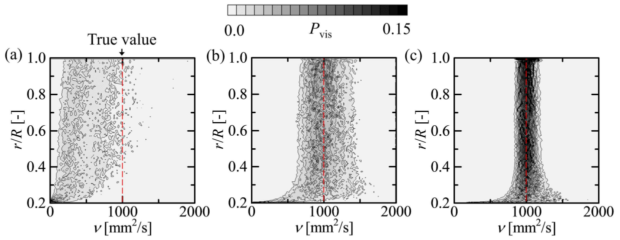

Figure 6: Histogram in probability density distribution of the viscosity at cases (a) $N = 1$, (b) $N = 80$, (c) $N = 320$

At noise amplitudes in different N, mode value (highest probability density distribution), +25% summation of the distribution from the mode value, and −25% of that are summarized in Table 1, where these results were averaged by $0.6 < r/R < 1.0$ and obtained from the viscosity. It indicates the accuracy of the viscosity depending on the averaging cycle times N. Arithmetic mean calculations are, however, limited when test fluids have constant rheological properties with changing shear rate (Newtonian fluid).

Table 1: Mode, +25%, and −25% values calculated from histograms of the viscosity, which are averaged by $0.6 < r/R < 1.0$

N	1	20	40	80	160	320
Mode [mm^2/s]	316	919	938	965	981	993
+25% [mm^2/s]	684	1122	1083	1051	1040	1032
−25% [mm^2/s]	-	695	754	818	919	952

4.2 Spectral subtraction method utilizing periodic functionalized algorithm

Considering noise reductions in phase-lag profiles obtained from instantaneous velocity fluctuations, it is expected that spectral subtraction method utilizing periodic functionalized algorithm is efficient. A restricting condition in both ends of the phase-lag profiles was given to apply the DFT filtering for the phase-lag profiles. The condition is a periodic functionalized formula, φ, which is defined as following formula (schematic details in Fig. 7a):

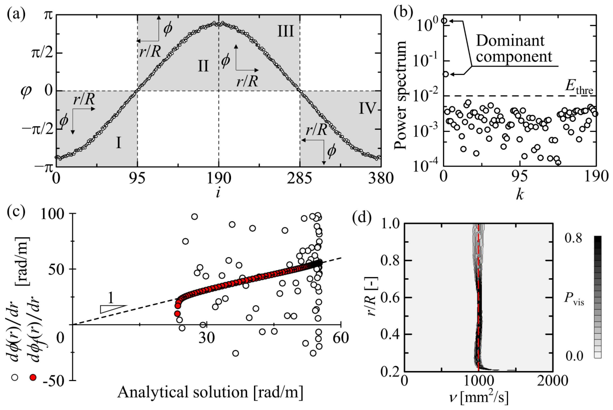

Figure 7: (a) Periodic function defined in Eq. 5, (b) power spectrum obtained from periodic function, (c) analytical solution versus spatial gradient of $\phi(r)$ and $\phi_f(r)$, (d) probability density distribution of the measurement from filtered phase-lag profiles

$$\varphi(i)=\begin{cases}-\phi_{X-i-1} & (\mathrm{I}: 0\le i<X)\\ \phi_{i-X+1} & (\mathrm{II}: X\le i<2X-1)\\ \phi_{3X-i-2} & (\mathrm{III}: 2X-1\le i<3X-2)\\ -\phi_{i-3X+3} & (\mathrm{IV}: 3X-2\le i<4X-4)\end{cases} \tag{5}$$

X indicates a total number of radial profiles. Power spectra in $\varphi(i)$ calculated by DFT have dominant Fourier components (Fig. 7b), where the power smaller than E_{thre} (= 10^{-2}) are regarded as additive noise components due to white noise characteristics. Removing the noise components on the spectra, the original phase-lag profiles $\phi(r)$ were filtered by inverse DFT. Comparing analytical solution with spatial gradients obtained from filtered phase-lag profiles $\phi_f(r)$ and $\phi(r)$, gradients of the filtered profiles are better agreement with the analytical solution than that of original profiles (Fig. 7c). By using this filtering process, the probability density distributions (Fig. 7d) indicate higher accuracy compared to the original histogram shown in Fig. 6a.

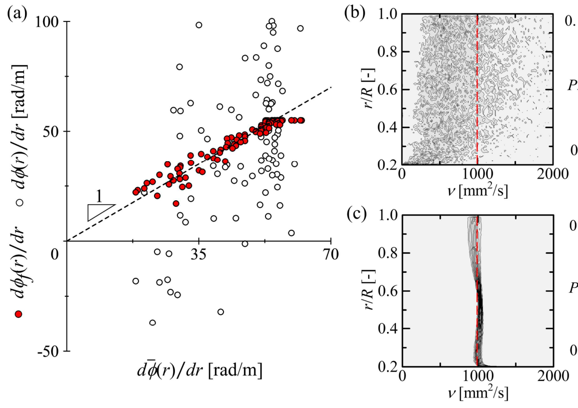

Figure 8: (a) Spatial gradient of $\bar{\phi}(r)$ versus $\phi(r)$ and $\phi_f(r)$ at each radial position, and probability density distribution of viscosity measurement from (b)$\phi(r)$ and (c)$\phi_f(r)$ in $\Delta t = 1$ s ($N = 500$) of viscosity measurement

Actual measurement results (silicon oil: 1000 mm²/s) were analyzed to confirm the applicability of this spectral subtraction method. $d\phi(r)/dr$ and $d\phi_f(r)/dr$ obtained from $N = 1$ were compared with $d\bar{\phi}(r)/dr$ (Fig. 8a), where $\bar{\phi}(r)$ was averaged by $N = 500$ times of phase-lag profiles. $d\phi_f(r)/dr$ has a correlation with $d\bar{\phi}(r)/dr$ compared to $d\phi(r)/dr$, therefore this filtering method can reduce the noises equal to or greater than the arithmetic mean calculation. Probability density distributions of the kinematic viscosity obtained from $d\phi(r)/dr$ and $d\phi_f(r)/dr$ were evaluated as shown in Fig. 8b and c. The precision of viscosity measurement from $\phi_f(r)$ became higher than that of $\phi(r)$, although silicon oil may not be given accurate kinematic viscosity value due to fluid quality and temperature control.

5. Summary

We estimated the accuracy of the rheological evaluation using phase-lag analysis. Artificial random noises with the normal distribution, which can represent actual velocity by estimating experimental noises in UVP, were produced. This production of artificial random noises can realize statistical evaluations from numerical calculations. Thus, it is possible to estimate the accuracy of the measurement system by iterative computing. The measurement noises of viscosity were caused by the noise of differential amplification in phase-lag profiles. To apply the spectral subtraction to the phase-lag profiles, the additive noises can be eliminated. These results were obtained from $N = 1$ ($\Delta t = 1$ s), so the filtering process is expected to be applied to complex fluids with instantaneously changeable rheological properties, such as polymer solutions, thixotro-pic fluids, and bubbly liquids. This can lead to highly accurate and real-time rheometry. As future prospects, the accuracy of another analytical procedure in USR will be validated by the iterative calculation using the artificial random noises assuming actual measurement errors.

References

[1] Divoux T, *et al.*: Shear banding of complex fluids, Annu. Rev. Fluid Mech., 45 (2016), 81−103.

[2] Takeda Y: Ultrasonic Doppler velocity profiler for fluid flow, Springer (2012).

[3] Shiratori T, *et al.*: Development of ultrasonic visualizer for capturing the characteristics of viscoelastic fluids, J. Vis., 16.4 (2013), 275−286.

[4] Shiratori T, *et al.*: Ultrasonic velocity profiling rheometry based on a widened circular Couette flow, Meas. Sci. Technol., 26 (2015), 085302.

[5] Tasaka Y, *et al.*: Estimating the effective viscosity of bubble suspensions in oscillatory shear flows by means of ultrasonic spinning rheometry, Exp. Fluids, 56 (2015), 1867.

[6] Shiratori T *et al.*: Rapid rheological characterization of a viscoelastic fluid based on spatiotemporal flow velocimetry, Exp. Therm. Fluid Sci., 71 (2016), 1−13.

[7] Yoshida T, *et al.*: Rheological evaluation of complex fluids using ultrasonic spinning rheometry in an open container, J. Rheol., 61.3 (2017), 537−549.

[8] Tasaka Y, *et al.*: Linear viscoelastic analysis using frequency-domain algorithm on oscillating circular shear flows for bubble suspensions, Rheologica Acta, 57.3 (2018), 229−240.

[9] Yoshida T, *et al.*: Rheological properties of montmorillonite dispersions in dilute NaCl concentration investigated by ultrasonic spinning rheometry. Appl. Clay Sci., 161 (2018), 513−523.

[10] Box GEP, *et al.*: A note on the generation of random normal deviates. Annu. Math. Statist., 29.2 (1958), 610-611.

[11] Matsumoto M and Nishimura T: Mersenne twister: a 623-dimensionally equidistributed uniform pseudo-random number generator, ACM TOMACS, 8.1 (1998), 3−30.

Implementation of a Staggered Trigger Algorithm by Velocity Difference Dealiasing Rules: Experimental Results

Fábio Rizental Coutinho[1], Cesar Yutaka Ofuchi[2], Andre Luis Stakowian[2], Flavio Neves Jr[2] and Rigoberto Eleazar Melgarejo Morales[3]

[1] Department of Electronic Engineering, Federal University of Technology-Paraná (UTFPR) Campus Toledo-PR 85902-490 Brazil
[2] Graduate School of Electrical Engineering and Computer Science (CPGEI), Federal University of Technology- Paraná (UTFPR), Avenida 7 de Setembro 3165, Curitiba, Paraná, Brazil
[3] Mechanical & Materials Engineering Postgraduate Program (PPGEM), Federal University of Technology- Paraná (UTFPR), Avenida 7 de Setembro 3165, Curitiba, Paraná, Brazil

The staggered trigger technique consists of alternating between a long and a short Pulse Repetition Time (PRT) to mitigate the range-velocity ambiguity. Two different flow velocities are estimated due to the two PRT. The difference of these two velocities is used to estimate in which Nyquist interval is the real flow velocity. This method was originally proposed for Doppler weather radar where velocity folding factors are restricted to 2 times the conventional maximum velocity of the short PRT. In this work the staggered trigger method using the velocity difference for dealiasing purpose is applied to a rotating cylinder flow. Experimental results show that the method can be applied to fluid engineering. Results also shown that this method achieves a finer temporal resolution relatively to other methods proposed, which makes it suitable to be applied in flows with fast velocity transitions. The performance of the technique was also evaluated on two different reception gain settings.

Keywords: staggered trigger, dealiasing, velocity aliasing, ultrasound velocity profiling.

1. Introduction

Ultrasonic Doppler velocity profiler (UVP) is a technique that estimates the velocity along the measurement line by using periodic short bursts of ultrasound. However, this methodology has its limitations regarding the maximum range that could be measured. Increasing the period between emissions can overcome the measurement range but with a proportional reduction in the maximum velocity measured. If flow velocity is higher than the maximum measurable velocity, then velocity aliasing occurs [1]. Dealiasing techniques may be used to solve this issue. The use of two transducers with dissimilar frequencies can be used to measure velocity unambiguously. Such method, was proposed by [2-4]. This technique combines the information of the velocity from each transducer in such a way that the whole system can be viewed as one, which frequency is the difference between the two transducers frequencies. There are velocity estimation algorithms that can avoid aliasing. In the velocity-matched spectrum analysis, a velocity spectrum is obtained by analyzing the shift in each pulse emission through iso-velocity lines [5]. Still, to further extend the maximum velocity this technique uses much more computer power compared to the conventional phase-shift estimator (PSE). If a high SNR condition is guaranteed, time-shift estimators such as cross-correlation (CC) [6] can be used. However, CC algorithms are more time consuming than the conventional PSE. Extended autocorrelation technique [7] combines PSE with CC estimation. The combination can reduce significantly the amount of computation. However, the processing time of this approach is still very high (approximately 55 times slower) than the PSE [8,9]. Staggered trigger (ST) or staggered PRT (Pulse Repetition Time) is characterized by using a non-uniform pulse repetition time. ST alternates the pulse emission with a short-time and a long-time period. Compared to multi-frequency, ST only needs one transducer and the computation power is comparable with the PSE. It was first introduced for blood flow measurement by Nishiyama e Katakura [10]. Later, it was extended for weather radar field [11-12]. Recently, Murakawa et al [13] adapted it to fluid engineering, implementing a higher flowrate measurement system. They reported that the velocity error of the practical system was too high to measure velocity directly. Thus, they used the ST velocity only to discover aliasing factor. However, this strategy still was not enough to deliver an accurate flow rate. Therefore, they have used a moving average filter and relaxed the velocity time resolution. The measurement configuration used a high number of pulse (N_{pulse}=512) for every velocity estimate, and velocity profile was obtained through averaging 1,000 instantaneous velocity profiles. They reported an error of -0.8% (N_{cycle}=8 at flowrate of 500 m^3/h) and maximum measured velocity of 6 times larger than the conventional UVP method [13]. Torres and Dubel [14] proposed a new algorithm for ST that uses the velocity difference from the velocities estimated by the long and short PRT to decide the velocity dealiasing factor. Their work was focused in weather radar and they showed that their method could measure velocity up to 3 times greater than the maximum conventional velocity regarding the long PRT. In a previous work [15], we adapted the methodology of [14] for fluid engineering. It was showed, by simulation, that the method proposed can reach even higher velocities than described in [14]. Simulation results of [15] also show that the technique can perform well with a short time resolution (N_{pulse}=50). In this work, the technique developed in [15] is applied in real flow: a rotating cylinder flow. A measurement system was developed to implement the ST

https://doi.org/10.7795/810.20190809

method. Results shows that the system can measure velocity up to 2 times higher than the conventional velocity regarding short PRT. Spatial velocity profiles estimated are obtained with a finer temporal resolution. Results are also tested under two different reception gain settings. The main purpose of this research is to develop a technique that: is computational comparable to the conventional PSE; can achieve temporal and spatial velocity resolution that is similar to the PSE; and can measure the same range of velocities of PSE but using a much longer PRT. A measurement system with similar performance of the conventional but using a longer PRT will imply in much less data to process resulting in a simpler acquisition hardware thus reducing the overall system cost. Another benefit is to achieve longer measurements range.

2. Staggered trigger by velocity difference method

2.1 Foundation of staggered trigger method

In ST, an ultrasonic pulsed wave is emitted in alternating time intervals, T_1 and T_2, with $T_2 > T_1$. Velocity estimation is evaluated by the lag one autocorrelation algorithm [7] using only adjacent pulses whose time interval is equal. The velocity relative to T_1, v_1, and the velocity relative to T_2, v_2, can be estimated using the following relations

$$v_1 = \frac{c}{4\pi f T_1} \arg\big(R(T_1)\big), \tag{1}$$

$$v_2 = \frac{c}{4\pi f T_2} \arg\big(R(T_2)\big), \tag{2}$$

respectively, where c denotes the sound velocity in the considered medium, f represents the transducer central frequency, arg is the principal argument restricted to the range (-π,π] and $R(\cdot)$ is the autocorrelation function. The maximum measured velocity is determined by the range of the principal argument as

$$v_{a1} = \frac{c}{4fT_1}, \tag{3}$$

$$v_{a2} = \frac{c}{4fT_2}. \tag{4}$$

Conventional ST method combines each lag one autocorrelation to result in a dealiased velocity estimated by

$$v_{st} = \frac{c}{4\pi f (T_2 - T_1)} \Big(\arg\big(R(T_1)\big) - \arg\big(R(T_2)\big)\Big). \tag{5}$$

And the staggered trigger maximum velocity will be

$$v_{max,st} = \frac{c}{4f(T_2 - T_1)}, \tag{6}$$

which will be higher than Eqs. (3) and (4) if $T_2 - T_1$ were small relatively to T_1 or T_2. However, velocity estimated using Eq. (5) will have a high uncertainty for some velocity intervals [15]. Therefore, to measure velocity above Nyquist limit, Eqs. (1) and (2) should be combined to discover the velocity aliasing factor.

2.2 Velocity difference by dealiasing rules

The $v_1 - v_2$ velocity difference can be used to determine the aliasing factor of v_1 or v_2 if the ratio $T_1/T_2 = m/n$, follow the condition that m and n should be relatively prime integers [14]. Applying this ratio, the maximum unambiguous velocity that can be measure are $v_{ua1} = m v_{a1}$ and $v_{ua2} = n v_{a2}$, for v_1 and v_2, respectively. The velocity difference rule can be demonstrated graphically. The velocity aliasing incurs that v_1 or v_2 cannot be higher than $\pm v_{a1}$ or $\pm v_{a2}$, respectively. By plotting the real velocity versus $v_1 - v_2$ the graph of Fig. 1 is obtained, for $m/n = 3/4$. Note in Fig.1, that, when v_1 is aliased, or $v_{a1} < v_1 < 3v_{a1}$, the velocity difference assumes two unique constant values ($-0.5v_{a1}$ and $+v_{a1}$). A similar behavior happens to negative aliasing in v_1, or the condition that $-3v_{a1} < v_1 < -v_{a1}$, in this case $v_1 - v_2$ assumes $+0.5v_{a1}$ and $-v_{a1}$. In the case of aliasing in v_2, one can notice (Fig.1) that for the first aliasing, i.e. when $v_{a2} < v_2 < 3v_{a2}$ (or $-3v_{a2} < v_2 < -v_{a2}$ for negative aliasing) the velocity difference assumes $2v_{a2}$ and $-0.5v_{a1}$ (or $-2v_{a2}$ and $+0.5v_{a1}$ for negative aliasing). When v_2 aliases for the second time, i.e. when $v_2 > 3v_{a2}$ (or $v_2 < -3v_{a2}$ for negative aliasing) then $v_1 - v_2$ equals to v_{a1} (or $-v_{a1}$ for negative aliasing). Therefore, $v_1 - v_2$ maps the aliasing factor in v_1 or v_2. In [14] it is shown that this function bijection occurs for any m/n, if m and n are relatively prime integers.

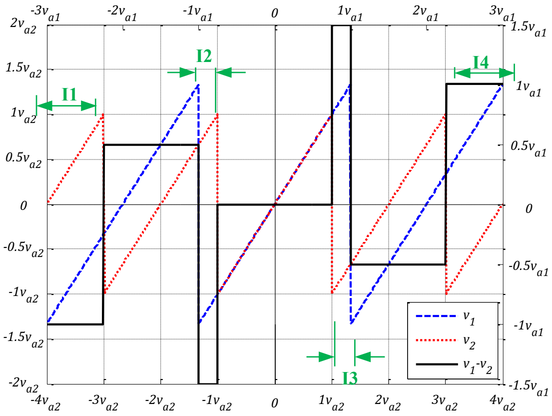

Figure 1: Velocity difference ($v_1 - v_2$) and aliased velocities v_1 and v_2 as a function of the real Doppler velocity. Time interval ratio used was $T_1/T_2 = m/n = 3/4$.

3. Experimental procedure

To evaluate the technique, a rotating cylinder flow experiment was set-up. A plexiglass cylinder was submerged in a water tank (Fig.2). The inner cylinder radius is 70 mm. Ultrasound transducer was positioned at *Δr=20 mm* from central axis (Fig.3). With this arrangement, Doppler velocity measured by the transducer will have a uniform velocity profile (Fig.3) [1].

Rotation is established through a motor/encoder from Maxon® EPOS2 24/5. Angular speed of the motor can be configured by a software, EPOS2® Studio (Maxon®), from a computer (PC). Ultrasound control and data acquisition is performed by a PXI system from National Instruments®,

https://doi.org/10.7795/810.20190809

model NI5752R. The PXI system is programed using Labview® software running in a PC. An Olympus® pulser/receiver, model 5077PR, is used for excitation and reception of ultrasound pulses from a 4 MHz transducer (Met-flow).

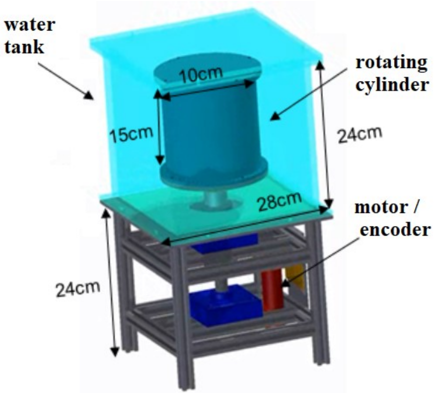

Figure 2: Rotating cylinder flow apparatus [16].

The pulser/receiver frequency was set to 1000 Hz (pulse repetition frequency). Pulse voltage used was 100 V. This pulser is limited to a 1-cycle pulse duration. Analog gain of 49 dB and 39 dB were used to amplify the echoes.

Sampling frequency of 50 MHz was set at the PXI system. A total of 2000 pulses or 2 seconds of data were recorded for each cylinder velocity tested. Cylinder rotations of 10 to 50 RPM in steps of 5 RPM were tested. A 0.5 g of nylon particles of 80 µm to 200 µm (EMS GRILTECH 1A P82), with 1.07 g/cm3 were added into the cylinder. Cylinder was filled with a density matching solution of water and glycerol. Sound velocity of the solution was characterized by having the value of 1680 m/s.

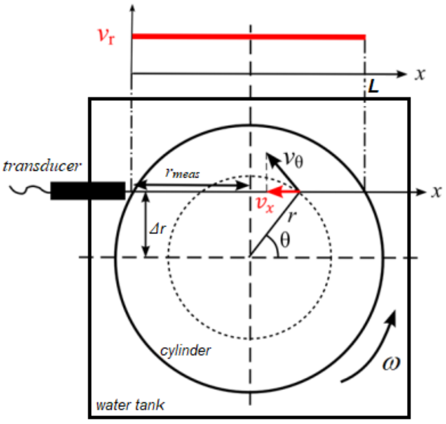

Figure 3: Top view of cylinder, transducer position and expected velocity profile. Adapted from [9].

3.1 Signal Processing

Each pulse was acquired with a fixed base frequency of 1 kHz resulting in a $T_{Base} = 1\,ms$ To achieve a PRT ratio of $T_1/T_2 = 2/3$, it was adopted the following method: $T_1 = 2T_{Base}$ and $T_2 = 3T_{Base}$. So, with all the 2000 RF pulses sampled (or 2 seconds of data), to transform this uniform sampled data to a non-uniform set, the system takes the first pulse, ignores the second pulse, takes the third pulse, ignores the fourth and fifth pulse and takes the sixth pulse repeating this procedure for all pulses.

Clutter filtering of a ST data cannot be done by a standard algorithm for uniform sampled data. Therefore, stationary echoes from cylinder boundaries were filtered using a polynomial regression filter technique described in [16]. The length of the polynomial regression filter used was $M_f = 30$. A second order polynomial was chosen.

Velocities data regarding each PRT (v_1 and v_2) were calculated every 50 emissions ($N_{pulse} = 50$). Dealiasing rules were applied to velocities estimated resulting in the dealiased velocities (v_{1d} and v_{2d}). By averaging each dealiased velocity the final flow dealiased velocity was obtained. The spatiotemporal velocity maps were post-processed using a median filter with 2x2 matrix size.

4. Results

To evaluate the performance of the ST, the mean value of the spatial velocity profile was calculated for PRT ratio $T_1/T_2 = 2/3$. In this case the maximum velocities are $v_{a1} = 52.5\,mm/s$ or 25.06 RPM and $v_{a2} = 35\,mm/s$ or 16.71 RPM. The mean value was computed for cylinder velocities from 10 RPM up to 50 RPM or from $0.3989v_{a1}$ up to $1.995v_{a1}$ (maximum velocity for 2/3 ratio is $2v_{a1}$ or $3v_{a2}$). Analog gain of the pulser was set to 49 dB and 39 dB. The technique provides a mean velocity value with error below ±5% for almost the entire range (Fig.5). Cylinder velocity of $1.995v_{a1}$ was the only value that the technique fails to measure. This behavior may be occurred because it is a velocity that is too close of the technique limit. Fig.5 also shows that the technique performance was similar considering the SNR reduction of 10 dB (39 dB).

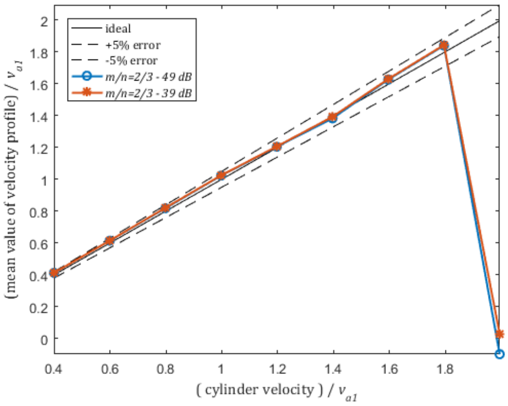

Figure 5: Accuracy assessment of ST for 2/3 ratio.

Accuracy performance of the ST was also assessed for the PRT ratio of $T_1/T_2 = 3/4$. In this condition the maximum velocities are $v_{a1} = 35\,mm/s$ or 16.71 RPM. The mean value was computed for cylinder velocities from 10 RPM up to 50 RPM or from $0.598v_{a1}$ up to $2.992v_{a1}$ (maximum velocity for 3/4 ratio is $3v_{a1}$ or $4v_{a2}$). Analog gain of the pulser was set to 49 dB and 39 dB. Results of Fig.6 indicate that, in this case, the technique fails before the theoretical maximum. At cylinder velocity of $2.693v_{a1}$ the error is far beyond the 5% error line. The condition is the same for 49 dB or 39 dB, possible showing that the

https://doi.org/10.7795/810.20190809

limitation is not on SNR.

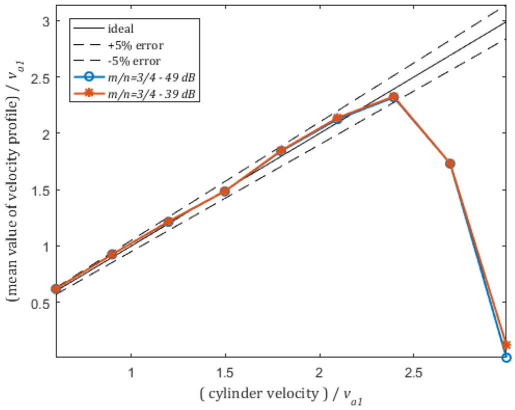

Figure 6: Accuracy assessment of ST for 3/4 ratio.

Spatial profile reproducibility is assessed in Fig. 7. It can be noticed that when velocity approaches 2 times Nyquist standard deviation (error bars) increases. Also, the polynomial regression filter fails to filter some stationary echoes from cylinder walls (x/L≈0.05 and x/L≈0.95).

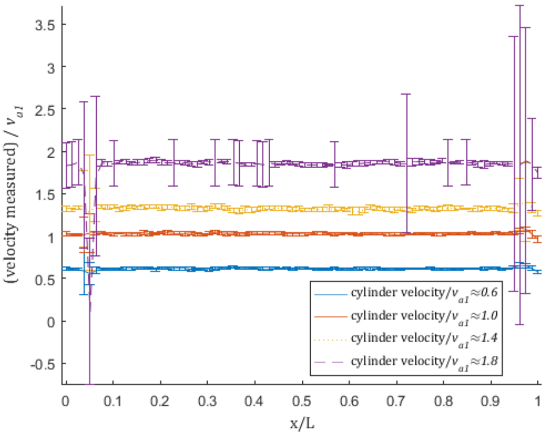

Figure 7: Spatial velocity profiles with errorbar (49 dB, 2/3 ratio).

A velocity temporal series for *x=0.08L* was obtained to evaluate the time accuracy of the technique. The average error relative (AER) to cylinder velocity (CV) and standard deviation normalized by v_{a1} (STD) is shown in Tab. 1.

Table 1: Temporal series accuracy results (49 dB , N_{pulse}=50).

CV/v_{a1}	0.6	0.8	1.0	1.2	1.4	1.6	1.8
AER (%)	2.4	2.6	3.0	-0.9	-3.7	1.9	3.2
STD	0.08	0.09	0.06	0.03	0.06	0.14	0.06

5. Summary

A Doppler measurement system and signal processing algorithms for ST were developed and tested in a real flow situation. Results shows that the system can measure velocities beyond Nyquist limit with accuracy of less than 5% for $T_1/T_2 = 2/3$. Also, the system can measure velocity with a reduced value of pulses ($N_{pulse} = 50$) or with a finer temporal resolution, thus enabling the system to be used for fast transient flow analysis. Increasing the ST ratio to $T_1/T_2 = 3/4$ showed that the accuracy of the mean velocity value degrades as it surpasses two times the maximum conventional velocity. Therefore, for the experimental conditions tested, the ratio of 2/3 would be the best choice for application of the technique proposed because it will result in accurate velocity profiles. In the previous work of [15] higher PRT ratios were feasible to use with good accuracy. We think that it might be related to the size of the measurement volume. In [15], the ultrasound was excited by a 4-cycle pulse that is four times larger than the excitation used in this work. In a future work, we intend to test the system in pipe flows. Also, we intend to investigate if exists a tradeoff between the number of cycles emitted and the PRT ratio concerning the accuracy of velocity profiles.

References

[1] Takeda Y: Ultrasonic Doppler fluid flow, Springer, (2012).

[2] Fer R, *et al.*: New Advances in colour flow mapping: quantitative velocity measurement beyond Nyquist limit. Br J Radio 64 (1991), 651.

[3] Nitzpon HJ, *et al.*: A new pulsed wave Doppler ultrasound system to measure blod velocities beyond Niquist limit. IEEE Trans Ultrason. Ferrroelec. Freq. Contr. 42 (1995), 265-279.

[4] Zedel L & Hay AE: Design and performance of a new Multi-frequency coherent Doppler profiler. 33rd IAHR Congress, 2009.

[5] Torp H & Kristoffersen K: Velocity matched spectrum analysis: a new method for suppressing velocity ambiguity in pulsed-wave Doppler. Ultrasound Med. Biol. 21(1995), 937-944.

[6] Jensen, JA: Estimation of blood velocities using ultrasound: A signal processing approach. Cambridge Univ. Press, (2006).

[7] Lai X & Torp H: An Extended Autocorrelation Method for Estimation of Blood Velocity, IEEE Trans. Ultrason., Ferroelec., Freq. Contr. 44 (2007), 1332-1342.

[8] Ofuchi, CY, *et al.*: Extended autocorrelation velocity estimator applied to fluid engineering, Proc. of the 9th ISUD, Strasbourg (2014), 109-112.

[9] Ofuchi C. Y. et al. Evaluation of an extended autocorrelation phase estimator for ultrasonic velocity profiles using nondestructive testing systems. Sensors. 16 (2016), 1250.

[10] Nishiyama H & Katakura K. Non-equally-spaced pulse transmission for non-aliasing ultrasonic pulsed Doppler measurement, J. Acoust. Soc. Jpn. 13, 4 (1992), 215-222.

[11] Franca MJ & Lemmin U: Eliminating velocity aliasing in acoustic Doppler velocity profiler data, Meas. Sci. Tech. 17 (2006), 313-322.

[12] Holleman I & Beekhuis H: Analysis and Correction of Dual PRF Velocity Data, J. Atmos. Ocean. Tech. 20 (2003), 443-453.

[13] Murakawa H, *et al.*: Higher flowrate measurement using ultrasonic pulsed Doppler method with staggered trigger. Proc. of ISUD9, Strasbourg (2014), 117-120.

[14] Torres SM & Dubel Y: Design, implementation, and demonstration of a staggered PRT algorithm for the WSR-88D. J. Atmos. Oceanic Tech. 21 (2004), 1389-1399.

[15] Coutinho, F. R. Implementation of a staggered trigger algorithm by velocity difference dealiasing rules. Proc. of ISUD10, Tokyo (2016), 45-48.

[16] Bostelmann P. Ultrasonic instrumentation for characterization of the process of hydrate formation. Msc Thesis. CPGEI – Federal University of Technology -Parana (2016).

[17] Torres S. M. & Zrnic D. S.. Ground clutter cancelling with a regression filter. J. Atmos. Ocean. Tech. 16 (1999), 1364-1372.

Flow Monitoring of Particle-laden Flows Combining Ultrasonic Doppler and Echo Intensity Profiling Techniques

Jumpei Hitomi[1,2], Shun Nomura[2,3], Giovanni De Cesare[2], Yasushi Takeda[4], Hyun Jin Park[1], Yuji Tasaka[1], and Yuichi Murai[1]

[1] Laboratory for Flow Control, Hokkaido University, N13-W8, Kita-ku, Sapporo, Hokkaido 060-8628, Japan
[2] Ecole polytechnique fédérale de Lausanne EPFL, Plateforme de constructions hydrauliques PL-LCH, Station 18, CH-1015 Lausanne, Switzerland
[3] Mathematical Science and Advanced Technology, JAMSTEC, Yokohama Institute of Earth Sciences, 3173-25 Showa-machi, Kanazawa-ku, Yokohama 236-001, Japan
[4] Laboratory for Food Research Engineering, Swiss Federal Institute of Technology Zurich, Zurich 8092, Switzerland

The methodology to reveal inner structures of turbidity currents are required. Their behaviors have important roles to affect the sedimentation or transportation of fine particles. We have proposed a novel monitoring methodology for flows containing fine particles, combing Doppler velocity and echo information obtained from ultrasonic velocity profiler (UVP). In this study, we captured the relationship between the echo profiles and particle number distributions. To simplify turbidity currents, stirring flows in a cylindrical container were chosen. As suspended particles, quartz particles with 13.5 μm in the central diameter was examined. In a certain range of quartz volume fraction α, UVP can detect integral echo signals obeying Rayleigh scattering and Doppler-shift frequencies, although the quartz diameter is much smaller than ordinary tracer particles adopted for UVP. The echo distribution of $\alpha = 1\%$ showed that the stirring flow causes the local particle number distributions. Moreover, the possibility to reconstruct particle number distributions from echo amplitude distributions was indicated.

Keywords: Echo intensity, Particle-laden fluid, Particle number density distribution, Solid-liquid two-phase flow, Rotational flow

1. Introduction

In the hydraulic industry, liquid-solid two-phase flows which contain solid particles have important roles to utilize aquatic resources. For example, collecting minerals and fossil fuels under the sea and transportation or sedimentation mechanisms of solid particles in reservoirs have been paid attention to. An example of them and main topic of our research group is turbidity currents [1-3] which are gravity currents driven by the density difference between particle-laden fluid and ambient fluid. They have complicated flow structures due to turbulence and complex interaction caused between each particle. They show local mixture density fluctuation accompanying clusters and clouds of particles, which is hardly investigated by optical approaches and numerical simulations. Our research group, therefore, has proposed the direct monitoring methodology of such particle-laden flows using ultrasonic technique. Ultrasonic velocity profiler (UVP) [4] can be applied to opaque fluids and measure the spatio-temporal velocity distributions using frequency veering based on Doppler effects. In addition, echo signals which are reflected waves scattered by suspended particles give us beneficial information on particle number distributions. In past studies, scattering processes from clouds of fine particles are researched [5, 6]. Even echo signals obtained from UVP could be used to detect moving interfaces of multi-phase or multi-layer flows [7, 8]. In addition, they were applied to obtain the profiles of suspended sediment concentration [9] and to measure void fractions [10]. Combining two distributions of Doppler velocity and echo information, a novel monitoring methodology for turbidity currents expects to be established.

The objective of this study is to reveal relationship between number density distribution of fine particles and echo information. Stirring flows in a cylindrical container were chosen to simplify particle-laden flows like turbidity currents. As suspension particles, quartz particles with order of 10 μm in the central diameter are examined. This range of particle diameter is less than one-tenth the ultrasonic wavelength of central frequency 4 MHz in water, so Rayleigh scattering, which is almost isotropic scattering, occurs. They are not used for UVP measurement basically, because the intensity of reflected waves from a quartz particle is too small to be detected by ultrasonic transducers. It was, therefore, another objective to elucidate the flow conditions and the volume fractions of the quartz particles that UVP can measure reasonable velocity distributions of particle-laden flows.

2. Experiments

2.1 Experimental setup

The experimental setup is shown in figure 1. The experiments were conducted in a cylindrical container with 100 mm outer diameter, and 3 mm thickness of lateral wall and 120 mm height. The cylinder is made of acrylic resin and filled with test fluids containing the fine particles. The cylinder does not have a lid and thus top of fluid layer is free surface. The cylinder was mounted inside the water jacket to keep uniform temperature and allow transmission of ultrasonic wave from the outside of

https://doi.org/10.7795/810.20190809

the cylinder. The flow was driven by a stirrer with 60 rpms in the rotational speed, and a stirring bar dipped into the bottom of the cylinder.

Velocity distribution and echo information were measured by UVP. The obtained ultrasonic signals reflected from clouds of particles were processed by UVP monitor model Duo (Met-Flow S.A.) into spatio-temporal distributions of Doppler velocity and echo information. An ultrasonic transducer with 4 MHz central frequency was fixed in the jacket with a horizontal displacement 10 mm from the center line. This off-axis measurement makes it possible to obtain the velocity component including not only radial but also azimuthal velocity component. In case of rigid body rotation, the obtained velocity components show uniform profile along the measurement line. The advantage of this method, therefore, is that flow structures can be imagined from obtained velocity distributions relatively easily and reconstructed assuming axisymmetric flow field. The transducer was set at 25 mm from the bottom of the cylinder to avoid the blind of ultrasonic propagation due to the free surface. Table 1 summarizes the setting parameters of UVP measurement. Especially, amplification is important parameter in this study. Both values of “gain start” and “gain end” were fixed at constant values not to amplify the echo value depending on the distance from the transducer.

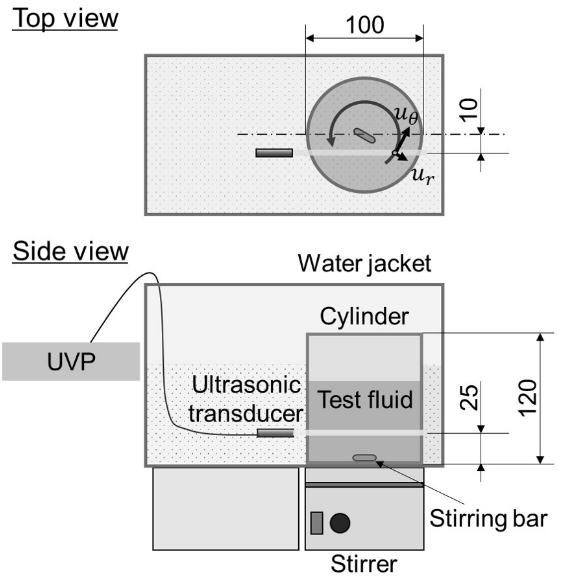

Figure 1: Schematic diagram of experimental setup and arrangement of the measurement line.

2.2 Test fluid

In this study, quartz (Quartz K13, Carlo Bernasconi AG) which is often used as laden particles of experimental turbidity currents was examined. Quartz has particle size distribution and the central diameter is 13.5 μm, and density equals to 2650 kg/m^3. It is predicted that Rayleigh scattering, which is almost isotropic scattering, occurs in the test fluids, because quartz diameter is less than about one-tenth the ultrasonic wavelength of central frequency 4 MHz in water. The cylinder was filled with 500 mL of tap water and quartz was added based on each volume fraction α. Total seven cases with different volume fractions α = 0, 0.01, 0.1, 1, 5, 10, and 15% were conducted.

Table 1: Setting parameters of UVP.

Central frequency	4	MHz
Temporal resolution	10	ms
Spatial resolution	0.74	mm
Velocity resolution	4.75	mm/s
Number of cycles	4	-
Number of repetitions	32	-
Amplification (gain)	6-6	-

3. Results and discussions

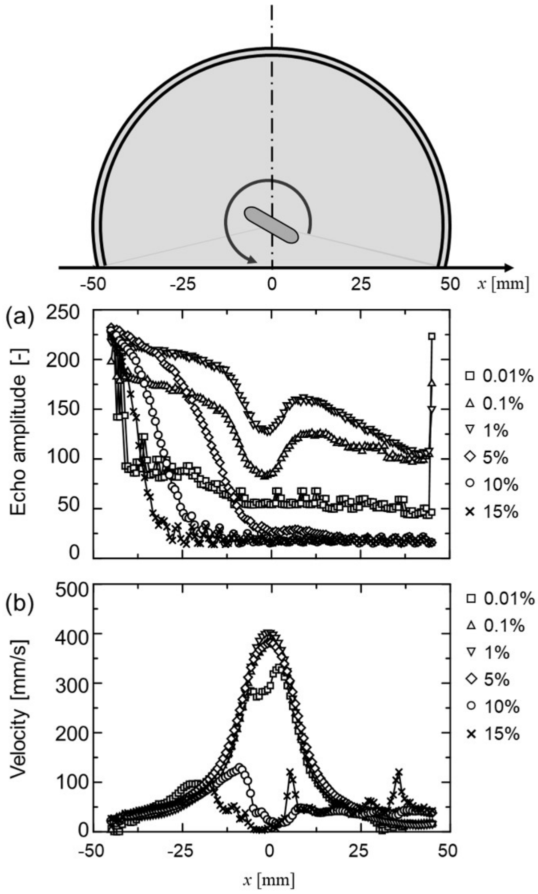

Figure 2: Distributions of time-averaged value of each volume fraction; (a) echo amplitude and (b) Doppler velocity distribution.

Firstly, we tried to comprehend the trends of echo distribution measured in this setup. Figure 2 (a) shows the echo amplitude profiles obtained by UVP in each case. The measurements were conducted for 40 s after the flows reached adequate developed states, and the corresponding number of the velocity profiles for time-averaging is 4000. These echo amplitudes were calculated as the absolute values of difference from background ($\alpha = 0\%$) UVP echo values. In this figure, x axis indicates the distance from the center of the cylinder and the ultrasonic measurement direction is from left to right side. As the volume fraction becomes larger in the cases of $\alpha = 0.01$, 0.1, and 1%, echo amplitude values are getting lager. Their echo amplitudes of these cases show large values on the opposite side from the ultrasonic transducer because of the reflection from the wall. In contrast, the reflected waves from the wall disappears under the conditions $\alpha \geq 5\%$ due to the attenuation of ultrasonic waves and the attenuation is getting larger depending on their volume fractions. Figure 2 (b) shows velocity distributions measured by UVP. These velocities show the components of the measurement direction that contain the azimuthal and radial velocity components. In the cases of $0.1 \leq \alpha \leq 5\%$, reasonable velocity distributions can be observed. In this study, the velocity profiles measured with usual tracer particles (DIAION HP20SS, Mitsubishi Chemical, diameter 60 - 150 μm, density 1020 kg/m^3) is defined as correct distribution, and "reasonable velocity distribution" means having good agreement with the correct distribution. The velocity profiles of $0.1 \leq \alpha \leq 5\%$ have an accuracy that has a high cross-correlation value exceeding 0.95 for the correct distribution. The cases of $\alpha = 10$ and 15%, however, do not show the reasonable velocity distributions. It seems that the attenuation of ultrasonic waves prevents the detection of echo signals by the ultrasonic transducer. In addition, the case of $\alpha = 0.01$ shows a notable result. The velocity values of this case drop irregularly near the center of the cylinder. This phenomenon implies that the amount of quartz particles is much fewer than wall side due to the centrifugal force. As known from the velocity distribution, high velocity values can be observed near the center. As the distance from the center becomes longer, the velocity values are getting smaller. From these distributions, the existence of a free vortex is indicated. The density of quartz is about 2.65 times larger than that of water, so it is possible that particles are blown from the center to near the wall sides by the centrifugal force. These phenomena are indicated by echo distributions too, because their values also drop near the center under the cases of $\alpha = 0.1$ and 1%.

Basically, UVP measurements are applied to flows containing tracer particles with adequate size, density, and concentration to reflect ultrasonic waves. However, the concentrations of particles in these experiments are relatively larger in comparison with the flows of normal UVP measurements. The experimental results for $0.1 \leq \alpha \leq 5\%$ show reasonable velocity distributions. This range of particle concentration, therefore, might be useful to detect integral echo signals obeying Rayleigh scattering. That is why UVP can obtain velocity distribution, although quartz diameter is much smaller than tracer particles.

To reveal the particle number distributions, a supplemental experiment was conducted. The mean volume fraction α was fixed at 1%, because the echo amplitude dramatically dropped near the center comparing to other conditions and reasonable velocity distributions could be obtained. In this experiment, the stirrer worked in the same manner as previous experiments until 20 s. After 20 s later from start of the measurement, the stirrer was turned off. The results of echo amplitude and velocity distributions are shown in figure 3. The velocity distribution shows that the free vortex near the center disappeared immediately after turning the stirrer off. The echo amplitude distribution, moreover, dramatically changes. During the time from 20 to 40 s, homogeneous dispersion of the quartz particles can be assumed, because it had been completely mixed for the first 20 s. During the first 20 s, the low echo region exists near the center. In contrast, that band near the center disappears after 20 s later, and the echo values measured in the far region from the ultrasonic transducer becomes smaller than that of the first 20 s. As the result of this experiment, it is revealed that not only velocity but also echo distribution were changed dramatically depending on the motion of stirrer. It seems that the change of flow velocity induces the local particle number distribution.

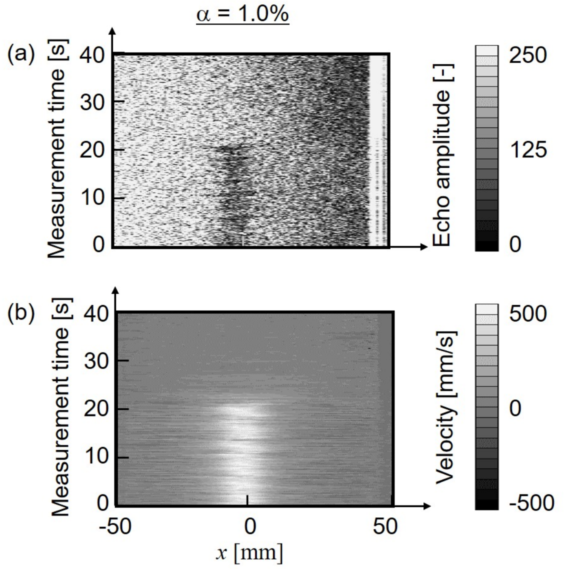

Figure 3: Spatio-temporal distribution of (a) Echo amplitude and (b) Doppler velocity when stirrer was turned off at 20 s later.

To evaluate the relationship between echo amplitude and particle number distribution, time-averaged values of echo amplitude of two cases were calculated. The first is averaged values of the first 15 s and the second is that of the last 15 s. These results are shown in figure 4. The figure 4 shows the characteristic distribution of echo values. The echo values measured in the first 20 s are larger than that of the last 20 s near the both walls, roughly $|x| > 15$. In contrast, the echo values measured in the first 20 s drop sharply near the center. This trend of the echo distribution seems to be related to the particle number distribution. That is to say, the stirring flow causes the free vortex and it blows particles from the center to near the wall sides due to the centrifugal force.

The echo amplitude ratio at two conditions are shown in figure 5 (a). In this graph, the range of x axis shows from 0 to 45 mm which is far side from the ultrasonic transducer. To capture the characteristics of the flow field, Shiratori *et al.* [11] had established the methodology to obtain two velocity components of azimuthal and radial direction assuming axisymmetric flow field. The two velocity components obtained by this methodology are shown in figure 5 (b). In these profiles, the azimuthal velocity is dominant in the cylinder. Range of the lower echo amplitude ratio shown in figure 5 (a), roughly $0 \leq x \leq 15$ mm, corresponds to relatively higher azimuthal velocity range.

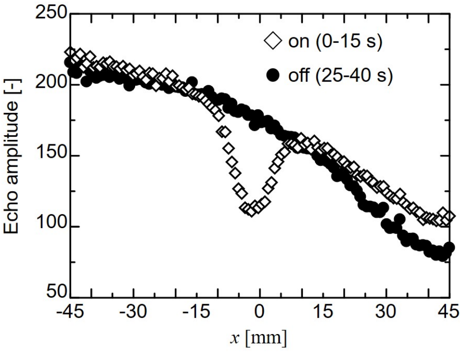

Figure 4: Time-averaged echo amplitude of each case

It would be possible to reconstruct the particle number distributions from echo amplitude ratio. Echo intensity values are the resultant values after some interactions between ultrasonic waves and media including the particles and water, such as attenuation, scattering, and so on. Theoretical models and equations are required to establish the methodology and its applicable range, which can reconstruct particle number distributions.

4. Conclusions

This study revealed the relationship between echo information and number density distribution of fine particles which are much smaller than the wavelength of emitted ultrasonic wave. UVP was applied to particulate rotating flows driven by a stirrer in a cylindrical container. As suspension particles, quartz particles with order of 10 µm in the diameter are examined. Although this range of particle diameter is smaller than ordinary tracer particles adopted for UVP, reasonable velocity distributions could be obtained under the condition where the volume faction of particles α is from 0.1 to 5% due to the detection of the integral echo signals which obeys Rayleigh scattering. Paying attention to the echo distribution observed at α = 1%, the trend of particle number distribution in the cylinder was newly explored. As the result of the experiment, it was confirmed that the range of lower echo amplitude ratio corresponded to the range such that azimuthal velocity is relatively large. It is therefore inferred that the free vortex containing the dominant azimuthal velocity components relates to the local particle number density, which can be predicted from echo amplitude distribution. As the future work, the theoretical models and equations describing the model are required to establish comprehensive methodology to reconstruct particle number distributions from echo values.

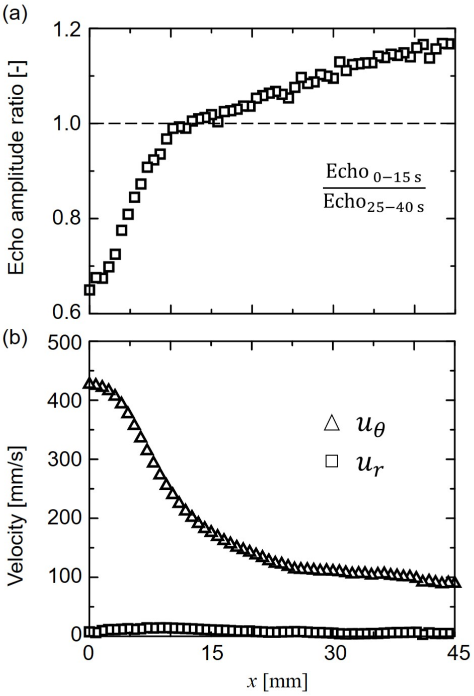

Figure 5: (a) Profiles of echo amplitude ratio at two conditions and (b) profiles of the azimuthal and radial velocity component.

References

[1] Altinaker MS *et al.*: Flow structure in turbidity currents, J. Hydraul. Res., 34 (1996), 713-718.

[2] Simpson, JE: Gravity currents in the environment and the laboraotory, Cambridge University Press, London, (1997).

[3] De Cesare G *et al.*: Experiments on turbidity currents influenced by solid and permeable obstacles and water jet screens, ISUD6, (2008).

[4] Takeda Y: Ultrasonic Doppler velocity profiler for fluid flow, Springer, (2012).

[5] Thorne PD & Hanes DM: A review of acoustic measurement of small-scale sediment processes, Cont. Shelf. Res., 22 (2002), 603−632.

[6] Lee TH & Hanes DM: Direct inversion method to measure the concentration profile of suspended particles using backscattered sound, J. Geophys. Res., 100 (C2) (1995), 2649−2657.

[7] Murai Y *et al.*: Ultrasonic detection of moving interfaces in gas–liquid two-phase flow, Flow Meas. Instrum., 21 (2010), 356-366

[8] Hitomi J *et al.*: Ultrasound flow-monitoring and flow-metering of air–oil–water three-layer pipe flows, IEEE access, 5 (2017), 15021-15029.

[9] Pedocchi F & García MH: Acoustic measurement of suspended sediment concentration profiles in an oscillatory boundary layer, Cont. Shelf. Res., 46 (2012), 87−95.

[10] Murai Y *et al.*: Development of an ultrasonic void fraction profiler, Meas. Sci. Technol., 20(11), (2009), 114003.

[11] Shiratori *et al.*: Development of ultrasonic visualizer for capturing the characteristics of viscoelastic fluids, J. Vis., 16 (2013), 275–286.

https://doi.org/10.7795/810.20190809

11th International Symposium on Ultrasonic Doppler Methods for Fluid Mechanics and Fluid Engineering
Berlin, Germany (5-7. September 2018)

Application of Ultrasound Doppler Technique for In-Vitro Flow Visualization of Human Swallowing

Johan Wiklund[1,2], Waqas Mohammad[2], Reinhardt Kotzé[1,2] and Mats Stading[2]

[1] Incipientus Ultrasound Flow Technologies AB, Frans Perssons Väg 6, 412 76 Göteborg, Sweden
[2] RISE- Research Institutes of Sweden, Frans Perssons Väg 6, 412 76 Göteborg, Sweden

Swallowing disorders, known as “Dysphagia” is a growing global problem and it is estimated that dysphagia affects roughly 8% of the world population. The number of aged people with Dysphagia has increased in the world with the advent of an aging society. Dysphagia can be the consequence of several pathologies, such as throat and neck cancer, stroke, dementia, or other neurodegenerative conditions and Dysphagia patients are not capable of controlling laryngeal closure, and therefore often aspirate liquid foods. The aspiration problem is especially caused by low viscosity foods as they are easily deformed during swallowing. The bolus is formed in the mouth under the pressure produced by the tongue surface, moving toward the hard palate, which results in the formation of a bolus and a downward flow. The bolus is subjected to large shear rates as it flows down into the pharynx via a peristaltic motion. It is important to be able to study the flow properties of liquid foods during human swallowing in order to develop innovative foods for dysphagia patients. At the moment the only tools available in clinical examination of dysphagia are manometry, which is invasive, and video-fluorography, which exposes the patients to radiation. In this work an in-vitro device which mimics human swallowing was developed and equipped with a novel ultrasonic velocity profiling (UVP) sensor to study the flow properties of liquid in the same way as during in-vivo experiments but non-invasively and without using any contrast media.

Keywords: Dysphagia, human swallowing, Gothenburg Throat Model, Ultrasonic Velocity Profiling, rheology, non-Newtonian

1. INTRODUCTION

Dysphagia is referred to the condition when individuals fail to adequately transfer food and liquids from mouth to the stomach. Dysphagia is often noticed in patient’s suffering from neuro disorders such as; Parkinson’s disease, Alzheimer diseases, brain damage and head injuries etc. [1] Symptoms of dysphagia is more common in aging population due to diminished co-ordination between the muscles involved to undergo the swallowing process in a normal way [2]. According to estimates dysphagia effects 8% of the world population and the condition is projected to increase due to increase in elderly population [3].

People suffering from dysphagia cannot handle the fast flow of fluids through their oropharynx due to eddies and vortices formation. Such individuals are restricted to textured modified diet. Texture modification is commonly performed by either using gum or starch thickened fluids. Both gum and starch-based thickeners differ in the way they increase consistency. Starch based thickener swells upon hydration while a gum-based thickener arrests water forming network in the solution upon hydration [4]. In either case the fluid becomes highly shear thinning, that is the viscosity becomes shear thinning. Clinically, dysphagia is diagnosed by either video-fluoroscopy or manometry. Video-fluoroscopy is based on adding contrast media typically barium or iodine based to enhance visualization while in manometry a catheter with pressure sensors is inserted into patients’ airways. Both the methods are invasive and often lead to inconsistent results [5]. Based on a patient’s response to a given consistency of a liquid from clinical diagnosis, a certain consistency is recommended often following American National Dysphagia Diet (NDD, 2002) standards. The scale characterized fluids from thin (1-50mPa.s) to pudding (>1750 mPas) consistency at 25C and shear rate 50s^{-1}. A patient recommended for honey-consistency liquid might still aspirate due to unexpectedly high shear rates in swallowing process thereby reducing the consistency to a different range on the scale. Accurate shear rate prediction in swallowing is extremely difficult due to complex pharyngeal geometry and nature of swallowing process. Transit time of bolus flow in pharynx is typically <1 second and swallowing can be considered as batch process with a time interval of 1-10 seconds between individual swallows. Performing such experiments using in-vivo experiments leads to both ethical issues and patient’s discomfort. Numerical simulations used to determine the shear rate distribution in pharynx assumes highly idealized conditions such as; homogeneity, Newtonian consistency and isotropy which is not analogous to the actual biological process. Hence an in-vitro simulator in which the bolus can be deformed in the same manner as in actual bio-processes is greatly needed. This paper presents the measurements using ultrasound velocimetry in maltodextrin with three different viscosities. This work is the first step to verify the UVP technique by using high speed camera images. Continuous and bolus flow was tested using the UVP technique.

2. METHODS AND APPARATUS

2.1 The Gothenburg Throat Model

In this work an in-vitro device which mimics human swallowing was developed, the so-called “Gothenburg Throat Model”. A detailed description of the in-vitro swallowing simulator has been submitted for publication elsewhere, [6-7], and an overview is given below. The model consists of a fluid storage tank and a syringe with circular cross section for bolus delivery that can inject a

https://doi.org/10.7795/810.20190809

specified volume of liquid, up to 20 ml. The pharynx in the model is elliptical with a length ~6.3 cm and a width of 2.8-3 cm at the largest measure and a circular entrance area of 314 mm² (20 mm diameter). The model was 3D printed from Accura ® Clear vue™ due to its suitability for usage in medical models, transparency for fluid flow visualization and liquid resistance. The Gothenburg Throat Model is shown in Figure 1. The model has similar geometry to the human pharynx, simulation of closing of the vocal chords and the upper esophageal sphincter, opening and closing of the epiglottis and the opening to the nasopharynx. The Gothenburg Throat is equipped with sensors for monitoring of bolus velocity profile during swallowing, temperature control and pressure measurement at different locations of interest e.g. at the entrance of pharynx, mid-pharynx, nasopharynx and UES. The pharynx channel is transparent for visual observations and high-speed camera measurements.

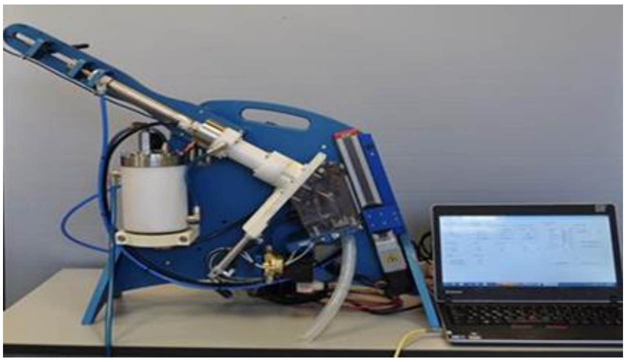

Figure 1: Photo of the Gothenburg Throat Model.

2.2 Flow visualization and Bolus flow measurements using high-speed camera

A high-speed camera (Sony, DSC-RX100M5) was installed at 50 cm from the flow model and was used to capture the bolus flow and images were captured at 500 frames per second. The bolus was color dyed blue for better contrast and it was ensured that the color addition did not influence bolus rheology. A linear ruler was attached to the model to determine the true velocity of the bolus flow from the high-speed camera photos. The determined velocities were used to validate the UVP measurements and to optimize the time delay settings for the valves in the model and the syringe to accurately mimic the human swallowing process.

2.3 Flow visualization and Bolus flow measurements using ultrasonics

The Incipientus system is a commercial and fully integrated platform for high resolution Doppler measurements as well as in-line rheometry. It features 2 transmit/receive (TX/RX) channels that can work in stand-alone or pitch-catch configuration. The transmitters, based on an Arbitrary Waveform Generator (AWG), can produce bursts, typically at 30-80 Vpp with a frequency of 5 MHz. The inputs are amplified with Time Gain Control (TGC) units featuring a gain up to 55 dB, converted to digital at 16-bit 100 MS/s, and processed in an FPGA. The FPGA include coherent demodulators, filters and an FFT processor for spectral analysis [8-9]. The base frequency of the non-invasive ultrasound transducer was 5 MHz, and 5 cycles per pulse were used for velocity profile measurements. The Gothenburg Throat was equipped with a novel Flow-Viz sensor (Incipientus AB, Sweden) to study the flow properties of liquid in the same way as during in-vivo experiments but non-invasively and without using any contrast media. The non-invasive UVP sensor set-up is shown in Figure 2. The ultrasonic beam passes through the polycarbonate material of the model into the actual fluid flow (Fig. 1) which means that it will be refracted at each interface. The Doppler angle inside the model cavity was determined using a combination of the angled Flow-Viz and a reference 90° ultrasound beam. The RF data time delay differences were used to determine the Doppler angle of 59.5° and ellipse short axis radius 8.4mm. An average of 8192 and 128 pulses were used to determine the velocity profiles in continues and bolus flow respectively. The sound velocity in maltodextrin was determined to be in the range 1486-1492 m/s.

Figure 2: Photo of the customized UVP sensor measuring the flow of ketchup inside the pharynx.

2.4 Materials

In this work, three aqueous solutions of maltodextrin with viscosities of 0.78 Pa.s, 1 Pa.s and 1.7 Pa.s were used to validate the flow in the pharynx of the Gothenburg Throat Model. The maltodextrin was dyed blue using a commercial food dye for the high-speed camera measurements to improve the contrast.

2.5 Experimental procedure for continuous- and bolus flow measurements

In the continuous flow experiments, the maltodextrin solutions were continuously pumped from a tank using a rotatory lobe pump (Sterilobe SLAS; Johnsons Pumps, Lanarkshire, UK) through the Gothenburg Throat Model in a closed circulation system using 1” flexible PVC hoses to ensure that the entire model was filled with the fluid. The valves on the trachea and nasal cavity were closed during all tests. The ultrasound transducer was attached to the model using a specially designed holder to ensure firm contact between the transducer face and the model. The position of the UVP sensor can be adjusted vertically as it is mounted on a high-precision linear axis equipped with a stepper motor. but it was installed at a fixed position in the center of the pharynx for all the measurements reported in this work. Continuous flow experiments were carried out at two different pump speed settings, corresponding to two different flow rates, 5 L/min and 10 L/min. In the bolus experiments a total volume of 15 ±1.2 ml was injected for each bolus. The temperature of the fluid was monitored during the experiments within 20.5˚–22.0˚C.

3. Results

Figure 3 shows high-speed camera images of maltodextrin bolus flow in the pharynx. As can be seen from the obtained photos the model can be used to deliver bolus with realistic velocity that will not break up during swallowing if the viscosity exceeds a certain value. The bolus velocity was determined to be in the range of 0.03 m/s to 0.08 m/s, using the camera and image processing software. This is in good agreement with velocities reported in clinical studies in the literature for bolus flow.

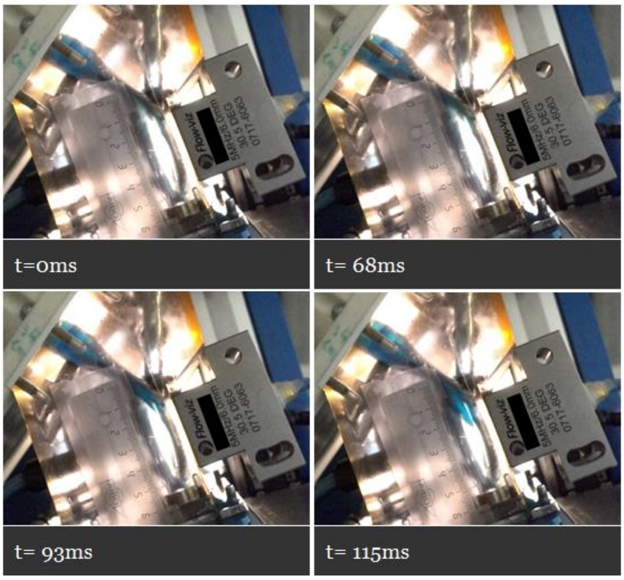

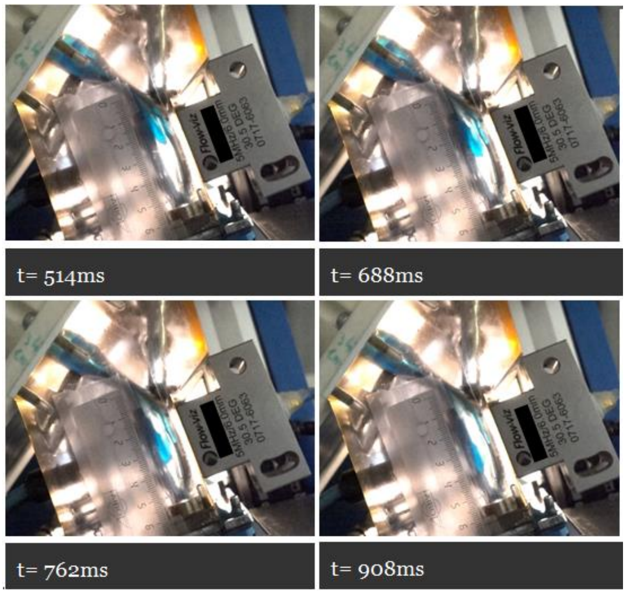

Figure 3: High-speed camera images of maltodextrin bolus flow in the pharynx, after 93ms up to 908ms.

Figure 4 shows and example of a velocity profile (Doppler spectra) of maltodextrin measured in continuous flow in the pharynx. A total of 8192 pulses were used to plot the Doppler spectra and to calculate the corresponding velocity profile. The acquired maximum velocities from the camera images was 0.044-0.049 m/s, which is in good agreement to the ones noticed in clinical studies and the maximum velocities measured by UVP, 0.042-0.048 m/s.

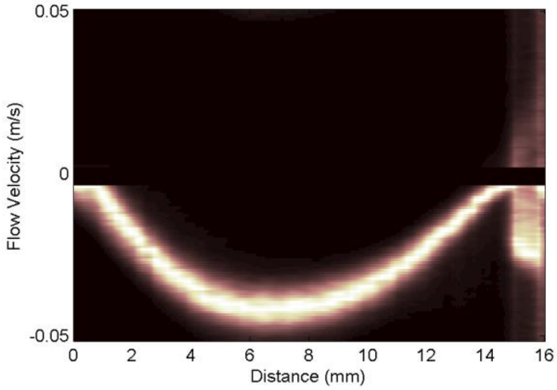

Figure 4: Velocity profile of maltodextrin measured in continuous flow in the pharynx.

Figures 5 shows examples of a velocity profiles (Doppler spectra) of maltodextrin bolus flow in the pharynx at three different viscosities ranging from 0.78 Pa.s, 1 Pa.s and 1.7 Pa.s. Due to the quick swallowing a total of 128 pulses were used to plot the Doppler spectra and to calculate the corresponding bolus velocity profile. Practically this means that high transmission and sampling frequencies must be used for UVP measurements in e.g. the pharynx model. The shapes of the measured bolus velocity profiles are not axis symmetric, which is expected due to the geometry of the pharynx. The shape of the measured profiles did not change significantly with increasing viscosity. This is however expected since the maltodextrin solutions showed Newtonian flow behavior. However, the magnitude of velocities showed good agreement with camera technique.

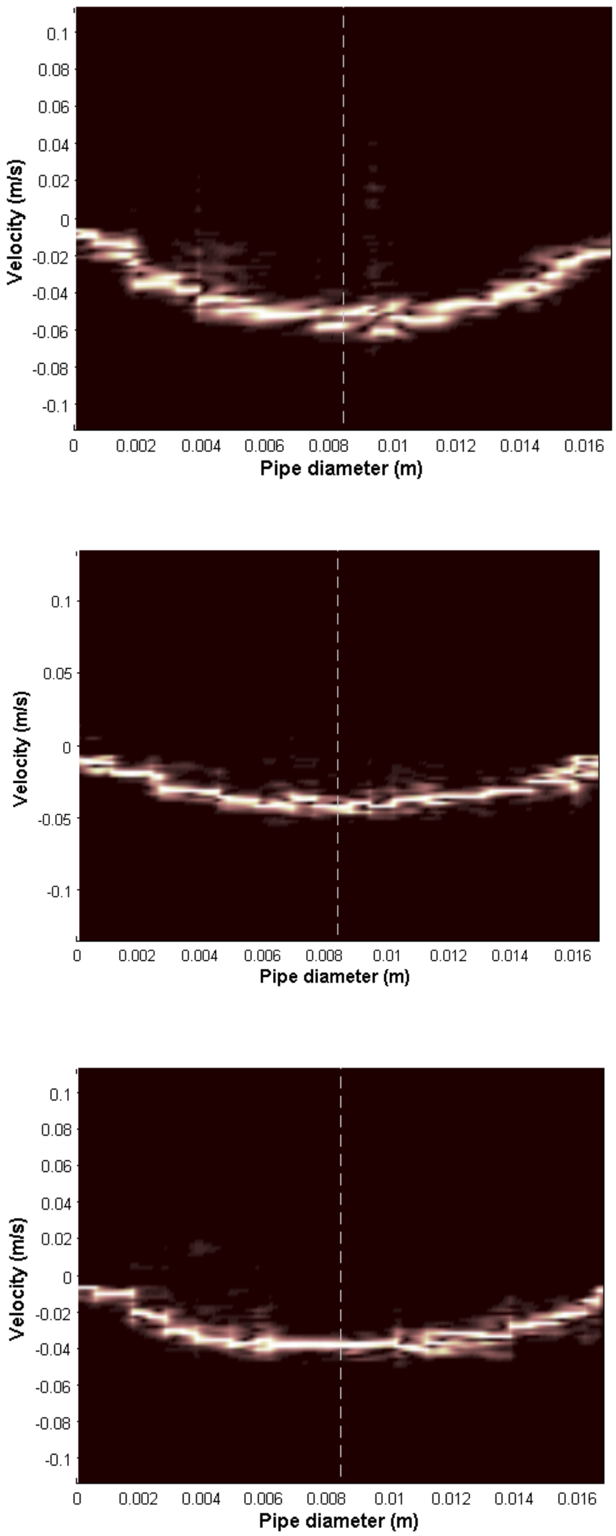

Figure 5: Velocity profiles of 0.78 Pa.s (top), 1.0 Pa.s (middle) and 1.7 Pa.s (bottom) maltodextrin bolus flow in the pharynx.

4. Summary

In this work an in-vitro device which mimics human swallowing was developed, the so-called “Gothenburg Throat Model”. The model was equipped with high-speed camera, several pressure and temperature sensors and a novel ultrasonic velocity profiling (UVP) sensor to study the flow properties of liquid in the same way as during in-vivo experiments but non-invasively and without using any contrast media. The high-speed camera measurements showed that the model can be used to deliver bolus with realistic velocity, viscosity to accurately mimic human swallowing. Our UVP results obtained using maltodextrin with three different viscosities showed that velocity profile measurements can be made in the pharynx, both in continuous flow and bolus flow conditions with a good signal-to-noise ratio. The challenge is to measure accurate bolus profiles at different positions in the model due to the quick human swallowing process. The next objective will be to determine the shear rate distribution from the wall to the center from the velocity profiles measured with UVP. Differentiation of the obtained velocity profiles can provide the entire shear rate distribution from a single measurement. This type of data is currently not available in the literature. The developed model set-up can therefore become a valuable new tool for studying Dysphagia and to develop personalized easy-to-swallow food products for Dysphagia patients.

References

1. Zargaraan, A., et al., Rheological aspects of dysphagia-oriented food products: A mini review. Food Science and Human Wellness, 2013. **2**(3–4): p. 173-178.
2. Clavé, P., et al., The effect of bolus viscosity on swallowing function in neurogenic dysphagia. Alimentary pharmacology & therapeutics, 2006. **24**(9): p. 1385-1394.
3. Steele, The Blind Scientists and the Elephant of Swallowing: A Review of Instrumental Perspectives on Swallowing Physiology. Journal of Texture Studies, 2015. **46**(3): p. 122-137.
4. Waqas, M.Q., et al., Shear and extensional rheology of commercial thickeners used for dysphagia management. Journal of Texture Studies, 2017: p. n/a-n/a.
5. Mowlavi, S., et al., In vivo observations and in vitro experiments on the oral phase of swallowing of Newtonian and shear-thinning liquids. Journal of Biomechanics, 2016. **49**(16): p. 3788-3795.
6. Waqas M. et al. A device that models human swallowing. 2017, p1-13. Submitted for publication.
7. Qazi, W.M. and M. Stading, In Vitro Models for Simulating Swallowing. 2018, Springer Berlin Heidelberg: Berlin, Heidelberg. p. 1-14.
8. Wiklund J et al.: Flow-Viz pulsed ultrasonic Doppler system with autotuning of analog- digital gain and threshold, Transactions ISUD10, Tokyo, Japan, 10 (2016) 29-33.
9. Ricci, S., Wiklund, J., Meacci V., (2017).Real-time staggered PRF for in-line industrial fluids characterization. DOI: 10.1109/ULTSYM.2017.8091778. Ultrasonics Symposium (IUS), 2017 IEEE International.

UDV Flow Measurements in a Model of the Czochralski Crystal Growth Process

Sven Franke[1], Josef Pal[2], and Sven Eckert[1]

[1]Helmholtz-Zentrum Dresden-Rossendorf (HZDR), Bautzner Landstr. 400, 01328 Dresden, Germany
[2] HZDR Innovation GmbH, Bautzner Landstraße 400, 01328 Dresden, Germany

This contribution describes a model experiment for the Czochralski crystal growth process. Low melting point liquid metals as GaInSn are an important tool to investigate the flow structure for such industrial processes. UDV flow measurements were conducted in a cylindrical Rayleigh-Bénard (RB) setup with modified thermal boundary conditions with and without the influence of an external rotating magnetic field. The topology of the prevailing thermally-driven convection might be very complex and is mainly determined by the aspect ratio of the liquid volume and the strength of the convection described by the characteristic dimensionless Grashof number. Two kinds of techniques were used to investigate the flow. Firstly, by means of single UDV transducers measurements of the radial velocity component were carried out shortly below the melt surface across the entire diameter of the cylindrical liquid column at various azimuthal angles. Secondly, a vertically arranged UDV array was applied at the side of the cylinder to obtain detailed information about the radial velocities in the covered meridional plane. The results reveal the complex flow structure of natural convection in a Czochralski crucible which gains in complexity with applied rotating magnetic field (RMF).

Keywords: Czochralski crystal growth, Rayleigh-Bénard convection, Ultrasound Doppler velocimetry, Flow measurements, Electromagnetic stirring

1. Introduction

Mono-crystalline silicon crystals are, nowadays, required in many electronic devices and the demand of energy such as the photovoltaic industry. One of the main objectives of the manufacturing process of photovoltaic silicon wafers by the Czochralski (Cz) method [1] is to produce crystals with low concentration of impurities such as oxygen, carbon and/or other materials. These adverse impurities might stem from the crucible and/or other inner parts of the crystal pulling equipment, transported by the melt flow and incorporated by the solidification process. Thus, the quality of the growing crystal and the yield of the wafers are crucially affected by the fluid flow.

Consequently, the mass production of mono-crystalline silicon by the Cz technique has initiated a huge amount of research on the convection inside the crucible. But reliable flow measurements in the real industrial process are practically nonexistent and the validation of numerical models can only be accomplished by laboratory model experiments. Moreover, further optimizations of the process by means of applied magnetic fields are still based on numerical simulations of the flow, the heat and mass transfer, and of the electromagnetic fields. Thus, the requirement of modeling the process on a laboratory scale still remains a valuable tool for the next future. For details on the growth of semiconductor silicon crystals [2] is referred to.

2. Basic principles in modelling the Czochralski technique

The simplest model of the Cz facility considers a Rayleigh-Bénard (RB) configuration, in particular a cylindrical cell with height H and diameter $2R$, heated from below, cooled at the top and adiabatic insulated side walls. Applying a temperature gradient ΔT between the bottom and top sides generates buoyant convection.

The dynamics of the mere thermally induced convection may be described by mainly three control parameters. The dimensionless Rayleigh number Ra is the crucial parameter in modelling buoyancy and describes its strength: $\mathrm{Ra} = \beta g \Delta T H^3/\nu\chi$, where β is the thermal expansion coefficient, ν the kinematic viscosity, χ the thermal diffusivity of the fluid, and g the gravitational acceleration. Instead Ra the Grashof number Gr is also commonly used for that purpose which is coupled to Ra by the second control parameter the Prandtl number Pr according to $\mathrm{Ra} = \mathrm{Gr} \times \mathrm{Pr}$. Pr takes into account the heat transport within the fluid and is given by the ratio of the thickness of viscous and thermal boundary layers: $\mathrm{Pr} = \nu/\chi$. In general, molten metals and semiconductor melts are low Prandtl number fluids with Pr in the order of 10^{-2}, which means that the heat diffuses quickly in comparison with the convective transport. The third control parameter, the aspect ratio $a = H/(2R)$ concerns the geometry of the setup and affects crucially the convective pattern inside the melt. More details, in particular about varying aspect ratios, can be found in [3,4] and references therein. The initial filling level in a real industrial Cz facility does not reach $a = 1$, it is even lower than $a = 0.5$ and decreases continuously during the process.

Other control parameter may occur if external magnetic fields are exposed to the system, such as the Taylor number $\mathrm{Ta} = \sigma\omega B^2R^4/2\rho\nu^2$ in case of the rotating magnetic field (RMF). σ and ρ ν are the electrical conductivity and density of the melt, and ω is the frequency of the magnetic field B. As the relevant parameter, Ta describes the driving action on the melt being under investigation, which is primarily of swirling type but also causing a

https://doi.org/10.7795/810.20190809

meridional secondary flow [5,6].

3. Description of the model

The object of the investigation is a modified Rayleigh-Bénard configuration, a cylindrical melt column of variable aspect ratio homogeneously heated from below. The photo in Fig. 1 illustrates the experimental setup mounted inside the magnetic coil system MULTIMAG [7]. Besides the already mentioned RMF, it offers a variety of other magnetic field types, such as the traveling (TMF), pulsed (PMF), vertical DC or vertical DC of cusp type, and even linear superposition thereof. As working fluid the ternary alloy GaInSn [8] was used because it remains liquid at room temperature and as distinguished from mercury it is non-poisonous. Moreover, its low Prandtl number is similar to that of molten silicon.

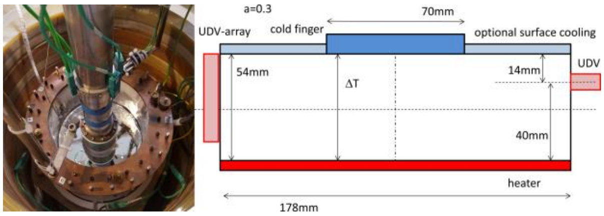

Figure 1: View to the experimental setup mounted inside the coil system on the left side. Some geometrical parameters are indicated in the schema on the right side.

The heating was realized by an electrical heating plate embedded in a massive copper disc to achieve isothermal boundary conditions. Several thermocouples were installed inside the copper disc to monitor its temperature. The upper thermal boundary condition in a Cz system is realized by a partially cooled surface. The partial cooling in our experiment covers approximately the same fraction area as the crystal does in an industrial facility. It is realized with a circular heat exchanger (cold finger) mounted concentrically at the top of the experimental cell. The cold finger is optionally rotable, a precise control of the temperature is realized by supplying it with coolant fluid at high flow rate from a thermostat having a large reservoir. The temperature of the cold finger is also monitored at various positions. During the measurements, the apparatus was embedded in mineral wool to minimize the lateral heat loss.

Flow velocities were measured by the UDV technique, the principle of operation is described in the pioneering work by Takeda [9]. Mainly two features render UDV predestinated for the present work. Firstly, it works in opaque media including liquid metals. Secondly, it allows the quasi-simultaneous measurement of an entire profile of the local velocity component in direction of the sound propagation along the ultrasonic beam.

Two different sensor arrangements were used which are shown in Fig. 2. Most of the measurements were taken by a DOP2000 velocimeter (Signal-Processing, Lausanne, Switzerland) with single ultrasound transducers. As it can be seen on the left side of Fig. 2 six single sensors were arranged at different azimuthal positions, each one differing by 30° to the next one. This allows gathering flow information over the whole circumference of the vessel. Furthermore, the different mounting levels allow measurements for variable aspect ratios.

Figure 2: View to the instrumentation for the flow measurements. On the left side the option with single transducers and on the right with the ultrasound array. The single transducers are coupled through holes directly to the melt whereas the UDV array measures through the wall of 2.3 mm thickness.

The right side in Fig. 2 shows a second setup with an attached transducer array. The reason for this setup was of preliminary character to check and qualify the UDV array technique for a more complex setup in the near future. The UDV array consists of 25 single transducer elements arranged linearly, each of a size of 2.3×5 mm^2 with an element pitch of 2.7 mm. Thus, it allows flow measurements of the velocity component perpendicular to the transducer surface over a field width of 67 mm. Moreover, multiple array arrangements would allow measurements of more velocity components and therefore complex flow mapping in the covered plane. For details on the UDV array technique [10,11] are referred to.

4. Results

For the present study flow velocity measurements were performed at mainly two different aspect ratios, $a = 0.45$ ($H = 80$ mm) and $a = 0.3$ ($H = 54$ mm), and under the influence of different types of magnetic fields (RMF, TMF, cusp). Nevertheless, only a small cutout of some selected aspects can be presented in this paper.

In the range $1.4\times10^6 \leq \mathrm{Gr} \leq 1.6\times10^8$ two different flow regimes were identified and investigated for $a = 0.3$. The vertical position of the sensors was thereby at $h = 40$ mm. For a low temperature gradient of $\Delta T = 1$ K ($\mathrm{Gr} = 1.6\times10^6$) an axisymmetric flow structure occurs. The fluid heated from the bottom rises along the rim, continues towards the center axis, drops in the central region below the cold finger and closes outward to the rim. Fig. 3 on the left illustrates such a measurement done with one single transducer at the randomly selected azimuthal position $\varphi = 0°$. Already for slightly higher $\Delta T = 3.1$ K ($\mathrm{Gr} = 5.1\times10^6$) the axisymmetric flow topology becomes instable (cf. Fig. 3-right) and for further increased Gr ($\mathrm{Gr} = 4.2\times10^7$, $\Delta T = 22$ K) the flow develops the wind structure which is a large scale single roll circulating inside the vessel. Such a structure is well-known in general RB systems and frequently observed for $a = 1.0$.

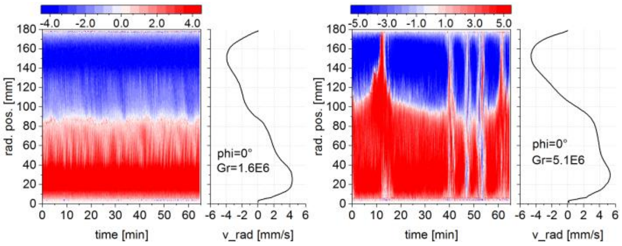

Figure 3: Left: time series and the related mean profile of the radial velocity component measured at $\varphi = 0°$ in the axisymmetric case. Right: typical velocity signal in the transitional range. In both cases, similar diagrams result at the other azimuthal positions φ.

It should be mentioned here that the preferred main flow direction of the wind develops randomly and is influenced mainly from the circumstances of the experimental setup. Fig. 4 shows two time series measurements in the wind-mode at the positions $\varphi = 0°$ and $\varphi = 90°$. The latter one corresponds thereby to the main circulation loop of the flow.

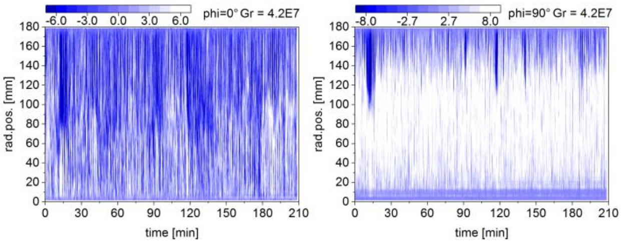

Figure 4: Time series observed for long term measurements in the wind-mode. The velocity units are given in mm/s.

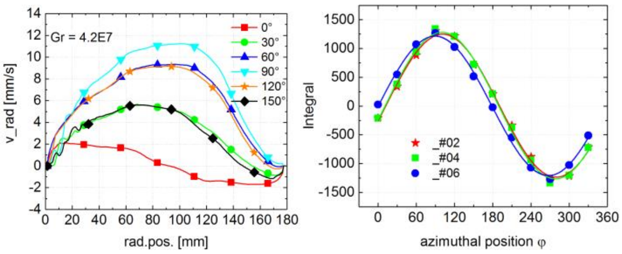

Figure 5: Left: Mean radial velocity profiles across the diameter for the wind-mode. Right: typical surface integrals of the mean profiles for different measurements.

The orientation of the wind becomes clearer from Fig. 5 where the left diagram shows the mean radial velocity profiles at each of the azimuthal positions and the right one surface integral of the respective profile. The maximum in the curve at approximately $\varphi = 90°$ indicates therewith clearly the main circulation loop of the wind. Furthermore, the right part of Fig. 5 summarizes three different measurements performed at different days and demonstrates well the stability .of the wind. At the same time it can be mentioned, that this was not the case for $a = 0.45$. Although here not shown, the wind was in that sense instable, that the maximum of the integral curves varied in time over a large azimuthal range, even flow reversals were occasionally observed.

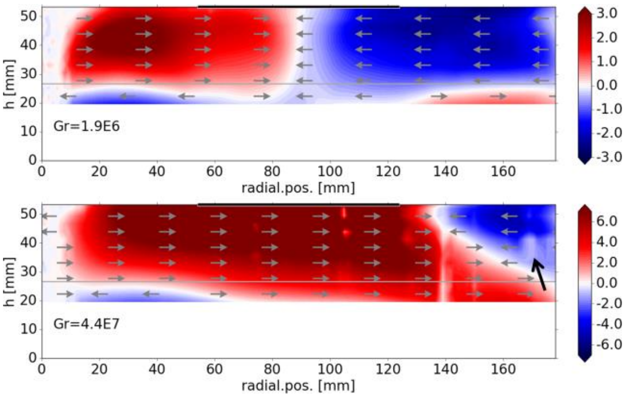

Figure 6: Radial flow maps measured using the UDV array. Arrows indicate only the flow direction and are not scaled. Due to construction reasons the lower 20 mm could not be measured. Since the array measures through the wall of the vessel, the quality of the signal is significantly influenced by the ultrasonic coupling both at the inner and outer interface of the wall. In “suboptimal” cases stationary echoes may occur which appear as “abnormal spots” in the flow map (also present in the above diagram marked with the thick black arrow). The velocity units are given in mm/s.

As mentioned in section 3, some selected measurements were done by means of the UDV array in a second setup. Due to the ability to measure quasi simultaneously along several sensor lines, a more informative radial flow map is achieved. Fig. 6 shows in the upper diagram such a purely buoyancy driven radial flow map in the axisymmetric low Gr case and for the fully developed wind-mode in the lower part. Furthermore, it is obvious from the lower diagram that the azimuthal position of the UDV array does not corresponds fully with the main circulation loop of the flow, which is again a consequence of the random character of the wind.

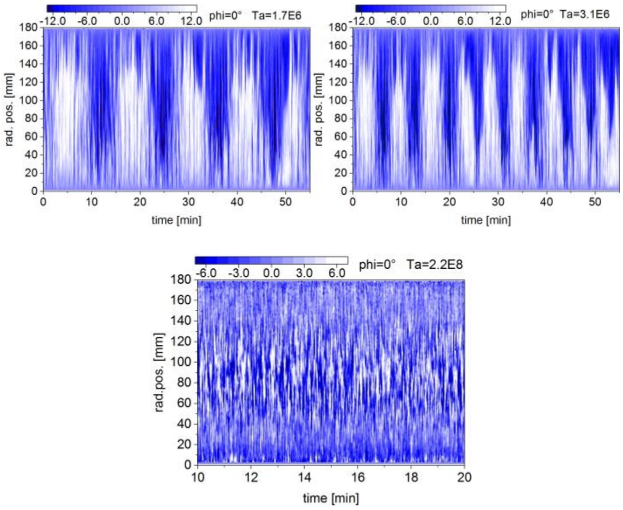

Figure 7: Influence of the RMF on the wind-mode ($Gr = 4.5 \times 10^7$). In the upper part time series of the radial flow measured at $\varphi = 0°$ for two different, relatively low strengths of the RMF. The lower diagram shows the case for a strong RMF. The velocity units are given in mm/s.

Applying an increasing RMF to the wind-mode it causes in the first instance a co-rotation of the wind as well - cf.

upper part of Fig. 7. For a high enough Ta the wind completely disappears (see in the lower diagram of Fig. 7).

A different influence of the RMF is observed by applying it to the axisymmetric case. The diagrams in Fig. 8 visualize the single sensor measurements for three different Ta numbers. At first glance, common to the diagrams are the first few minutes in which the RMF was not yet switched on. The axisymmetric structure is clearly observed here. When the RMF is switched on, some minor differences are observed between Ta = 1.0×10^6 and Ta = 1.4×10^6. For Ta = 2.6×10^6 the axial symmetry disappears, rather a similarity to the wind structure is observed – at least along the single sensor measurement line (h = 40 mm).

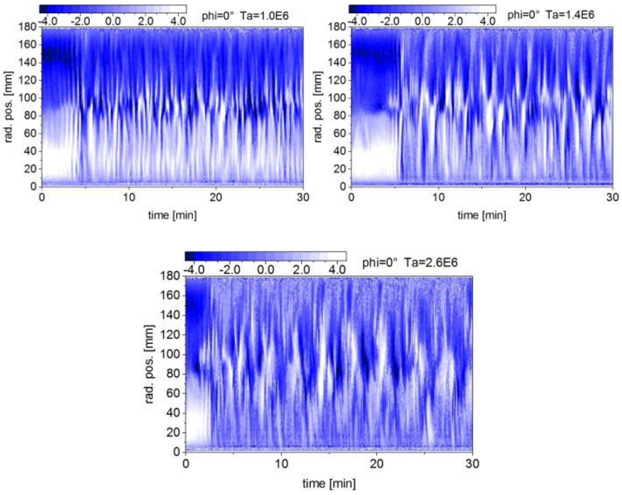

Figure 8: The flow under the influence of different RMFs in the axisymmetric case with Gr = 1.6×10^6. The velocity units are given in mm/s.

Of course it might be somewhat misleading to conclude from a one line measurement to the overall flow structure. In this regard, the major feature of the UDV array to measure simultaneously several lines becomes rather advantageous. The diagrams in Fig. 9 illustrate the mean radial flow maps for the same Gr and Ta numbers as specified in Fig. 8. By increasing the RMF strength rather a kind of squeezing occurs and the inward flow at the upper part of the vessel concentrates more and more to the region below the surface. Since the diagrams in Fig. 9 are the result of an averaging process over the measuring time of about 1 hour, the flow still has a time dependent and complex behaviour. Thus, care has to be taken by interpreting the overall flow topology.

5. Summary

A Cz-like crystal growth model exposed to different magnetic fields was the object of the present investigation. Ultrasound measurements of the fluid flow were performed by varying the strength of the RMF (Ta) and that of the buoyancy (Gr). Besides the single ultrasound transducers, the UDV array, whenever applicable to the specific setup, might provide a deeper insight into the complex flow topology in a Cz setup. Furthermore, the experimental data here serve as a benchmark object for numerical codes which are still under development.

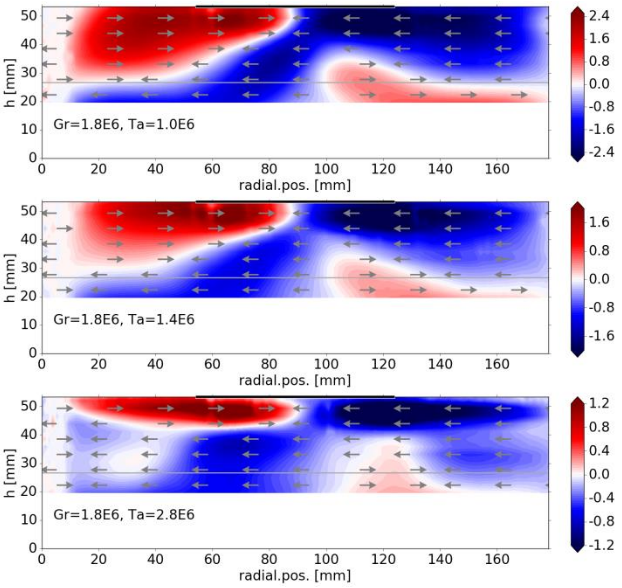

Figure 9: Mean radial flow maps under the same conditions as indicated in Fig. 8. The velocity units are given in mm/s.

6. Acknowledgements

Financial support by the Federal Ministry for Economic Affairs and Energy in the framework of the KORONA project is gratefully acknowledged.

References

[1] J. Czochralski: Ein neues Verfahren zur Messung der Kristallisationsgeschwindigkeit der Metalle (in german), Z. Physik. Chem. 92 (1917), 219–221.

[2] K. Kakimoto, *et al.*: Review. Growth of semiconductor silicon crystals, Progress in Crystal Growth and Characterization of Materials 62 (2016), 273-285.

[3] F. Hébert, *et al.*: Onset of Rayleigh-Bénard convection in cylindrical containers, Phys. Rev. E 81 (2001), 046318.

[4] J. Niemela, *et al.*: The wind in confined thermal convection, J. Fluid Mech. 449 (2001), 169–178.

[5] LP. Gorbatchev, *et al.*: Magnetohydrodynamic rotation of an electrically conductive liquid in a cylindrical vessel of finite dimensions, Magnetohydrodynamics 10 (1974), 406–414.

[6] P.A. Davidson: Swirling flow in an axisymmetric cavity of arbitrary profile driven by a rotating magnetic field, J Fluid Mech. 245 (1992), 669–699.

[7] J. Pal *et al.*: MULTIMAG - A MULTIpurpose MAGnetic system for physical modelling in magnetohydrodynamics, Flow. Meas. Instrum., 20 (2009), 241-251.

[8] Y. Plevachuk, *et al.*: Thermophysical Properties of the Liquid Ga−In−Sn Eutectic Alloy, J. Chem. Eng. Data 59(3) (2014), 757–763.

[9] Y. Takeda: Development of an ultrasound velocity profile monitor, Nucl. Eng. Des. 126 (1991), 277-284.

[10] S. Franke *et al.*: 2d-2c Ultrasound Doppler Array Velocimeter for Flow Investigations in Liquid Metals, Proceedings of ISUD7 Gothenburg/Sweden, (2010), 89-92.

[11] S. Franke *et al.*: Two-dimensional ultrasound Doppler velocimeter for flow mapping of unsteady liquid metal flows, Ultrasonics 53 (2013), 691-700.

11th International Symposium on Ultrasonic Doppler Methods for Fluid Mechanics and Fluid Engineering
Berlin, Germany (5.-7. September 2018)

Ultrasound Flow Metering for the Distorted Velocity Distribution by Means of the Parallel Shift Method

Tatsuya Kawaguchi, Isao Satoh and Takushi Saito

Tokyo Institute of Technology, 2-12-1 Ookayama, Meguro-ku, Tokyo 152-8552, Japan

The objective of the study is to improve the accuracy of the ultrasound flow rate measurement for the distorted velocity distribution. Velocity profile after bended pipes and expansion section were firstly calculated by a commercial CFD software. Using the CFD result, the suitable estimation method of acoustic intensity shift was examined and resulted that the three parallel paths is sufficient. From the experimental result, the present flow meter could apply to the measurement of flow rate just after the double-bend and expanded pipes.

Keywords: Flow rate measurement, Ultrasound shift method, distorted flow, CFD, Signal processing

1. Introduction

Precise management and control have been important issue in a large scale energy plant or reaction device using such gaseous fluid as steam and air. In order to obtain the accurate flow rate, longer straight pipe or section, by which the flow is fully developed, must be prepared to stabilize the velocity profile around the following measurement section. However, the space-saving flow rate metering with low pressure drop and high reliability is desired for the industrial and consumer applications. Moreover, transient flow rate determination will contribute to the reliable and real-time operation of the system and enables to control the local fluid behavior with the higher temporal resolution.

Ultrasound flow meter has the significant characteristics that the pressure drop at the measurement section is negligibly small. Higher temporal resolution is one of the other advantages. Conventional ultrasound transit-time or sing-around methods, however, have difficulties in determining the flow rate with distorted velocity profile, which is caused by the various reasons such as a bending, elbow, bulb and sudden change of pipe diameters. Therefore, the numerous number of studies were reported, e.g., non-axisymmetric flow rate determination by means of a time-based ultrasonic flow meter with theoretical velocity profiles [1], developments of the tomographic reconstruction method to obtain the sectional velocity distribution with multi-path flow meter [2,3] and so on.

The objective of the study to develop the novel flow rate measurement method that could be applied to the distorted or nonaxisymmetric velocity profile. In our previous works [4-8], ultrasound shift method were developed and applied to the measurement of the gaseous flow in pipes. In order to improve the accuracy and robustness of the system, multiple beams were employed and various type of the beam alignments were compared. The investigations resulted that the parallel beam alignment enables to improve the accuracy of the flow rate determination in the vicinity of the single elbow. That led us to apply the proposed technique to the practical and more complicated flow fields found in the actual pipe flow systems. In this study, the investigation was extended to the measurement at the downstream of the double elbow section as well as the expansion flow. In the measurement system, the displacement of the acoustic intensity distribution due to the cross-wind effect was determined by means of the ultrasound receiver array. Expected amount of the shift as a function of the velocity distributions as well as the probe beam orientation was firstly predicted by means of a commercial CFD software that is followed by the experimental validation of the measurement accuracy of resultant flow rate.

2. Flow rate measurement by the multi-beam ultrasound shift method

Volume flow rate, *Qv*, is defined as the following integral equation.

$$Qv = \iint u \, dy \, dz \qquad (1)$$

The equation indicated that the flow rate is the integral of the axial velocity component, u (y, z), throughout the area of the test section that is perpendicular to the main flow in a pipe or a duct. In other words, the flow rate determination requires the two dimensional measurement of the axial velocity component. However, non-intrusive multi-dimensional measurement of the velocity distribution within an enclosure or such internal flows as pipe or duct flows is quite difficult. Figure 1 depicts the fundamental principle of the ultrasound shift method [4].

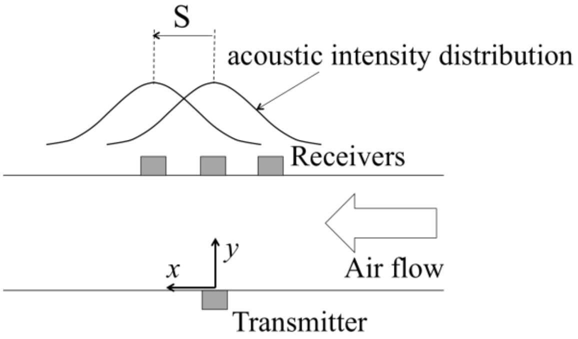

Figure 1 Schematic diagram of the ultrasound shift method.

In contrast to the conventional time-based ultrasound flow meter methods, which employ the inclined ultrasound beams to the pipe axis, the probe beam is emitted and propagates perpendicularly to the axis of the pipe. Ultrasound beam that reached to the opposed side of the transmitter was diverged and was also shifted due to the convection of the fluid flow passing through the test section. Therefore, the intensity profile of the received beam is moved to the downward of mean flow and the degree of the displacement is proportional to the flow rate.

The magnitude of the shift of the acoustic intensity distribution, *S*, can be obtained by the following equation.

$$\boldsymbol{S = \int_0^D \frac{u}{c} dy} \qquad (2)$$

Where *c* denotes the sound velocity, representative value of *c* is equal to 340 m/s for the air at room temperature and atmospheric pressure, and 1480 m/s for water. *D* denotes the internal diameter of the pipe, $u = u\ (y,\ z)$ is the radial velocity distribution of the flow. For the air flow measurement with the pipe diameter of 160 mm, the magnitude of the shift is a few mm. When the velocity distribution in the test section is assumed to be axisymmetric, the flow rate could be directly obtained by using Abel transform of the amount of the shift. If the flow is distorted due to the bend, elbow, bulb or any kind of the disturbing element in the flow systems, the single path methodology could not be applied or suffered from the terrible measurement error. Since the secondary flow and backward flow after the aforementioned elements generates the distorted velocity profile, it becomes difficult to assume the symmetric velocity profile, i.e., the error will significantly be increased depending on the orientation of the probe beam. In contrast, the multi-path ultrasound shift method have the possibility to reflect the velocity modulation and is effective in reducing the bias error and in improving the accuracy of the resultant flow rate. In our previous works, quad ultrasound shift method at the radial alignments were proposed and applied to the distorted flow after the single 90 deg L-bend section. The investigation resulted that the oversampling effect at the intersection of radial beams causes the bias error of the measured flow rate. In the present study, the parallel beam alignment was employed. By integrating the spatial distribution of shift, *S*, the flow rate could be obtained by the following equation.

$$\boldsymbol{Qv = c \int_0^D S(z)dz} \qquad (3)$$

To calculate the flow rate on the basis of Eqn. 3, infinite number of shift values are required. As the distortion of velocity distribution in a pipe flow is not drastic, the distribution of the shift could be approximated by using the lower order polynomials. The order is limited by the number of measured shift values.

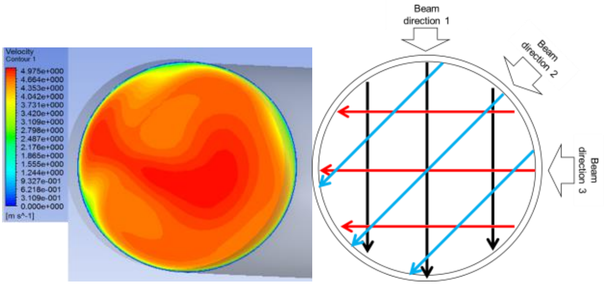

Figure 2 Velocity distribution after the double bended pipe (Z bend) by means of CFD software. The orientation of the parallel ultrasound beams is depicted as well.

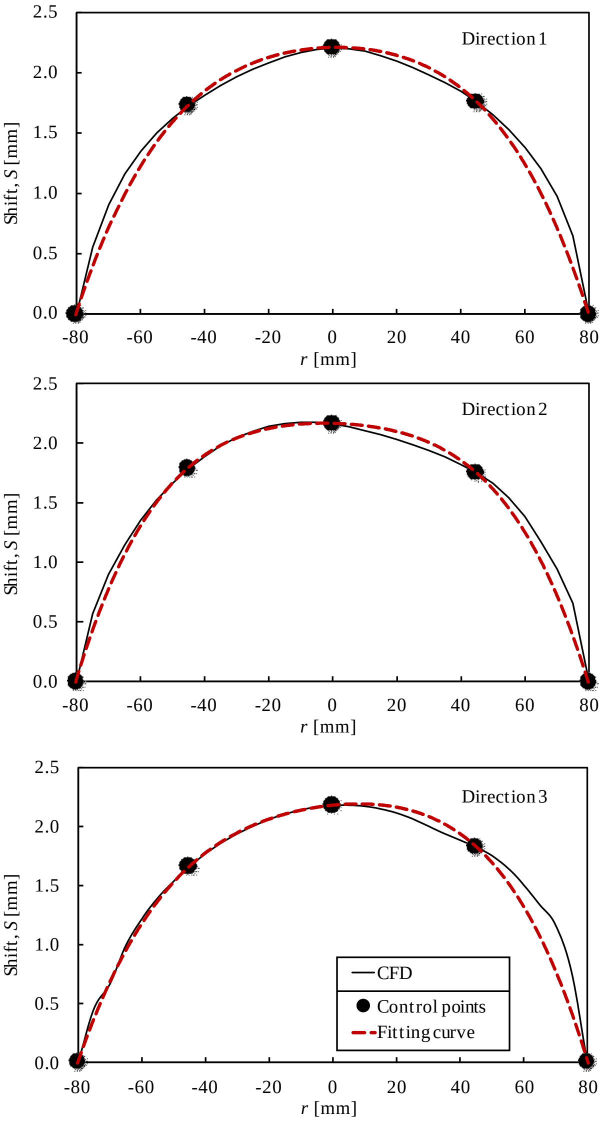

Figure 3 Predicted shift distribution after the double elbow from the CFD result of the velocity distribution. Fitting curve was obtained with the 4th order polynomials using the 3 measuring points as well as the boundary condition (*S*=0) at the pipe surfaces. Solid circular plots corresponds the measurement point. Velocity profile after bended pipes was calculated by CFD software.

https://doi.org/10.7795/810.20190809

Figure 2 shows the example of the calculated velocity distribution as well as the angular alignment of the parallel 3 beams through the cross section of pipe. The inner diameter of pipe was 160 mm, distance between the end of the second bend and the test section was 220 mm. Detailed geometry of the pipes will be appeared in the following section. The k-ε model was used as a turbulent model. Homogeneous inlet velocity and outlet pressure were used as the boundary conditions. Expected shift distributions in terms of the beam orientation were depicted in figure 3. The separation between parallel beams was 45 mm. Fitting with the corresponding three-point shift values as well as the $s = 0$ at the both edges, the fitting curves show good agreement with the shift distribution obtained from the velocity distribution from the numerical simulation.

3. Experiments and results

Figure 4 and figure 5 illustrate the detailed geometry of the experimental set up used in the experiments. Both diameter of pipe and dimension of bended pipe were identical to the previous numerical simulation. In both cases, the test sections were located at 220 mm from the 2nd bend or expanded section in which the conventional single path flowmeters could not be applied. A centrifugal fan was installed at the further downstream from the test section and was controlled with the variable frequency inverter with the shielded enclosure in order not to affect the electrical circuit. Frequency of the emitted ultrasound was 40 kHz, maximum voltage for the ultrasound transmitter was 20 V. The magnitude of the shift of the ultrasound intensity distribution was determined with the 3ch receiver array. Other equipment such as analog circuit, A/D convertor and signal processing software were identical to the previous study [8]. Figure 6 compares the measured flow rate by using the reference orifice flow meter and the present method. Since the angular alignment of the parallel beam will significantly affect the obtained flow rate in practical applications, the effect of the angle was evaluated. Flow rate was varied from 0 to 0.16 m^3/s, which is equal to 576 m^3/h. Re number was 21000. The comparisons show that the linear relation between flow rates were obtained with every angular alignment. Maximum error was 15 % in the worst case at the particular flow rate with the angular alignment of direction 2. The proposed three-parallel paths method could be applied to the flow rate measurement with the distorted velocity profile after the consecutive elbows.

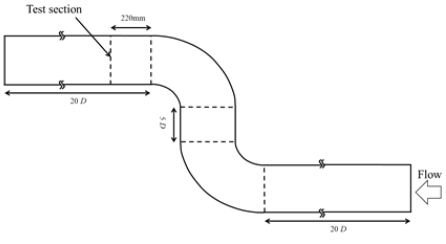

Figure 4 Schematic diagram of the consecutive double-elbow and test section.

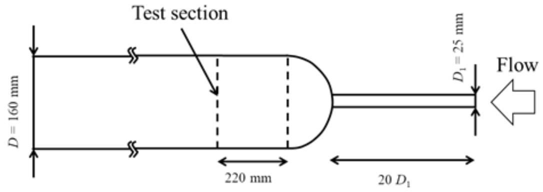

Figure 5 Schematic diagram of the expansion flow and test section.

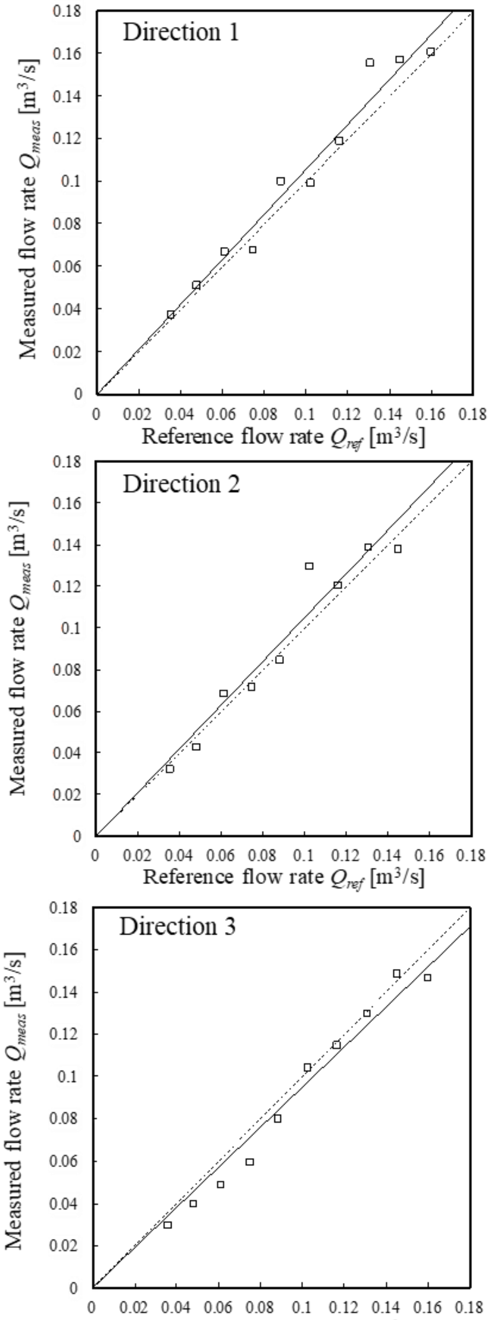

Figure 6 Comparison of results by means of the present shift method and the orifice flow meter as a reference. Flow rate and the angular beam alignment was varied.

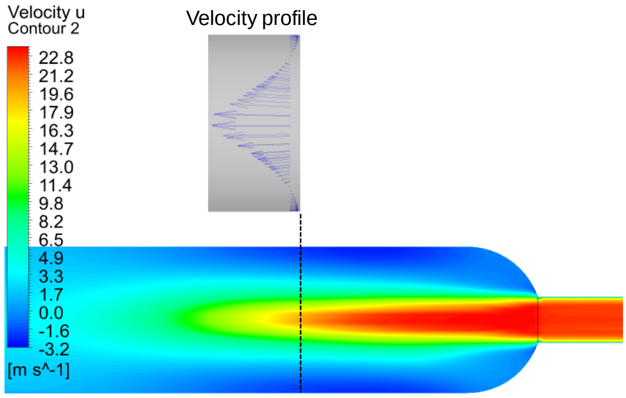

Figure 7 Contour map of the axial velocity distribution at the expansion flow. Corresponding velocity profile at the ultrasound beam path is extracted and depicted.

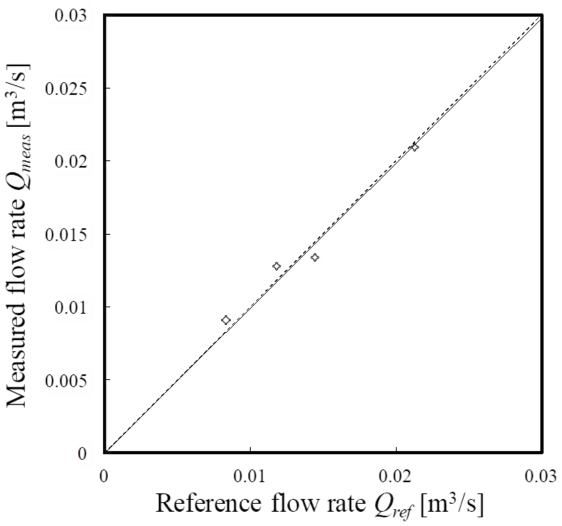

Figure 8 Flow rate measurement just after the expansion section. Orifice flow meters.

Figure 7 depicts the CFD result in the vicinity of the expansion section. At the section, pipe diameter was expanded from 25mm to 160 mm. Contour map of the axial velocity component was described in the figure. Corresponding velocity profile at the ultrasound beam path was also shown in the figure. In the expanding section, width of the radial velocity distribution was rapidly increased due to the higher shear rate at the boundary layer. That is the reason why the higher spatial resolution is desired, especially for the direction of the pipe axis. Moreover, the symmetric recirculation flow is occurred after the backward facing step due to the larger expansion ratio at the section. Figure 8 compares the measured flow rates just after the expansion section. The comparison demonstrated that the present technique could also be applied to the flow rate measurement with the significant velocity distortion. In this case, gradient error was negligible, and the maximum value of the resultant error was 5%.

5. Conclusion

The flow rate measurement after a pair of bended pipes as well as the expansion section was developed that employed the ultrasound shift method with parallel beams. The detailed velocity profiles after the disturbing sections were firstly calculated by a commercial CFD software. From the numerical analysis, the three-point shift measurement enables to obtain the coefficients of the fitting curve of the shift distribution and is sufficient for the determination of the volume flow rate under the present configurations. From the experiments results, it was confirmed that the measurement error of the flow rate with the consecutive double bend system was 15%, that with the expansion flow was 5 %.

References

[1] P. I. Moore, G. J. Brown and B. P. Stimpson: Ultrasonic transit-time flowmeters modelled with theoretical velocity profiles: methodology, *Meas. Sci. Technol.*, 11 (2000), 1802-1811

[2] R. A. Rahim, M. H. F. Rahiman, K. S. Chan, S. W. Nawawi: Non-invasive imaging of liquid/gas flow using ultrasonic transmission-mode tomography, *Sensors and Actuators*, A 135 (2007), 337–345

[3] D. Kurniadi, A. Trisnobudi: Multi-Path Ultrasonic Transit Time Flow Meter Using a Tomography Method for Gas Flow Velocity Profile Measurement, *Part. Part. Syst. Charact.*, 23 (2006), 330-338

[4] T. Abe, T. Kawaguchi, T., Saito and I. Satoh: Development of new gas flowmeter by ultra sound tuft method, *Proc. 49th HTSJ Symp*. Vol.I+II, SP27 (2012), p123.

[5] I. Satoh, T. Saito and T. Kawaguchi: Development of new gas flowmeter by ultra sound tuft method, *Chemical Engineering*, **58**, 2 (2013), 123-139.

[6] Z. Yang, T. Kawaguchi, T. Saito and I. Satoh: Flow metering of distorted pipe flow by means of multi-path ultrasonic shift method, *12th Int. Symp. on Fld. Ctrl, Meas. and Visual.* (2013), 0120.

[7] K Kuramoto T. Kawaguchi, T. Saito and I. Satoh: Verification of flow rate measurement using ultrasound shift method after bended pipe, The National Symposium on Power and Energy System (2015).

[8] K. Kuramoto, T. Kawaguchi, I. Satoh and T. Saito: Flow rate measurement after 90 degrees bended pipe using multi-path ultrasound shift method, *Proc. 10th Int. Symp. on Ultrasonic Doppler Methods for Fld Mech. and Fld Eng.* (2016).

Velocity Profile Measurement Using Ultrasonic Pulse-Train Doppler Method Under the Disturbed Flow Condition

Sanehiro Wada[1], Noriyuki Furuichi[1]

[1] Advance Industrial Science and Technology, National Metrology Institute of Japan, Central 3, 1-1-1, Umezono, Tsukuba, Ibaraki, 305-8563, Japan

This paper presents experimental measurements using the novel technique for measuring the velocity profile and flow rate in a pipe. This method, named the ultrasonic pulse-train Doppler method (UPTD), has the advantages of expanding the velocity range and setting the smaller measurement volume with low calculation and instrument costs in comparison with the conventional ultrasonic pulse Doppler method. In addition, previous reports indicate that a smaller measurement volume increases the accuracy of the measurement. In consideration of the application of the conventional method to actual flow fields, such as industrial facilities and power plants, the issues of velocity range and measurement volume are important. Experimental measurements were conducted, and the results were evaluated at the national standard calibration facility of water flow rate in Japan. The results show that UPTD can measure the velocity profiles over the pipe diameter, even if the velocities exceed the measurable velocity range under the straight pipe condition. In addition, to examine the applicability of UPTD to the flow condition with large velocity fluctuation, velocity profiles were measured using UPTD under the disturbed flow condition and compared with the conventional Doppler method.

Keywords: Flowrate, Velocity profile, Ultrasound, Doppler, Pulse-train

1. Introduction

It is well known that the measured flow rate given by flowmeters, such as ultrasonic, electromagnetic, and turbine flowmeters, generally depends on the velocity profile in a pipe. This dependence demonstrates that the measurement accuracy of these flowmeters is influenced by the upstream pipe configuration, even if the flowmeters are calibrated by a calibration facility. In calibration facilities, the construction of a complete equivalent pipe layout in an actual field is often difficult, and thus on-site calibration is the only practical method of checking the accuracy of the flow rate measurement. Although an on-site flowrate calibration method with high accuracy is expected for actual field measurements, few existing methods achieve high accuracy. For example, Guntermann et al. [1] proposed an on-site calibration method using a laser Doppler velocimetry (LDV) system. In this method, the reference flowrate in the actual flow field was estimated by using the velocity profile measured by the LDV system. However, modifications of the pipe were necessary before using the LDV system.

The ultrasonic pulse Doppler method was developed to measure blood flow [2]. Due to its outstanding advantages, such as non-invasiveness and spatiotemporal measurement, this method has been applied in the engineering field by Takeda [3] and widely used to investigate flow dynamics [4]. Mori et al. developed a flowmeter for pipe flow by employing this method [5]. This type of flowmetering method can possibly be applied to on-site calibration as a clamp-on measurement [6]. In other words, this method is expected to avoid modifications of the existing pipe. Because the basic principle of flow rate measurement consists of measuring the velocity profile over a pipe diameter and integrating the measured profile, this method can also reduce the influence of a disturbed flow caused by upstream pipe conditions. Furuichi performed a fundamental uncertainty analysis of this flowmetering method under ideal flow condition, i.e., an asymmetric velocity profile [7].

On the other hand, the ultrasonic pulse Doppler method, which is based on the Nyquist sampling theorem, has a limited velocity measurement range. In consideration of the application of this method to actual flow fields, such as industrial facilities and power plants, one major issue is its limitation for large pipes and flow rates. Developments, such as the staggered frequency of the pulse repetition method [8][9] and the multiple demodulation frequency method to overcome the Nyquist limitation, have been widely studied [10][11]. In recent years, Tanaka et al. [12] investigated the wideband Doppler method. These studies were conducted for blood measurements and weather radar measurements. However, the literature concerning the accuracy of velocity and flowrate measurements in a pipe flow is limited. An application of the staggered frequency of pulse repetition on a pipe flowrate measurement was presented by Murakawa et al. [13]. The report indicates that the accuracy of the velocity profile obtained by the conventional staggered frequency method is low for industrial applications. Although they also reported the result of flow rate measurements with high accuracy by using the multi-wave method [14], applying the multi-wave method as a clamp-on measurement will be difficult due to the multiple scattering of ultrasound in a pipe wall. In addition, they noted that a smaller measurement volume increases the accuracy of the measurement.

We presented a novel technique of measuring a velocity profile, named the ultrasonic pulse-train Doppler method (UPTD) [15]. This method has the advantages of expanding the velocity range and setting the smaller measurement volume with low calculation and instrument costs in comparison with the conventional ultrasonic pulse

https://doi.org/10.7795/810.20190809

Doppler method. The algorithm is to exploit a few pulses of ultrasound with a short interval and an envelope detection. In this paper, to examine the applicability of UPTD to the flow condition with large velocity fluctuation, velocity profiles were measured using UPTD under the disturbed flow condition and compared with the conventional Doppler method.

2. UPTD

2.1 Principle of measurement

A schematic representation of the signal processing of UPTD is given in Figure 1. First, two pulses are transmitted with a delay of T_{pt} from the transducer and repeated with an interval of T_{prf}. Then, a set of two pulses with delay T_{pt} is reflected on a particle and detected by the same transducer. The detected pulse is amplified and processed by envelope detection, which consists of the calculation of the absolute value and low-pass filtering. The cutoff frequency of the low-pass filter is determined by considering the frequency of the ultrasound and the delay of the pulse train. The T_{pt} is better to be set over the duration of a single pulse for the envelope detection. Consequently, the path, diverging angle and straightness of the pulsed ultrasound of UPTD is almost same with the case of using a single pulse.

A block diagram of signal processing for the UPTD method is shown in Figure 2. The output signal through the envelope detection has frequency f_{pt}, which is defined by the delay time of pulse train T_{pt}. The Doppler frequency can be obtained by quadrature detection using a reference wave with frequency f_{pt}. As a result, the velocity range depends on frequency f_{pt}. In other words, the maximum measurable velocity is denoted in the following equation.

$$v_{\max\_\mathrm{UPTD}} = \frac{c}{4 f_{pt} T_{prf} \sin\alpha} \tag{1}$$

From this equation, we can observe that UPTD can determine the velocity range flexibly, because f_{pt} is independent of the center frequency of the ultrasound. This flexibility also means that UPTD can employ a smaller measurement volume by using the higher central frequency of the ultrasound.

Table 1 shows the velocity ranges of the conventional method for f_0 = 1 MHz and 4 MHz in the direction of the pipe axis. In this experiment, the velocity range using UPTD is expected to extend as high as the range using the conventional method with f_0 = 1 MHz, because the delay of the pulse train is set at 1 μs.

Table 1 Velocity range of the conventional ultrasonic pulse Doppler method

Center frequency: f_0	Velocity range: v_{range}
1 MHz	5.7 m/s
4 MHz	1.4 m/s

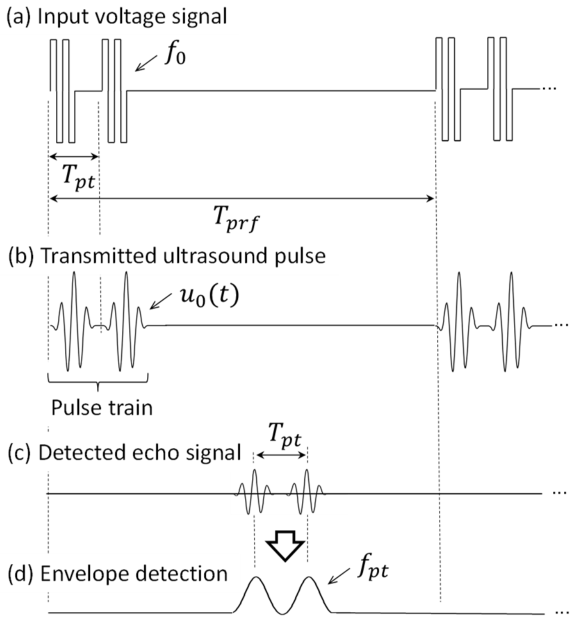

Figure 1: Schematic of signal processing of ultrasonic pulse-train Doppler method.

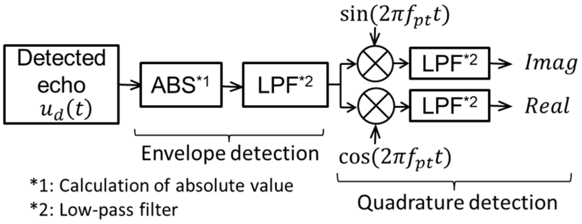

Figure 2: Block diagram of ultrasonic pulse-train Doppler method.

3. Experiment

3.1 Experimental apparatus and conditions

Experiments were performed at the water flow rate calibration facility of the National Institute of Advanced Industrial Science and Technology, National Metrology Institute of Japan (AIST, NMIJ). This facility is the national standard calibration facility of water flow in Japan. The flow rate given by the UPTD method was evaluated with respect to the reference flow rate given by the electromagnetic flowmeter calibrated by the static gravimetric method using a tank system weighing 50 t. The uncertainty of the reference flow rate given by the 50 t weighing tank system was 0.060% (k = 2). For details of the system, see reference [16]. The flow rate range of this experiment was 200 m^3/h, and the water temperature condition was 27.3 ± 1.0 °C. The temperature variation was within 0.1°C during one measurement. The Reynolds number was $Re = 4.12 \times 10^5$. Figure 3 shows the schematic of the test facility and the test section. The pipe layout with the bubble generator was the same as that used in the previous study by Furuichi [7]. The flow conditioner was installed at a distance of 55D upstream of the test section. Small air bubbles that act as reflectors of ultrasound were inserted upstream of the flow conditioner. The bubble sizes were confirmed using a high-speed camera to be much smaller than 1mm [17]. The ultrasonic transducer was installed in the test pipe and placed in direct contact with the water. The incident angle of the transducer was α = 19.3°, which was obtained from actual measurement. The inner diameter of the test pipe was D = 199 mm.

To generate a disturbed (non-axisymmetric) flow, obstacle plate as shown in Figure 4 is installed upstream of the test section. This type of plate is frequently used in performance tests of flowmeters [18]. The aperture ratio of these obstacle plates in this paper is 0.66. The installation direction of the obstacle plates is shown in Figure 4. The expected velocity profile downstream of the single plate is similar to one of an elbow. The inlet length, the distance between the plate and the test section, is 8*D*.

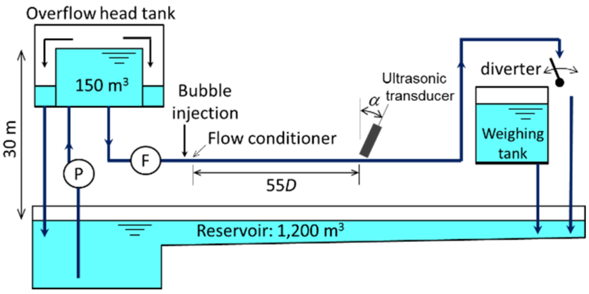

Figure 3: Experimental facility and test section.

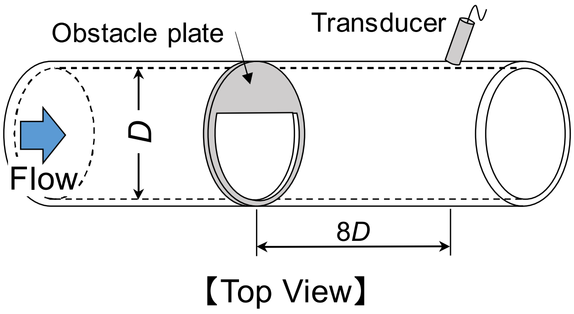

Figure 4: Layout of the obstacle plate.

An input voltage signal with two cycles per pulse generated by using the pulser-receiver instrument (JPR-10CN, Japan Probe Co., LTD.) was applied to the ultrasonic transducer, and pulsed ultrasound was transmitted into water. The reflected pulses of ultrasound were detected by the same transducer and amplified by the same pulser-receiver. These amplified signals were transferred to the digitizing instrument (NI-5122, National Instruments Co.). The pulse train was also generated and transmitted by the same pulser-receiver. Table 2 shows the experimental conditions in this experiment. All the measurements were made with the same receiving gain and power amplification settings.

Table 2 Experimental conditions

Center frequency of ultrasound: f_0	4 MHz
Incident angle of ultrasound: α	19.3°
Length between transducer and internal pipe wall: L_s	39 mm
Length of measurement volume along ultrasonic beam: L_{cw}	1.5 mm
Diameter of piezo element: d_{us}	5 mm
Diameter of pipe: D	199 mm
Sound speed of water: c	1504 m/s
The time interval of pulse repetition: T_{prf}	400 µs
The delay time of the pulse-train: T_{pt}	1 µs

3.2 Results

The time-averaged velocity profile under the straight pipe condition is shown in Figure 5. The horizontal axis means that r/D = –0.5 is the inner pipe wall near the transducer, r/D = 0 is the center of the pipe and r/D = 0.5 is the opposite inner pipe wall of the transducer. The distance between measurement points along the ultrasonic path is 2.3 mm. This figure indicates that UPTD can measure velocity profiles over the pipe diameter, even if these velocities exceed the measurable velocity range of the conventional pulse Doppler method.

Figure 6 shows the time-averaged velocity profiles under the disturbed flow condition. The conventional method using the 4MHz transducer cannot measure the velocity profile due to the velocity range and the large velocity fluctuation. On the other hand, UPTD with 4MHz and the conventional method with 1MHz can measure velocity profile because the wide velocity range. However, the velocities near the pipe wall measured by the conventional method with 1MHz are estimated to be influenced by the larger measuring volume and the reflected ultrasound on the pipe wall.

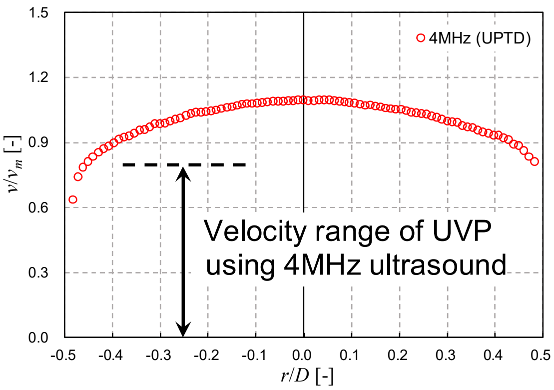

Figure 5: Time-averaged velocity profile measured by UPTD using 4MHz ultrasound under the straight pipe condition.

https://doi.org/10.7795/810.20190809

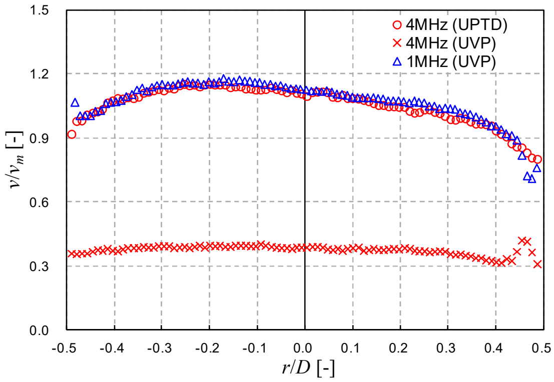

Figure 6: Time-averaged velocity profiles measured by UPTD (4MHz) and UVP (4MHz and 1MHz) with the obstacle plate condition.

4. Conclusions

This paper presents the ultrasonic pulse-train Doppler method (UPTD), a novel technique of measuring the velocity profile and flow rate in a pipe. UPTD has the advantages of expansion of the velocity range and a capability to decrease in measurement volume with low calculation and instrument costs in comparison with the conventional method. The UPTD algorithm exploits two pulses of ultrasound with a short interval and envelope detection. Experimental measurements were performed at the national standard calibration facility of water flow rate in Japan. The result shows that UPTD can measure the velocity profiles over the pipe diameter, even if these velocities exceed the measurable velocity range of the conventional pulse Doppler method. In addition, to examine the applicability of UPTD to the flow condition with large velocity fluctuation, velocity profiles were measured using UPTD under the disturbed flow condition and compared with the conventional Doppler method. These results show that UPTD can measure velocity profile under the disturbed flow condition.

Acknowledgment

The work was supported by JPSP KAKENHI Grant Number JP15H05566.

References

[1] Guntermann P., Rose J., Lederer T., Dues M., Müller U., and Duckwe A., In situ calibration of heat meters in operation, *Euro Heat and Power*, 8, pp. 46–49 (2011)

[2] Baker D.W., Pulsed ultrasonic Doppler blood-flow sensing, *IEEE Trans Sonics Ultrasound*, 17(3), pp. 170–185 (1970)

[3] Takeda Y., Velocity profile measurement by ultrasonic Doppler shift method, *Int. J. Heat Fluid Flow*, 7, pp. 313–318 (1986)

[4] Takeda Y. (editor), Ultrasonic Doppler Velocity Profiler for Fluid Flow, *Springer* (2012)

[5] Mori M., Takeda Y., Taishi T., Furuichi N., Aritomi M., and Kikura H., Development of a novel flow metering system using ultrasonic velocity profile measurement, *Experiments in Fluid*, 32, pp. 153–160 (2002)

[6] Tezuka K., Mori M., Wada S., Aritomi M., Kikura H., and Sakai Y., Analysis of ultrasound propagation in high-temperature nuclear reactor feedwater to investigate a clamp-on ultrasonic pulse Doppler flowmeter, *Journal of Nuclear Science and Technology*, 45(8), pp. 752–762 (2008)

[7] Furuichi N., Fundamental uncertainty analysis of flowrate measurement using the ultrasonic Doppler velocity profile method, *Flow Measurement and Instrumentation*, 30, pp. 202–211 (2013)

[8] Newhouse V.L., LeCong P., Furgason E.S., and Ho C.T., On increasing the range of pulsed Doppler systems for blood flow measurement, *Ultrasound Med. Biol.*, UMB-6, pp. 233–237 (1980)

[9] Nishiyama H. and Katakura K., Non-equally spaced pulse transmission for non-aliasing pulsed Doppler measurement, *Journal of Acoust. Soc. Japan (E)* Vol. 1 3-4, pp. 215–222 (1992)

[10] Doviak R.J., Sirmans D., Zrnic D.S., and Walker G.B., Considerations for pulse-Doppler radar observation of severe thunderstorms, *Journal of Appl. Meteorol*, pp. 189–205 (1978)

[11] Fan P., Nanda N.C., Cooper J.W., et al., Color Doppler assessment of high flow velocities using a new technology: in vitro and clinical studies, *Journal of CV Ultrasound Allied Tech.*, Vol. 7(6), pp. 763–769 (1990)

[12] Tanaka N., Experimental verification of color flow imaging based on wideband Doppler method, *Journal of Medical Ultrasonics*, Vol. 4, 1, pp. 23–30 (2014)

[13] Murakawa H., Muramatsu E., Sugumoto K., Takenaka N., and Furuichi N., A dealiasing method for use with ultrasonic pulsed Doppler in measuring velocity profiles and flow rates in pipes, *Measurement Science and Technology*, Vol. 26, 085301 (2015)

[14] Muramatsu E., Murakawa H., Sugimoto K., Asano H., Takenaka N., and Furuichi N., Multi-wave ultrasonic Doppler method for measuring high flow-rates using staggered pulse intervals, *Measurement Science and Technology*, Vol. 27, 025303 (2016)

[15] Wada A., Furuichi N. and Shimada T., Development of ultrasonic pulse-train Doppler method for velocity profile and flowrate measurement, *Measurement Science and Technology*, Vol. 27, 115302 (2016)

[16] Furuichi N., Terao Y., and Takamoto, M., Calibration facilities for water flowrate in NMIJ, *Proceedings of 7th International Symposium on Fluid Flow Measurement*, Anchorage, USA, August, pp. 12–14, (2009)

[17] Tezuka K., Mori M., Suzuki T., Aritomi M., Kikura H., and Takeda Y., Assessment of effects of pipe surface roughness and pipe elbows on the accuracy of meter factors using the ultrasonic pulse Doppler method, *J. of Nuclear Science and Technology*, 45(4), pp. 304–312 (2008)

[18] OIML R 137-1 & 2 Edition (E), International Organization of Legal Metrology, Including Amendment 2014, 60-61

11th International Symposium on Ultrasonic Doppler Methods for Fluid Mechanics and Fluid Engineering
Berlin, Germany (5.-7. September 2018)

Noise Model Implementation in Ultrasonic Velocity Vector Reconstruction with Array Configuration

Tomonori Ihara[1], Hideharu Takahashi[2], and Hiroshige Kikura[2]

[1] Tokyo University of Marine Science and Technology, 2-1-6 Etchujima, Koto, Tokyo, 135-8533, Japan.
[2] Laboratory for Advanced Nuclear Energy, Tokyo Institute of Technology, 2-12-1 Ookayama, Meguro, Tokyo 152-8550, Japan.

Ultrasonic velocity profiler (UVP) is usually used with a single transducer configuration. Array configuration enables two-dimensional or three-dimensional flow mapping. Phased array ultrasonic technique can be utilized to steer ultrasonic beam, which allows wide range scanning even with a smaller transducer. Velocity vector reconstruction technique was developed to estimate two or more-dimensional velocity components while original UVP only obtain one-dimensional velocity component along with an ultrasonic beam. One of the issues regarding the vector reconstruction is the accuracy of the vector. Moreover, there is a mathematical issue. Only two or three 'unknown' velocity components are determined from much larger number of velocity data obtained from multiple array elements. This paper proposes noise model to solve those problems and validates its performance. The design of the array sensor and measurement system are also discussed.

Keywords: Phased array technique, Velocity reconstruction, Noise model

1. Introduction

In March 11th, 2011, the massive earthquake hits north-eastern Japan, which is followed by the devastating tsunami. Then, the nuclear accident at Fukushima Daiichi Nuclear Power Plant of Tokyo Electric Power Company (TEPCO) occurred due to the disaster. TEPCO is currently working on its decommissioning [1]. One of the biggest challenges is the determination of the leakage point of contaminated water from the reactors. High dose rate in the primary containment vessel and reactor building precludes direct human access. Specially developed robots are therefore used to investigate the reactors. Visual investigations are principally accomplished with radiation tolerant camera setups. Stagnant water in the reactors is found to be turbid. Therefore, determination of the leakage point requires other investigation method besides optical observation. Ultrasound measurement is one of the applicable methods. This has also been done before at Three Mile Island-2 in U.S. for determination of the final state of its meltdown core [2].

We have been developing the ultrasonic measurement system for its decommissioning task [3, 4]. Investigation robots suffers size limitation due to the deployment and operation restrictions. Since payload is also restricted, ultrasound measurement system as such is preferably small. Nevertheless, capability of large area measurement is highly requested considering the large space in the reactors. We are proposing the measurement system using the phased array ultrasonic technique to realize those demands. Phased array ultrasonic technique is widely used in non-destructive evaluation (NDE) [5]. Many extensive researches are performed, and advanced measurements are developed and proved, for example, high-resolution imaging technique termed total focusing method. Together with NDE techniques, ultrasonic Doppler method (UVP) can provide valuable insights about the measurement target; NDE technique visualizes objects over the measurement field and UVP depicts flow. There are few literatures of UVP with array sensor configuration [6, 7]. We have been expanding conventional UVP to vector UVP by simultaneous multi-channel signal processing. When an ultrasonic array sensor is designed to realize phased array measurement, ultrasound aperture tends to be relatively small compared to a measurement area. Vector reconstruction relies on the difference of array element positions. Therefore, small aperture compared to measurement area cause vector estimation error. This paper proposes a noise model to solve that. Firstly, specially designed phased array measurement setup is described. Newly proposed signal processing is discussed. Then, performance of the measurement system is evaluated with an experiment.

2. Measurement System

2.1 Cross-Plane Phased Array Sensor

Electric steering is one of the unique features of phased array technique. Multi-channel pulser drives elements in an array sensor with certain time delays. Due to those delays, focused ultrasound beam is formed along beam axis. This focusing can be used to steer ultrasonic beam in different lateral angle. Maximum steering angle is defined by the inter-element pitch and wavelength. Solid body for NDE permits large inter-element pitch compared to liquid media for UVP. For example, steel has a sound speed of approximately 5,900 m/s while water has only that of 1,500 m/s. Therefore, the array sensor design is the key point of the phased array ultrasonic measurement especially for UVP. It is possible to 3D measurements but it is not in the scope of this paper. Ultrasonic array sensor was designed so that maximum beam steering angle of 30 degrees can be formed without significant grading lobe. Basic frequency of 4 MHz was chosen to obtain back-scattered echo from even small particle in turbid water. Each array plane consists of 16 elements since ultrasonic pulser/receiver has a total TRX channel of32. Sound

https://doi.org/10.7795/810.20190809

pressure is computed with the discrete point source method [8]. After the parametric survey, inter-element is decided to be 0.25 mm. Computed sound pressure for the array sensor is shown in Fig. 1.

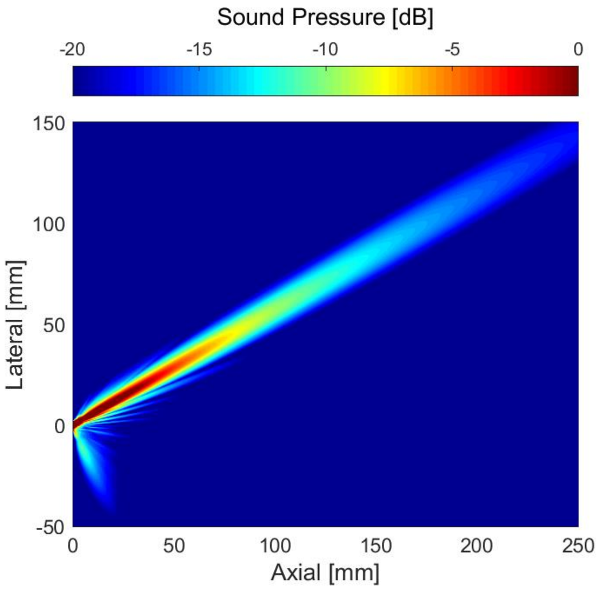

Figure 1: Computed sound pressure with electric steering angle of 30 degrees.

2.2 Pulser/Receiver

Phased array technique requires multi-channel simultaneous ultrasonic excitation. In addition, UVP requires continuous measurement of echo signal in time-series. Pulses are emitted at the predetermined pulse repetition frequency (PRF) and echo signals are sampled with the same interval. In order to realize phased array UVP measurement with larger number of element channels, 32ch pulser/receiver (JAS-21, Japan Probe Co. Ltd.) is custom manufactured (Fig. 2). The pulser/receiver has integrated AD converter and very fast data link to the host computer. Detailed specifications of the pulser/receiver is summarized in Tab. 1. Number of pulse repetitions is implemented using focal law function. Ultrasonic emission and receptions are carried out at certain repetitions. Digitized data is temporally stored on the device memory. After the repetitions, the host device fetches data via USB3 data link and then restart the emission with a command.

Figure 2: Photograph of 32ch pulser/receiver and array sensor.

Table 1: Specification of the 32ch pulser/receiver

TRX Channel	32ch.
Voltage	-300 V (Adjustable, Negative square)
Frequency	10k‑11 MHz (up to 100 cycles)
PRF	up to 1 MHz
Focal Law	up to 4,096
Amplifier	+92dB (TGC)
Analog Filter	LPF, HPF
Digitizer	32 MS/s, 12-bit
Memory Length	8M points/ch.
Data Link	USB3 (max. 400MB/s)

2.3 Software

Each pulse repetition results in a numerous size of echo data sets. Low-level control interface is designed with C++ library to handle data efficiently. The library communicates with a FPGA on the device over the WinUSB driver. The user-side interface was written on NI LabVIEW. State machine is divided into three loops: acquisition, Doppler signal processing and vector reconstruction. Acquisition loop monitors the control settings and communicates with the pulser/receiver via C++ library. Acquired echo data sets are fed to the FIFO. Doppler signal processing loops analyze data on the FIFO sequentially on an independent thread. The analysis algorithm is vectorized and paralleled to improve the performance. Amplitude and quadrature sequence are stored on the data queue. Vector reconstruction loop fetches data from the queue. Moving average filter and algorithm described in section 3 are computed. Results are shown in real-time on the user interface. Snapshot of the program is shown in Fig. 3.

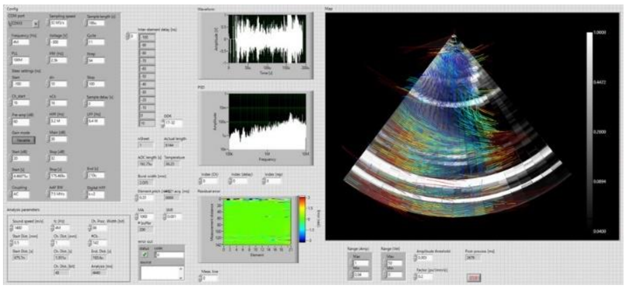

Figure 3: User interface of the measurement software.

3. Vector Reconstruction

3.1 Basic Principle

Fig. 4 illustrates the basic principle of the vector reconstruction for 8 elements configuration. Ultrasonic beam is formed on the designated steering angle with phased array technique. The emission vector is $\boldsymbol{e_e}$. Due to the motion of the reflector particle, reflected echo signal is slightly Doppler shifted. The reception vector varies depending among element channels and Doppler frequency varies as well. Velocity is independently computed for each element at first. Then, those results are combined among N channel as follows.

$$\begin{pmatrix} e'_{1x} & e'_{1y} \\ e'_{2x} & e'_{2y} \\ \vdots & \vdots \\ e'_{Nx} & e'_{Ny} \end{pmatrix} \begin{pmatrix} v_x \\ v_y \end{pmatrix} = \begin{pmatrix} v_1 \\ v_2 \\ \vdots \\ v_N \end{pmatrix} \tag{1}$$

where reconstruction vector $\overrightarrow{\boldsymbol{e}'}$ is defined as

$$\overrightarrow{\boldsymbol{e}'} \equiv (\overrightarrow{\boldsymbol{e}_{\mathrm{T}}} + \overrightarrow{\boldsymbol{e}_{\mathrm{R}}})/2. \tag{2}$$

Previous vector reconstruction was performed along those procedures. However, instantaneous velocity reconstruction was difficult due to vector estimation errors, and time-averaging was required to reduce errors.

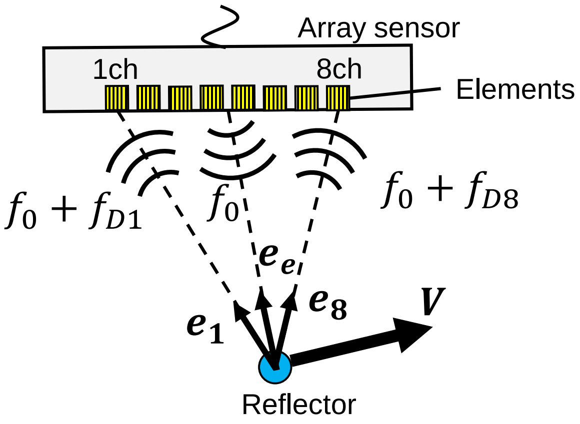

Figure 4: Doppler frequency difference with array configuration.

3.2 Noise Model

As one can see in Eq. (1), the previous reconstruction system was over-determination; only two unknown values are derived from *N* known values. In order to obtain exact solutions, additional factors shall be introduced. Noise model is proposed to solve this issue. First, define error ratio ER_i as

$$v_i = \overrightarrow{\boldsymbol{e}'_i} \cdot \vec{\boldsymbol{v}} + ER_i. \tag{3}$$

We firstly assumed that fraction of measured data is an error (either plus or minus). This fraction varies in one measurement plane. Second assumption is that error ratio is proportional to the emission and reception directivities *D*. Total noise level is decided by user-defined SNR.

$$\frac{1}{\mathrm{SNR}} \cdot \vec{\boldsymbol{v}} = \sum \overrightarrow{\boldsymbol{e}'_i} \cdot ER_i \cdot D_T \cdot D_{Ri} \tag{4}$$

Directivity of elements [5] is calculated with inter-element pitch *a*, basic frequency f_c and sound speed *c*.

$$D = \mathrm{sinc}\left(\frac{\pi f_c a}{c}\right) \tag{5}$$

Finally, modified vector reconstruction can be written as follows.

$$\begin{pmatrix} e'_{1x} & e'_{1y} & 1 & \cdots & 0 \\ e'_{2x} & e'_{2y} & 0 & \cdots & 0 \\ \vdots & \vdots & \vdots & \ddots & \vdots \\ e'_{Nx} & e'_{Ny} & 0 & \cdots & 1 \\ -1/D_{\mathrm{T}} \cdot SNR & 0 & e'_{1x} \cdot D_{\mathrm{R1}} & \cdots & e'_{Nx} \cdot D_{\mathrm{R}N} \\ 0 & -1/D_{\mathrm{T}} \cdot SNR & e'_{1y} \cdot D_{\mathrm{R1}} & \cdots & e'_{Ny} \cdot D_{\mathrm{R}N} \end{pmatrix} \begin{pmatrix} v_x \\ v_y \\ \mathrm{ER}_1 \\ \mathrm{ER}_2 \\ \vdots \\ \mathrm{ER}_N \end{pmatrix} = \begin{pmatrix} v_1 \\ v_2 \\ \vdots \\ v_N \\ 0 \\ 0 \end{pmatrix} \tag{6}$$

Two velocity components and *N* errors are estimated by solving this equation (e.g. LU factorization) for each measurement volume.

4. Experiment

4.1 Setup

The experimental setup is illustrated in Fig. 5. The experiment was performed in a tall water tank. The bore diameter of the tank was 580 mm and the height is 1,500 mm. At the bottom of the tank, there is a drain hole of which diameter is 60 mm. Water is slowly drained out at the flow rate of 9 liter/min. Bulk velocity is approximately 50 mm/s.

Cross-plane phased array transducer is installed at the bottom of the tank so that measurement plane covers the drain hole. The sensor surface faced 60 mm behind the edge of the hole. Ultrasonic beam is scanned +/- 36 degrees, which is slightly larger beyond the design discussed in Sec. 2.1. Therefore, results from end beamlines are not reliable. Measurement distance is 140 mm. Pulse is repeated at 2,500 Hz. Measurement time was approximately 540 ms/plane. Velocity profiles are averaged over 200 planes. While two planes are measured during the experiment, only data of vertical plane is discussed here.

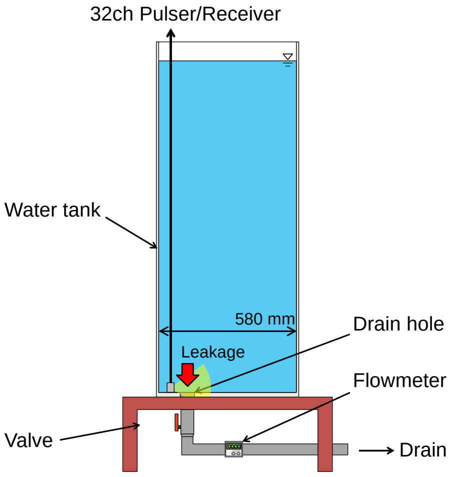

Figure 5: Water drainage observation setup.

4.2 Results and Discussion

Fig. 6 shows comparison of the reconstructed vector maps without and with noise model. Echo amplitude is illustrated in grayscale and velocity vector is color coded (see digital PDF for color). Vector length changes according to the velocity. Three white circumferential zones are observed. Those lines are due to the strong echo reflection from the edges of holes or bottom reflection in the solid wall. Previous reconstruction method causes many erroneous vectors. Since error vector tends to have higher velocity, it is hard to distinguish flow pattern. On the other hand, the map with the noise model successfully eliminates error vectors. Leakage flow can be clearly seen. However, maximum velocity in the drain hole is less than 50 mm/s. It might be associated to inappropriate SNR value used for the reconstruction. Since the purpose of the research itself is to determine the leakage, quantitative velocity measurement was not originally the biggest concern. Yet, for the further investigation, optimized SNR determination will be important.

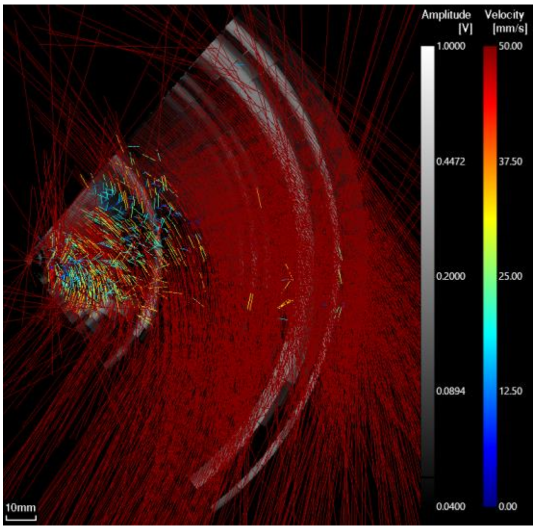

(a)Without noise model.

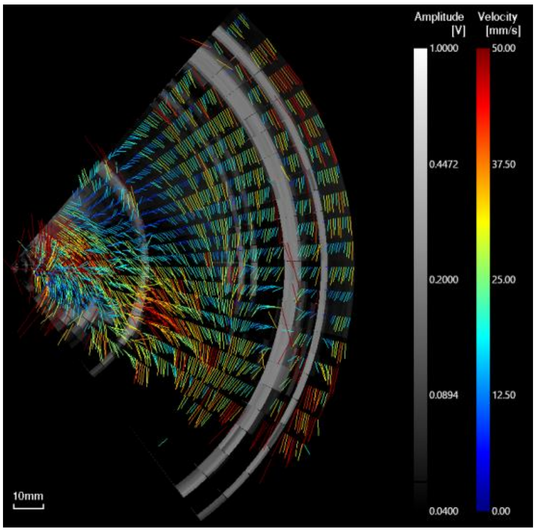

(b) With noise model.

Figure 6: Comparison of reconstructed velocity vector maps.

5. Summary

Vector map reconstruction is discussed. Phased array technique is used to emit ultrasound in wide angle. Cross-plane phased array sensor is designed using the discrete point source method. Newly developed 32ch pulser/receiver enabled real-time measurement together with specially developed software. Noise model was proposed to mitigate the erroneous velocities in vector reconstruction. The performance of the proposed model is evaluated in the experiment. The flow pattern became clear to identify while the quantitative value deviation is still open for question. Further optimizations of the algorithm and quantitative comparisons will be performed in future work.

References

[1] Tokyo Electric Power Company: Progress status and future challenges of the mid-and-long-term roadmap toward the decommissioning of TEPCO’s Fukushima daiichi nuclear power station units 1-4 (Outline).

[2] Beller LS & Brown HL: Design and operation of the core topography data acquisition system forTMI-2, EG & G Idaho, Inc., GEND-INF-012 (1984).

[3] Ihara T, *et al*.: Fundamental study of ultrasonic measurement for leakage flow mapping and debris inspection, The 26th International Symposium on Transport Phenomena (2015), 96.

[4] Malkin RE, *et al*.: Surface reconstruction accuracy using ultrasonic arrays: Application to non-destructive testing, NDT&E Int., 96 (2018), 26-34.

[5] Drinkwater BW, *et al*.: Ultrasonic arrays for non-destructive evaluation: A review, NDT&E Int., 39 (2006), 525-541

[6] Franke S, *et al*.: Two-dimensional ultrasound Doppler velocimeter for flow mapping of unsteady liquid metal flows, Ultrason., 53 (2013), 691-700.

[7] Hamdani A, *et al*.: Experimental study of bubbly swirling flow in a vertical tube using ultrasonic velocity profiler (UVP) and wire mesh sensor (WMS), J. Mech. Sci. Tech., 30 (2016), 9, 3897-3905.

[8] Ahmad R, *et al*.: Modelling of phased array transducers, J. Acoust. Soc. Am., 117 (2005), 1762-1776.

Development of a Remote Water Leakage Localization System Combined with Phased Array UVP and Robot

Ryo NISHIWAKI [1], Ari HAMDANI [2], Hideharu TAKAHASHI [2], Gen Endo [3] and Hiroshige KIKURA [2]

[1] Department of Nuclear Engineering, Tokyo Institute of Technology / N1-7, 2-12-1, Ookayama, Meguro-Ku, Tokyo, 152-8550, Japan
[2] Research Laboratory for Nuclear Reactors, Tokyo Institute of Technology / N1-7, 2-12-1, Ookayama, Meguro-Ku, Tokyo, 152-8550, Japan
[3] School of Engineering, Tokyo Institute of Technology / I1-68, 2-12-1, Ookayama, Meguro-Ku, Tokyo, 152-8550, Japan

At the Fukushima Dai-ichi Nuclear Power Station (NPS), investigations of NPS condition are conducted to take out fuel debris in order to achieve the decommissioning. However, the primary containment vessels (PCVs) was damaged in the accident and the cooling water injected to cool the fuel debris is leaking out. Therefore, investigating the leakage locations of PCVs is needed to stop leaking. In this research, we developed a system to investigate leakage locations remotely. We applied a flow vector mapping by Phased Array UVP method as a method of investigating leakage locations, and we considered that this method is possible to estimate leakage locations by measuring water flow in the bottom of the PCVs. In order to measure remotely using this method, we have developed a self-localization method. We also have developed a robot which can control sensor positions. After that, we experimented a leakage location estimation by remotely using the developed system, and we confirmed that it is possible to estimate leakage positions from the flow vector map we measured. Therefore, we have developed a basic remote leakage locating system that has the possibility to be applied to investigate the leaking locations.

Keywords: Phased array, Vector UVP, Robot, Remote measurement, Self-localization

1. Introduction

The severe accident at Fukushima Dai-ichi nuclear power station (Fukushima Dai-ichi NPS) occurred due to Tohoku earthquake and tsunami in 2011. At president, Fukushima Dai-ichi NPS has been able to keep stable state while injecting water for cooling fuel debris into primary containment vessels (PCVs), and decommissioning process of Fukushima Dai-ichi NPS is underway [1]. However, because the PCVs have been damaged in the accident, the injected water which is contaminated by debris leaks out from the PCVs. Leakage of contaminated water has become a large problem in taking out fuel debris and proceeding the decommissioning. In order to stop the leakages, detections of these leakages are required. However, because the PCVs are highly-dosed environments, people cannot enter the PCVs and find leakages. Therefore, a remote measurement by robot is required to search for leak locations. Apart from the purpose of identifying the leakage locations, robots have already been inserted for the purpose of investigating the PCVs internal condition. Investigations were conducted by robots which have cameras, and as a result, they are revealed that the existence of fuel debris and the staying water inside of PCV is cloudy. For this reason, optical measurements in a wide range of in-vessel inspection is difficult. Therefore, we focused on the ultrasonic measurement technic for PVCs survey, as this is a measurement method which is possible to meet demands in the environment of PCVs. Because ultrasonic measurement applied measurement for opaque liquid and internal investigation of Three Mile Island nuclear power plant accident, this technique can overcome the environment of PCVs such as a cloudy water and highly-dosed environment. Therefore, we have been developing a technique for identifying leakage locations from flow map using the ultrasonic measurement. For the flow mapping measurement, a phased array vector ultrasonic velocity profiler (UVP) method is proposed by Kikura [2]. The phased array UVP method is a flow measurement method combined with phased array technique which can measure 2-D velocity map of flow in cloudy water. Using this method, we can measure 2-D flow map and it is assumed that the leakage position can be estimated from the flow patterns around leakages.

In order to apply this measurement technology to the investigations in PCVs, it is necessary to consider a method of remotely measuring. Therefore, we aim to develop a remote measurement technology integrating phased array vector UVP method with robot technique. To develop the remote measurement system, we examined the specifications of the robot necessary for identifying leakage locations and furthermore made a basic prototype robot which is composed of a body of four wheels and 3 degrees of freedom robot arm. In addition, we also developed a measurement method to identify the position of the sensor in water. In the self-position identification system, we assumed the estimation of the self-position within a known environment and developed a basic self-position estimation system using particle filter [3]. Then, a verification experiment which measured a flow pattern around mockup leakage were conducted using the developed remote measurement system.

2. Phased array vector UVP

https://doi.org/10.7795/810.20190809

Phased array vector UVP method is a combination technique of phased array method and UVP method. This measurement method can measure a two-dimensional velocity vector map of flow using only one small sensor. However, the measurable flow is limited to the steady flow at the present time because the time resolution is low due to the necessary of averaging.

2.1 Phased array technique

A picture of ultrasonic phased array sensor and its elements arrangement is shown Fig. 2.1. Phased array sensor has 8 small elements, and the elements are aligned on a straight line in the linear type. By controlling the transmission timing (delay time) independently of each element, generating an arbitrary wave from the principle of Huygens is applicable. By setting the delay time, changing the direction of the ultrasonic beam to provide a steering angle or focus beam is possible. The steering angle θ_s is expressed by the following equation (2.1), where the sound velocity is c, the pitch of elements is d, and the delay time interval between the oscillators is Δt.

$$\theta_s = sin^{-1}\left(\frac{c\Delta t}{d}\right) \tag{2.1}$$

This steering angle control is one of the major advantages of the phased array method. However, the applicable oblique angle depends on the individual characteristics of sensors and the oblique angle is set within a range in which grating lobes do not occur.

2.2 Phased array vector UVP method

An explanation drawing of the measurement principle of a two-dimensional flow mapping technique using a phased array sensor is shown in Fig. 2.2. It is assumed that the phased array sensor which has eight elements is used in this explanation. Ultrasonic pulses of the center frequency f_0 transmitted from the sensor are reflected at the interface of the tracer particles on the measurement line. After that, the first and eighth elements at both ends receive the Doppler frequencies f_{D1} and f_{D8}. By making simultaneous equations of Doppler frequency and particle velocity equation, the two-dimensional velocity vector V of the tracer particle can be obtained as follows.

$$\boldsymbol{V} = \frac{c}{f_0}\begin{bmatrix}\boldsymbol{e_0}+\boldsymbol{e_1}\\ \boldsymbol{e_0}+\boldsymbol{e_8}\end{bmatrix}^{-1}\cdot\begin{bmatrix}f_{D1}\\ f_{D8}\end{bmatrix} \tag{2.2}$$

Then, by solving the above equation at each point on the measurement line, it is possible to obtain the velocity vector at a number of measurement points on the measurement line. Furthermore, measuring velocity vector distribution in various directions by changing the transmission direction angle of ultrasonic waves is possible. Therefore, two-dimensional flow mapping can be obtained.

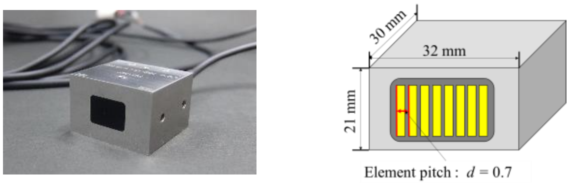

Fig.2.1. Phased array sensor picture and geometry.

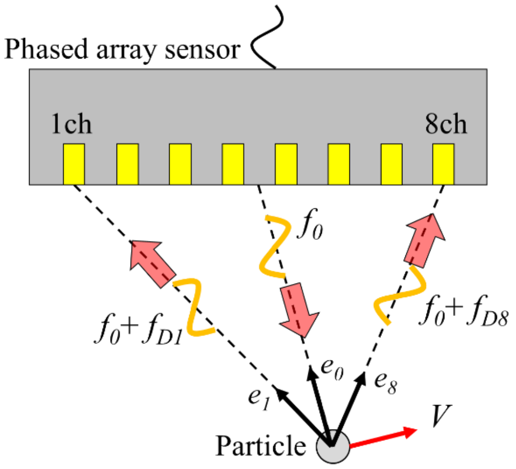

Fig.2.2. The measurement method of phased array vector UVP.

3. Self-locating system

Particle filter is a method of sequentially estimating a state of the system based on the Monte Carlo method. Because the particle filter method can be applied to nonlinear and non-Gaussian state space model, the usefulness of it has been reported in simultaneous localization and mapping (SLAM) method of robotics [4]. In this study, we applied particle filter algorithm to estimate the self-location in the known environment map.

3.1 Particle filter algorithm

Particle filter can be divided into two steps which are prediction step and filtering step. In the prediction step, the state is estimated at time t from the state space model at time $t-1$. The equation of state estimation at this time is expressed as follows. Note that f represents the prediction model and w_t represents the prediction noise.

$$X_{t|t-1} = f\left(X_{t-1|t-1}\right) + w_t \tag{3.1}$$

Then, in the filtering step, likelihood calculation is conducted at first. The likelihood is a probability distribution $\mathrm{P}\left(Y_t|X_{t|t-1}\right)$ in which the observation quantity Y_t is observed when the state quantity is $X_{t|t-1}$. Then, resampling is conducted in proportion to the calculated likelihood. Resampling is an operation which delete existing particles numbers of a place where the ratio of likelihood is small and copy other existing particles numbers from a place where the ratio of likelihood is large. While repeating the above prediction step and filtering step, particle filter estimates state on time series data. Then, the estimated value of state is a value with the largest number of particles.

3.2 Self-locating system with particle filter

In self-location estimation underwater, six state quantities (x, y, z, Φ, Θ, Ψ) which considers the three-dimensional coordinate system and the posture angle is required. In this research, we aimed to develop a fundamental system of particle filter, thus the estimated state quantity was limited to two (x, y). For self-location estimation in particle filter, 4 ultrasonic sensors are used. Using these sensors, the distance from the wall surface are measured within the

https://doi.org/10.7795/810.20190809

known environmental map and self-location is estimated. In the developed particle filter, uniform linear motion is assumed for the prediction step. In addition, to estimate (x, y), we used (x, y, $\dot{x}$, $\dot{y}$) which added the speed to the state quantity and (v_x, $v_{⍰}$, $v_{\dot{x}}$, $v_{\dot{y}}$) which is prediction noises. Then, the prediction model can be expressed as follows.

$$\begin{pmatrix} x_{t+1} \\ y_{t+1} \\ \dot{x}_{t+1} \\ \dot{y}_{t+1} \end{pmatrix} = \begin{pmatrix} 1 & 0 & 1 & 0 \\ 0 & 1 & 0 & 1 \\ 0 & 0 & 1 & 0 \\ 0 & 0 & 0 & 1 \end{pmatrix} \begin{pmatrix} x_t \\ y_t \\ \dot{x}_t \\ \dot{y}_t \end{pmatrix} + \begin{pmatrix} v_x \\ v_y \\ v_{\dot{x}} \\ v_{\dot{y}} \end{pmatrix} \quad (3.2)$$

In the filtering step, the likelihood calculation assumed a Gaussian distribution for the distance measurements of the sensors. From the positional information D in the water box by the distance measurement of the sensors and the position X^k of the kth particle, the likelihood P^k is obtained as follows. Note that σ^2 is the variance.

$$P^k = \frac{1}{\sqrt{2\pi\sigma^2}} exp\left(-\frac{\left(X^k - D\right)^2}{2\sigma^2}\right) \quad (3.3)$$

3.3 Verification experiment of self-locating system

In order to fundamentally verify the developed self-location estimation system, sensors were controlled position in a water tank which is an internal dimension of 380 × 380 mm by a 3-axis automatic stage and carry out a self-locating experiment in water. Four sensors with a center frequency of 4 MHz manufactured by IMASONIC were used, and four sensors were arranged at a pitch of 90° as shown in Fig. 3.1. The experimental results are shown in Fig. 3.2. In the experiment, the 3-axis automatic stage was applied for position control, the movement was started from the position (250, 90) in the water box. Then, the sensors were moved 200 mm on the Y direction and 145 mm on the X direction, the trajectory became a rectangle. From the result shown in Fig. 3.2, it could be confirmed that the result of the self-location estimation tracked routes almost same with the routes set for the stage. The error between the tracked routes and the route set in the stage was 1.06 mm on average. In addition, the standard deviation was 0.82 and the mode of error was 0.4 mm. Therefore, the certainty of the self-location system was verified.

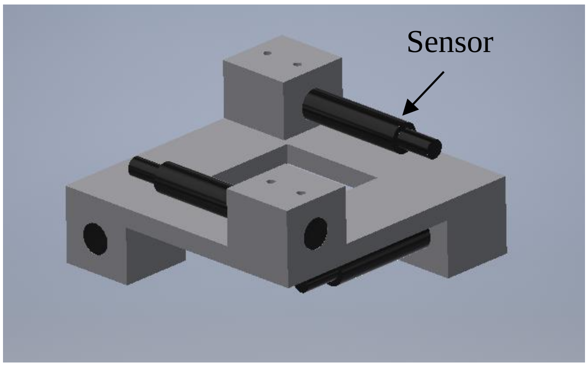

Fig.3.1. Sensor holder for self-locating

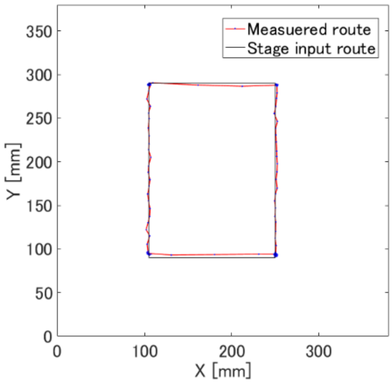

Fig.3.2. Experimental results of self-locating

4. Robot system

In order to conduct the remote measurement, carrying the measurement sensors and controlling the position of them are necessary. Therefore, for a basic remote measurement system, a robot which has four-wheel body with a 3 degree of freedom arm were developed. The picture of the robot system is shown in Fig. 4.1. The robot arm has three-degree-of-freedom using two link mechanism, and the second joint adopts a wire pulley mechanism [5]. The advantage of this robotic arm is lightweight that contributes saving the output of motors. Therefore, the robotic arm is compact and has enough output for transporting phased array sensor. The array sensor was controlled its position by a motor driver (EPOS2 24/5, MAXSON) using a DC motor (RE25 ϕ25 24V 20W, MAXSON). The position of phased array sensor is calculated from the rotary encoder attached to the DC motor. The wheel body robot has EC motor (EC 25 φ 60 24 V 100 W, MAXSON) mounted on each wheels, and independent control is possible by using each motor controller (EPOS2 24/5, MAXSON). Therefore, the mobility of the robot is high and rotating on the spot is possible.

Fig.4.1. Picture of the robot system

5. System Varification and Flow Measurement

We conducted experiments to verify the effectiveness of the remote measurement system developed in a mock-up environment. The outline of the experimental setup is shown in Fig. 5.1. The sensors were carried into a water box by the robot system, and they were controlled their positions near the mock-up leakage location in the water box by the robot arm. After that, self-locating estimation and flow measurement were conducted. The sensors were connected with the robot arm by the sensor holder. At the bottom of the holder, 8ch phased array sensor was attached for flow mapping and 4 other sensors were attached at 150 mm from the bottom for self-location estimatiuon using the holder shown in Fig. 3.1. The phased array sensor applied in the experiemnt has 2 MHz frequency, the elements size are 0.65 × 7.5 mm, and the elements pitch is 0.7 mm. As the environment for mock-up measurement experiment, a mock-up leakage port with an 52 mm inside diameter was made in an acrylic water box which the size is 1200 × 600 × 600 mm and the inner size is 1165 × 550 × 550 mm. Water was circulated at 20 L / min by a magnet pump. Nylon particles which average particle size was 80 µm were mixed in the water as tracer particles. The measurement line of the ultrasonic beam was controlled from -10° to 10° at intervals of 5°, hence five measurement lines were scanned. The flow velocity distribution was measured and averaged 1000 times on each measurement line.

In the experiment, the flow pattern close ot the leak port was measured. We planned to place the sensors in order of measurement points A, B and C as shown in Fig. 5.2.

The measurement results are shown in Fig. 5.3. By self-locating system using particle filter, position informations of points A (229.9, 105.5), B (272.9, 99.0) and C (324.9, 101.9) were measured. Moreover, the flow pattern can be confirmed flow toward to the leakage location from the measured flow map, especially the strongest flow can be confirmed at measurement point B where the position was in front of the leak port. In the measurement of point B, the flow from the positive direction of the X-axis is more strongly measured. However, this is considered to be due to the position of the inlet port. From the results, the effectiveness of the remote measurement system was confirmed.

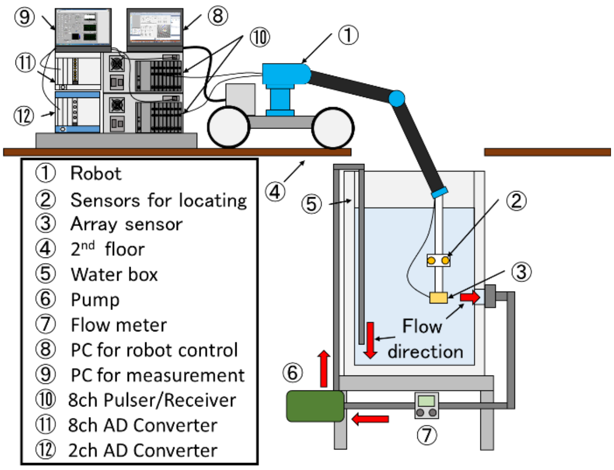

Fig.5.1 Setup of measuring flow field around mock-up leakage

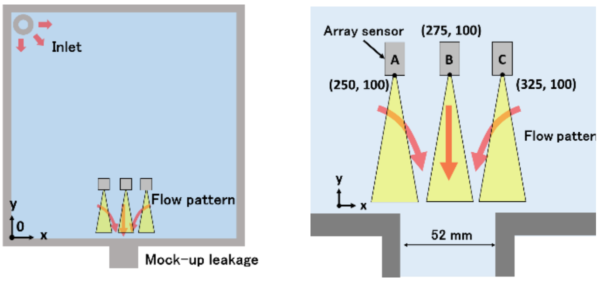

(a) Top view (b) Near the leak port

Fig.5.2. Measurement points in the water box

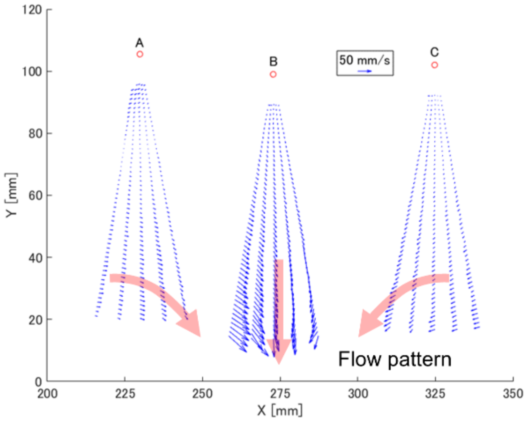

Fig.5.3. Measurement results of self-locating and flow mapping

6. Conclusion

In this research, the basic development of the remote measurement system for investigating the PCVs leakage locations of the Fukushima Daiichi Nuclear Power Station was conducted. We developed a remote measurement system by integrating the robot and the measurement system which is consist the self-position estimation system and Phased array vector UVP method. Then, we conducted 2D-flow field measurement near the leak port in mock-up environment using the developed system. From the experimental results, we could confirm the effectiveness of the system.

References

[1]Ministry of Economy, Trade and Industry of Japan: TEPCO Medium and long term road map for decommissioning of Fukushima Daiichi Nuclear Power Station http://www.meti.go.jp/earthquake/nuclear/pdf/20171003.pdf, (in Japanese), (2017).

[2] H. Kikura, et al.: Study on Ultrasonic Measurement for Determination of Leakage from Reactor Vessel and Debris Inspection, The 11th National Conference on Nuclear Science and Technology, Da Nang, (2015).

[3] G. Kitagawa: Monte Carlo filter and smoother for non-Gaussian nonlinear state space models. Journal of computational and graphical statistics, 5(1), (1996), 1-25.

[4] F. Dellaert, et al. Monte Carlo localization for mobile robots. 1999 IEEE International Conference on Robotics and Automation, Detroit, (1999).

[5] S. Hirose, et al: Development of Tendon Driven Multi-Joint Manipulator Based on Coupled Drive, The Society of Instrument and Control Engineers, 26(11), (1990), 1291-1298.

https://doi.org/10.7795/810.20190809

11th International Symposium on Ultrasonic Doppler Methods for Fluid Mechanics and Fluid Engineering
Berlin, Germany (5.-7. September 2018)

Characteristics of Large-scale Structures in Turbulent Rayleigh-Bénard Convection in a Liquid Metal Layer

Takatoshi YANAGISAWA[1], Megumi AKASHI[2], Yuji TASAKA[2], Yuichi MURAI[2], Tobias VOGT[3] and Sven ECKERT[3]

[1] Japan Agency for Marine-Earth Science and Technology, 2-15 Natsushima-cho Yokosuka 237-0061, Japan
[2] Laboratory for Flow Control, Hokkaido University, Sapporo 060-8628, Japan
[3] Helmholtz Zentrum Dresden-Rossendorf, Dresden, Germany

We performed laboratory experiments on Rayleigh-Bénard convection with a liquid metal in a square box geometry having an aspect ratio five. Horizontal velocity profiles of convective flow were measured at several lines by using ultrasonic velocity profiling (UVP). By combining the information from profiles, we can reconstruct organized large-scale flow structures with turbulent fluctuations. Systematic variation of the structure was detected with increasing the Rayleigh number (*Ra*) from 10^4 to 10^5; a quasi-two-dimensional roll changes to a cell having a relatively larger horizontal scale. In addition, we found that the large-scale structure, whether it is roll or cell, show quasi-periodic oscillation whose representative period is approximately same as the circulation time of the large-scale flow. We also performed numerical simulations of convection with the same geometry as our experiments by setting a small Prandtl number (Pr=0.025) like a liquid metal. Quantitative comparison on the velocity profiles between experiments and simulations provided quite satisfactory agreement, and we analyzed the whole structure of the flow and the style of oscillation in detail based on the result of simulation.

Keywords: Rayleigh-Bénard convection, thermal turbulence, liquid metal, coherent structures, multi-dimensional measurement

1. Introduction

Rayleigh-Bénard convection (RBC) is an important problem in fluid dynamics and is also a basic configuration for various issues in geophysics, astrophysics and engineering. The RBC system is defined by the three dimensionless parameters, Rayleigh number (*Ra*), Prandtl number (*Pr*) and the aspect ratio of the fluid container (Γ). The convective flow structures were summarized on *Ra*-*Pr* parameter space and the convective flow reaches thermal turbulence regime for sufficiently large *Ra* depending on *Pr* [1]. Stable region of the two-dimensional (2D) steady roll structures on the *Ra*-wavenumber plane, named as "Busse balloon", was theoretically established for various *Pr* [2]. For very low *Pr* condition, $Pr \sim O(10^{-2})$, the Busse balloon shrinks into quite narrow area and the 2D rolls easily become time dependent slightly beyond the critical value of *Ra* as suggested by laboratory experiments [3]. Some numerical simulations demonstrated the behavior of travelling waves on the roll structures beyond the boundary of the Busse balloon until $Ra \sim 5 \times 10^3$ even with irregular time dependent flow [4]. Transitions to turbulence regime occurs with further increase of *Ra* and thus emergence of fully developed thermal turbulence are expected at relatively lower *Ra* values in low *Pr* convection compared with higher *Pr* fluids, such as air ($Pr \sim 1$) and water ($Pr \sim 7$). However, the process of the transitions to turbulence and the spatio-temporal characteristics of thermal turbulence in low *Pr* convection are not fully understood because liquid metals, representatives of very low *Pr* fluids, are opaque fluids and usual optical methods are not applicable.

Visualizations of the flow field in the opaque fluids have been realized by the ultrasonic velocity profiler (UVP) method [5] and UVP has been applied for investigations of thermal turbulence in low *Pr* convection. Instantaneous velocity distributions in convection of a cylindrical mercury layer were measured by UVP and complex coherent structures with periodic oscillations as called "large-scale circulations" were observed [6,7]. While the range of *Ra* is quite large in their studies, the aspect ratios of the fluid vessels are limited to around unity. The behaviors of RBCs of a liquid gallium layer under various intensities of a uniform imposed horizontal magnetic field in a square container with $\Gamma = 5$ have been investigated by our group [8]. Steady 2D roll patterns aligned parallel to the magnetic field under sufficiently strong intensities of the magnetic field change to the convection pattern having no principal direction under a weak or no magnetic field, and more complex, large-scale fluctuating patterns are observed. Investigations of the complex pattern are, however, limited in a narrow range of *Ra* and its spatio-temporal characteristics have not been elucidated.

The primary objective of this study is to reveal coherent structures connecting between the regular roll structures and the large-scale circulations in the low *Pr* turbulent convection confined by a square container with a moderate aspect ratio. The range of *Ra* is moderate, $O(10^4)$–$O(10^5)$, where convective flow reaches developed thermal turbulence at the maximum *Ra*. Multiple horizontal measurement lines of UVP were set perpendicularly at two heights in the fluid layer and three-dimensional (3D) flow structures were elucidated by combining the information from different profiles

https://doi.org/10.7795/810.20190809

obtained simultaneously. The experimental results were supplemented by direct numerical simulations and the comparison between them have developed understanding whole structures of turbulent flow in low *Pr* convection.

2. Apparatus and method

2.1 Experimental Setup

Schematic diagrams of the experimental setup, the square container filled with the fluid and arrangements of measurement lines of ultrasonic beams, are shown in Fig. 1, (a) top and (b) side view. The lateral walls of the vessel are made of 10-mm-thick PVC to attain thermal insulation. The fluid layer has a square horizontal cross section of 200 mm × 200 mm and a height of 40 mm, giving an aspect ratio of five. It is sandwiched between the top and bottom copper plates which ensure isothermal heating and cooling the system. The temperatures of each copper plate were controlled by water flow through channels inside the plates. *Ra* and *Pr* are described as

$$Ra = \frac{\beta g \Delta T L^3}{\nu\kappa} \cdots (1) \qquad Pr = \frac{\nu}{\kappa} \cdots (2)$$

Here, g, L and ΔT are gravitational acceleration, the height of the fluid layer and vertical temperature difference of the fluid layer, β, κ, and ν are thermal expansivity, thermal diffusivity and kinematic viscosity of the test fluid, respectively. The test fluid is the eutectic alloy of gallium, $Ga^{67}In^{20.5}Sn^{12.5}$ with Pr = 0.03 and the Ra can be controlled in the range from 7.9×10^3 to 1.0×10^5. UVP was adopted for obtaining instantaneous velocity profiles. Ten ultrasonic transducers with the basic frequency of 8 MHz were mounted horizontally in the holes at two side-walls of the vessel shown in Fig. 1 and contacted directly with the test fluid, where the gray lines in the figure indicate each measurement line crossing perpendicularly. Four transducers were set at 10 mm from the top plate (z = 30 mm) and other six transducers were set at 10 mm from the bottom plate (z = 10 mm). The temporal, spatial and velocity resolutions of the UVP measurements are 1.2 s, 1.4 mm and 0.5 mm/s, respectively. Measurements on the ten transducers were switched in time and velocity profiles along each measurement line were acquired sequentially. Thermistor (see T in Fig.1) was installed in the fluid layer 3mm below the top plate to measure temperature fluctuations with 10 Hz.

2.2 Method of numerical simulation

Direct numerical simulations are performed for the same geometry as experiments enclosed by no-slip velocity boundaries. The temperature is fixed at the top and bottom boundaries, while it is assumed to be adiabatic at side-walls. A set of governing equations are solved by the finite difference method with a uniform grid interval. The *Pr* is set as 0.025 to simulate a liquid metal. The detail of the simulation code is referred in [9].

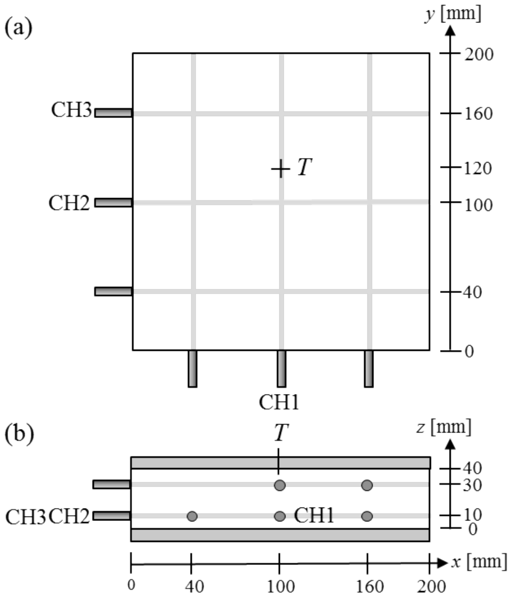

Figure 1: Experimental setup and arrangement of measurement lines: (a) top view and (b) side view, where gray lines indicate the measurement lines of UVP

3. Experimental results

Roll-like structures are observed at the lower range of *Ra* in this experiment as shown by spatio-temporal velocity maps in Fig. 2 (a,b), where velocity distribution was obtained parallel to the y-direction ((a) CH1) and the x-direction ((b) CH2) at $Ra = 7.9 \times 10^3$. The velocity maps (a) show wavy patterns with four stripes corresponding to four rolls whose time averaged axes are aligned parallel to the x-direction. Such pattern is commonly observed by other measurement lines parallel to the y-direction. The period of the oscillation is around 120 s and is the same order with the thermal diffusion time of the test fluid, $L^2/\kappa \approx 153$ s. The velocity map (b) shows patches, which are smaller than 30 mm and are synchronized with the wavy pattern observed in (a). The maximum velocity measured on the line of the x-direction is about half of that on the y-direction. This "four-roll structure" is stable and keeps the direction of roll axes throughout the measurement time once the structure emerges.

Fig. 2 (c,d) shows spatio-temporal velocity maps measured at $Ra = 2.1 \times 10^4$. Wavy patterns corresponding to four or three rolls with axes parallel to x- and y-direction are observed alternately in this flow state. In this flow state, roll-like structure corresponding to four-roll or three-roll aligned to the x- or y-direction are formed, but they are unstable and structures like rolls with a diagonal direction might be observed. And, they take transitions to different structures in some hundred seconds. It is understood as an intermediate regime from "four-roll structure" to the "three-roll structure", therefore, we defined this flow state as "four-three roll transitions".

Quasi-steady roll structures are observed again with the increase of *Ra* as shown in Fig. 2 (e,f) at $Ra = 4.4 \times 10^4$. The velocity map (f) shows a wavy pattern with three

https://doi.org/10.7795/810.20190809

stripes corresponding to three rolls parallel to the y-direction. The magnitude of velocity is larger than that in the lower Ra. And, the period of oscillation of the wavy pattern is shorter than that in the lower Ra.

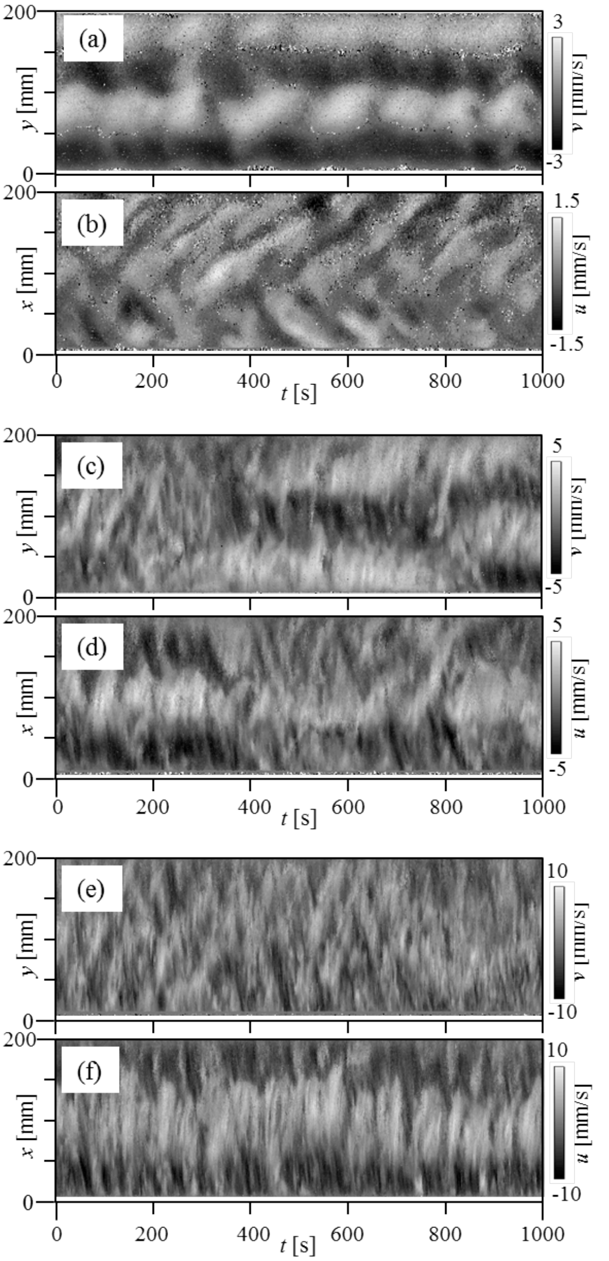

Figure 2: Spatio-temporal velocity distributions obtained on measurement lines CH1 and CH2 at (a,b) $Ra = 7.9\times10^3$, (c,d) $Ra = 2.1\times10^4$, (e,f) $Ra = 4.4\times10^4$

The velocity map (e) shows small patches oscillating synchronized with the wavy pattern. The maximum velocity measured in the y-direction is about 70% of that in the x-direction. This "three-roll structure" is quasi-stable and keeps the direction of roll axes for some thousand seconds, but sudden changes of the direction occur in a long duration.

The roll-like structure does not exist anymore at $Ra = 9.0 \times 10^4$ as shown in Fig. 3 (a,b). The velocity map (a) is obtained on the center lines parallel to the y-direction and shows a wavy band dividing the vessel into two parts. And, the velocity map on center lines to the x-direction shows similar flow patterns. The flow is heading for the center of the vessel from each wall side, hence, upwelling flow at the center is expected. The period of the oscillation is shorter than that in the former regime; it is almost the half of thermal diffusion time of the fluid layer. Fig. 3 (b) shows the velocity map obtained in the measurement line near the wall parallel to the x-direction and show patches dividing the layer length into three or four and oscillating with the same period as the wavy structure on the center lines. The velocity map near the wall parallel to the y-direction shows similar flow patterns. The magnitudes of velocities depend on the positions; the maximum velocities near the wall are about half of the values obtained on the center lines. The main structure is, therefore, a 3D wavy flow dividing the container into two parts. We named this flow state as "cell structure".

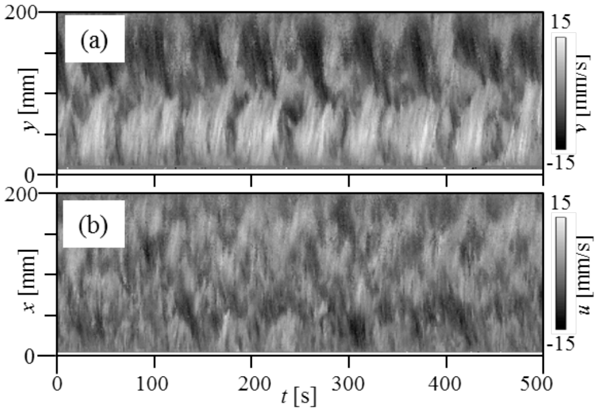

Figure 3: Spatio-temporal velocity distributions along (a) CH1 and (b) CH3 at $Ra = 9.0\times10^4$

The Rayleigh number dependence of the representative flow velocity U in this study can be summarized in a power law as $U(L/\kappa) = 0.1\ Ra^{0.5}$ throughout the structural transitions of flow. Typical oscillation frequencies f_{OS} have also systematic dependency on Ra, where the frequencies are defined as the frequency of the most energetic component in the spatial averaged power spectrum densities of velocity fluctuations. It can be expressed as $f_{OS}(L^2/\kappa) = 0.04\ Ra^{0.4}$. In Fig. 4, the typical period of wavy motions, $\tau = 1/f_{OS}$, is compared with the turn-over time, the time scale of the circulation of the fluid particle in flow structures. The turn-over time, τ_{TO}, is estimated in this system using the variable horizontal wavelength of the flow structure λ, the fluid layer thickness L, and flow velocity U as $\tau_{TO} = (2L+\lambda)/U$. Different symbols in Fig. 4 describe different flow regimes categorized above. A striking feature is that the ratio of τ to τ_{TO} takes values around unity through the studied range of Ra. This graph indicates that the oscillation period of observed wavy motion is comparable to the turn-over time of the flow, not only when the structure is roll-like but also when cell-like with developed thermal turbulence.

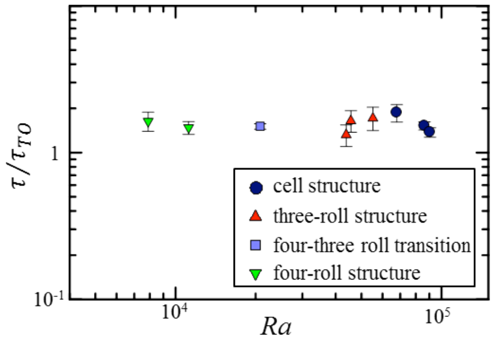

Figure 4: Plots of the periods of oscillation normalized by the turn-over times τ_{TO} with respect to *Ra*

4. Numerical simulations

We successfully reproduced in numerical simulations various behaviors observed in the experiment. Spatio-temporal velocity maps drawn by the data of simulations are useful for direct comparison with experiments, and Fig. 5 shows an example for a cell structure at *Ra* = 1.0×10^5. The large-scale structure, together with the period of oscillation, is consistent with the result of the experiment shown in Fig. 3. The time scale is enlarged for five cycles of oscillation to identify fine structures in the flow. In Fig. 5 (a), we can see narrow oblique stripes in broad bands; they correspond to small vortices advected from the center to sides by the large-scale flow.

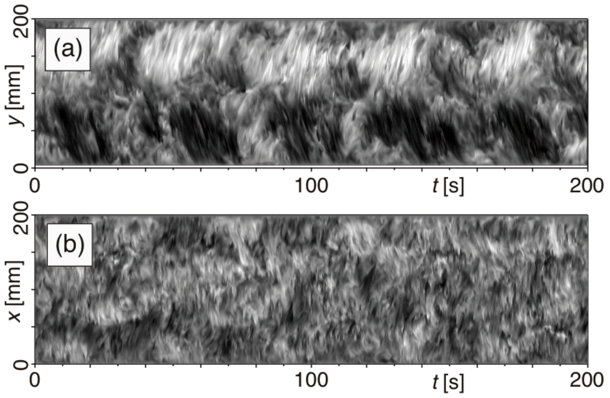

Figure 5: Numerical simulation: spatio-temporal velocity distributions obtained on lines CH1 and CH3. *Ra* = $1.0{\times}10^5$

We can make up 3D image of flow structure from data sets of simulation. Two snapshots at different times are shown in Fig. 6 for the case of Fig. 5. They are indicated by isosurfaces of temperature. Temperature field is much more diffusive than velocity field due to low *Pr* of the fluid, hence isosurfaces of temperature are suitable to see a dominant structure. In this case, upwellings are located around the middle of four sides, while downwellings are located at the center and four corners of the container. While this basic cell-like structure is preserved throughout oscillations, the cell repeats expansion and shrink along *x*- and *y*-direction alternately. The oscillations observed in velocity profiles at center lines reflect this type of quasi-periodic motion of a cell.

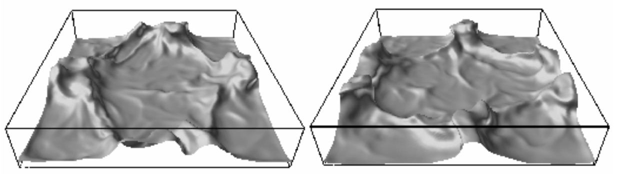

Figure 6: Numerical simulation: 3D view by an isosurface of the temperature. Snapshots at two moments indicating a style of oscillation for a cell-like structure. *Ra* = $1.0{\times}10^5$

5. Summary

Transitions of flow structures in a low *Pr* convection were investigated by using a gallium alloy with multiple lines of UVP measurements. Distinct structures are observed in velocity profiles, those are roll-like up to *Ra* ~ 6×10^4, while cell-like for the larger *Ra*. We found that both structures show quasi-regular periodicity in time. The typical periods of oscillation are comparable to the turn-over time of flow estimated by the measurement of velocity, and this relation holds throughout the transitions in the flow structure.

These transitions can be induced owing to the horizontal scale of the vessel, aspect ratio five. If the scale is short, flow structures are fixed to be roll-like or a single circulation. On the other hand, the cell-like structure and its oscillation observed in the present experiment is strongly constrained by the geometry of the square container. Experiments in wider geometries are expected in a future study to quantify natural horizontal scales of cell-like structures.

References

[1] Krishnamurti R: Some further studies on the transition to turbulent convection, J. Fluid Mech., 60 (1973), 285-303.

[2] Busse F.H: Non-linear properties of thermal convection, Rep. Prog. Phys., 41 (1978), 1929-1967.

[3] Rossby H.T: A study of Bénard convection with and without rotation, J. Fluid Mech., 36, (1969), 309-335.

[4] Nakano A, *et al.*: Numerical simulation of natural convection for a low-Prandtl-number fluid in a shallow rectangular region heated from below, Chem. Eng. J., 71 (1998), 175-182.

[5] Takeda Y (ed.): Ultrasonic Doppler Velocity Profiler for fluid flow, Springer (2012)

[6] Mashiko T, *et al.*: Instantaneous measurement of velocity fields in developed thermal turbulence in mercury, Phys. Rev. E, 69 (2004), 036306.

[7] Tsuji Y, *et al.*: Mean wind in convective turbulence of mercury, Phys. Rev. Lett., 94 (2005), 034501.

[8] Yanagisawa T, *et al.*: Convection patterns in a liquid metal under an imposed horizontal magnetic field, Phys. Rev. E, 88 (2013), 063020.

[9] Yanagisawa T, *et al.*: Flow reversals in low-Prandtl-number Rayleigh-Bénard convection controlled by horizontal circulations, Phys. Rev. E, 92 (2015), 023018.

11th International Symposium on Ultrasonic Doppler Methods for Fluid Mechanics and Fluid Engineering
Berlin, Germany (5.-7. September 2018)

2D Ultrasonic Flow Mapping of the Secondary Flow Field in Free-Surface Vortices

Sean Mulligan[1], Richard Sherlock[2], John Casserly[3], Giovanni De Cesare[4]

[1] College of Engineering and Informatics, National University of Ireland, Galway, University Road, Galway, Ireland
[2] School of Science, Institute of Technology, Sligo, Sligo, Ireland
[3] Department of Civil Engineering and Construction, Institute of Technology, Sligo, Sligo, Ireland
[4] Laboratory of Hydraulic Constructions (LCH), Ecole Polytechnique Fédérale de Lausanne (EPFL), CH-1015, Lausanne, Switzerland

In this study, an application of two dimensional ultrasonic doppler flow mapping was undertaken on a strong full air core free-surface vortex. The vortex was generated in a scroll type vortex chamber with a subcritical approach flow which have common application in hydraulic structures such as sewer vortex dropshafts and energy dissipaters. A 2D array of ultrasonic Doppler profilers was arranged on the vortex chamber using 7 vertical and 7 horizontally arranged transducers to generate 2D flow maps of the secondary flow field to capture the radial and axial velocity fields. The transducers were multiplexed in a diagonal fashion to generate quasi-instantaneous flow maps of the secondary flow. The 2D velocity fields were smoothed using kriging interpolation and post processed using ParaView. The results highlight interesting cellular structures which develop in the secondary flow along with other global features. These observations have strong implications to improve an understanding of free-surface vortex mechanics and stability.

Keywords: Free-surface vortex, vortex dropshafts, UDP array, vector maps, Taylor-Couette flows

1. Introduction

The re-emerging field of hydraulic structure engineering is in full swing due to existing infrastructure upgrade requirements and the development of innovative hydraulic structures [1]. With this, the hydraulics laboratory environment is being continuously challenged to integrate novel experimental methods to aid in a deeper understanding of flow behaviour within such systems [1]. In this article, we present the application of ultrasonic Doppler profiling in vortex drop shaft chambers which are being increasingly deployed in several hydraulic applications [2]. As will be discussed, free-surface vortex flows exhibit quite complex flow behaviour with regards to turbulence and instability mechanisms which can only be resolvable using advanced measurement techniques [3].

Vortex dropshafts are hydraulic structures which utilize the principles of vortex motion to safely drop water flows through significant height differences thus rendering them applicable in sewer systems or hydropower energy dissipation applications. The free-surface vortex flow is generated in a vortex chamber where the flow enters tangentially and discharges axially through the base of the system [4]. Upon discharge into the dropshaft, the residual centrifugal motion causes the fluid to attach to the shaft walls on its course to the bottom of the shaft where the energy is dissipated through friction along the walls.

One of the main indicators which reflects good performance is the stability of the vortex structure. However, vortex flows contain many complex flow features in the secondary flow field which can trigger often severe turbulence and instability in the main vortex core structure [5]. Characterised by the circulation number N_Γ, the vortex strength and stability are dependent on the ratio of the primary tangential (rotating) velocity v_θ field to the secondary radial v_r and axial velocity v_z field [4]; where the latter induces instability in the flow. Many studies have been undertaken on the general hydraulics of the free-surface vortex and vortex dropshaft structures as is summarised in [4] with minimal studies undertaken on the composition of the secondary flow field [3].

Recently, the technique of ultrasonic Doppler profiling [6] was undertaken on the flow in the subcritical vortex chamber by the current authors [5]. In this interesting study, the authors discovered similarities between the secondary flow field in the turbulent free-surface vortex and the classic Taylor-Couette flow [7] through the existence of cellular structures termed Taylor-like vortices. The structures were quantified using the ultrasonic Doppler profiling (UDP) technique amongst other methods such as analytical modelling, laser induced fluorescence observation and numerical modelling. In this article, the UDP program that was undertaken will be discussed in detail. In the study, the authors developed an application of UDP for vortex chamber flows in order to gain independent radial and axial velocity profiles together with flow maps of the aforementioned secondary flow field using a 2D array of ultrasonic Doppler profilers.

2. Testing Configuration

2.1 Physical Model Test Rig

The physical model employed in the experimental study was constructed from 6 mm transparent acrylic and had an orifice diameter of $d = 0.067$ m, inlet width of $b = 0.067$ m and an inlet radius of $r_{in} = 0.207$ m. The walls scrolled inwards according to the logarithmic spiral. The test geometries were mounted in a 0.85×0.95 m tank

https://doi.org/10.7795/810.20190809

which was 0.5 m deep as highlighted in Figure 1, 4 and 5. The tank contained a centrally positioned 0.1 m orifice and rested on a platform over the storage reservoir. A 0.15 m high chamber was used to allow a void underneath the model to give ample space for UDP transducers on the underside of the chamber.

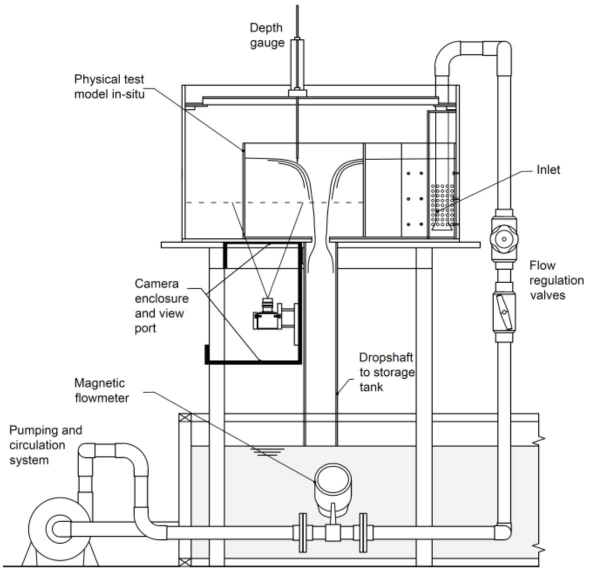

Figure 1: Cross sectional schematic of the vortex flow test rig highlighting the position of the vortex chamber and ancillary hydraulics apparatus.

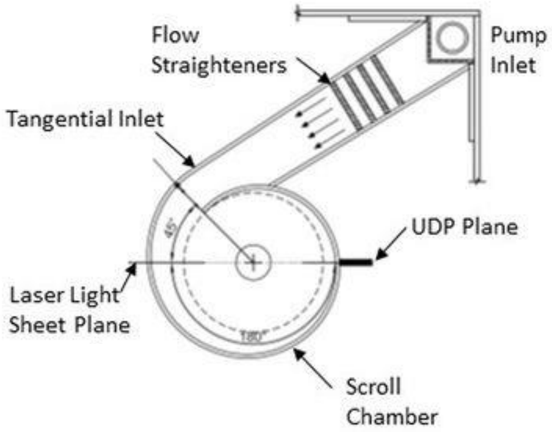

Figure 2: Plan view of the vortex chamber highlighting the inlet, flow straightening plates, laser light sheet plane used in earlier experiments and the UDP plane.

The inlet to the test models comprised a 0.065 m pipe entrance, 0.14 m perforated plates which homogenised the incoming velocity profile. Water was circulated through the system using a centrifugal pump (flow rate of 0 to 3.5 l/s) and was monitored using a magnetic flow meter and regulated using valves. The system delivered a monitoring resolution corresponding to maximum error bars for intake Froude and radial Reynolds numbers of $\mathsf{F_d} = v_z/\sqrt{gd} = \pm 0.019$ and $\mathsf{R_r} = Q/hr = \pm 34$, respectively. Approach flow depths h were expressed as a ratio of the constant orifice diameter $d = 67$ mm by h/d. Tests were performed for 6 approach flow depths corresponding to $h/d = 0.5$, 1.0, 1.5, 2.0, 2.5 and 3.0. This resulted in an experimental range of vortex Reynolds number $\mathsf{Re}_\Gamma = 1.38 \times 10^5$ to 2.07×10^5 and circulation numbers $\mathsf{N}_\Gamma = 5.8$ to 31.0. Further details on the hydraulic test rig can be found in [8].

2.2 Ultrasonic Doppler Profiling

The ultrasound Doppler velocity profile method (UDP method) was applied to analyse the secondary flow field in the free-surface vortex. The UDP principle utilises both echography and the Doppler effect to determine the position and velocity of a particle along an ultrasonic beam profile and is described in detail by Takeda [6],[9]. In this application, two-dimensional (2D) flow mapping was implemented by establishing a 7 × 7 array of ultrasonic transducers along the $r - z$ plane of the vortex to ascertain 2D velocity vectors [10]. The UDP system was supplied by MetFlow SA (Lausanne, Switzerland). Vertical transducers placed at 25 mm centres along the horizontal (r −axis) measured the axial velocity profiles and horizontal transducers spaced at 22 mm along the vertical (z−axis) as highlighted in Figure 3, 4 and 5. The array of transducers were carefully positioned to ensure that the plane was perpendicular to the primary flow field.

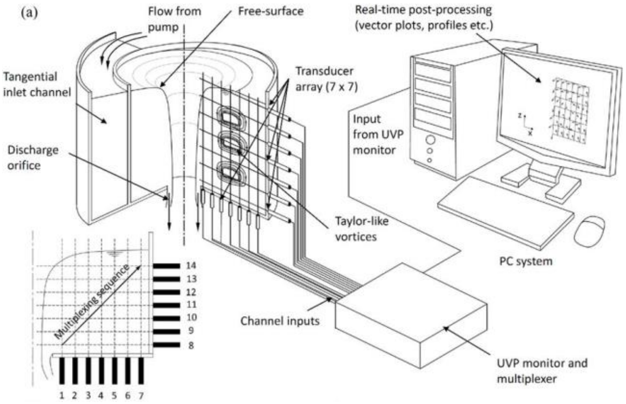

Figure 3: 3D schematic overview of the UDP flow mapping configuration highlighting the transducer array and multiplexing sequence.

A transmitting frequency of 4 MHz was used together with 4 cycles per pulse resulting in a minimum measurable channel width of 0.74 mm. The distance between channels was 0.74 mm. A pulse repetition frequency of 3.52 kHz was used resulting in an in-axis velocity resolution of 2.55 mm/s. 10 micron hollow glass spheres were used for seeding and the number of repetitions $\mathrm{N_{rep}} = 32$ was used resulting in a time resolution of 9 ms. The transducers were multiplexed in a diagonal fashion using the following trigger sequence with reference to Fig. 3 ($\mathrm{S_t}$ = 1–8, 2–9, 3–10, 4–11, 5–12, 6–13, 7–14). 40 flow maps were obtained for each test over a duration of 224 seconds. The 2D velocity fields were smoothed using kriging interpolation and post processed using ParaView.

https://doi.org/10.7795/810.20190809

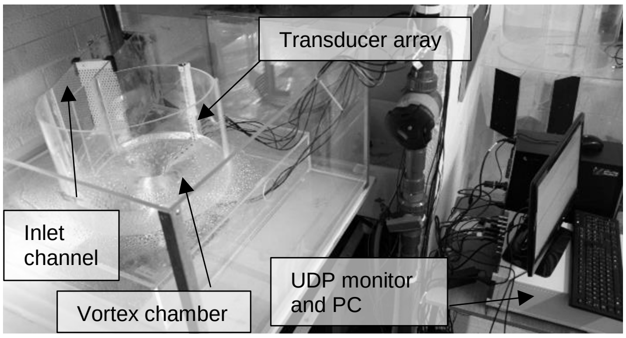

Figure 4: 3D schematic overview of the UDP flow mapping configuration highlighting the transducer array and multiplexing sequence.

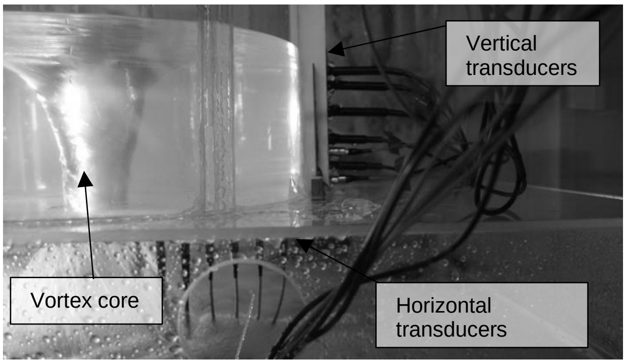

Figure 5: 3D schematic overview of the UDP flow mapping configuration highlighting the transducer array and multiplexing sequence.

3. Results

3.2 Radial and Axial Velocity Profiles

Figure 6 and 7 presents the instantaneous radial and axial velocity profiles for Transducer 8 (T8) and Transducer 4 (T4) respectively (see Figure 3). In the radial case, it can be seen that there was a switch between a positive velocity near the periphery of the chamber and a negative velocity near the outlet. This indicated that a separation point was forming at some region in the radial flow field.

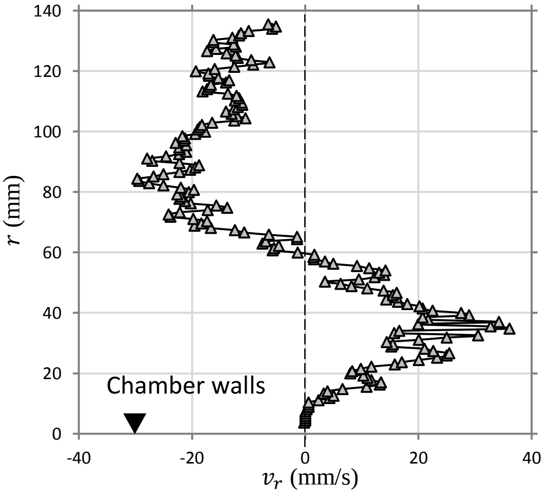

Figure 6: Radial velocity profile at transducers T8

In the axial case, T4 which is positioned close to this separation point highlighted that the velocity switches between positive and negative values at multiple positions throughout the vertical extent of the vortex chamber. Other velocity profiles (not shown here) identified that the axial velocity is in a strong upward direction near the periphery of the chamber.

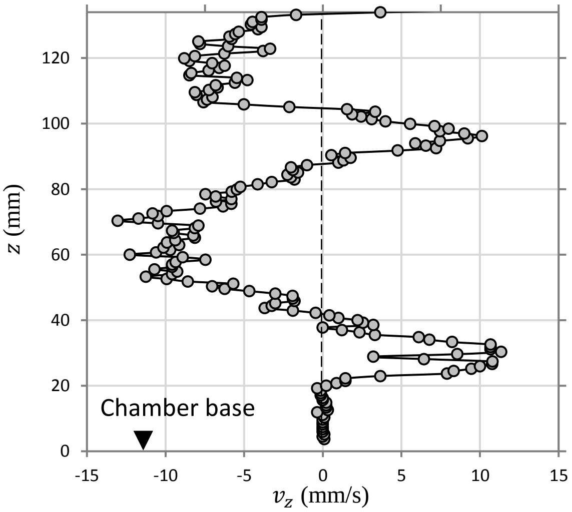

Figure 7: Axial velocity profile at transducers T4

3.3 Spatiotemporal Flow Map

Figure 8 presents a spatiotemporal map of the axial velocity profile over 0.3 seconds time period. The flow map indicates that the profile does not vary significantly within the time frame as indicated by the approximate positive and negative bands determined along the transducer 4 profile. The standard deviation of the axial velocity is also presented using data from 16 profiles.

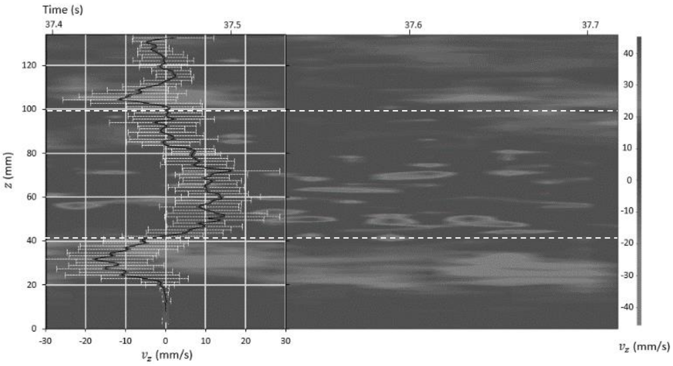

Figure 8: Axial velocity profile at transducers T4

3.4 Secondary Flow Field Vector Maps

Figure 9 (a) and 9 (b) presents the velocity vector maps generated for $Q = 0.635$ l/s and $Q = 1.1$ l/s respectively. Each vector map presents the global flow pattern across the secondary flow field. In each case, the 2D flow maps confirmed the existence of cellular vortices where loosely structured counter rotating vortex cells can be observed.

https://doi.org/10.7795/810.20190809

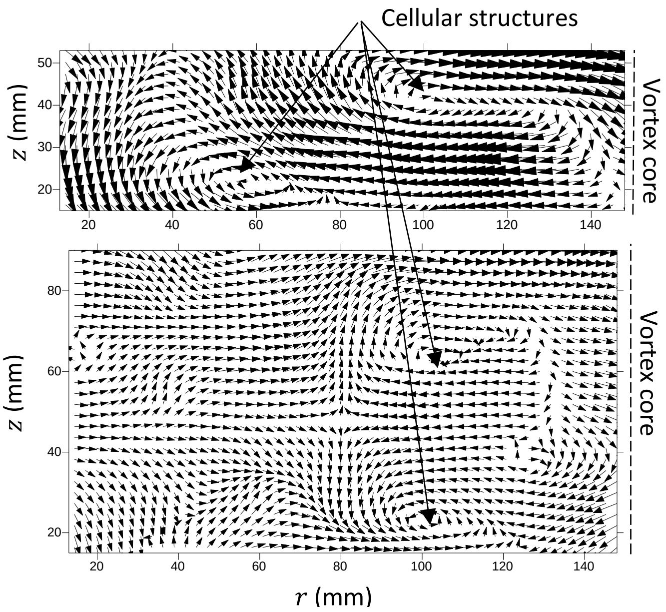

Figure 9: Velocity vector maps generated for (a) $h/d = 1.0$, $Q = 0.635$ l/s and (b) $h/d = 1.5$, $Q = 1.1$ l/s

4. Discussion

As discussed previously, using the horizontal and vertical transducers it was possible to isolate certain regions of the flow to consider instantaneous radial and axial velocities and flow patterns. For the purpose of the previous study carried out by the authors [5], the main aim of the UDP method was to identify signs of cellular flow structures which are recognisable through abrupt changes in the axial velocity field manifesting as a change from a negative velocity to a positive velocity. The change in the sign of the axial velocity is attributed to the UDP beam passing through the edge of a vortex cell. These cellular flow signatures were further substantiated in the generation of the 2D secondary flow field vector maps which also highlighted the structures.

The significance of these findings was that the free-surface vortex flow field, comparable in many ways to the classic Taylor-Couette flow, also exhibited similar instability mechanisms through the presence of Taylor-like vortices. The Taylor-like vortices form due to the presence of a centrifugal driving force which can develop for wall bounded vortex flows. It is pondered that such cellular structures are responsible for producing highly anisotropic turbulence conditions near the core region of a free-surface vortex and may perturb the primary flow field under higher energy conditions causing instability of the free-surface and air core.

Understanding further such flow structures using techniques such as UDP is useful knowledge for applications such as vortex drop shafts where stability of the vortex core is paramount to operation. This study outlines the value of utilising UDP for resolving such complex spatial and temporal flow behaviour.

Conclusions

In this study, an interesting application of the UDP technique was undertaken on a subcritical scroll type vortex chamber which yields application in vortex dropshafts and energy systems. The study highlighted that the UDP technique was valuable in deciphering the complex secondary flow field in a turbulent free-surface vortex comprising axial and radial velocity components which are a function of both space and time. The 7 x 7 array of UDP transducers can resolve a number of instantaneous radial and axial velocities throughout the secondary flow field to identify main global flow features. In addition, signatures for cellular flow structures were identified in the axial velocity profiles which was further substantiated by the velocity vector maps. The cellular flow structures identified were attributed to an unstable centrifugal driving force in the flow and can help explain why free-surface vortices tend to become unstable. Further work is being undertaken by the authors to determine time-series data to resolve turbulence characteristics in the near-field region of the vortex core using the UDP approach and data sets gathered.

References

[1] Hager, W.H. and Boes, R.M., 2014. Hydraulic structures: a positive outlook into the future. Journal of hydraulic research, 52(3), pp.299-310.

[2] Plant, J. and Crawford, D., 2016. Pushing The Limits Of Tangential Vortex Intakes: Is Higher Capacity And Flow Measurement Possible In A Smaller Footprint?. Proceedings of the Water Environment Federation, 2016(12), pp.4108-4136.

[3] Andersen, A., Bohr, T., Stenum, B., Rasmussen, J. J. & Lautrup, B. 2003 Anatomy of a bathtub vortex. Phys. Rev. Lett. 91(10).

[4] Mulligan, S., Casserly, J. & Sherlock, R. 2016. Effects of Geometry on Strong Free-Surface Vortices in Subcritical Approach Flows. J. Hyd. Eng. 142(11)

[5] Mulligan, S., De Cesare, G., Casserly, J. and Sherlock, R., 2018. Understanding turbulent free-surface vortex flows using a Taylor-Couette flow analogy. Scientific reports, 8(1), p.824.

[6] Takeda, Y. 2012. Ultrasonic Doppler velocity profiler for fluid flow. (Vol. 101) (Springer Science & Business Media)

[7] Taylor, G. I. 1923. Stability of a viscous liquid contained between two rotating cylinders. Phil. Trans. Roy. Soc. Lond. Ser. A, Math. Phys. 223, 289–343,

[8] Mulligan, S. 2015. Experimental and numerical analysis of three-dimensional free-surface turbulent vortex flows with strong circulation

[9] Takeda, Y. & Kobayashi, K. 1991. Ultrasonic flow visualization of transient behavior of taylor vortex flow. Exp. Numer. Flow Visual. ASME FED 128, P231–237

[10] Althaus, J.M.J., De Cesare, G. and Schleiss, A.J., 2016. Release of suspension particles from a prismatic tank by multiple jet arrangements. Chemical Engineering Science, 144, pp.153-164.

Instantaneous Flow Vector Measurement by a Pair of Ultrasound Doppler Instruments

Shun Nomura[1,2], Jumpei Hitomi[3], Giovanni De Cesare[2], Yuichi Murai[3], Yuji Tasaka[3], Yasushi Takeda[4] and Hide Sakaguchi[5]

[1]Mathematical Science and Advanced Technology, JAMSTEC, 3173-25 Showa-machi Kanazawa-ku Yokohama, 2360001, Japan
[2]Laboratoire de Constructions Hydrauliques, EPFL, Station 18, CH-1015, Lausanne, Switzerland
[3]Laboratory for Flow Control, Hokkaido University, Kita 13 Nishi 8, Kita-ku Sapporo, Hokkaido, 0608628, Japan
[4]Laboratory for Food Research Engineering, ETH Zurich, Rämistrasse 101, Zurich CH-8092, Switzerland
[5]Japan Agency for Marine-Earth Science and Technology, 2-15 Natsushima-cho Yokosuka, 2370061, Japan

Ultrasound Doppler velocity profiling is an effective method for instantaneous fluid velocity measurement along a measurement line. However, measuring vector components in multiple dimensions requires the development of multiple transducers, with the exact number depending on numbers of required cross-sections. This study provides a technique to extract two-dimensional velocity data along the bisector between two transducers by using a reasonable correction of the time lag or progress between the transducers. The observed time differences arise from geometry of the set-up and depend on the distance from the crossing point, intersection angle, and representative velocity in the main flow direction. The developed methodology is applied to the measurement of a quartz-particle-laden turbidity current produced in a lock-gate flume. After opening the gate, the suspension intrudes into the ambient water and is transported downstream according to a density difference. A convex-shape velocity distribution in the direction of stream flow and the vertically generated instabilities along the interface with ambient water are observed using this simple and convenient velocity measurement technique, which can characterize flow structure and aid statistical analyses of parameters such as vorticity.

Keywords: Flow field monitoring, Vector field, Double-cast UVP system, Turbidity current, Particle-laden flow

1. Introduction

An ultrasound Doppler velocity profiler (UVP) is an ideal tool for measuring flow behavior along its beam axis [1], [2]. However, vector profiling in multiple dimensions requires multiple transducers (TDX) arranged to give cross-sections, with the exact amount depending on the required dimensionality of the results and number of observation points (e.g. [3], [4]). There are some difficulties when analyzing velocity fields by UVP with high temporal and spatial resolution, especially in unsteady flow. We developed a system to approximate the vector field based on a pair of TDXs along the bisector of their measurement lines. Using the representative velocity and geometry in the area, the time lag and progress are corrected according to the distance from the crossing point, and the vector field can be detected in high resolution.

To validate the method's applicability, we investigated the vector field of a turbidity current generated in a lock-gate-type flume. We observed not only the abrupt velocity increase in the direction of the stream after intrusion of the flow but also the vertical uplift flow due to shear with the ambient water. The provided method proved useful in estimating the vector map, even for an unsteady flow.

2. Velocity measurement

Fig. 1 outlines the vector field measurement. At the cross-section of the measurement lines of two individual UVPs, the velocity components in the stream direction and normal to the bed (i.e. u and v, respectively) are represented as follows [5].

$$u = \frac{u_1 - u_2}{2\sin\alpha} \tag{1}$$

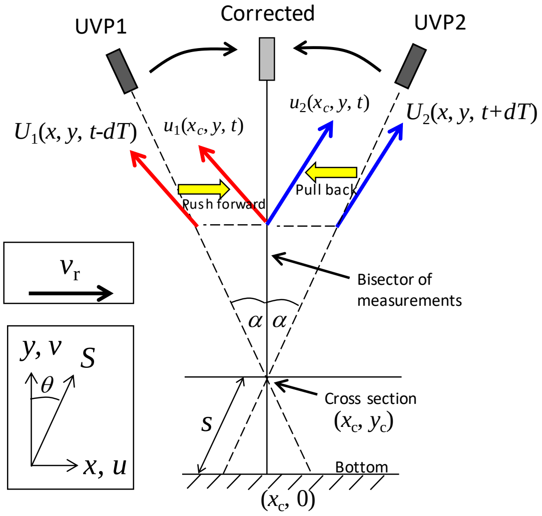

Figure 1: Overview of streamwise and bed-normal velocity measurement

https://doi.org/10.7795/810.20190809

$$v = \frac{u_1 + u_2}{2\cos\alpha} \qquad (2)$$

where u_1 and u_2 are the respective velocities measured by an upstream and a downstream UVP in cross-section, and α is the acute angle from the y axis.

The original velocity (U_1 and U_2) can be advected assuming that the rate of change of velocity components during a certain short time is sufficiently small relative to the ratio of the inspection area to the representative flow velocity (v_r) and that velocity components are preserved in that period. The time lag or progress (dT) occurs owing to the inclination of the measurement lines from the bed-normal direction, and is corrected as follows:

$$\mathrm{d}T = \frac{(S - s)\sin\alpha}{v_\mathrm{r}} \qquad (3)$$

where, s is the length from the bottom to the intersection (x_c, y_c) along the measurement line, and S is the length from the bottom to the target along the measurement line. The variables x, y and S are related as follows:

$$|x_c - x| = S\sin\alpha \qquad (4)$$

$$y = S\cos\alpha \qquad (5)$$

Based on equations (3) and (4), U_1 and U_2 are advected from the measurement lines to the bisector as

$$u_1(t, x_c, y) = U_1(t - dT, x, y) \qquad (6)$$

$$u_2(t, x_c, y) = U_2(t + dT, x, y) \qquad (7)$$

Applying equation (6) and (7) to (1) and (2) allows approximations of u and v at any t in $x = x_c$.

3. Results

3.1 Experimental setup

To validate the efficiency of the provided equations, we investigated the flow of a turbidity current produced in a lock-gate-type straight channel at the Laboratory of Hydraulic Constructions, EPFL. The experimental setup, coordinate definitions, and flow image are shown in Fig.2. The coordinate origin is set to be at the bottom of the gate. The flume is tilted at a slope of 1.38°, it is 4550 mm long, 210 mm high, and 143 mm wide. The gate was installed 2258 mm downstream from the beginning of the flume to divide the area into two. Before the experiment, the upstream reach was filled with the denser suspension with density ρ_1 = 1032 kg m^{-3}, whereas the downstream reach was filled with water with density ρ_0 = 1000 kg m^{-3} < ρ_1. Once the suspension had been well mixed and reached to predetermined density in the upstream reach, the gate was removed suddenly, and the denser suspension flowed under the ambient water with front velocity v_f. The sediment material for the turbidity current was quartz flour composed of SiO$_2$ with a mass density ρ_s = 2650 kg m^{-3}. Its grain size at D_{50} was 12.2 µm, and the settling velocity (v_s) for this size, based on Stokes' law, is 0.133 mm s^{-1}.

For the velocity measurement, a pair of 4-MHz UVP transducers which was synchronized using the external trigger of two UVP-Duo devices (Met-Flow, Switzerland) to start measurement, was installed at (x, y) = (951, 130) and (1059, 130) in mm at an inclination of 25° from the bed-normal (Fig. 2). The individual UVP measurements were continued before the head front had reached the end

Table 1: Parameters of UVP measurement

Parameter	Value
Ultrasound frequency (MHz)	4
Speed of sound (m/s)	1480
Maximum velocity range (mm/s)	179.1
Velocity resolution (mm/s)	1.399
Maximum measurement length (mm)	382.5
Number of channels	285
Number of profiles	4096
Sampling period for each profile (ms)	50
Window start (mm)	8.88
Window end (mm)	219.04
Channel distance(mm)	0.74
Channel width (mm)	0.74
Pulse repetition frequency (kHz)	1.936
Sampling rate (Hz)	20.0

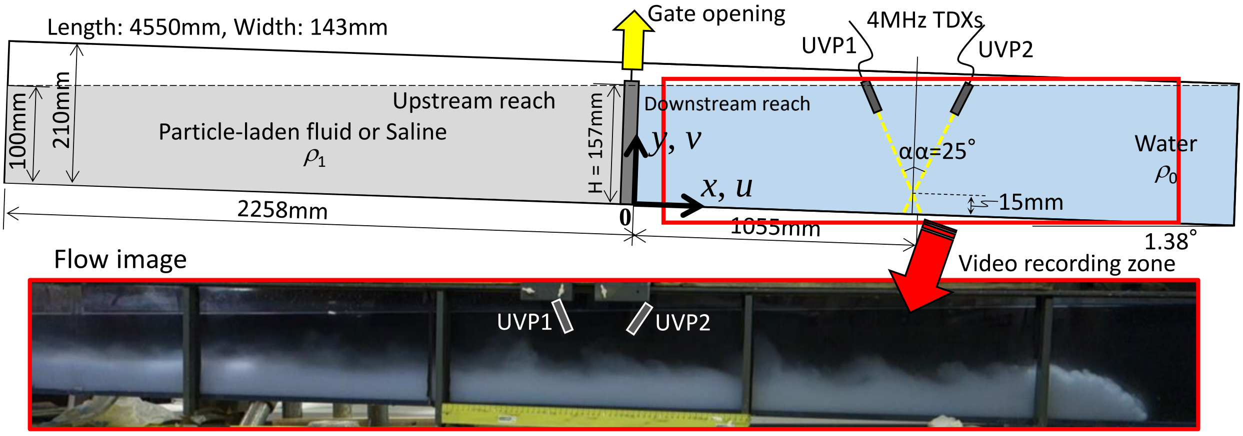

Figure 2: Experimental setup, coordinate definition, and flow image in downstream reach

of the flume. The UVP measurement parameters are listed in Table 1. The measurement lines of the pair of transducers crossed at (x_c, y_c) = (1055, 15) [mm], which was almost half the height of the produced flow.

3.2 Measurement Result

Fig. 3 shows the measurement of data by UVP1 and UVP2 after eliminating noise by a median filter in 3 × 3 velocity recording plots. A positive value denotes flow away from the TDX, and vice versa. Although both figures represent almost inverse values derived from the opposite measurement angles from the bed-normal, the presence of a vertical velocity leads to discrepancies in their distributions. Here the dashed lines at the height of 16.5 mm correspond to the position of the cross-section.

3.3 Streamwise and bed-normal velocity

Fig. 4 shows streamwise and bed-normal velocities (i.e. u and v) converted from Fig. 3 by equations (1) - (7). The front velocity (v_f = 76.4 mm/s) found from image analysis is a suitable representative velocity we confirmed that it remains constant in the measuring section owing to a suspension supply [6]. Here the absolute values of dT at y = 0 and 40 mm are 83 and 138 ms, respectively, which are less than the duration of three profiles and thus small enough to conclude that u and v can be transformed in the present experimental setup. Correcting the inclination of measurement lines improves the spatial resolution from 0.74 to 0.67 mm.

The abrupt intrusion of the turbidity current results in a specific rising slope along the interface with the ambient water in the streamwise direction. Simultaneously, a vertically lifting-up flow develops, as shown in Fig. 4. After reaching a maximum, streamwise velocity sharply decreases in the upper flow area, and a vertically downward flow develops, which indicates that the suspension is lifted by the shear with the ambient water and is entrained by the flow. This unsteady process due to flow arrival and passing is the typical for the head of a turbidity current [7]. After the passing of the head, we observe quasi-steady body area from t = 20 s. Due to shear with the bottom, the streamwise velocity there converges to zero; it initially increases in the vertical direction, but later decreases with height due to shear with the upper ambient water. As a result, the velocity maximum in the streamwise direction occurs at a specific height. To satisfy continuity in the area, a negative streamwise velocity develops in the upper area as a counterflow. A pair of positive and negative v layers is observed at the upper and lower zones relative to the height of the velocity maximum, implying that the suspended sediments are vertically separated due to the intrusion of the high velocity suspension in the streamwise direction, as reported by [8], [9].

4. Discussion

Fig. 5 shows the absolute and relative vector fields. Here, the velocity magnitude is normalized by its maximum value. In the relative velocity fields, the averaged velocities from 30 to 40 s (i.e. u = 21.8 and v = 1.2 mm/s) are extracted from absolute values. The relative vector field clearly shows the upward and backward flow after the flow arrival. There is evidently strong shear at the bottom and at the interface between the turbidity current and the ambient water.

To evaluate the flow structure in the turbidity current, normalized vorticity distributions are depicted in Fig. 6 according to the following equation:

$$\omega \approx \frac{\Delta v}{\Delta x} - \frac{\Delta u}{\Delta y} \tag{8}$$

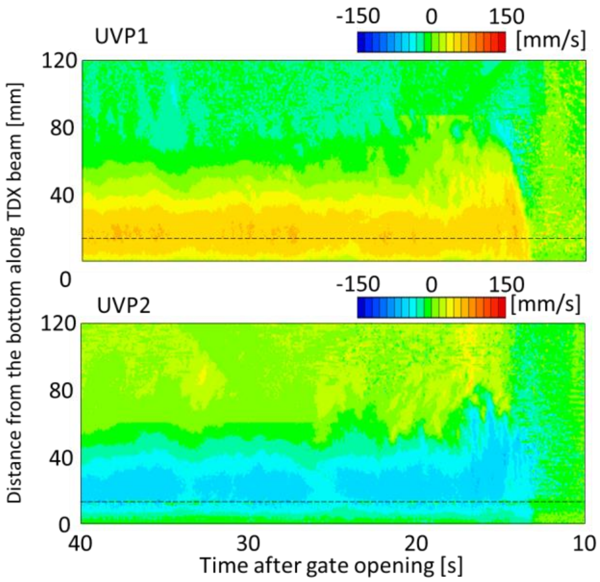

Figure 3: Data measured by UVP1 (upper) and UVP2 (lower). Dashed lines indicate the cross-section height

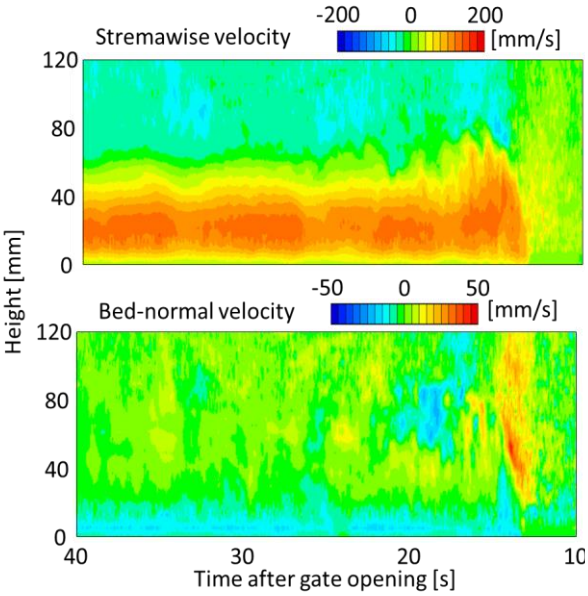

Figure 4: Streamwise (upper) and bed-normal (lower) velocity distribution

Where, ω is vorticity, Δx is the product of Δt and v_f (i.e., $dx = dt\ v_f$ = 3.8 mm), and dy is fixed to six times the channel width (i.e., dy = 4.0 mm). After the flow arrival, positive vorticity develops along the sloping interface with the ambient water. This indicates that an anti-clockwise flow develops due to unsteady shear process. The body part shows negative and positive layers. As discussed in section 3.3, the turbidity current held back by the rigid bottom and static ambient water in the upper area. Because of the instabilities that results from these factors, the velocity maximum is located at a specific height and the velocity distribution becomes layered. While the vorticity is high at the bottom, its distribution is narrower than that in the upper area, indicating that the material characteristics at the boundaries cause such discrepancies and influence the disturbances.

5. Summary

We developed a method for instantaneous flow vector measurement using a pair of ultrasound Doppler instruments. By correcting the time lag and progress owing to the different positions of the measurement lines, we succeeded in approximating velocity components with high temporal and spatial resolution. The developed method is applied to investigate the dynamics of an experimentally produced turbidity current. In addition to the typical flow structure in the current such as an unsteady uplift flow in the head and a quasi-steady flow in the body, we observe some noteworthy flow dynamics such as entrainment after the passing of the upper head part, vertical separation around the velocity maximum, and other finer instabilities in the flow. Overall, the proposed method can effectively observe the 2-D velocity structure. Although it is relatively simple and only in the validation phase, the method may be applicable to a wide range of measurements. Extending the set-up to observe the 3-D structure would be possible using a triple-cast UVP system and applying the same proposed system to correct the time lag or progress.

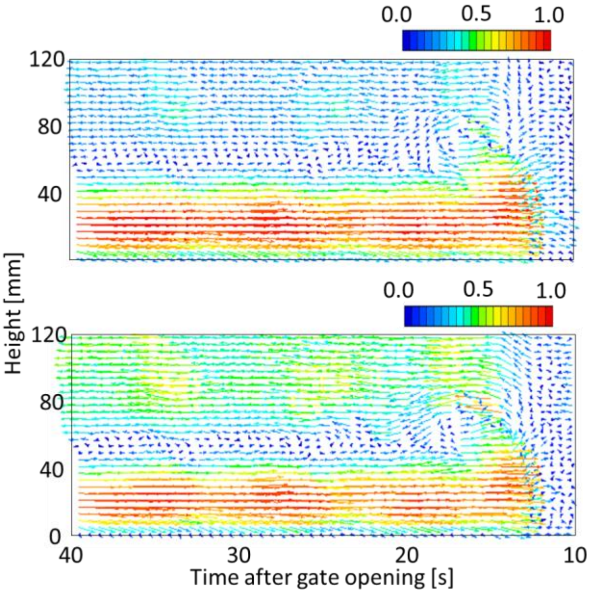

Figure 5: Normalized absolute (upper) and relative (lower) velocity vector

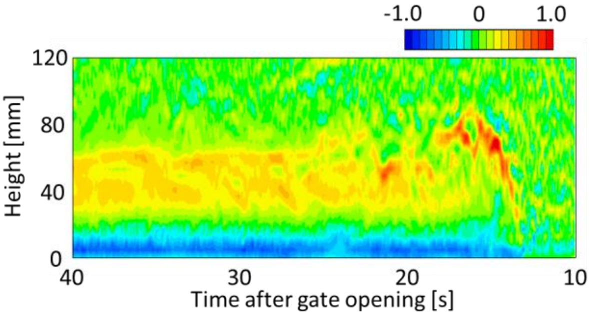

Figure 6: Normalized vorticity distribution

Acknowledgments

The authors thank Dr. S Chamoun S and Dr. D Nishiura for their technical assistance with the experiments and helpful comments. This work was supported by the JAMSTEC Researcher Overseas Dispatch Budget and a Grant-in-Aid for Young Scientists (15K18115) from the Japan Society for the Promotion of Science.

References

[1] Takeda Y: Measurement of velocity profile of mercury flow by ultrasound Doppler shift method, Nucl. Technol. 79 (1987), 120-124.

[2] Takeda Y: Development of an ultrasound velocity Profile monitor, Nucl. Eng. Design 126 (1991), 277-284.

[3] Nauber R *et al.*: Dual-plane Ultrasound Array Doppler Velocimeter for Flow, 8th ISUD, (2012), 7-10.

[4] Andreew O & Thess A: R *et al.*: Two-dimensional flow mapping past a circular cylinder using a 7-channel UDV system, 8th ISUD, (2012), 11-14.

[5] Takeda, Y *et al.*: Ultrasonic Doppler velocity profiler for fluid flow (Fluid mechanics and its applications) (2012), Springer, New York.

[6] Hitomi, J *et al.*: Extensive use of UVP data from experimental turbidity currents to evaluate their flow structure, The Visualization Society of Japan annual conference, (2017). (in Japanese)

[7] Baas JH *et al.*: Coupling between suspended sediment distribution and turbulence structure in a laboratory turbidity current, J Geophys Res 110 (2005), C11015.

[8] Gray TE *et al.*: Longitudinal flow evolution and turbulence structure of dynamically similar, sustained, saline density and turbidity currents, J. Geophy. Res. 111 (2006), C08015.

[9] Nomura S *et al.*: Sediment mass movement of a particle-laden turbidity current based on ultrasound velocity profiling and the distribution of sediment concentration, GSL Special Pub. (2018).

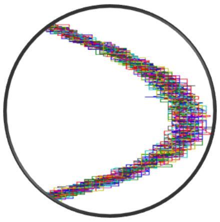

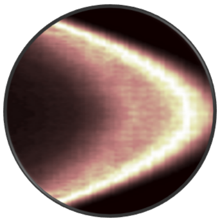

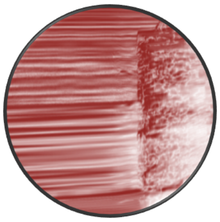

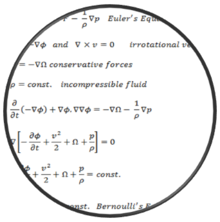

FlowBiz

超音波流速分布計測を中心として1998年より活動しています．世界中の分布計の開発にたずさわり，多くの経験やノウハウを使ったサービスを提供しています．日本国内での機器提供やシステムの構築，計測法などのお手伝いをしています．

MET-FLOW
Lausanne - Switzerland

スイス・メットフロー社の科学計測用の流速分布計測装置です．UVPの元祖的存在で，すでに15年以上，世界で100台以上の実績がある装置です．

Our UVP-DUO instrument controlled by a remote computer via Ethernet

3D measurement in a river bend with macro rugosities measured with UVP-DUO

Spatio-temporal velocity map of a Taylor-Couette flow measured with UVP-XW

News

Met-Flow new website to be released soon this Summer
More info in our latest news column...

Non intrusive

Ultrasound Doppler Velocity Profiling (UVP) method features a line measurement obtaining several 1D aligned velocity points away from the measuring probe, thus non-intrusive.

Opaque liquids

UVP method can be applied to opaque liquids as it is ultrasound-based, opening its scope to non-Newtonian highly viscous liquids such as liquid metals, food suspensions, etc...

Spatio-temporal

UVP method provides velocity information as a function of both space and time in an unidimensional Eulerian frame. Combining several probes allows 2D or 3D velocity measurements.

Design: Carbon317 | Technology: E-UNIT

UBERTONE

フランス・ユーバートーン社が開発した，環境計測用の流速分布計です．河川や湖水・開渠での測定のために開発されました．

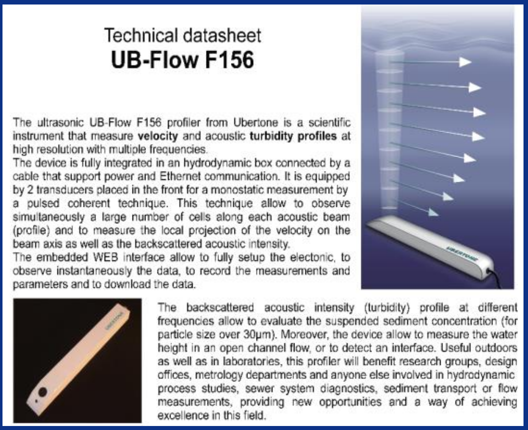

Technical datasheet

UB-Flow F156

The ultrasonic UB-Flow F156 profiler from Ubertone is a scientific instrument that measure **velocity** and acoustic **turbidity profiles** at high resolution with multiple frequencies.
The device is fully integrated in an hydrodynamic box connected by a cable that support power and Ethernet communication. It is equipped by 2 transducers placed in the front for a monostatic measurement by a pulsed coherent technique. This technique allow to observe simultaneously a large number of cells along each acoustic beam (profile) and to measure the local projection of the velocity on the beam axis as well as the backscattered acoustic intensity.
The embedded WEB interface allow to fully setup the electonic, to observe instantaneously the data, to record the measurements and parameters and to download the data.

The backscattered acoustic intensity (turbidity) profile at different frequencies allow to evaluate the suspended sediment concentration (for particle size over 30µm). Moreover, the device allow to measure the water height in an open channel flow, or to detect an interface. Useful outdoors as well as in laboratories, this profiler will benefit research groups, design offices, metrology departments and anyone else involved in hydrodynamic process studies, sewer system diagnostics, sediment transport or flow measurements, providing new opportunities and a way of achieving excellence in this field.

超音波流速分布流量計 UdFlow
Ultrasonic Doppler Velocity Profiling Flow meter

東京電力が開発した超高精度の水流量計測装置．流量計較正等に力を発揮します．

流動場についてのいろいろな研究，特に超音波流速分布計の応用の支援をしています．

- 超音波トランスジューサーの販売
- トランスジューサー支持用治具の製作

特殊な流量計測法の開発

- uMFlow – 混相流量計
- uGFlow – ガス流量計の開発

FlowBiz Research Inc.
フロウビズ・リサーチ

178-0065
東京都練馬区西大泉1-32-13
Tel：03-5935-0555
Fax：050-3737-0559
Mail：kt@flowbiz.jp
URL：www.flowbiz.jp

各社，各サービスの資料を個々に用意しておりますので，お問い合わせください．